Numerical Modelling of Fretting Fatigue Crack Nucleation
under Out-of-Phase Loading

Numerieke modellering van scheurnucleatie bij frettingvermoeiing
met belasting uit fase

Nadeem Ali Bhatti

Promotor: prof. dr. ir. M. Abdel Wahab
Proefschrift ingediend tot het behalen van de graad van
Doctor in de ingenieurswetenschappen: werktuigkunde-elektrotechniek

UNIVERSITEIT
GENT

Vakgroep Elektrische Energie, Metalen, Mechanische Constructies en Systemen
Voorzitter: prof. dr. ir. L. Dupré
Faculteit Ingenieurswetenschappen en Architectuur
Academiejaar 2018 - 2019

ISBN 978-94-6355-176-2
NUR 978
Wettelijk depot: D/2018/10.500/94

Promoter

prof. Magd Abdel Wahab
Ghent University, Belgium

Committee Members

prof. Patrick De Baets (Chair)
Ghent University, Belgium

prof. David Nowell
Imperial College London, UK

prof. Magd Abdel Wahab
Ghent University, Belgium

prof. José Alexander Araújo
University of Brasilia, Brazil

prof. Wim Van Paepegem
Ghent University, Belgium

dr. Xiaowei Wang
Ghent University, Belgium

Research Institute

Laboratory Soete
Department of Electrical Energy, Metals, Mechanical Constructions and Systems
Faculty of Engineering and Architecture
Ghent University

Technologiepark 903
B-9052 Zwijnaarde
Belgium

Email: NadeemAli.Bhatti@UGent.be, engr.nabhatti@gmail.com
http://www.soetelaboratory.ugent.be

This thesis is dedicated to my parents, Sakhawat Ali Bhatti and Zerina Sakhawat (late), brother Nauman Ali Bhatti, sister Erum Zulkifl and all teachers, who have enlightened the path of learning, motivated me to seek further knowledge and provided an unconditional support, to bring me this far.

ACKNOWLEDGEMENTS

First of all, I want to thank my supervisor, prof. dr. ir. Magd Abdel Wahab, for guiding and motivating me throughout the PhD degree. His experience, vision and ideas always provided a way forward to achieve research objectives. Specially, I appreciate his valuable contribution for paper writing and support in publishing my work. Leading the group with high standards of hard work and concern, he always motivated me to work one step further. I am also thankful to the committee members who reviewed my thesis and gave their respected suggestion to improve and finalize the thesis.

The work experience at Laboratory Soete of Ghent University is inspirational and collaborative. The success always come with a team work and synergic environment. Specially, the contribution of whole Finite Element Group is commendable. The formal and informal group meetings and discussions helped to comprehend the scientific concepts and provided a platform to share and enhance knowledge. Therefore, I want to thank all colleagues, researchers, students and friends of laboratory, who provided technical and non-technical support during my work. In addition to present group member, I also appreciate the work of the former students who provided the basis for the start of start and provided initial support in research and also helped to settle at a new place.

The administrative support also paly important role to manage everyday work. In this regard, I want to thank our laboratory secretory Mrs. Georgette D'hont, who always willing helped for all official and personal matters. In addition, I appreciate the support provided by the UGent library, to provide all publications and research papers.

The stay at Ghent University provided a great opportunity to work with professionals of different nationalities, culture and customs. The cosmopolitan environment of the city and lingual unbiasedness also made the stay pleasant and comfortable. It also gave me the opportunity to make new friends, learn different cultures and explore new ventures. I also want to thank all those people and friends, other than Ghent University, who gave me moral support in all ups and downs during my journey.

I would like to thank Government of Pakistan to provide scholarship for the PhD degree. In addition, I would also like to thank prof. dr. ir. Magd Abdel Wahab and Gent University for co-sponsoring my work, providing equipment and facilities at university, and expenses for conference travelling and participation.

Lastly, special thanks to my wife Rabia Naz, son Haziq Ali Bhatti and daughter Zenia Nadeem, for their love, faithful support, encouragement and comfort that allowed me to focus completely on my work.

Nadeem Ali Bhatti
Ghent University
2018.

TABLE OF CONTENTS

LIST OF TABLES

LIST OF FIGURES

LIST OF SYMBOLS AND ABBREVIATIONS

Symbols

a	Semi contact width
a_{anal}	Analytical semi contact width
a_{FEM}	Numerical semi contact width
a_{cric}	Critical contact size
A	Surface area
A	Material constant for CDM-PL
A_D	Total surface area of damage
A_{sp}	Area of slip plane
b	Fatigue strength exponent
b'	Fatigue strength exponent in torsion
b_s, b_p	Width of specimen and pad
b_1	Material constants for Chaboche model
b_2	Material constants for Chaboche model
B	Strain displacement transformation matrix
c	Semi stick zone width (contact mechanics)
c	Fatigue ductility exponent (strain life equation)
c'	New stick zone (contact mechanics)
c'	Fatigue ductility exponent in torsion (strain life equation)
c_1	Material constants for Chaboche model
C	Cylindrical pad
C	Constant for fretting damage parameter
C	Crack growth rate coefficient
C	Damage strength
C_c	Composite compliance of both bodies
C_1, C_2, C_3, C_4	Constant for SSR parameter and BM parameters
d_x	Relative tangential displacement
d_y	Gap between two bodies

$\mathbf{d}$	Vector of d_y
D	Damage variable
D_c	Critical damage
D_{n+1}	Damage after $n+1$ cycles
D_{N_i}	Damage at crack initiation stage
D_0	Initial damage
D_j	Damage in j direction
e	Stick zone offset
E	Extrusion
E_i	Elasticity modulus of body i
$\tilde{E}$	Effective elasticity modulus
f	Representative function
F	Flat pad
F	Applied load
F_s	Force along slip direction
$F1$	Ruiz wear parameter
$F2$	Ruiz initiation parameter
$\mathbf{F}$	Force vector
$\mathbf{F}^{ext}$	External force vector
$\mathbf{F}^{int}$	Internal resistance of material
$g_i(\theta)$	Functions for plane stress or strain conditions
G	Shear modulus
h	Number of elements in a domain
H	Hydrostatic stress
H_{mean}	Mean hydrostatic pressure
H_{max}	Maximum hydrostatic pressure
I	Intrusion
I	Intensity of stress singularity
I_c	Crack initiation criterion based on stress singularity
I_s	Isotropic drag strength
J_2	Second invariant of deviatoric stress tensor

k	Material constant for SI approach
k_1	Material constant for Findley parameter
k_2	Material constant for BM parameter
K_I, K_{II}, K_{III}	Stress intensity factor for modes I, II and III
K_{max}, K_{min}	Maximum and minimum stress intensity factors
K_s	Spring stiffness
K'	Cyclic strength coefficient
$\mathbf{K}$	Tangent stiffness matrix
$\mathbf{K}_0$	Initial stiffness matrix
l	Crack length
l_i	Initial crack length
l_f	Failure crack length
l_e	Element size
l_{th}	Threshold crack length
l_s, l_p	Length of specimen and pad
L_i^N	Loading in j direction
m	Crack growth rate exponent
m	Fitting parameter for SSR
m	Plastic flow exponent
m	Power constant in Ramberg-Osgood equation
M_0	Material constants for Chaboche model
n	Material constant in effective stress intensity factor range
n	Constant in FS parameter
n	Number of nodes for averaging process
n	Number of jumps for wear cycle
n	Constant for fretting damage parameter
n'	Cyclic strain hardening exponent
$\boldsymbol{n}$	Normal to slip plane
N	Number of cycles
N_f	Number of cycles to failure

N_i	Number of cycles to crack initiation
N_p	Number of cycles to crack propagation
$N_{i,j}$	Number of cycles to initiation for cycle *j*
$\overline{N^{pred}}$	Mean predicted life
$N_{i\text{-}OP}$	Initiation life for out of phase loading
$N_{i\text{-}IP}$	Initiation life for in phase loading
O	Order of
p	Contact pressure
$\dot{p}$	Micro plastic strain rate
p_0	Peak contact pressure
P	The normal contact load
q	Shear traction
q_p	Perturbed shear traction
Q	Tangential load
Q_c	Critical tangential load
Q_{max}	Maximum tangential load
r	Distance from the singularity point or crack tip
r_c	Critical radius for stress averaging
r_i	Distance from the singular point at critical conditions
R_{SWT}	Crack nucleation risk
R_τ	Shear stress ratio
R_a	Amplitude ratio
R_σ	Stress ratio
R_v	Triaxiality function
R_M , R_m	Maximum and minimum of a function depending on triaxiality function
R_P	Normal load ratio
R_i	Radius of contacting surface *i*
R_{SD}	Range of standard deviation
$\mathbf{R}$	Residual vector
s_o	Damage exponent

S	Spherical pad
S	von Mises stress
S_M, S_m	Maximum and minimum von Mises stress
SD_x	Normalized standard deviation
SD_N	Standard deviation
t	Thickness of part
$ts,\ tp$	Thickness of specimen and pad
T	Time
T	Transpose (in superscript)
T_r	Triaxiality ratio
u	Applied displacement
u_n	Displacement vector for n variables
u_{xi}	Displacement of body i in x direction
u_0	Initial point for Newton's method
u_i	Subsequent points for Newton's method
u_{yi}	Displacement of body i in y direction
$u_i(r,\theta)$	Displacement near crack tip
$\mathbf{u}$	Displacement vector
U_x, U_y	Displacement in x and y direction
$\mathbf{U}$	Partial derivative of **d** w.r.t **u**
v_i	Poisson's ratio for body i
v_e	Elastic Poisson's ratio
v_p	Plastic Poisson's ratio
V_c	Volume for averaging
$\mathbf{V}$	Partial derivative of **U** w.r.t **u**
v , w	Constants depending on Poisson's ratio
w_e	Total elastic strain energy density
w_f	Weight function
W_{DP}	Strain energy based damage parameters
x_i	Initial guess for Newton iteration

$\bar{x}$	Normalized mean life
$\overline{X_i}$	Mean crack initiation location
x, y	Cartesian coordinate system
x', y'	Rotated coordinate system
y_i	Value of function at x_i
y_c	Crack depth for averaging
y_d	Fixed crack initiation depth
Y	Strain energy release rate
z	Mesh scaling factor
Z	Geometry influence factor
~	Range of values
α	Material parameter for CDM-NPL
β	Material constants for Chaboche model
κ	Bulk modulus
κ_r	Relative curvature
σ	Local stress
$\sigma_c, \sigma_m, \sigma_f$	Local stress for coarse, medium and fine mesh
σ_{ij}^d	Deviatoric stress
$\sigma_{ij}(r, \theta)$	Stresses near crack tip
$\sigma_{max}, \sigma_{min}$	Maximum and minimum applied stress
σ_x, σ_y	Stress at x and y face of an element
σ_a	Stress amplitude
σ_m	Mean stress
σ_f'	Fatigue strength coefficient
σ_n^{max}	Maximum normal stress
σ_{f-1}	Fatigue limit in tension
σ_u	Ultimate tensile strength
σ_y	Yield strength
σ^i	Back stress for i^{th} slip system
$\sigma_{1max,c}$	Critical maximum stress

$\tilde{\sigma}$	Effective stress
σ^*	Damage equivalent stress
σ_R	Reaction stress
σ_x'	Normal stress in rotated coordinates
σ_{DP}	Stress based damage parameters
$\boldsymbol{\sigma}$	Internal stress vector
τ^i	Resolved shear stress for i^{th} slip system
τ_{f-1}	Fatigue limit in torsion
τ_f'	Fatigue strength coefficient in shear
τ_{xy}	Shear stress
$\tau_{x'y'}$	Shear stress in rotated coordinates
τ_s	Shear stress resolved in the slip direction
τ_{cr}	Resolved critical shear stress
$(\tau d_x)_{th}$	Threshold wear parameter
τ_{min}, τ_{max}	Maximum and minimum shear stresses
ε_{ij}^d	Deviatoric strain
ε_e^h	Hydrostatic strain
$\varepsilon_1, \varepsilon_2, \varepsilon_3$	Principal strains in three directions
ε_f'	Fatigue ductility coefficient
ε_x'	Normal strain in rotated coordinates
ε_{DP}	Strain based damage parameters
$\boldsymbol{\varepsilon}$	Strain vector
γ_f'	Shear fatigue ductility coefficient
$\gamma_{x'y'}$	Shear strain in rotated coordinates
$\dot{\gamma}^i$	Plastic shearing strain rate on the i^{th} slip system
$\dot{\gamma}_0$	Reference shear strain rate
Π	System potential function
Π_{12}	Potential energy of bodies 1,2
Π_s	Potential energy of contact surface
λ	Lagrange multipliers

$\boldsymbol{\lambda}$	Vector of Lagrange multipliers
θ	Angle between normal to slip plane and specimen axis
θ	Orientation from the crack tip to the desired point
θ	Plane orientation
θ_h	Critical plane angle with *x* axis
θ_v	Critical plane angle with *y* axis
θ_c	Critical plane
θ_p	Principal plane orientation
ϑ	Angle between slip direction and specimen axis
$\emptyset$	Phase difference
φ	Dissipation potential function
μ	Coefficient of friction
η	Experimental constant for FRD parameter
ω	Singularity exponent
ω_c, ω_m, ω_f	Singularity exponent for coarse, medium and fine mesh
ξ	Experimental constant for FRD parameter
$\Delta\sigma$	Stress range
$\Delta\tau$	Shear stress range
$\Delta\tau_{max}$	Maximum shear stress range
ΔK	Stress intensity factor range
ΔK_{eff}	Effective stress intensity factor range
$\Delta K_{eff,EH}$	ElHaddad stress intensity factor range
ΔK_{th}	Threshold tress intensity factor range
Δd_x	Relative slip range
$\Delta\varepsilon$	Strain range
$\Delta\varepsilon_e$	Elastic strain range
$\Delta\varepsilon_p$	Plastic strain range
$\Delta\varepsilon_{p,max}$	Maximum principal stain range
$\Delta\varepsilon_n$	Normal strain range
$\Delta\varepsilon_1$	Principal strain range in *x* direction

$\Delta\gamma_{max}$	Maximum shear strain range
ΔN	Wear cycles
ΔW	Virtual strain energy
ΔW_e	Elastic strain energy
ΔW_p	Plastic strain energy
ΔW_I, ΔW_{II}	Virtual strain energy for mode I and II
ΔX_i	Crack initiation location range

Abbreviations

avg.	Average
BE	Bhattiacharya and Ellingwood model
BM	Brown-Miller parameter
CAL	Constant amplitude loading
CP	Critical plane approach
CDM	Continuum damage mechanics approach
CDM-PL	Continuum damage mechanics for proportional loading
CDM-NPL	Continuum damage mechanics for Non-proportional loading
CL	Crossland parameter
DV	Dang Van parameter
D_{fret2}	Fretting specific parameter
DP	Damage parameter
DP^{PF}	Damage parameter for plain fatigue
DP^{FF}	Damage parameter for fretting fatigue
Exp., exp.	Experiment
FEA	Finite element analysis
FEM	Finite element methods
FP	Findley parameter
FRD	Fretting related damage parameter
FS	Fatemi-Socie parameter
FF	Fretting fatigue
FSI	Fatigue strength index

HCF	High cycle fatigue
KT	Kuhn-Tucker
IP	In phase
LCF	Low cycle fatigue
LFEM	Linear Elastic Facture Mechanics
MD	McDiarmid parameter
MSSR	Modified shear stress range parameter
MPC	Multipoint constraint
Nr.	Number
NLCD	Non-Linear-Continuous-Damage
OP	Out of phase
PRH	Prismatic Hull parameter
PSWF	Principal stress weight function
PEEQ	Maximum equivalent plastic strain
RVE	Representative volume element
SSR	Shear stress range parameter
SI	Stress invariant approach
SWT	Smith-Watson-Topper parameter
SI	Stress invariant approach
SN	Stress life
vol	Volume
VAL	Variable amplitude loading
XFEM	Extended finite element methods

Mathematical Operators

$f'(x)$	Derivative of $f(x)$
δ	Variational operator
δ_{ij}	Kronecker delta
Δ	Forward difference operator

SUMMARY

The phenomenon of fretting fatigue occurs in most of engineering application and can lead to failure. The term, fretting, implies continuous small movements between contacting bodies, causing surface damage or initiation of a crack. In engineering terms, fatigue refers to the cyclic loading of a component. Thus, the term fretting fatigue describes the study or behaviour of engineering components that are in contact and undergo cyclic loading. Fretting fatigue phenomena is quite similar to plain fatigue, however, with an addition of contact interaction, another variable also contributes in the failure process. The topic of fretting fatigue is under study for about a century now and in many different fields, such as locomotive, automotive, civil, machine design, marine and aerospace industry.

The mechanical failures under plane and fretting fatigue can be characterized by two main stages. The first stage is generally referred as nucleation phase, whereas the growth of damage or crack, in the second stage, is known as propagation phase. Although there is no unified or standardized definition of crack nucleation length, it is generally accepted that damage up to mesoscale or few grain size of the material is considered as the length for nucleation phase. The term nucleation includes the process, from the start of loading to the development of flaw of this length scale. Therefore, nucleation is a damage accumulation process, which leads to crack initiation. The lifetime taken by the material during the nucleation phase or up to crack initiation is therefore dependent on its definition.

The mechanism of each crack phase is different, and is therefore required to be dealt with separately. The damage nucleates near to or along maximum shear planes, which are activated due to reversal of loading. These planes are known as slip planes, where damage accumulates and finally results in an observable void or crack. Under fretting fatigue, mostly the location of crack initiation is found near the contact edge and at the surface of the component. Therefore, apart from loading magnitude and material, surface roughness, coefficient of friction, slip amplitude and geometry of contacting bodies also affect nucleation process. All variables collectively define fretting fatigue crack initiation life.

Fretting fatigue or crack nucleation can be studied using different methods, which include analytical methods, experimental tests and numerical methods. The analytical solutions may provide simplified solution with some assumptions and only for simple geometries. However, it can be used to verify the results or to authenticate the design methodology. The experimental tests provide better understanding of the phenomena. The most common laboratory configuration includes cylinder pad and flat specimen or flat pad and flat specimen configuration. There are two

important factors which create difficulty during tests. Firstly, the damage nucleates under the contact surface, therefore it is difficult to monitor the evolution of damage. Secondly, generally specimens are analysed and data is recorded once specimen is broken. To evaluate damage at intermediate stages, the test is required to be stopped for analysis. In addition, obtaining damage parameters or required constants at the intermediate stage is also a challenging task. This brings us to the significance of finite element method, which enables to overcome these challenges. Firstly, it provides great flexibility to model complex geometries or real life structures. Secondly, it also allows to monitor intricate details throughout the complete load history. However, it does not imply that finite element method suffices the complete requirement, it also has its own limitations. Firstly, a simple scenario is modelled, whereas the actual or practical configuration is much more complicated. As an example, the material is generally considered to be isotropic and homogenous, whereas in reality it is not. Secondly, environmental factors are generally neglected. Thirdly, few other variables are sometimes assumed to be constant, such as temperature, coefficient of friction, wear or damage rate, etc., which may change during the complete load history. Therefore for better understanding of the crack nucleation phenomena, a good strategy includes; (a) the application of finite element method, (b) the verification of methodology by analytical solution, and (c) the validation of results by experimental tests. The present thesis therefore adopts this strategy, i.e. the numerical results are verified by analytical solution and validated by experimental results from literature.

In the present work, different boundary conditions are examined and compared to develop reliable numerical models. The main difference between different numerical models is, how to model the tangential load. Finally, one model is selected based on results, ease of application of loads and computational efficiency. For analysis of crack nucleation, the damage criteria or models can be classified into four different groups or approaches. These approaches include, critical plane approach, stress invariant approach, fretting specific parameters and continuum damage mechanics approach. This thesis also includes comprehensive literature review, explaining basic idea and formulation of these approaches, along with the application to fretting fatigue problems.

Using these approaches, the main aspects analysed includes, variation of contact stresses and slip amplitude, prediction of crack initiation site, initial crack orientation and fretting fatigue life. Most of the work so far in fretting fatigue, in the literature, is carried out for in phase loading conditions. However, in practical application, components can experience different loads with phase difference between them, therefore it is interesting to analyse contact interaction using loading phase difference. Since under fretting fatigue, multiaxial stress state exists, therefore stresses can be non-proportional especially if the loads are applied with phase difference. The present thesis therefore focuses on application of various damage models and approaches, under out of phase loading condition. Different approaches and damage models are implemented and

their efficacy to determine crack initiation location, orientation and lifetime, are compared. Moreover, a continuum damage mechanics model is proposed for non-proportional loading conditions.

From the present work it is found that fretting fatigue crack initiation location, orientation and lifetime are influenced by loading amplitudes and phase difference. The crack initiation location depends upon two conditions; (a) if the phase difference is applied between axial bulk stress and tangential load or (b) between normal contact load and other two loads (axial bulk stress and tangential load). For initial crack orientations, the phase difference may introduce more number of planes that can undergo crack initiation. The crack initiation life may increase or decrease with loading phase difference, depending upon, type and degree of phase difference. However to generalize the percentage increase or decrease with phase angles, further experimental work with different material and loading sequence is suggested.

The comparison between different approaches have shown that initiation location can be precisely determined from all approaches. The crack initiation angles, however, can only be found using critical plane approaches. The parameters (of critical plane), which are based on maximum shear stress or strain are most suitable to determine crack orientations. For estimation of life, fretting specific Ruiz parameters cannot be applied, since they cannot be correlated with any life estimation formulations. The stress invariant approach has shown relatively larger deviations, especially at large number of cycles, even for in phase loading. Critical plane and continuum damage mechanics approach have shown similar results for in phase loading, however, for out of phase loading, continuum damage mechanics approach has shown better results than critical plane approach. Using continuum damage mechanics approach, a modified damage model is proposed that incorporates the effect of triaxiality function variation, in addition to stress variation. It is found that by including triaxiality function variation, the life estimation capability of the damage model can be improved to some extent.

The present work shows the influence of out of phase loading on different aspects related to fretting fatigue crack nucleation. The results are based on limited experimental data, material properties, geometry of pad and specimen and load ranges. In addition, the life estimation capability of above mentioned approaches still produce errors ranging between 2 to 3 times the experimental lives. Including several other factors, such as micro plasticity, grains size and orientation, material properties including heterogeneity and precise length of crack initiation, may help to improve life prediction capability of damage parameters. These factors provide the basis for further work in this interesting and challenging field of engineering.

SAMENVATTING

Het fenomeen van wrijvingsmoeheid treedt op in de meeste technische toepassingen en kan tot storingen leiden. Het begrip “wrijving” impliceert continue kleine bewegingen tussen entiteiten die met elkaar in contact staan, die oppervlakteschade of het begin van een scheur kunnen veroorzaken. In technische termen verwijst “moeheid” naar de cyclische belasting van een component. De term “wrijvingsmoeheid” omschrijft dus de studie of het gedrag van technische componenten die met elkaar in contact staan en een cyclische belasting ondergaan. Het fenomeen wrijvingsmoeheid lijkt veel op gewone materiaalmoeheid, maar door de toevoeging van het element contactinteractie is er een extra variabele die bijdraagt tot het storingsproces. Het onderwerp wrijvingsmoeheid wordt nu al ongeveer een eeuw bestudeerd en dit in veel verschillende sectoren, zoals in de locomotief-en automobielindustrie, de civiele industrie, en bij machineontwerp, in de scheepvaart, en ruimtevaart.

De mechanische storingen bij gewone en wrijvingsmoeheid worden gekenmerkt door twee belangrijke fasen. De eerste fase wordt algemeen aangeduid als de “nuceatiefase”, terwijl de tweede fase, waarin de beschadiging of de scheur uitbreidt, de “propagatiefase” wordt genoemd. Hoewel er geen uniforme of gestandaardiseerde definitie bestaat van de lengte van een scheur bij nucleatie, wordt algemeen aanvaard dat schade tot op mesoschaal of tot op een kleine korrelgrootte van het materiaal beschouwd wordt als de lengte bij nucleatiefase. De term “nucleatie” omvat het proces vanaf het begin van de belasting tot aan de ontwikkeling van een storing op deze lengteschaal. Nucleatie is dus een proces van accumulatie van schade die leidt tot scheurinitiatie. De levensduur van het materiaal gedurende de nucleatiefase of tot aan de scheurinitiatie is daarom afhankelijk van de definitie daarvan.

Het mechanisme van elke scheurfase is anders en moet daarom ook afzonderlijk worden behandeld. De kern van de schade ontstaat dichtbij of langs maximale afschuifvlakken, die worden geactiveerd door een omkering in de belasting. Deze vlakken staan bekend als glijvlakken, waar schade zich ophoopt wat uiteindelijk resulteert in een waarneembare leegte of scheur. Bij wrijvingsmoeheid wordt de locatie van scheurinitiatie meestal gevonden nabij de contactrand en aan het oppervlak van de component. Daarom hebben, buiten de belastingomvang en het -materiaal, ook oppervlakteruwheid, wrijvingscoëfficiënt, glij-amplitude en de geometrie van de contactlichamen een invloed op het nucleatieproces. Al deze variabelen samen bepalen collectief het ogenblik van scheurinitiatie door wrijvingsmoeheid.

Wrijvingsmoeheid of scheurnucleatie kan worden bestudeerd met behulp van verschillende methoden, waaronder analytische methoden, experimentele tests en numerieke

methoden. De analytische oplossingen kunnen een vereenvoudigd antwoord bieden met enkele veronderstellingen en alleen voor eenvoudige geometrieën. Deze kunnen echter wel gebruikt worden om de resultaten of de ontwerpmethodologie te verifiëren. De experimentele methoden geven een beter inzicht in de verschijnselen. De meest gebruikelijke laboratoriumopstelling is een opstelling van een cylinderpad en een vlak monster, of een vlakke pad kussen en een vlak monster. Er zijn twee belangrijke factoren die problemen veroorzaken tijdens tests. Ten eerste ontstaat de kern van de schade onder het contactoppervlak, waardoor het moeilijk is om de evolutie van de schade te volgen. Ten tweede worden monsters meestal pas geanalyseerd en gegevens pas vastgelegd eenmaal het monster stuk is. Om de schade in tussenstadia te evalueren, moet de test worden gestopt voor analyse. Bovendien is ook het verkrijgen van schadeparameters of vereiste constanten in het tussenstadium een uitdaging. Dit brengt ons bij het belang van de eindige-elementenmethode, die het mogelijk maakt om aan deze uitdagingen tegemoet te komen. Ten eerste biedt deze methode een grote flexibiliteit om complexe geometrieën of structuren in de praktijk te modelleren. Ten tweede maakt deze methode het ook mogelijk om complexe details te volgen gedurende het volledige proces. Dit betekent echter niet dat de eindige-elementenmethode aan alle vereisten voldoet. Deze heeft ook haar eigen beperkingen. Ten eerste wordt een eenvoudig scenario gemodelleerd, terwijl de feitelijke of praktische configuratie veel complexer is. Zo wordt bijvoorbeeld het materiaal gewoonlijk beschouwd als isotroop en homogeen, terwijl dat het in werkelijkheid niet is. Ten tweede wordt doorgaans ook geen rekening gehouden met omgevingsfactoren. Ten derde worden andere variabelen, zoals temperatuur, wrijvingscoëfficiënt, slijtage- of beschadigingssnelheid, … verondersteld constant te blijven, hoewel die kunnen wijzigen gedurende het proces. Voor een beter inzicht in het fenomeen van scheurnucleatie omvat een goede strategie dus: (a) de toepassing van de eindige-elementenmethode, (b) de verificatie van de methodologie via een analytische oplossing, en (c) de validatie van de resultaten door middel van experimentele tests. In dit proefschrift wordt deze strategie toegepast, i.e. de numerieke resultaten worden geverifieerd door een analytische oplossing en gevalideerd door experimentele resultaten uit de literatuur.

In deze studie worden verschillende randvoorwaarden onderzocht en vergeleken om betrouwbare numerieke modellen te ontwikkelen. Het belangrijkste verschil tussen diverse numerieke modellen is de wijze waarop de tangentiële belasting wordt gemodelleerd. Ten slotte wordt één model geselecteerd op basis van de resultaten, het gemak waarmee de belasting kan worden toegepast, en de berekeningsefficiëntie. Voor de analyse van scheurnucleatie kunnen de schadecriteria of -modellen worden ingedeeld in vier verschillende groepen of benaderingswijzen. Het gaat om de kritischevlakbenadering, de invariantespanningsbenadering, de benadering van wrijvingsspecifieke parameters en die van de continuumschademechanica. Dit proefschrift bevat ook een uitgebreid literatuuroverzicht, waar basisideeën worden uitgelegd en

deze benaderingswijzen worden gedefinieerd, samen met de toepassing hiervan op problemen van wrijvingsmoeheid.

De belangrijkste aspecten die, op basis van deze benaderingswijzen, geanalyseerd worden, zijn de variatie van contactspanningen en glij-amplitude, de voorspelling van de locatie van scheurinitiatie, de oriëntatie van de initiële scheur en de levensduur van de wrijvingsmoeheid. Het grootste deel van het onderzoek dat tot dusver werd gevoerd op het vlak van wrijvingsmoeheid, werd uitgevoerd onder binnen-fase laadcondities. In de praktijk kunnen componenten echter verschillende belastingen ervaren, met faseverschillen daartussen. Daarom is het interessant om de contactinteractie te analyseren met verschillen in belastingfase. Omdat er bij wrijvingsmoeheid een multi-axiale spanningstoestand bestaat, kunnen spanningen niet-proportioneel zijn, zeker als de belastingen met faseverschil worden toegepast. De focus van dit proefschrift ligt daarom op de toepassing van verschillende schademodellen en -benaderingen, onder buiten-fase laadcondities. Verschillende benaderingen en schademodellen worden geïmplementeerd en er wordt een vergelijking gemaakt in hun efficiëntie bij het bepalen van de locatie, oriëntatie en levensduur van de scheurinitiatie. Bovendien wordt een model van continuumschademechanica voorgesteld voor niet-proportionele laadcondities.

Uit de huidige studie is gebleken dat de locatie, oriëntatie en levensduur van scheurinitiatie bij wrijvingsmoeheid beïnvloed worden door laadamplitudes en faseverschillen. De locatie van scheurinitiatie hangt af van twee omstandigheden; (a) het faseverschil wordt toegepast tussen axiale bulkspanning en tangentiële belasting, of (b) tussen normale contactbelasting en de andere twee belastingen (axiale bulkspanning en tangentiële belasting). Voor de oriëntatie van initiële scheuren kan het faseverschil een groter aantal vlakken introduceren die scheurinitiatie kunnen ondergaan. De levensduur van de scheurinitiatie kan toenemen of afnemen bij faseverschil, afhankelijk van het type en de graad van het faseverschil. Om echter algemene conclusies te trekken wat betreft het stijgings- of dalingspercentage met fasehoeken, moeten verdere experimenten worden uitgevoerd, met verschillende materialen en volgordes van belasting.

De vergelijking tussen de verschillende benaderingswijzen heeft aangetoond dat de locatie van scheurinitiatie in alle benaderingswijzen nauwkeurig kan worden bepaald. De hoeken van de scheurinitiatie kunnen echter enkel worden bepaald met behulp van de kritischevlakbenadering. De parameters (van het kritische vlak), die gebaseerd zijn op maximale schuifspanning of -belasting, zijn het meest geschikt om scheuroriëntatie te bepalen. Voor het inschatten van de levensduur kunnen wrijvingsspecifieke Ruiz-parameters niet worden toegepast, omdat zij aan geen enkele formule voor levensverwachting kunnen worden gekoppeld. De invariantespanningssbenadering levert relatief grotere afwijkingen op, vooral bij een groot aantal cycli, zelfs bij binnen-fase belasting. Hoewel de kritischevlakbenadering en de benadering van de

continuumschademechanica gelijkaardige resultaten opleveren bij binnen-fase belasting, levert de benadering van de continuumschademechanica voor buiten-fase belasting betere resultaten op dan de kritischevlakbenadering. Op basis van de benadering van de continuumschademechanica wordt een aangepast schademodel voorgesteld dat, naast spanningsvariatie, ook het effect van variatie van de triaxialiteitsfunctie incorporeert. Het is gebleken dat door het toevoegen van variatie van de triaxialaliteitsfunctie, het vermogen van het schademodel om levensduur in te schatten tot op zekere hoogte kan worden verbeterd.

De huidige studie legt de impact bloot van buiten-fase belasting op verschillende aspecten gerelateerd aan scheurnucleatie bij wrijvingsmoeheid. De resultaten zijn echter gebaseerd op een beperkt aantal experimentele gegevens, materiaaleigenschappen, geometrieën van pads kussens en monsters, en laadbereik. Bovendien levert het vermogen van bovenvermelde methoden om levensduur in te schatten nog steeds fouten op, die variëren van 2 tot 3 keer de experimentele levensduur. Door het in rekening brengen van andere factoren, zoals microplasticiteit, korrelgrootte, materiaaleigenschappen, inclusief heterogeniteit en de precieze lengte van de scheurinitiatie, kan het vermogen om de levensduur te voorspellen van schadeparameters verbeterd worden. Deze factoren vormen de basis voor verdere studie in dit interessante en uitdagende gebied van de ingenieurswetenschappen.

Chapter 1

Introduction

1.1 Introduction to fretting fatigue

It is well known fact that presence of fatigue load reduces the mechanical life of component in comparison with monotonic or static load. The mechanical failure of a component may occur due to the presence of prior defect in material or due to highly localized stress concentration. The failure may also occur in an assembly due to movement of components, often connected together in pre-stressed condition. The presence of fretting, which may affect fatigue performance, is related to fretting fatigue scenario and poses a design challenge especially due to constraints of volume, weight and cost.

Fretting occurs at the junction of contacting bodies due to presence of oscillating force, which generates small relative displacement. The contact surface generally involves slip regions, where relative tangential displacement occurs near the contact edge, and complemented by stick region in the middle. This relative displacement causes surface degradation and heat at the expense of frictional energy [1]. The form of surface degradation depends largely on material and geometry of contacting bodies, surface and environmental conditions, magnitude and sequence of loads. The amplitude of slip plays an important role under fretting conditions. At higher slip amplitude (gross slip regime), wear causes severe surface damage, while crack formation is limited, this phenomenon is known as *fretting wear*. On the other hand, at lower slip amplitude (partial slip regime), wear effects are small and development of crack is dominant, which can be termed as *fretting fatigue* [2]. Therefore, fretting can induce wear and development of micro cracks at the contact interface, leading to the failure of a component.

1.1.1 History of fretting fatigue and contact mechanics

The history of fretting starts in 1911 when Eden et al. [3] found debris formation in steel grips of fatigue machine, which were in contact with steel specimen. The first fretting fatigue machine was designed in 1927 by Tomilson [4], to study corrosion and damage under fretting conditions for two cases. In the first case, small amplitude rotational displacement was produced between the two annuli and in the second case, between an annulus and flat surface. He found that damage can occur due to small amplitudes of displacement between contacting bodies and coined the term of *slip*. Furthermore, he termed the red iron oxide debris formation as *fretting corrosion*. In 1941, Warlow Davies [5] investigated the effect of fretting on fatigue strength due to pitting of the surface. The combined effect of fretting and fatigue was investigated in 1953 by McDowell [6]. They found a reduction in fatigue strength of the material under fretting fatigue condition. Liu et al. [7] investigated the fretting fatigue strength of a Titanium alloy. In 1958, Fenner and Field [8] showed that fretting can significantly accelerate the crack nucleation process. Waterhouse [9] in 1961 found that recrystallization occurred in the contact region under fretting fatigue condition. Nishioka and Hirakawa conducted series of studies in 1968-69, on various

aspects related to fretting fatigue, including; effect of relative slip amplitude, effect of mean stress, contact pressure and hardness [10-15]. Waterhouse and Taylor [16] in 1971, investigated fretting fatigue crack initiation in carbon steel. Later, Waterhouse and co-workers added significant contribution in the subject field, related to fretting corrosion [17], fretting wear [18] and fretting fatigue [19, 20]. Endo and Goto [21] studied crack initiation and propagation phases by conducting fretting fatigue experiments on carbon steel. Hills and Nowell [22, 23] demonstrated the significance of size effect on fretting fatigue behaviour. Vingsbo and Söderberg [2] related wear rate and fatigue life with slip amplitude and showed that contact conditions in fretting changed with increasing slip amplitude. They presented the concept of *fretting maps* to determine fretting regimes under given loading conditions. A fretting map is a two dimensional plane in a space that describes these regimes using testing parameters or variables. Dobromirski [24] mentioned that fretting process is dependent on myriad variables and can be classified as *primary variables* and *secondary variables*. The secondary variables impact fretting process by influencing primary variables. These variables include, normal load, tangential load, bulk load, load ratio, coefficient of friction, slip amplitude, contact area, vibration frequency, number of cycles, hardness of materials, surface roughness, ambient temperature and pressure, humidity, oxide layer, lubricant (if any), metallurgical compatibility and micro structure, etc. However, he declared coefficient of friction as the main primary variable of the fretting process.

The other complementary field related to fretting fatigue is the mechanics of contact. The field of contact mechanics originated in 1882 when Hertz [25] studied the contact of elastic bodies. The Hertzian contact stress, refers to generation of localized stresses that develop when two curved bodies come in contact and deforms under the application of load. Mindlin [26] in 1949 provided the solution of Hertzian contact under partial slip condition. The work of Mindlin was extended by Johnson [27] by performing experiments under fretting conditions. Further advancement in modelling of contact was made by Wright and O'Connor [28] in 1972. They investigated the influence of fretting and geometric stress concentrations on fatigue strength of clamped joints. Bramhall [29] introduced in 1973 the application of Hertzian contact instead of complete contact under fretting conditions. Hamilton [30, 31] studied and developed the formulation for stresses beneath a sliding Hertzian spherical contact. A more recent work related to mechanics of elastic contact was presented by Hills et al. [32]. Another significant work was contributed in 1994 by Hills and Nowell [1], where mechanics of contacting bodies (for various contact geometries), phenomena of crack nucleation and propagation under fretting fatigue were elaborated in detail.

1.1.2 Applications

Fretting fatigue has wide range of applications in variety of fields such as automotive, marine, aerospace, machine design, bio-mechanics industry, etc. Although most of these

applications involve state of the art high strength alloys of aluminium, steel and titanium, still failures were observed at the contacting regions. The fretting fatigue occurs mostly in mechanically fastened joints, e.g. bolted and riveted connections or any other assembly undergoing small oscillatory movement. Figure 1 shows two common cases that undergo fretting fatigue failure. The other failures examples include, output shaft flange of a helicopter, turbine disc and blade failure of aero-engines [33, 34], power station generator rotor [35], steel ropes [36], connections of railway line [37], artificial hip joints [38], riveted connections in aeroplane fuselage [39] and bolted flange connections between pipes and other mechanical assemblies.

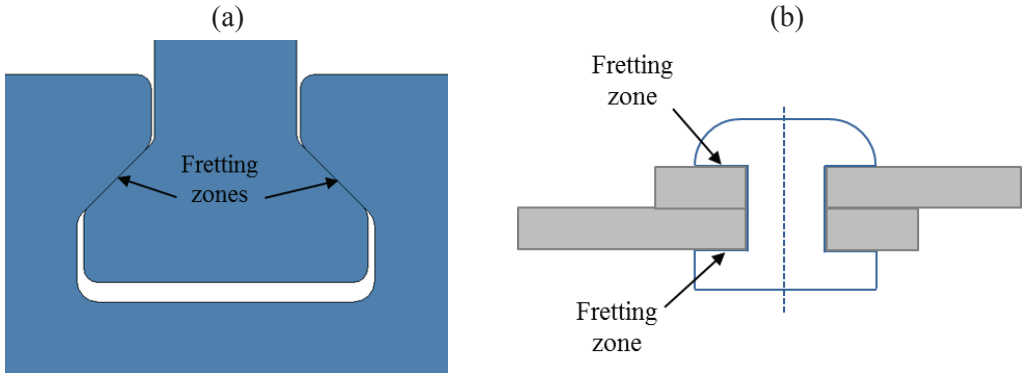

Figure 1. Examples of fretting fatigue problems showing fretting zones for (a) dove tail joint and (b) riveted lap joint.

1.1.3 Failure process

For estimation of life in fretting fatigue problems, the failure process is usually divided in two phases, namely, crack nucleation and crack propagation. The proportion of life taken by each phase significantly depends on type of failure mode and definition of initiation crack length. The damage in a material may be considered as a continuous physical process, which leads to the failure of material. On physical basis, damage is related to plastic or irreversible strains either on microscale or on mesoscale. Considering the microscale, this process involves the accumulation of micro stresses in the vicinity of defects and breaking of bonds. At mesoscale, it represents the coalescence of the micro cracks or voids, which together can initiate one crack [40]. Considering crack nucleation as a process, the start of nucleation phase may be termed as damage initiation and end as crack initiation. Although crack nucleation and initiation are sometimes used interchangeably, the current thesis uses the terminologies as shown in Figure 2. Therefore crack initiation life implies, lifetime computed at the end of nucleation phase. In general, the crack initiation refers to formation of flaw, which encompasses a few grain sizes in length. When the

crack surpass the initiation length, further crack growth is driven by crack tip stress intensity factors. The propagation is often considered as the proportion of life, where crack behaviour can be described by fracture mechanics. Figure 2 describes the sequence of the failure process or the involved crack phases. Fretting fatigue may cause an early damage as it can affect both nucleation and propagation phases of crack life.

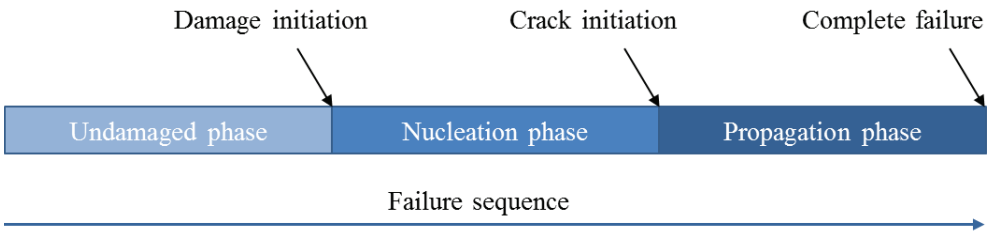

Figure 2. Description of failure process with crack nucleation and propagation phases.

In fretting fatigue, crack nucleation may take significant proportion of life under given loading conditions. Various factors are involved in crack nucleation process under fretting fatigue conditions, as described above. The initiation of damage requires reversal of shear stress to form a slip band, the more severe the reversing state of stress, the higher are the chances to form a slip band. This of course, implies that higher tangential, normal and bulk load are more detrimental for the loaded component. It is generally accepted that crack initiation is dominated by shear forces and therefore initiates a crack near to maximum shear plane. However, at some critical crack length, the crack may change direction and propagate perpendicular to the surface due to the influence of dominant bulk load. In addition, the nucleation phase and early development of crack also undergo micro plasticity which forms the basis for damage initiation. It is also pertinent to mention here some basic understanding of the scale of damage phenomena. On one hand, *elasticity* takes place at the level of atoms, whereas *plasticity* is governed by slips at the level of crystal or molecules. *Damage*, on the other hand, is the debonding from the level of atoms to the mesoscale level for crack initiation.

Researchers have used various numerical and experimental techniques to predict crack initiation location, orientation and life. Some approaches are based on empirical laws and physical observations, while some are based on thermodynamics principles. The process of fretting fatigue involve multiple loads in different directions, which give rise to multiaxiality and non-proportional stresses. Therefore, for complete description of stress state, multiaxial theories are considered for analysis of crack nucleation. This implies that stresses, strains and displacements at or just below the contact interface are the important parameters that affect nucleation phase.

This fact also highlights the significance of Finite Element Method (FEM), which can be applied for analysis and evaluation of nucleation phase. FEM provides a useful tool to efficiently model contact conditions by reducing time and effort. There are several approaches and damage parameters in the literature, which can be employed with FEM. These approaches include critical plane approach, stress invariant approach, damage mechanics and fretting specific parameters. Various damage parameters and models can be used to study different aspects of crack nucleation, however usually more focus is given to crack initiation location, initial crack orientation and life.

1.2 Objectives

The current work provides an insight on different aspects related to fretting fatigue crack nucleation under out of phase loading condition. Majority of the research under fretting fatigue is done for in phase loading. However, in most of the practical applications, components and assemblies undergo asynchronous loads. Therefore, it is imperative to analyse the effect of different loads including phase difference. Although complete failure process includes initiation and propagation phase (normally dealt with fracture mechanics), the present work is related to crack nucleation under partial slip condition.

Under fretting fatigue condition, non-proportional stress state may be produced and can have a significant effect on fatigue life as compared to plane fatigue. The criterion or parameter employed, therefore, should be able to accommodate this effect. Most of the damage models, especially, based on continuum damage mechanics approach assume the proportional loading condition during cyclic loading. Hence, these models neglect the stress non-proportionality and its effect of damage with respect to cycle.

This thesis adds contribution in fretting fatigue crack nucleation analysis by presenting damage model for non-proportional loading and comparing crack nucleation approaches under out of phase loading. The effect of out of phase loading on crack initiation orientation and comparison with experimental life is also shown. Furthermore, to estimate crack initiation angles, a quadrant method is proposed. In addition, the literature review presented is more comprehensive than the already published reviews on crack nucleation approaches. The previous published reviews only included critical plane approach, whereas the present review contains three more approaches, which allows us to compare the advantages and disadvantages of each approach. This leads to the main objectives of the present thesis, as follows:

- To provide the detailed review on different approaches, damage models or parameters for fretting fatigue problems.
- To compare different approaches and damage models under out of phase loading conditions.

- To analyse the effect of phase difference between loads on crack initiation location, orientation and life.
- To develop a damage model suitable for out of phase and non-proportional loading conditions.

1.3 Sequence of thesis

This section provides the outline for the remaining thesis. In total it contains six chapters including this introduction chapter.

Chapter 2 presents theoretical background of four relevant topics. First section contains theory about contact mechanics. Second section provides an insight into FEM of contact problems. It is related to different aspects associated to contact formulation used in numerical simulations. Third section provides theoretical background related to crack nucleation and propagation phases, with a focus on mechanics of crack nucleation. The last section presents some basic terminologies related to plain and fretting fatigue.

Chapter 3 presents a detailed review on fretting fatigue crack nucleation. Different approaches and damage models are categorized and within each approach popular damage models and parameters are discussed. It also contains mathematical background of damage parameters and provides details on application to various case studies related to fretting fatigue problems. In addition, a comparison of different approaches is presented. Some generalized conclusions are also drawn at the end.

Chapter 4 describes the methodologies used in the present work. This includes description of numerical modelling techniques, mathematical modelling of the continuum damage based model for proportional and non-proportional loading (proposed model). In addition, it describes the implementation or flow sequence for critical plane, stress invariant, Ruiz parameter and continuum damage mechanics approaches.

Chapter 5 contains all results and discussion, which includes variation of contact stresses, effect of boundary conditions of stresses and damage parameters under out of phase loading condition, influence of phase difference on damage initiation location, initial crack orientation and life. Efficacy of the various approaches and damage models is compared, especially under out of phase loading. Furthermore, the effect of including triaxiality function variation in damage model is elaborated by comparing proposed damage model with existing ones.

Finally, in *Chapter 6*, main conclusions are drawn from the present work. It also includes main sources of errors in numerical predictions. In addition, future recommendations and a way forward for the current work is also presented.

Chapter 2

Theoretical background

Crack nucleation under fretting fatigue is complex phenomena and therefore its numerical modelling requires understanding of several fields. These fields include mechanics of solids, continuum damage mechanics, fatigue of materials, finite element method and contact mechanics. This chapter will briefly introduce some of the necessary theoretical background concerning these areas. The first section describes basic type of contacts and analytical formulation of some basic cases. The second section describes formulation of finite element method related to contact interactions and solution of nonlinear contact problems. The third section gives background knowledge on mechanics of crack nucleation and propagation and finally the fourth section defines some basic terminologies that are regularly used in plain and fretting fatigue.

2.1 Contact mechanics

2.1.1 Classification of contacts

The mechanics of contact mainly depends on geometry of contacting bodies. The difference in geometry leads to various contact types. Therefore, the contacts can be categorized as follows.

2.1.1.1 Incomplete contact

The contact is called an *incomplete contact*, when the contact width, $2a$, increases with increase in application of load. The example of incomplete contact is shown in Figure 3 (a). The line contact between cylinder and elastic half space will transform to area of contact, on application of load. In addition, there is a common tangent at the contact edge, which ensures continuous slope of the deformed surfaces. The *half space* is either of the two parts into which a plane divides the three dimensional space.

2.1.1.2 Complete contact

A contact is said to be *complete contact*, when the contact width is independent of applied load. Further, the contacting surface does not share a common tangent at the contact edge. Therefore the slope of elastic half space is not continuous, leading to singular contact pressure. An example of complete contact is shown in Figure 3 (b). A combination of singular contact pressure at one end and continuously decaying to zero on the other end is also possible. Such a case is shown in Figure 3 (c), e.g. in case of D-shaped punch.

2.1.1.3 Conformal contact

The other type of contact involves condition of conformality. When the semi contact width, a, is significant in comparison to characteristic radius of the cylinder. This type of contact is known as *conformal contact* and the related example is shown in Figure 3 (d). In this case

neither of the contacting bodies can be approximated by half plane. The solution of such a problem requires formulation of a disc and an infinite plane containing a hole.

2.1.1.4 Non-conformal contact

If the semi contact width is much less than radius of the cylinder, then the deformation of the cylinder will be limited to small arc length. The deformation and the stress can therefore be approximated by half plane. This type of contact is known as *non-conformal contact* and the representative example is shown again in Figure 3 (a).

2.1.1.5 Receding contact

A contact is said to be *receding*, if an elastic plate is pressing an elastic block under the application of normal load. It will lift the contact edges and the contact width will recede.

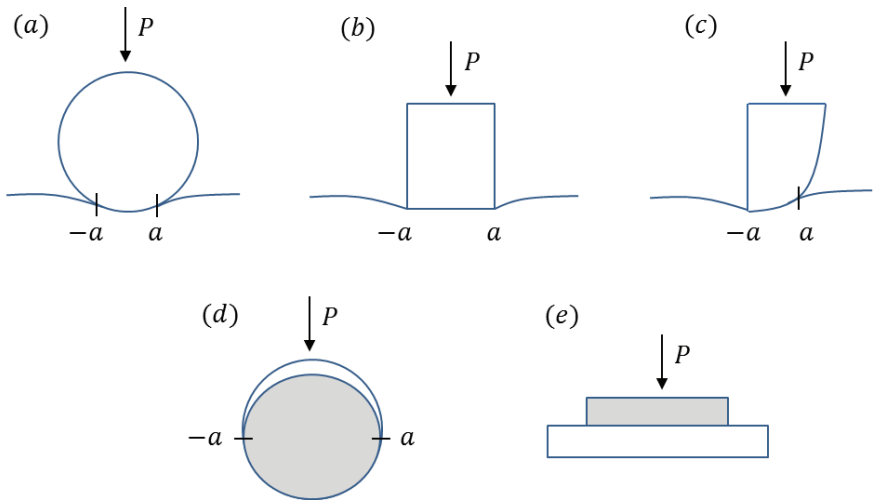

Figure 3. Classification of contacts, (a) incomplete and non-conformal (b) complete (c) incomplete with singularity (d) incomplete and conformal and (e) receding [1].

2.1.2 Partial slip contact

In the present thesis, the focus of analysis will remain on contacts, which can be modelled with half space assumption. The analytical expression for normal pressure distribution and shearing traction can be obtained for a generalized case. When two elastically similar bodies are brought in contact with each other by normal load, P, the normal contact pressure develops at the contacting surfaces. In addition, they undergo displacement parallel to the deformed surfaces. As

long as the bodies are elastically similar, the displacement for both parts will be the same, implying there is no relative displacement between the parts and hence no frictional forces. Under the application of tangential load, Q, macroscopic relative displacement will be generated, leading to shear traction at the contact interface. The shear traction will be generated, which is limited by the coefficient of friction, μ. The shear traction, q, can be related to contact pressure p as follows:

$$|q(x,y)| = -\mu p(x,y) \tag{1}$$

The shear traction will also lead to a normal displacement of both surfaces. However, the normal displacement will be equal for both parts since the bodies are elastically similar. Generally, under fretting contact, the tangential load is small and cannot cause complete sliding. Under such condition, $Q < \mu P$ and the contact area consists of stick zone $(-c < x < c)$ and slip zone $(c < x < a)$ or $(-a < x < -c)$ as shown in Figure 4. The stick zone is the region where there is no relative tangential displacement, d_x, whereas slip zone is characterized by relative displacement and shear traction is limited by friction. In slip zone, the shear traction can be obtained using Eq. (1). The direction however is opposite to relative tangential displacement. Inside the stick zone, shear traction is less than the limiting value. On each body they are equal in magnitude but opposite in direction:

$$|q(x,y)| < -\mu p(x,y) \tag{2}$$

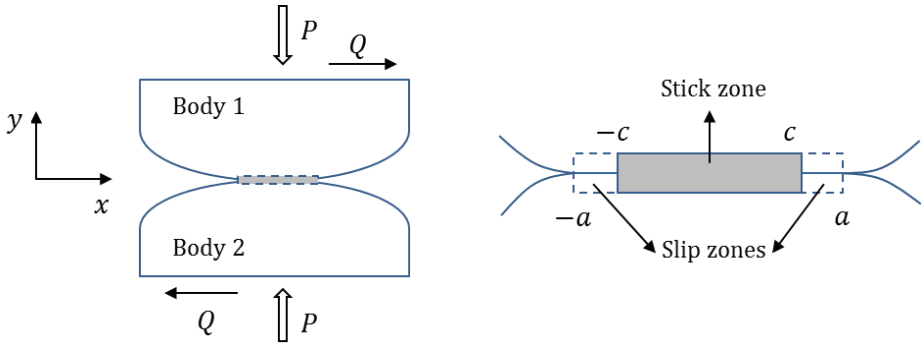

Figure 4. Contact under normal load between two bodies. Contact zone consists of stick and slip zones.

The fretting contacts generally involve two conditions. First, the contact interface undergoes shear traction, which implies that tangential force is transferred from one body to another. Second, tangential displacement exists between the contacting surfaces, which give rise

to slip due to cyclic loading. The shear traction can also be generated from only normal force, when the contacting bodies have different materials. The contact interaction generally follows Coulomb friction law, which was based on experimental observations of contact between rigid bodies. According to this model:

- The tangential force or friction force, Q, is proportional to normal force, P, i.e. $Q = \mu P$ and it acts opposite to relative motion between the bodies.
- The tangential force is independent of the contact area.
- The tangential force, produced during gross sliding, is independent of sliding velocity.

It is also pertinent to mention here that the application of frictional model requires some modification, to be applied to elastic contacts. Considering single coordinate (x) for simplification and understanding, the shear traction for slip region can be written as:

$$|q(x)| = -\mu p(x) \tag{3}$$

The minus sign shows that compressive shear tractions are taken as negative. Since direction of shear traction opposes the relative motion, therefore:

$$sgn(q(x)) = -sgn\left(\frac{\partial d_x}{\partial T}\right) \tag{4}$$

where T represents time. The relative tangential displacement,d_x, can be written in terms of displacement for both bodies as:

$$d_x = u_{x1} - u_{x2} \tag{5}$$

For the point where there is no relative slip, the shear traction will be less than or equal to limiting friction value, i.e.:

$$|q(x)| \leq -\mu p(x) \tag{6}$$

Equations (3), (4) and (6) provide necessary conditions for frictional model to be applied to elastic contacts. This model needs to be applied individually at all points of the contact. Equations (3) and (4) are applicable to slip zone whereas Eq. (6) is applicable to stick zone. This kind of contact, which has both stick and slip zones is known as *partial slip* contact.

2.1.3 Analytical solution

2.1.3.1 Under normal and tangential load

This section presents the analytical solution for Hertzian type contact. The Hertz theory [25, 41] allows to determine contact stresses between the two curved bodies, usually associated closer to the area of contact. The contact pressure and shear traction distribution at the surface can be obtained. The classical Hertzian theory is based on following assumptions:

- Each body can be considered as elastic half space. This implies that area of the contact is much smaller than characteristic radius of the body.
- The surfaces are continuous and non-conforming. The initial contact is a point or line in the absence of forces.
- The strains are small and within elastic limit.
- The contact is assumed to be frictionless, which implies that normal stress will be translated between the bodies.

Considering both parts have the same material and initially under the action of normal load only. Under plane strain condition, the composite compliance C_c of both bodies can be written as [1]:

$$C_c \equiv 2\left[\frac{1-\nu_1^2}{E_1}+\frac{1-\nu_2^2}{E_2}\right] \tag{7}$$

The material properties E_i and ν_i are elasticity modulus and Poisson's ratio for body i, respectively. The contact pressure distribution along the contact interface is given by:

$$p(x) = -\frac{\kappa_r}{C_c}\sqrt{a^2-x^2} \tag{8}$$

where, κ_r is the relative curvature that depends on radii of contacting surfaces R_1 and R_2.

$$\kappa_r = \frac{1}{R_1}+\frac{1}{R_2} \tag{9}$$

The semi contact width, a, can be expressed in terms of applied load and geometrical parameters as:

$$a^2 = \frac{2PC_c}{\pi t \kappa_r} \tag{10}$$

where, t is the thickness of bodies or contact surfaces. The resulting contact pressure distribution can be rewritten as:

$$p(x) = -\frac{2P}{\pi a}\sqrt{1-\frac{x^2}{a^2}} \tag{11}$$

or in terms of peak contact pressure p_0:

$$p(x) = -p_0\sqrt{1-\frac{x^2}{a^2}} \tag{12}$$

Now adding the tangential load on both bodies such that $Q < \mu$P, the contact is under partial slip condition. Considering the symmetry of load and boundary condition, the stick zone will be symmetric about the centre of contact as shown in Figure 4. The shear traction can be modelled as perturbation of fully sliding case, i.e.:

$$q(x) = \mu p_0\sqrt{1-\left(\frac{x}{a}\right)^2} + q_p(x) \tag{13}$$

where, perturbation $q_p(x) = 0$ in the slip zone. For the stick zone $q_p(x)$ is given by:

$$q_p(x) = -\mu p_0\frac{c}{a}\sqrt{1-\left(\frac{x}{c}\right)^2} \quad , \quad |x/c| < 1 \tag{14}$$

Hence, total shear traction becomes:

$$q(x) = \mu p_0\sqrt{1-\left(\frac{x}{a}\right)^2} - \mu p_0\frac{c}{a}\sqrt{1-\left(\frac{x}{c}\right)^2} \tag{15}$$

The stick zone in the above formulation can be determined by tangential equilibrium:

$$Q = \frac{\mu\pi p_0}{2a}(a^2 - c^2) \tag{16}$$

which leads to semi stick zone width as:

$$c = a\sqrt{1 - \left|\frac{Q}{\mu P}\right|} \tag{17}$$

The above solution can also be applied to cylinder on a flat configuration by taking R_2 equals to infinity, since the radius of a flat plane is infinite. The above analytical solution is also known as Mindlin solution [26].

2.1.3.2 Under fretting fatigue loads

The addition of bulk cyclic stress, σ_A, (to normal and tangential load) gives rise to fretting fatigue failures. A typical fretting fatigue experimental setup is shown in Figure 5, where a flat specimen is in contact with two fretting pads, under the action of contact and axial cyclic stress. The fretting pads are restrained by the attached springs that give rise to tangential load, Q. A constant normal load, P, ensures the presence of contact throughout the loading. The spring stiffness can be adjusted to produce the partial slip condition. The addition of cyclic stress will produce strain in the specimen and a different shear traction will be generated. This configuration was first analysed by Nowell and Hills [42]. The presence of cyclic stress will now shift the stick zone from the central and symmetric position, $\pm c$. The offset of the stick zone can be represented as, e. The new position of the stick zone now ranges from $x = e - c$ to $x = e + c$. Using the similar method, as shown in previous section, the shear traction can be written as:

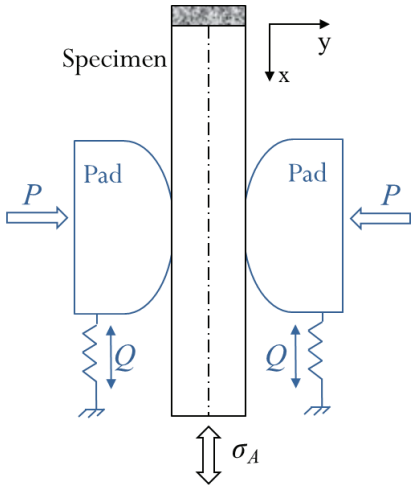

Figure 5. Schematic of experimental setup for a fretting fatigue test with cylindrical pad and flat specimen.

$$q(x) = \mu p_0 \sqrt{1 - \left(\frac{x}{a}\right)^2} + q_p(x) \tag{18}$$

where perturbation $q_p(x)$ is zero in the slip zone.

$$q_p(x) = 0 \quad , \quad |x - e| < c \tag{19}$$

The offset *e* in the shift zone can be determined as:

$$e = \frac{\sigma_A a}{4\mu p_0} \tag{20}$$

For the stick zone $q_p(x)$ is now given by:

$$q_p(x) = -\mu p_0 \frac{c}{a} \sqrt{1 - \left(\frac{x - e}{c}\right)^2} \quad , \quad |x - e| < c \tag{21}$$

which leads to the total shear traction as:

$$q(x) = \mu p_0 \sqrt{1 - \left(\frac{x}{a}\right)^2} - \mu p_0 \frac{c}{a} \sqrt{1 - \left(\frac{x - e}{c}\right)^2} \tag{22}$$

This analytical solution holds true for cases when bulk cyclic stress is much less than tangential force. With application of larger cyclic stress, the stick zone may approach one end of the contact, leading to reverse slip. The applicable limits of the solution can therefore be written as $e + c \leq a$. The limiting cyclic stress can be determined as:

$$\sigma_A \leq 4\mu p_0 \left(1 - \sqrt{1 - \frac{Q}{\mu P}}\right) \tag{23}$$

The presence of fatigue load thus affects the shear traction distribution, which will consequently affect the stress field. In addition, the shear traction and stress field will be different if the loads are applied with phase difference.

2.2 Non-linear FEM

The initiation of fretting fatigue failure is a local process. The most important factor is to locate the critical site which depends on the time history of stress or strain. The primary reason of employing Finite Element Method (FEM) is to analyse the fretting fatigue behaviour for the complete load history. This can be achieved by performing Finite Element Analysis (FEA), which is application of FEM for practical application. It also enables to focus of any chosen location and intrinsic details, which are not possible otherwise. In addition, the parametric studies with minor variation in design variables can be conducted efficiently. However, it is imperative to evaluate the accuracy of predictions based on FEM, by comparing numerical results with experimental ones. The most important part in fretting fatigue simulation is the contact analysis, which provides all required internal variables. This section therefore focuses on FEM of contact and on contact algorithm. The details of finite element models and mesh size effect are covered in the next chapter.

In many engineering application displacements may become a nonlinear function of the applied load. For accurate investigation, linear analysis in not sufficient. There are different kinds of non-linearity in solid mechanics, which include geometric non-linearity, material non-linearity and contact non-linearity. At the instant of contact, the displacement suddenly changes, which makes the contact phenomena highly nonlinear. In equilibrium condition, the nonlinear problem can be written as:

$$\mathbf{K}(\mathbf{u}).\mathbf{u} = \mathbf{F}(\mathbf{u}) \tag{24}$$

where stiffness **K** is a function of displacement **u** and **F** is the externally applied load.

2.2.1 Newton method

Nonlinear problems are generally solved by using incremental or iterative methods. For the current work only Newton's method is used, which is an iterative approach, therefore only iterative methods and their finite element equations are presented in this section. Newton's method allows to determine roots of function $y = f(x) = 0$. For a single variable, the iterative scheme can be written as [43]:

$$x_{i+1} = x_i - \frac{f(x_i)}{f'(x_i)} \tag{25}$$

or

$$x_{i+1} = x_i + \left(\frac{df(x)}{dx}|_{x=x_i}\right)^{-1}\left(-f(x_i)\right) \tag{26}$$

where, x_i represents the initiation value or the initial guess for the iteration and $y_i = f(x_i)$ is the initial value of the function. The tangent at point y_i will lead to new point x_{i+1} and with a better approximation y_{i+1} of the function at the desired point. With subsequent iterations, the error can be minimized to an acceptable value. For *n* variables, the displacement vector may be represented as:

$$(u_n)_{i+1} = (u_n)_i + \Delta(u_n)_i \tag{27}$$

or

$$\mathbf{u}_{i+1} = \mathbf{u}_i + \Delta\mathbf{u}_i \tag{28}$$

The potential function Π of a system can be expressed by using truncated Taylor series [44]. The function Π should be convex and its second derivative should be positive to assist minimization procedure, i.e.:

$$[\Pi(u_1, u_2, \dots u_n)]_{i+1} = [\Pi(u_1, u_2, \dots u_n)]_i + \sum_{j=1}^{n} \left(\frac{\partial \Pi}{\partial u_j}\right)_i \Delta(u_j)_i + \frac{1}{2}\sum_{j}^{n}\sum_{k}^{n} \left(\frac{\partial^2 \Pi}{\partial u_j \partial u_k}\right)_i \Delta(u_j)_i \Delta(u_k)_i \tag{29}$$

Converting into matrix form, the system of equations can be written as:

$$[\Pi(u_1, u_2, \dots u_n)]_{i+1} = [\Pi(u_1, u_2, \dots u_n)]_i + \begin{Bmatrix} \left(\frac{\partial \Pi}{\partial u_1}\right)_i \\ \left(\frac{\partial \Pi}{\partial u_2}\right)_i \\ \dots \\ \left(\frac{\partial \Pi}{\partial u_n}\right)_i \end{Bmatrix}^T \begin{Bmatrix} \Delta(u_1)_i \\ \Delta(u_2)_i \\ \dots \\ \Delta(u_n)_i \end{Bmatrix} + \frac{1}{2}\begin{Bmatrix} \Delta(u_1)_i \\ \Delta(u_2)_i \\ \dots \\ \Delta(u_n)_i \end{Bmatrix}^T \begin{bmatrix} \left(\frac{\partial^2 \Pi}{\partial u_1 \partial u_1}\right)_i & \left(\frac{\partial^2 \Pi}{\partial u_1 \partial u_2}\right)_i & \dots & \left(\frac{\partial^2 \Pi}{\partial u_1 \partial u_n}\right)_i \\ \left(\frac{\partial^2 \Pi}{\partial u_2 \partial u_1}\right)_i & \left(\frac{\partial^2 \Pi}{\partial u_2 \partial u_2}\right)_i & \dots & \left(\frac{\partial^2 \Pi}{\partial u_2 \partial u_n}\right)_i \\ \dots & \dots & \dots & \dots \\ \left(\frac{\partial^2 \Pi}{\partial u_n \partial u_1}\right)_i & \left(\frac{\partial^2 \Pi}{\partial u_n \partial u_2}\right)_i & \dots & \left(\frac{\partial^2 \Pi}{\partial u_n \partial u_n}\right)_i \end{bmatrix} \begin{Bmatrix} \Delta(u_1)_i \\ \Delta(u_2)_i \\ \dots \\ \Delta(u_n)_i \end{Bmatrix} \tag{30}$$

The first derivative of the potential Π represents residual vector $\mathbf{R}_i$ and second derivative (the Hessian matric) represents tangent stiffness $\mathbf{K}_i$, at point $\mathbf{u}_i$. This implies:

$$\begin{Bmatrix} \left(\frac{\partial \Pi}{\partial u_1}\right)_i \\ \left(\frac{\partial \Pi}{\partial u_2}\right)_i \\ \cdots \\ \left(\frac{\partial \Pi}{\partial u_n}\right)_i \end{Bmatrix} = \mathbf{R}(\mathbf{u}_i) = \mathbf{R}_i \tag{31}$$

and

$$\begin{bmatrix} \left(\frac{\partial^2 \Pi}{\partial u_1 \partial u_1}\right)_i & \left(\frac{\partial^2 \Pi}{\partial u_1 \partial u_2}\right)_i & \cdots & \left(\frac{\partial^2 \Pi}{\partial u_1 \partial u_n}\right)_i \\ \left(\frac{\partial^2 \Pi}{\partial u_2 \partial u_1}\right)_i & \left(\frac{\partial^2 \Pi}{\partial u_2 \partial u_2}\right)_i & \cdots & \left(\frac{\partial^2 \Pi}{\partial u_2 \partial u_n}\right)_i \\ \cdots & \cdots & \cdots & \cdots \\ \left(\frac{\partial^2 \Pi}{\partial u_n \partial u_1}\right)_i & \left(\frac{\partial^2 \Pi}{\partial u_n \partial u_2}\right)_i & \cdots & \left(\frac{\partial^2 \Pi}{\partial u_n \partial u_n}\right)_i \end{bmatrix} = \mathbf{K}(\mathbf{u}_i) = \mathbf{K}_i \tag{32}$$

Therefore, Eq. (30) can be rewritten as:

$$\Pi(\mathbf{u})_{i+1} = \Pi_i + \mathbf{R}_i^T \Delta \mathbf{u}_i + \frac{1}{2} \Delta \mathbf{u}_i^T \mathbf{K}_i \Delta \mathbf{u}_i \tag{33}$$

At equilibrium position, the potential $\Pi(\mathbf{u})$ reaches minimum and the first derivative must be equal to zero:

$$\mathbf{R}_i^T + \mathbf{K}_i \Delta \mathbf{u}_i = 0 \tag{34}$$

$$\Delta \mathbf{u}_i = -[\mathbf{K}_i]^{-1} \mathbf{R}_i \tag{35}$$

Eq. (28) now becomes:

$$\mathbf{u}_{i+1} = \mathbf{u}_i - [\mathbf{K}_i]^{-1} \mathbf{R}_i \tag{36}$$

Eq. (36) enables to reach the minimum value of $\mathbf{u}_i$ through iterative process. The residual vector $\mathbf{R}_i$ represents unbalanced nodal forces acting during the iterative process and describes the difference between external applied load $\mathbf{F}^{ext}$ and internal resistance $\mathbf{F}^{int}$ at particular iteration. The convergence is achieved when error reduces to an acceptable limit:

$$\mathbf{R}_i = \mathbf{F}^{ext} - \mathbf{F}_i^{int} \tag{37}$$

$$\mathbf{F}_i^{int} = \int_{vol} \mathbf{B}^T \boldsymbol{\sigma}(\mathbf{u}_i) dvol \tag{38}$$

where, **B** is the strain displacement transformation matrix.

The graphical representation of Newton's method for strain hardening system is shown in Figure 6 (a). For strain hardening system the stiffness increases with load. Starting from the initial point, the iterations are shown as u_i. The tangent from the initial point is drawn till it intersects the external load F^{ext}. The first approximation of the function is calculated at u_1 and residual force after first iteration is shown as R_1. Then the tangent from point 1 is drawn and same procedure is repeated. After three iterations, the system achieves its goal if the residual is less than prescribed limit. The similar procedure for the strain softening system is shown in Figure 6 (b). For such systems, the displacement corrections are in the positive (axes) directions.

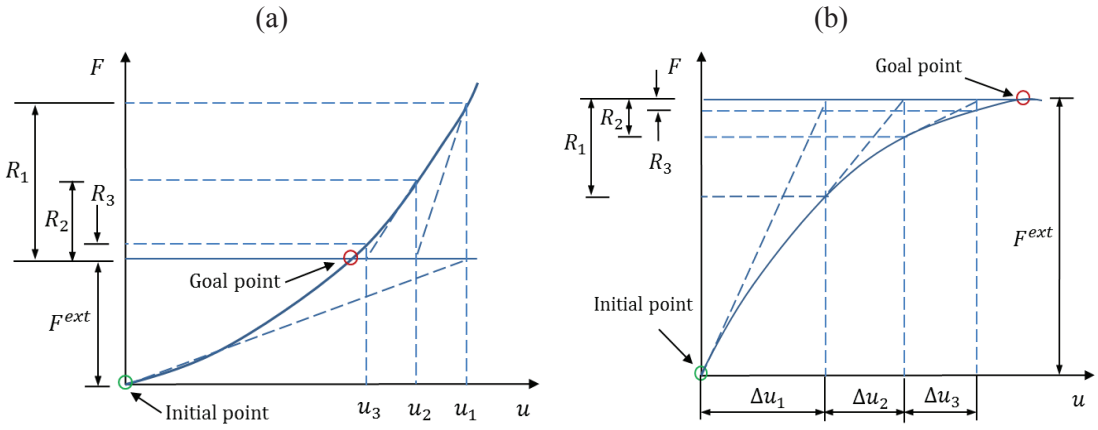

Figure 6. Iteration scheme of Newton method, applied to (a) strain hardening system and (b) strain softening system.

Another variant of Newton's method uses the initial stiffness matrix throughout the iterative process. The displacements are approximated without matrix inversion. The variant is known as modified Newton's method as shown in Figure 7. Although this method takes more iterations for convergence, however, the process is faster due to less computational effort. The displacement update scheme can be written as:

$$\mathbf{u}_{i+1} = \mathbf{u}_i - [\mathbf{K}_0]^{-1}\mathbf{R}_i \tag{39}$$

where, $\mathbf{K}_0$ is the initial stiffness matrix. Both equations (36) and (39) represent implicit method, since Newton's iterations are used to enforce equilibrium. For cases where loading process is irreversible, Newton's methods can be combined with incremental methods for better convergence. In this scheme, the total load is divided into number of ΔF_i and for each load increment, similar iterative correction scheme is applied. This method is known as mixed iteration method. To increase the efficiency of Newton's methods, line-search option can also be used. It allows to determine minimum point along any line. It improves the convergence when Taylor series of the potential function Π include terms, higher than quadratic order.

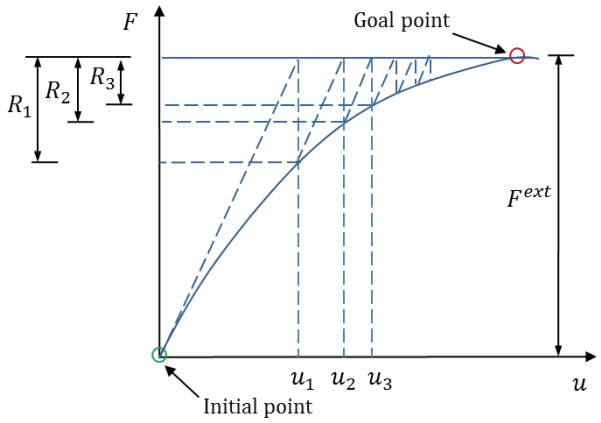

Figure 7. Iteration scheme of modified Newton method.

2.2.2 FEM of contact problems

For contact problems, the application of FEM requires the potential energy of the complete system. In addition, potential energy of the contact region is also required. The contact is established when surface of one body encounters the second body. There are several ways and options to establish the contact.

- The *contact discretization* can be carried out using node-to-surface contact and surface to surface contact. For nodes to surface contact, nodes of the slave surface establish the contact with elements of master surface. The contact is enforced at the slave nodes. For surface-to-surface method, the shape of both master and slave surfaces are considered and the contact is enforced in an average sense over the slave surface.
- To model contact, the desired behaviour is no-penetration. This can be achieved by using *constraint enforcement* method. These methods include; direct

Lagrange method, penalty method and augmented Lagrange method which combines the other two methods. The main difference between these methods is the formulation of potential energy.

- The *contact tracking* or *relative sliding* shows how the constraints evolve. This can be achieved by opting either *finite sliding* or *small sliding* method. Small sliding establishes which slave node and master surface interact initially and do not update during analysis, however, finite sliding allows to track continuously which slave node contact the master surface.

To compute the total potential energy of the system, consider two contacting bodies as shown in Figure 8. The normal pressure in the contact zone will be generated when the gap d_y between the two bodies become zero, i.e.:

$$p \leq 0 \tag{40}$$

$$d_y = u_{y1} - u_{y2} = 0 \tag{41}$$

Eqs. (40) and (41) are dependent on each other, when Eq. (40) changes to equality then Eq. (41) changes to inequality. This leads to Kuhn-Tucker (KT) condition, which can be expressed as:

$$pd_y = 0 \tag{42}$$

These equations provide basis for contact analysis in the absence of friction. When friction is under consideration, the contact conditions can be represented by Eqs. (3) to (6). Now, the total potential energy of the system can be written as:

$$\Pi = \Pi_{12} + \Pi_s \tag{43}$$

$$\Pi = \int_{vol} \boldsymbol{\varepsilon}^T \boldsymbol{\sigma} dvol - \int_A \mathbf{u}^T \mathbf{F}^{\boldsymbol{ext}} dA + \Pi_s \tag{44}$$

where, Π_{12} and Π_s are the potential energies of the bodies and contact surface, respectively. To solve for unknown displacements, $\mathbf{u}$, the potential function can be minimized by using the constraints shown in Eqs. (40) and (41).

$$\Pi = \frac{\partial(\Pi_{12} + \Pi_s)}{\partial \mathbf{u}} \delta \mathbf{u} = 0 \tag{45}$$

To solve the above equation numerically, method of constrained optimization is required. The popular methods include, penalty method, Lagrange and augmented Lagrange method. The penalty methods are generally more efficient, whereas Lagrange methods are more accurate. The accuracy is achieved due to the concept of contact constraints and therefore does not require assumption for imaginary penetration. Considering the accuracy, Lagrange method is opted for the present work. Since only Lagrange multiplier method is used, therefore only finite element formulation of this method is presented.

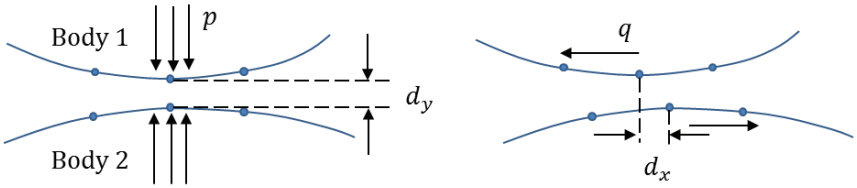

Figure 8. Representation of two contacting bodies with normal and tangential relative displacements.

2.2.3 Lagrange multiplier method

In Lagrange multiplier method, a linear term is added to the optimized function, which contains contact constraints and unknown variables called Lagrange multipliers. The Lagrange multipliers (λ) represents the contact forces (p, q) and the linear term describes the potential energy of the contact surface, Π_s, obtained from KT conditions. This method can be applied to frictionless, as well as, sticking-frictional contact with some modifications.

For frictionless contact, total potential energy includes, potential energy of the bodies and normal forces (represented by KT condition). The energy potential to be minimized can be written as [44]:

$$\Pi(\mathbf{u}, \lambda_y) = \Pi_{12}(\mathbf{u}) + \sum_{j=1}^{n} \lambda_y^j \, d_y^j \tag{46}$$

where, j represents number of elements in the contact zone. In vector form the potential function can be written as:

$$\Pi(\mathbf{u}, \boldsymbol{\lambda}) = \Pi_{12}(\mathbf{u}) + \boldsymbol{\lambda}^T \mathbf{d} \tag{47}$$

where,

$$\boldsymbol{\lambda}^T = \left[\lambda_y^1, \quad \lambda_y^2, \quad \ldots, \quad \lambda_y^n\right] \tag{48}$$

and $$\mathbf{d} = \left[d_y^1, \quad d_y^2, \quad \dots, \quad d_y^n \right]^T \tag{49}$$

For sticking frictional contact, both normal and tangential forces are considered. KT conditions can be written as:

$$q \neq 0 \quad at \quad d_x = 0 \tag{50}$$

or $$q d_x = 0 \tag{51}$$

The total potential energy for stick frictional contact can be formulated as:

$$\Pi(\mathbf{u}, \lambda_y, \lambda_x) = \Pi_{12}(\mathbf{u}) + \sum_{j=1}^{n} (\lambda_y^j \, d_y^j + \lambda_x^j d_x^j) \tag{52}$$

where, $$\boldsymbol{\lambda}^T = \left[\begin{Bmatrix} \lambda_y^1 \\ \lambda_x^1 \end{Bmatrix}, \quad \begin{Bmatrix} \lambda_y^2 \\ \lambda_x^2 \end{Bmatrix}, \quad \dots, \quad \begin{Bmatrix} \lambda_y^n \\ \lambda_x^n \end{Bmatrix} \right] \tag{53}$$

and $$\mathbf{d} = \left[\begin{Bmatrix} d_y^1 \\ d_x^1 \end{Bmatrix}, \quad \begin{Bmatrix} d_y^2 \\ d_x^2 \end{Bmatrix}, \quad \dots, \quad \begin{Bmatrix} d_y^n \\ d_x^n \end{Bmatrix} \right]^T \tag{54}$$

2.2.3.1 Potential minimization

Final system of equations can be derived by minimizing the total potential function. The first variation of potential provides residual vector which can be equated to zero.

$$\delta\Pi(\mathbf{u}, \boldsymbol{\lambda}) = \delta\Pi_{12}(\mathbf{u}) + \delta\boldsymbol{\lambda}^T \mathbf{d} + \boldsymbol{\lambda}^T \delta\mathbf{d} \tag{55}$$

Let $$\mathbf{U} = \frac{\delta \mathbf{d}}{\delta \mathbf{u}} \tag{56}$$

and $$\mathbf{R} = \mathbf{R}(\mathbf{u}) = \frac{\delta \Pi_{12}}{\delta \mathbf{u}} \tag{57}$$

Eq. (55) can be written as:

$$\delta\Pi(\mathbf{u}, \boldsymbol{\lambda}) = \mathbf{R}\delta\mathbf{u} + \boldsymbol{\lambda}^T \mathbf{U}\delta\mathbf{u} + \delta\boldsymbol{\lambda}^T \mathbf{d} \tag{58}$$

$$= (\mathbf{R} + \boldsymbol{\lambda}^T \mathbf{U})\delta\mathbf{u} + \mathbf{d}^T \, \delta\boldsymbol{\lambda} \tag{59}$$

Minimizing above equation and equating to zero leads to:

$$\mathbf{R}(\mathbf{u}) + \boldsymbol{\lambda}^T \mathbf{U} = 0 \tag{60}$$

$$\mathbf{d}(\mathbf{u}) = 0 \tag{61}$$

2.2.3.2 Linearization

Linearization can be performed by expanding Eqs. (60) and (61) using Taylor series and skipping the higher order terms. For iterative solution, these expressions are required to be transformed in terms of linear increments i.e. $\Delta\mathbf{u}$ and $\Delta\boldsymbol{\lambda}$. Let $\mathbf{u}_i$ is the solution at increment *i*. The first term of Eq. (60) can be expanded as:

$$\mathbf{R}_{i+1} = \mathbf{R}_i + \left(\frac{\partial \mathbf{R}}{\partial \mathbf{u}}\right) \Delta_{i+1}\mathbf{u} \tag{62}$$

$$= \mathbf{R}_i + \mathbf{K}\Delta_{i+1}\mathbf{u} - \Delta_i \mathbf{F}^{ext} \tag{63}$$

where,

$$\mathbf{K} = \frac{\partial^2 \Pi_{12}}{\partial \mathbf{u}^2} \tag{64}$$

$\mathbf{K}$ represents tangent stiffness matrix and $\Delta_i \mathbf{F}^{ext}$ is the increment of external load. The second term of Eq. (60) can be written as:

$$\boldsymbol{\lambda}_{i+1}^T \mathbf{U}_{i+1} = \left(\boldsymbol{\lambda}_i^T + \Delta_{i+1}\boldsymbol{\lambda}^T\right)\left[\mathbf{U}_i + \left(\frac{\partial \mathbf{U}}{\partial \mathbf{u}}\right)_i \Delta_{i+1}\mathbf{u}\right] \tag{65}$$

$$= \boldsymbol{\lambda}_i^T \mathbf{U}_i + \mathbf{U}_i^T \Delta_{i+1}\boldsymbol{\lambda} + \boldsymbol{\lambda}_i^T \mathbf{V}_i \Delta_{i+1}\mathbf{u} \tag{66}$$

where,

$$\mathbf{V} = \frac{\partial \mathbf{U}}{\partial \mathbf{u}} = \frac{\partial^2 \mathbf{d}}{\partial \mathbf{u}^2} \tag{67}$$

Eq. (61) can be expanded as:

$$\mathbf{d}_{i+1} = \mathbf{d}_i + \left(\frac{\partial \mathbf{d}}{\partial \mathbf{u}}\right)_i \Delta_{i+1}\mathbf{u} \tag{68}$$

$$= \mathbf{d}_i + \mathbf{U}_i \Delta_{i+1}\mathbf{u} \tag{69}$$

The system of equations at increment *i*+1 is given by:

$$\left(\mathbf{K}_i + \boldsymbol{\lambda}_i^T \mathbf{V}_i\right)\Delta_{i+1}\mathbf{u} + \mathbf{U}_i^T \Delta_{i+1}\boldsymbol{\lambda} = -\mathbf{R}_i - \boldsymbol{\lambda}_i^T \mathbf{U}_i + \Delta_i \mathbf{F}^{ext} \tag{70}$$

and

$$\mathbf{U}_i \Delta_{i+1}\mathbf{u} = -\mathbf{d}_i \tag{71}$$

or

$$\begin{bmatrix} \mathbf{K}_i + \boldsymbol{\lambda}_i^T \mathbf{V}_i & \mathbf{U}_i^T \\ \mathbf{U}_i & 0 \end{bmatrix} \begin{Bmatrix} \Delta_{i+1}\mathbf{u} \\ \Delta_{i+1}\boldsymbol{\lambda} \end{Bmatrix} = \begin{Bmatrix} -\mathbf{R}_i - \boldsymbol{\lambda}_i^T \mathbf{U}_i + \Delta_i \mathbf{F}^{ext} \\ -\mathbf{d}_i \end{Bmatrix} \tag{72}$$

2.2.4 Contact algorithm scheme

The schematic of ABAQUS contact algorithm within one increment is shown in Figure 9 [45]. The process can be explained by using following steps.

- The first step is to identify initially active contact constraints. This step is based on the initial model state. The contact state of each point is analysed, if it's open or closed.
- Then the stiffness of the system is calculated by enforcing contact constraints. The system of equations is solved by using iterative approach.
- The changes in contact status are identified by comparing contact pressure and clearances with initial contact state. The iterations in which contact status changes are known as sever-discontinuity iterations. During these iterations, load displacement curve suddenly changes, producing a discontinuity in the slope of the curve.

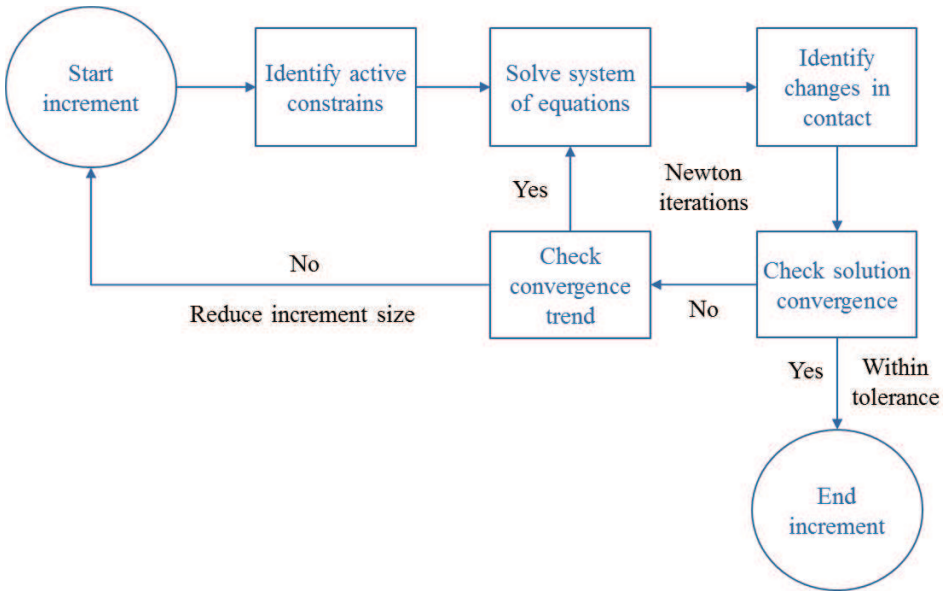

Figure 9. Schematic of contact algorithm within one increment.

- Then the contact state and equilibrium conditions convergence criteria are checked. The incompatibilities related to severe discontinuity iterations must be small enough in comparison to contact state to achieve contact state convergence. To satisfy equilibrium condition, force residual and solution correction must be satisfactorily small. If the convergence criteria are met then the increment is complete.
- If the convergence criteria are not met, then the convergence trend is checked. The number of contact status changes are evaluated in consecutive iterations. If the convergence is observed, contact constraints and stiffness are updated. If there is no convergence, then increment is started again with smaller step size.

2.3 Mechanics of crack phases

The model describing crack stages in fatigue failure was described by Forsyth [46]. The complete process is mainly divided into two stages. The evolution of micro cracks during the early crystallographic phase, starts from some fraction of Angstrom (1 Angstrom=10^{-10}m) to some tens of Angstrom per cycle. During this phase damage accumulation is very slow. Stage I includes the breakthrough of first few grains and is generally dominated by shear cracking. In HCF, this may take significant proportion of the total fatigue life. Due to random distribution of grains, the shearing stress may not have continuous orientation in these few surface grains. The orientation of slip plane may therefore varies depending on grains orientation, as shown in Figure 10. In stage I, growth of crack depends mainly on metallurgical factors like inclusions, interphases and grain boundaries, etc. Once the crack is large enough to pass few grains, it's already macroscopic in length and does not depends on local metallurgical factors. This stage is known as stage II. In this stage, the local shearing stress in not effective anymore and crack growth is influenced by tensile stress, hence crack changes the direction and grows on a plane perpendicular to maximum tensile stress direction or external tensile load. The crack growth rate at the end of stage I and beginning to stage II can be of the order of 10^{-4} to 10^{-3} μm/cycle. At the final phase of stage II it can increase up to 10^{-2} to 10^{-1} mm/cycle [47]. The crack growth in stage II depends on stress intensity factor range at the crack tip.

During the last part of failure, rapid crack growth occurs. The crack tip stress rises as the crack grows longer which increases the cross slipping intensity. Consequently, shear component dominates again and crack orientation may take 45° turn with respect to maximum tensile stress direction. However, during this stage the crack does not grow in crystallographic planes, rather it progresses on grain boundaries. The high overload leads to rapid fracture due to enlargement and joining of pores around inclusions. This phase is sometimes termed as stage III. Although Forsyth did not term this phase as stage III, however this phenomenon was explained as high stress failure. Generally, at this stage crack grows very rapidly and therefore neglected for design purposes.

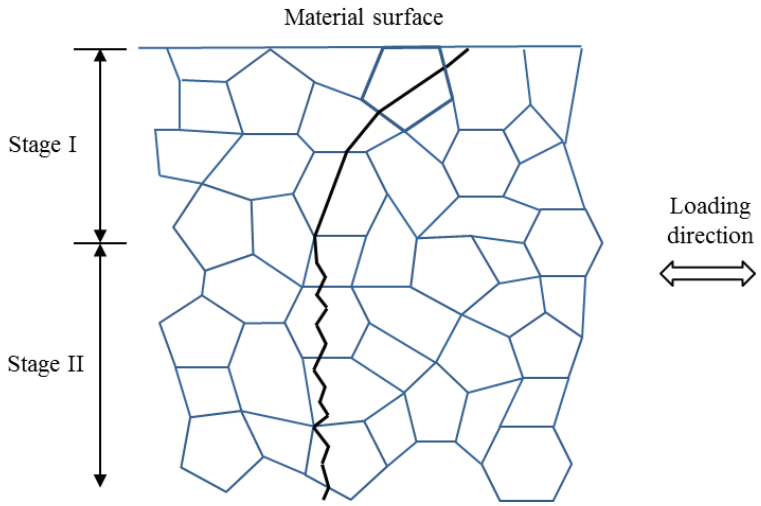

Figure 10. Stages of crack growth.

2.3.1 Crack nucleation

As mentioned earlier, the complete failure process consists of two phases, namely nucleation and propagation. Each phase has its own mechanics and therefore should be dealt with using different theories. The analysis of crack nucleation has its own significance, since it can take major proportion of complete failure life. On the other hand, it is still a challenging task since, damage initiation starts at micro scale and develops inside the contact zone. As mentioned in the introduction section, the crack nucleation is a phase or process starting from damage initiation ends at crack initiation. Based on continuum mechanics, damage initiates at a certain threshold level, whereas crack initiation refers to formation of flaw up to few grains size of the material. The crack initiation life, therefore, is designated to the life taken at the end of crack initiation or at the start of crack propagation. The experimental crack initiation life also depends on the measurement approach and hence limited by the method or equipment employed. The popular methods include digital image correlation (DIC) [48], infrared thermography [49, 50], magnetic particle testing (MPT), ultrasonic and vibro-acoustic method [51, 52], potential drop and radiography testing [53].

It is interesting to compare few observations between fretting fatigue and plain fatigue crack initiation. In fretting fatigue, the surface damage can produce more than one crack due to interaction of two surfaces. Whereas in plain fatigue generally there is single crack, which develops and grows further. In fretting fatigue crack originates from the surface whereas in plain fatigue crack may start at subsurface. This leads to another difference between plain and fretting

fatigue. In plain fatigue, crack develops from an existing void or inclusion present due to manufacturing process. For fretting fatigue, crack initiates from the region of high stress concentration usually observed at the edge of the contact. Although multiple loads and contact interaction is involved in fretting fatigue, still it cannot be generalized that fretting fatigue life will always be lower than plain fatigue life. The life for each case depends on particular conditions. The damage caused by fretting can also vary from mild fretting to severe fretting. Most of the researchers use plain fatigue data for estimation under fretting fatigue conditions.

There are numerous factors or variables that can affect crack initiation life, broadly they can be divided into three groups [1].

i. Mechanical variables like stresses, strain, slip amplitude or coefficient of friction, etc.
ii. Material variables that include micro scale properties such as grain size, crystallographic orientation and bulk properties e.g. yield strength or fracture toughness.
iii. Environmental variables such as ambient temperature, pressure or humidity.

Most researchers have studied crack nucleation using mechanical variables, whereas relatively less work is carried out with material and environmental variables. The analysis of crack initiation life is dominated by analysing stresses at the contact interface or just below it. The other important parameter is relative displacement or slip amplitude between the contacting bodies. The effect of both variables play vital role in crack initiation life. Vingsbo and Söderberg [2] presented the effect of fretting fatigue life, slip amplitude and wear rate. Based on slip amplitude, they distinguished three contact regimes at the contact interface. These regimes were termed as *stick regime*, *mixed stick-slip regime* and *gross slip regime*. The stick regime was referred to zero or very low slip amplitude, whereas mixed stick-slip regime referred to partial slip condition, where there was a stick zone in the middle and slip zones towards the edges. The gross slip (or sliding) referred to the condition when there was displacement at the whole interface region between the two bodies. It was observed that at low slip amplitudes, wear rate was also low, whereas fatigue lives were long. With the increase of slip amplitude, the wear rate increased and fatigue life reduced. Minimum fatigue life was observed at a transition point between stick-slip regime and gross slip regime. On further increase of slip amplitude, the wear rate also increased, as well as, fatigue life. The increase in fatigue life was observed due the fact that the initial crack were removed in the wear process and could not get a change to grow further. This work also bifurcates two main fields relating to fretting process, namely, fretting fatigue and fretting wear. Hence it is essential to identify the fretting regime of any practical problem for analysis and application.

The analysis of crack nucleation is generally carried out in two different ways. The first method uses mechanical variables like stresses, strains and displacements, which are then used to estimate crack initiation location and life. However, these methods do not elaborate physical

evolution of nucleation process and generally neglect the effect of surface conditions. Examples of this method include critical plane approach, stress invariant approach and fretting specific parameters. The detail about these approaches is covered in the next chapter. The other method uses micromechanics of the material and models the nucleation mechanism based on local conditions, which lead to the formation of flaw. These micro models are based on crystal plasticity and includes the effect of grain boundaries, crystallographic orientation and surface texture [54].

2.3.1.1 Slip plane

During cyclic loading, if the applied loads exceeds fatigue limit of the material, the shear stresses activate highly localized process in few grains that undergo plastic slip condition. In these grains the crystallographic planes, known as slip planes, are oriented to maximize the effect of resolved shear stress. The slip planes generally start from the directions, which are oriented favourably to the external load and hence start plastic flow. Considering a single grain with a cross sectional area A subjected to tensile load, F. The slip plane in the grain can be defined by its normal, $\boldsymbol{n}$, which makes an angle θ with the specimen axis. The slip direction on the slip plane can be defined by angle ϑ with the specimen axis as shown in Figure 11. The area of slip plane A_{sp} and force along slip direction F_s can be written as [55]:

$$A_{sp} = \frac{A}{cos\theta} \tag{73}$$

$$F_s = Fcos\vartheta \tag{74}$$

$$\tau_s = \frac{F_s}{A_{sp}} = \frac{F}{A} cos\vartheta cos\theta \tag{75}$$

where, τ_s is the shear stress resolved in the slip direction whereas the factor $cos\vartheta cos\theta$ is known as Schmid's factor. The expression shown in Eq. (75) is known as Schmid's law, which has been verified for large number of metallic single crystals.

The magnitude of shear stress required to initiate slip in a single crystal is termed as *resolved critical shear stress,*τ_{cr}. According to this law, plastic flow occurs on the plane and in direction, where Schmid's factor is maximum. Therefore, crystal orientation can facilitate or hamper the dislocations. If the slip plane or slip direction are normal (ϑ = 90° or θ = 90°) to the applied tensile load, then τ_s is zero and plastic flow cannot occur, irrespective of the loading magnitude. The Schmid's factor attains its maximum for $\vartheta = \theta$ = 45° and resolved shear stress τ_s reaches the critical value, τ_{cr}.

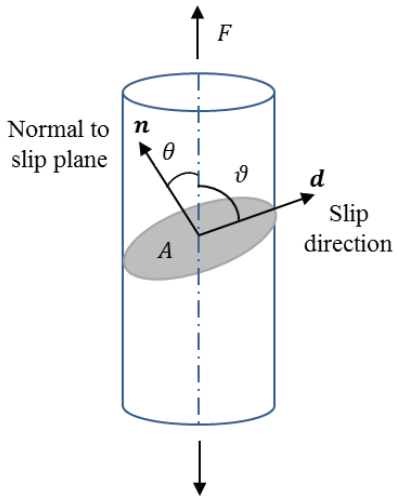

Figure 11. Conceptual diagram of slip plane and slip orientation in a single grain.

For polycrystalline materials, grains may have random orientation as shown in Figure 12. An example of a grain, in which resolved shear stress can reach a critical value, is highlighted near the surface. In fretting fatigue, this phenomenon can occur in few grains near the contact edge, whereas the rest of the grains may behave elastically. On continuous application of fatigue load, more slip planes appear in grains, where Schmid's factor is maximum.

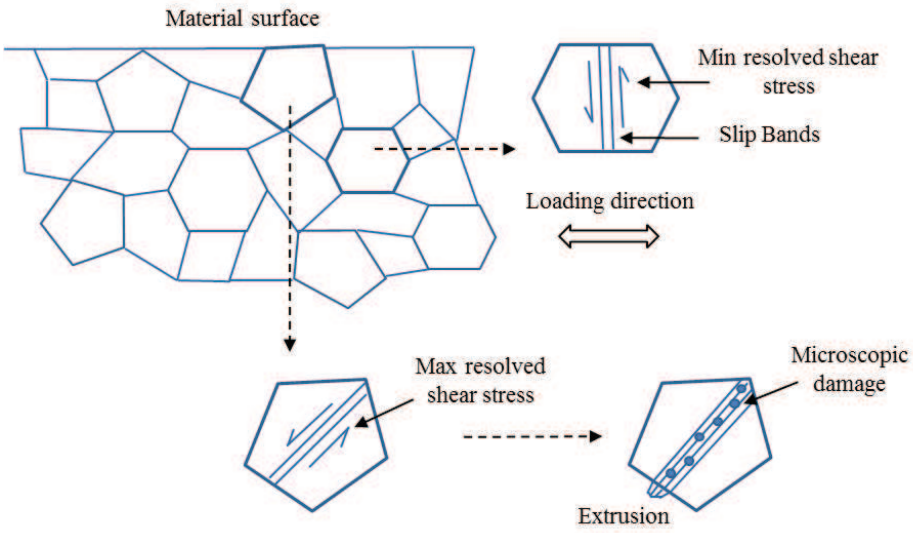

Figure 12. An example of polycrystalline material showing maximum and minimum resolved shear stresses orientation and microscopic damage.

In high cycle fatigue (HCF) and fretting fatigue, slips usually concentrate in separated bands since the plastic deformation is highly localized. The slips that occur in one direction later activate in opposite direction, however the process remain irreversible. The thin layer or bands protruded from the surface act as local stress risers as shown in Figure 13. On further amplification of process local deformations are produced, which lead to the formation of extrusion and cause nucleation of micro cracks. As the slip planes and bands remain on the surface, they are known as *persistent slip bands*. This phenomenon was observed and explained by Thompson et al. [56], during a study on development of fatigue cracks in copper. On these persistent slip bands, the damage nucleates generally in form of micro cavities and develop through coalescence of these cavities or pores. For HCF, crack initiates and grows in transgranular fashion, whereas in low cycle fatigue crack initiation is intergranular, however, it may switch to transgranular during propagation.

At this stage it is also important to define the length scale, which represent micro crack or point of damage initiation. The crack with a length of at least 3 μm can be referred as micro crack [57]. Smaller than this length, any imperfection may be referred as a cavity, void or sub-microscopic defect [55]. Below certain threshold value of applied stress, slip planes do not form. Even if they appear, these planes do not contain any microscopic defect. Above a stress threshold, persistent slip band start to form and damage initiates in the form of micro cavities or pores in some grains at the surface. These micro cavities are transgranular and are blocked by grain boundaries and located in the slip band. On further load reversals, multiplication of slip band occurs under the action of resolved shearing stress.

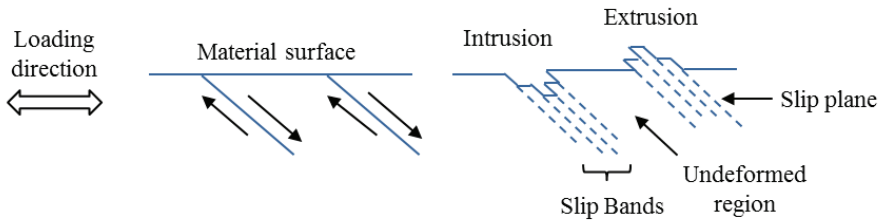

Figure 13. Formation of slip planes and bands in groups under fully reversed cyclic loading.

Slip planes are usually supplemented by the presence of a discontinuity. They generate intrusion or extrusion (see Figure 13) which converts slip plane into persistent slip bands where damage nucleation takes place in the form of pores or micro cracks. On further load reversals, the damage increases and extends to neighbouring grains, while crossing grain boundaries. The micro cracks in few grain coalesce to form a mesocrack. The mesocrack is generated on breaking of

inclusions and allows the coalescence process to occur. The micro crack when growing up to a length of 100 to 200 µm for light alloys and 200 to 500 µm for steel can be referred as mesocrack [58]. Most often, nucleation phase is considered up to this point and crack length is known as crack initiation length. The number of cycles required for crack initiation is known crack initiation life. After this length, generally crack is regarded as macro crack, which develop due to coalescence of mesocracks and several grains boundary break through. Further crack growth occurs perpendicular to the surface, under the influence of tensile stress till the complete failure of the specimen. The complete failure sequence is shown in Figure 14. In fretting fatigue, generally more than one crack originate at the surface, however only one primary crack grows further to cause final failure [59, 60].

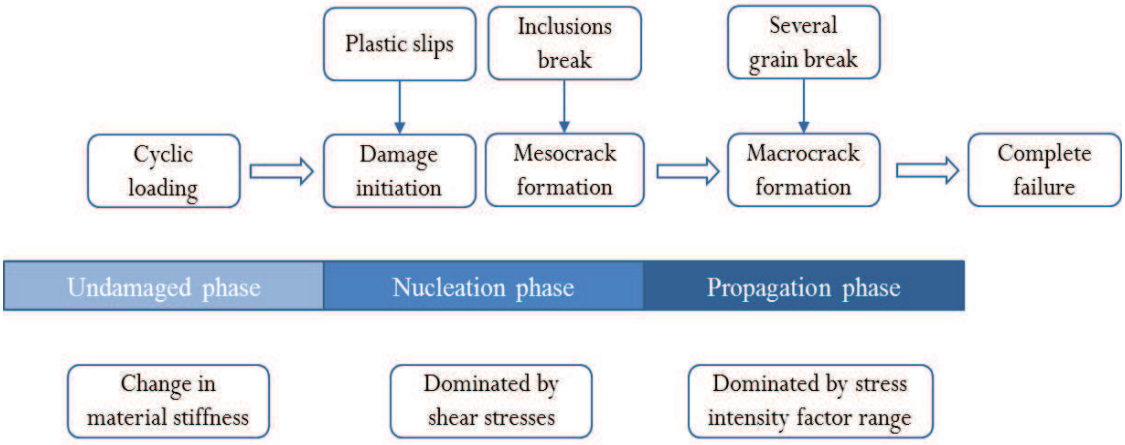

Figure 14. Schematic of failure sequence with processes involved in nucleation and propagation phase.

2.3.1.2 Extrusion-intrusion model

As described earlier slip planes are formed when resolved shear stress reach the critical value in some grains on the surface due to cyclic load. An *extrusion* is a small lamina of metals that protrude from the surface of a slip band due to dislocation resulting from cyclic load. The *intrusions* are crevices that are formed inwards due to reversal of load during tension compression cycle. The order of these discontinuities are 1 to 10 µm. Forsyth [61] observed extrusion formation in Cu-Al alloy specimen with thickness up to 0.1 µm and length 10 µm for the slip lines. The phenomena of slip formation are described by several researchers, however a brief description on model proposed by Cotrell and Hull [62] is presented in Figure 15. According to them, there are two potential slip planes, which are perpendicular to each other. During the tensile load, the discontinuity source S_1 activates the corresponding slip plane 1 along the direction shown in stage

(a). Successively, during the same tensile load, the second source S_2 activates a plane 2, perpendicular to the first one, as shown at stage (b). Also at stage (b), the source S_1 shifts towards right side, in comparison to stage (a). During unloading when plane 1 reactivates, it generates a groove while breaking the slip plane 2, shown as stage (c). This generate the intrusion, I, in the surface. When slip plane 2 reactivates during unloading, it forms the extrusion, E, on the surface as shown in stage (d). This model presents an example of intersecting slip bands. However, for some materials the intrusion extrusion may not be intersecting, rather they are unidirectional, as previously shown in Figure 13. Therefore, different materials may have different appearances of slip bands [63, 64].

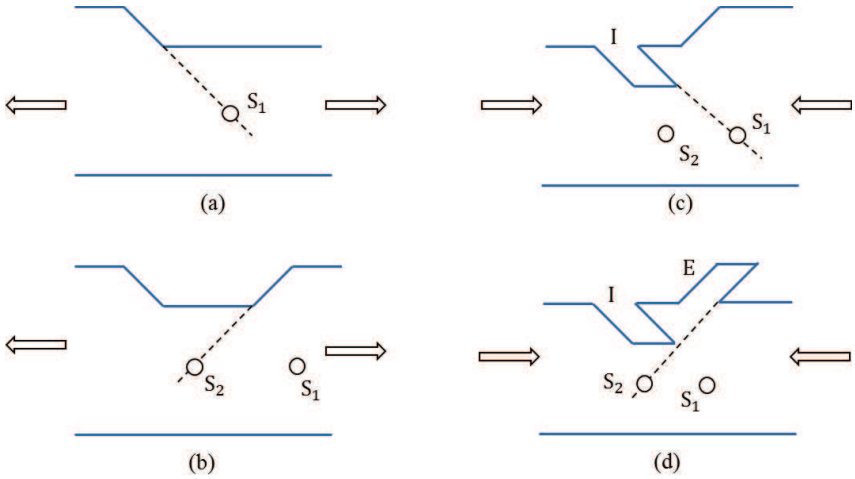

Figure 15. Extrusion-intrusion model with intersecting slip bands by Cotrell and Hull [62].

2.3.1.3 Effect of inclusion on crack nucleation

During fatigue loading, the two main factors, which may initiate a damage, in the absence of inclusions, are persistent slip bands and slips planes that are activated due to surface imperfections. The metallurgical variations lead to formation of persistent slip bands, whereas surface imperfections arise during manufacturing or machining process. The manufacturing process may introduce a third element, which may assist damage initiation in the form of inclusions. Generally, inclusions are generated during the heat treatment process or material processing at elevated temperatures. When deformation occurs, dislocation gather around the obstacles (grain boundary or an inclusion) and apply localized force inside the grain. This force may generate voids around inclusion by debonding or breaking, due to difference in hardness between inclusions and metal [65]. The failure progress due to growth of voids and coalescence,

especially in ductile failure. The damage nucleation accelerates with increase in inclusions percent volume. The typical inclusions contain, oxides, sulphites, silicates and carbides. The Aluminium inclusions Al_2O_3 are very hard and brittle. Titanium carbon-nitride can be formed in steel 4340, which are also brittle and may break at very low deformation, leading to a micro crack. The manganese sulphide MnS inclusions can be present in medium to low carbon steels, but are relatively less brittle.

The type of inclusions also affects the strength of the material, e.g. long and sharp inclusions may reduce the fracture strength of a specimen. The sharp locations act as high stress concentration areas that are capable to activate a slip band. Inclusions may also forestall damage initiation and reduce the fatigue limit. For high strength steel e.g. in tool steel, Al_2O_3 inclusions may be as long as 200 μm as they are not located in a single grain. When the micro cracks initiate at the surface inclusions, the slip bands are blocked by small size of the grains 5 to 10 μm. Due to presence and breaking of inclusions, micro crack may grow to next grain and consequently affects the fatigue limit. The high stress concentration at edge of two voids may also generate a slip band between them. Below certain critical length (initiation phase), fatigue limit is not much affected by inclusions [55]. For inclusions to compete for damage initiation with other two sources, plastic slips bands and surface imperfections, they need to be comparable in size and present closer to the surface. Duckworth and Ineson [66] showed that inclusions affected the fatigue strength for high strength steel, when its size was equal to or greater than 10 μm. When the inclusions were introduced 100 μm below the surface, the size required raised up to 30 μm to compete with extrusion and surface imperfection for crack initiation location. This shows that stress concentration at inclusion apex depends on inclusion size, geometry and location.

Under fretting fatigue condition, another source that contributes in crack nuclaetion is high stress concentration at the contact interface. The surface degradation due to contact and oscillatory loads may supplement the crack nucleation process. The crack initiation site for such cases is often observed at the edge and interface of the contact. The presence of inclusion at or near the surface under fretting fatigue condition adds another variable in the nucleation process. The presence of a discontinuity near the surface may lead to crack initiation from the surface or from the inclusion and is therefore also a topic of interest.

2.3.2 Crack propagation

Although the present work is related to crack nucleation phase, however a brief introduction of the propagation phase is given here, since for some cases total life (nucleation plus propagation) was predicted and compared with experimental results. One of the important factors of fatigue crack analysis is to measure the crack growth rate during the propagation phase. This can be done using fracture mechanics approach. The crack tip plastic zone causes sequential crack

growth, which is encompassed by elastic material. When the plastic zone is significantly small, the conditions can be described by surrounding elastic stress field and stress intensity factors. The stress state near the crack tip of an infinite plate can be determined as [67]:

$$\sigma_{ij}(r,\theta) = \frac{1}{\sqrt{2\pi r}}\left[K_I f_{ij}^{I}(\theta) + K_{II} f_{ij}^{II}(\theta) + K_{III} f_{ij}^{III}(\theta)\right] \tag{76}$$

where, r and θ are the distance and orientation from the crack tip to the desired point. K_I, K_{II}, K_{III} are the stress intensity factors for modes I, II and III, respectively. $f_{ij}(\theta)$ are functions defined in polar coordinates. Figure 16 shows the possible loading modes of the crack tip. By applying Hooke's law, strains and subsequently displacements can be computed as:

$$u_i(r,\theta) = \frac{\sqrt{r}}{2E\sqrt{2\pi}}\left[K_I g_i^{I}(\theta) + K_{II} g_i^{II}(\theta) + K_{III} g_i^{III}(\theta)\right] \tag{77}$$

where, $g_i(\theta)$ are the functions depending on Poisson's ratio ν and bulk modulus κ (under plane stress or plane strain condition). Eq. (76) and (77) show that stresses and displacements near the crack tip depends on stress intensity factors, which are of the form as:

$$K = Z\sigma_A\sqrt{\pi l} \tag{78}$$

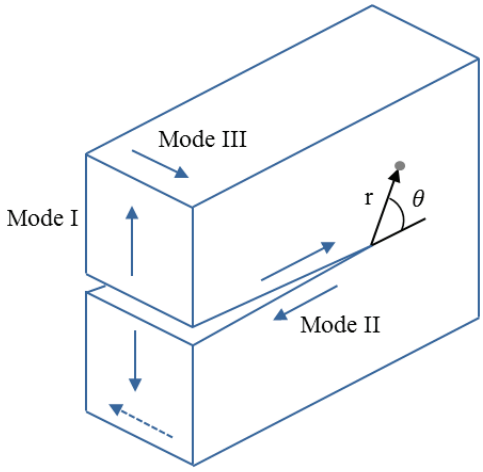

Figure 16. Loading modes for crack opening.

The function Z describes the influence of geometry, σ_A is the applied stress and l is crack half length. The stress intensity factors are also related to strain energy release rate Y, through bulk modulus κ and shear modulus G [68] as:

$$Y = \frac{1}{8G}[(1+\kappa)(K_I^2 + K_{II}^2) + 4K_{III}^2] \tag{79}$$

This energy based relation of crack growth is applicable to brittle fracture. The crack extends when Y reaches a critical value under any mixed mode loading. For any particular loading mode, the fracture criterion can also be defined by specific related stress intensity factor, commonly known as fracture toughness. The crack tip plastic zone causes crack growth under the fatigue load. The crack growth rate can be written as:

$$\frac{dl}{dN} = f(\Delta K) \tag{80}$$

$$\Delta K = K_{max} - K_{min} \tag{81}$$

$$\Delta K_{eff} = \Delta K(1-R)^{n-1} \tag{82}$$

$$R_\sigma = \frac{K_{min}}{K_{max}} = \frac{\sigma_{min}}{\sigma_{max}} \tag{83}$$

where, N represents number of cycles and ΔK denotes stress intensity factor range at the crack tip. The function, f, can be determined experimentally by performing fatigue tests for a range of geometries of crack having same stress intensity factor. K_{max} and K_{min} are the maximum and minimum stress intensity factors, σ_{max} and σ_{min} are the maximum and minimum applied stress, respectively. Eq. (82) represents effective stress intensity factor range ΔK_{eff} to incorporate effect of different R ratios [69]. n is a material constant, which ranges from 0 to 1. Figure 17 shows schematic diagram of crack growth rate and stress intensity factor range. Below certain threshold value of stress intensity factor range,ΔK_{th}, crack does not propagate. After ΔK_{th}, crack growth rate increases rapidly, which is synonymous to stage I crack as defined by Forsyth [46]. As described earlier, during this stage short crack develops under localized plasticity and dislocations along persistent slip band direction. On further increase of ΔK, the crack growth increases linearly in stage II. The crack also changes orientation at the start of stage II and grows under mode I loading. Stage II growth rate can be expressed by Paris' law [70], i.e.:

$$\frac{dl}{dN} = C(\Delta K)^m \tag{84}$$

where, C and m are constants. With further increase in ΔK, crack tip plastic zone triggers the rapid failure, which is represented as stage III.

It is generally believed that crack propagates under tensile mode, perpendicular to maximum principal stress. Under tension, the crack faces open and further increase stress intensity factor range. While under compression, the faces close and the presence of crack remains insignificant since there is no stress intensity at the crack tip. Under fretting fatigue, the initiated crack may undergo partial closure due to high stress gradient in the vicinity of the contact. Therefore, part of the crack may exist in tensile region, while remaining in compression [1].

It is important to mention here that application of linear elastic fracture mechanics is unsuitable for nucleation phase or for stage I of crack. The condition for elastic and isotropic material is invalid at this small scale. The crystallographic orientation of each grain will be different, which leads to anisotropy. The fracture planes and grains boundaries will provide hindrance for crack growth, which should be taken into account. The linear elastic fracture mechanics is applicable to fretting fatigue, while considering crack length scale, contact size and material microstructure. The propagation phase can be described for large contact size and for fine microstructures.

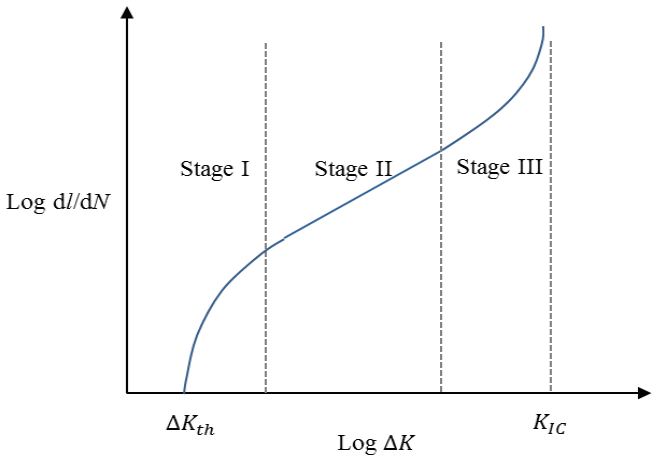

Figure 17. Schematic of crack growth stages by plotting crack growth rate against stress intensity factor range.

2.3.3 Stress non-proportionality

Multiaxial fatigue refers to the condition, when multiple loads are acting simultaneously in different directions or sequences. Also, if sequential loads of various kinds are acting on a

mechanical structure, this may lead to multiaxial stress state at some point in the specimen. For accurate analysis, it is important to predict stress state before hand to adopt a suitable strategy. Uniaxial or multiaxial loading and uniaxial or multiaxial stress state are not necessarily directly related to each other. A uniaxial load may produce multiaxial stress state, such as, at the root of a notch as shown in Figure 18. While multiaxial loading may lead to a stress state for which only uniaxial strength analysis is important for design, due to one of dominating stress components [71]. Therefore, there is no direct relationship between loading state and stress state.

Fretting fatigue involves multiaxial loading, which give rise to multiaxial stress state. Different stresses vary over the contact interface depending upon geometry and loading magnitude. The term non-proportional loading describes the condition, when components of multiaxial loading change in relation to each other non-proportionally. Similarly, the term non-proportional stress refers to the condition, when ratio of different stress components varies with respect to time. This condition is developed in cases such as periodic loads with phase difference between them, a periodic load with variable frequency of components, a multiaxial periodic load with a mean value, multiaxial random load or tension compression block load followed by torsion block [72].

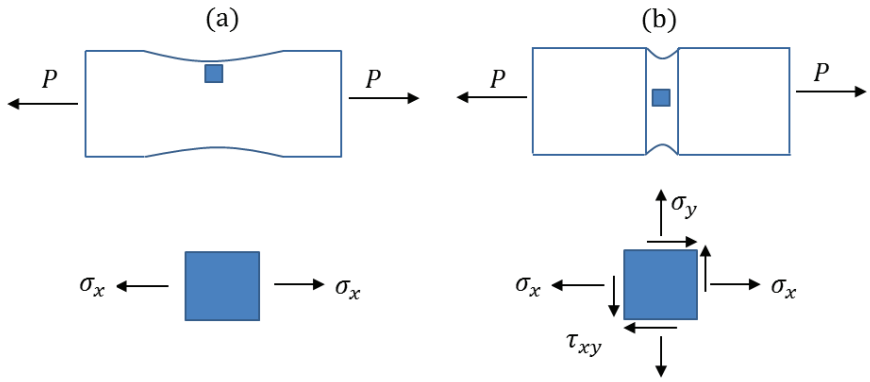

Figure 18. Local stress state for uniaxial load leading to (a) uniaxial stress state (b) multiaxial stress state

Non-proportional loading generally leads to non-proportional stress or strain state. The schematic of proportional and non-proportional stress state is shown in Figure 19. Most often non-proportional stress state can be characterized by change of direction of principal axes. If the principal axes of stress or strain changes orientation, it shows the presence of non-proportional stresses, which directly influences the damage mechanism. A uniaxial load may also lead to

rotation of principal axes as shown by Carpinteri et al. [73]. Thus, it is more meaningful to the term non-proportional stress state rather than non-proportional loading.

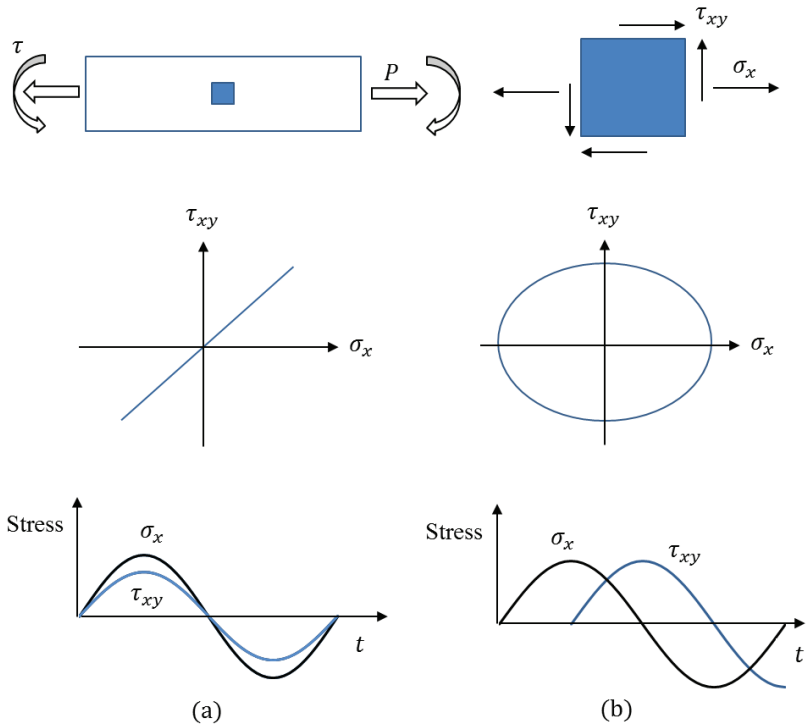

Figure 19. Loading state of a shaft under tensile and torsion, producing (a) proportional stress for in phase and (b) non-proportional stresses for out of phase loading.

2.3.3.1 Effect of non-proportionality on crack nucleation

Several researchers have shown that non-proportional loading affects the crack nucleation process during fatigue loading. Kanazawa et al. [74] analysed crack distribution for different phase angles ø ranging from 0° to 90° for 1CrMoV. They observed that mostly cracks were initiated in the direction of maximum shear stress, with some variation in distribution of crack directions. For ø =30°, the crack initiation angles were observed from -5° to -30°. With the increase in phase difference, more number of slip planes reached a critical value require for crack initiation. The standard deviation also increased and maximum value was observed for ø =90°. The crack initiation angles were observed ranging from +8° to -45°. Mcdowell et al. [75] showed that high degree of non-proportionality activated more number of slip systems for stainless steel specimen. Whereas only one slip system per grain was observed, which were subjected to pure tension or pure torsion loading. Ohkawa et al. [76] also studied the distribution of crack orientation for different ø, like Kanazawa et al., but for S45C steel. The cracks were observed in different directions, but maximum number of cracks were observed near maximum shear plane

for in phase loading. For ø =90° more uniform distribution of crack orientations were observed ranging from -90° to 90°. Zhang and Jiang [77] studied slip system in copper specimen using tension-compression and torsion tests. They also found that more number of slip systems were activated with phase shift of 90° than for in phase loading. Similar results were also reported by Ahmadi and Zenner [78], Verreman and Guo [79].

This shows that shear stresses act in multiple directions with out of phase or non-proportional loading than for in phase loading. It may also lead to crack initiation in more number of planes. For in phase loading most of the crack appear in maximum shear stress direction. With an increase of non-proportionality, due to phase difference, crack may initiate in different directions.

2.3.3.2 Effect of non-proportionality on fatigue life

The non-proportional stresses affect in both stages of fatigue process and consequently affects the fatigue life. The degree of non-proportionality can be described by phase difference of applied loads. Nisihara and Kawamoto [80] studied the influence of degree of non-proportionality on fatigue strength. It was observed that effect of non-proportionality increased with increase in phase difference and led to an increase in fatigue limit. McDiarmid [81] found a decrease in fatigue limit for mild steel, whereas an increase in fatigue limit was observed for cast iron. This shows that non-proportional loading may also improve the fatigue properties for some cases. Skibicki et al. [82] studied the influence of non-proportionality by using different tension-compression, torsion and phase shift loadings. For proportional cases the predicted life was observed within a scatter band of 2, whereas for non-proportional cases scatter band even greater than 3 was observed. Fatemi and Socie [83] found that out of phase loading was more damaging than for in phase loading for LCF regime. Whereas for HCF regime, it proved to be less damaging at the same loading amplitudes. In LCF regime, the additional cyclic hardening under out of phase loading, causes an increase in maximum normal stress, which leads to enhance fatigue behaviour. It can also be said that influence of non-proportionality on fatigue life depends on loading magnitudes. Higher loading magnitude will lead to higher plastic strain.

This shows that the non-proportionality affects the fatigue life depending upon the degree of non-proportionality (phase difference) and loading magnitudes, which describe HCF and LCF regimes. It is also important to realize that while evaluating the effect of non-proportionality, the capability of the damage model to incorporate non-proportional effects also influence the predicted results. Since in most of the practical application failure occurs due to fretting fatigue, it is important to analyse fretting fatigue behaviour under various degree of non-proportionality. This may significantly affect the service life of the product. The above discussion also leads to the main objective of the present thesis.

2.4 Basic fatigue terminologies

This section describes some basic definitions that apply to plain and fretting fatigue. These terminologies will be used and referred to in the text of the subsequent chapters.

2.4.1 Stress amplitude

The deviation of stress from mean is known as stress amplitude. It is also known as alternating stress. The same terminology can also be used for strain.

$$\sigma_a = \frac{\sigma_{max} - \sigma_{min}}{2} = \frac{\Delta\sigma}{2} \tag{85}$$

2.4.2 Mean stress

The average of maximum and minimum stress is known as mean stress.

$$\sigma_m = \frac{\sigma_{max} + \sigma_{min}}{2} \tag{86}$$

2.4.3 Stress range

The difference between maximum and minimum stress is known as stress range. The stress range, stress amplitude and mean stress are shown in Figure 20.

$$\Delta\sigma = \sigma_{max} - \sigma_{min} \tag{87}$$

2.4.4 Stress ratio

The ratio of minimum and maximum stress applied during the cycle is known as stress ratio.

$$R_\sigma = \frac{\sigma_{min}}{\sigma_{max}} \tag{88}$$

2.4.5 Nominal stress

The stress away from any local point of stress concentration is known as nominal stress.

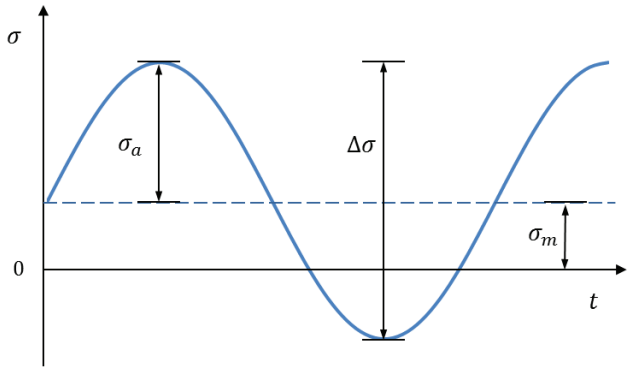

Figure 20. Description of stress amplitude, mean stress and stress range.

2.4.6 Amplitude ratio

The ratio of stress amplitude and mean stress is known as amplitude ratio. For a fully reversed case, R_σ equals -1 and R_a equals infinity. When σ_{min} is 0, R_a equals 1 and when σ_{max} is 0, R_a equals -1.

$$R_a = \frac{\sigma_a}{\sigma_m} \tag{89}$$

2.4.7 Fatigue strength

The magnitude of stress required to produce failure in specified number of cycles to failure is known as fatigue strength. Generally, for quoting fatigue strength of a material, number of cycles, at which it is taken, is also specified.

2.4.8 Fatigue limit

The stress level below, at which the failure does not occur is called fatigue limit.

2.4.9 Stress-life (SN) Curve

The stress life diagram is known SN curve or Wöhler curve, which shows the relationship between stress amplitude and number of cycles to failure. The tests are performed under fully reversed condition using load control tests that produce uniaxial state of stress. The stress life approach is based on the assumption that all strains remain elastic and is therefore only applicable for HCF. Generally, it is plotted on log-log scale using a power function to fit the measured data. One cycle can be represented as two reversals $2N_f$. The y-intercept of the fitted curve is known

as fatigue strength coefficient σ_f' and slope of the finite portion is known as fatigue strength exponent b. This relationship is known as Basquin's equation and can be written as:

$$\frac{\Delta\sigma}{2} = \sigma_f'(2N_f)^b \tag{90}$$

2.4.10 Strain life curve

The strain life curve describes the relationship between strain amplitude and number of cycle to failure. This method is applied, where loading magnitudes are higher (LCF regime) and uniaxial test are performed using strain controlled method. The cyclic stress strain response of the material is best described using strain controlled method, since deformation or plastic strain are directly measured and quantified. This method assumes that smooth specimens can simulate fatigue damage at the region of high stress concentration e.g. at the notch root [84]. During the fatigue test strain range $\Delta\varepsilon$ is controlled and the resulting stress range $\Delta\sigma$ is measured at specific number of cycles to failure. The total strain can be divided into elastic and plastic parts. The elastic part can be computed using measured stress range and elasticity modulus, whereas plastic part can be obtained by subtracting elastic part from total strain [85]. The strain life relationship can be written as:

$$\frac{\Delta\varepsilon}{2} = \frac{\sigma_f'}{E}(2N_f)^b + \varepsilon_f'(2N_f)^c \tag{91}$$

where, ε_f' and c are fatigue ductility coefficient and fatigue ductility exponent, respectively. The material constant can be obtained as shown in Figure 21. The first part of the Eq. (91) shows the elastic strain, whereas second part shows the plastic strain, which is also known as Manson-Coffin rule.

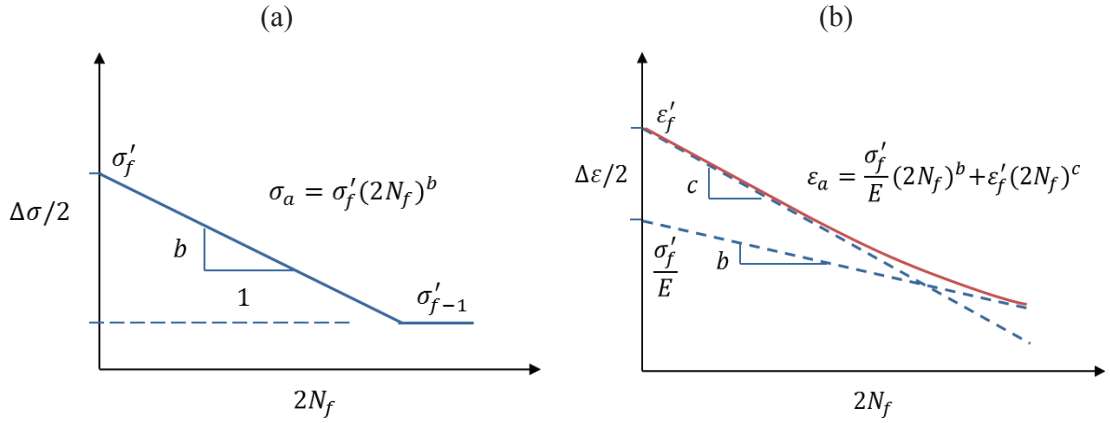

Figure 21. Conceptual diagram for (a) stress life and (b) strain life curve.

2.5 Summary

The analysis of fretting fatigue crack nucleation requires knowledge in multiple disciplines, which include contact mechanics, fatigue, CDM and FEM. The shape of the contacting bodies define the contact type that leads to change in mechanics of different contacts. The popular contact types include, complete contact, incomplete contact, conformal contact, non-conformal contact and receding contact. If the given loading conditions give rise to stick and slip zone at the contact interface, that contact is known as partial slip contact. The fretting loads lead to normal stress, shear traction and tensile stress. The analytical solution for normal stress and shear traction at the contact interface can be obtained as long as applied cyclic stress is much less than tangential load.

Apart of mechanics of contact, the other inter related field is the mechanics of crack formation. Generally, the failure process is divided into two phases; nucleation and propagation. There are various factors or variables, which affect crack nucleation. These include mechanical, material and environmental variables. Most of the studies are carried out using mechanical variables such as stresses, strains and displacements. These models do not consider damage evolution. The damage evolution is generally modelled using micromechanics of the material, which are based of crystal plasticity. The environmental variables, however, are usually neglected.

The modelling of fretting fatigue requires analysis of bodies under contact, which can be performed using FEA. The contact process is highly non-linear as it produces abrupt changes in displacement. To accurately solve nonlinear problems, Newton's methods can be employed which are based on iterative approach. The numerical solution of contact utilizes method of constrained optimization. The most widely used methods include, penalty method, Lagrange and augmented Lagrange method. The application of FEM allows to combine contact mechanics and damage mechanics. Therefore complete load history at contact interface can be analysed which leads to predict crack nucleation behaviour.

Chapter 3

Literature review on crack nucleation

This chapter provides an overview of numerical and experimental work, related to crack nucleation under fretting fatigue conditions. In fretting fatigue, multiaxial loads and severe stress gradient is present at the contact interface, which can lead to failure. Various damage models and approaches are available in literature to model nucleation phase. These approaches include, critical plane approach, stress invariant approach, fretting specific parameters and continuum damage mechanics. Apart from theoretical background, the work related to application of these approaches to fretting fatigue problems is also presented. It is observed that, to analyze various aspects, intricate details near the contact interface and mechanisms involved in fretting fatigue, the strength of finite element method can be employed. The sequence of the chapter includes, generalized classification of crack initiation criteria, then brief theoretical background and application of damage parameters to fretting fatigue problems is presented. To review each approach, summary is presented at the end of each approach. Similar work is combined depending on focus of the study and are not presented in strict chronological order. The last part provides a comparison of each approach and finally conclusions are presented.

3.1 Classification of damage models

The process of fretting fatigue involve multiple loads in different directions, which give rise to multiaxial and non-proportional stresses [86]. At the contact interface severe stress gradients are present due to frictional or tangential loads [87]. Various approaches have been used by researchers to predict initiation location and life. Some approaches are based on empirical laws and physical observations, while some are based on thermodynamics principles. One such approach is known as critical plane approach (CP), which uses certain preferential planes to define failure parameters [88]. Based on CP approach, different multiaxial criteria have been developed by researchers that can characterize nucleation behaviour. The other popular approaches include continuum damage mechanics (CDM) approach, stress invariant (SI) approach and fretting specific parameters. In general, to estimate crack initiation life, these parameters are equated to fatigue strength limit (in fully reversed tension/torsion) or to Manson-Coffin and Basquin type relation [89]. The CDM approach employs mechanical variables to describe nucleation process inside a representative volume element (RVE) of mesoscale [58]. There are some other numerical techniques for crack analysis, which are based on cracking particles method [90, 91] and dual-horizon peridynamics method [92, 93], however application of these methods are not proven under fretting fatigue crack nucleation. Therefore on conceptual basis these approaches can be classified as CP approach, SI approach, fretting specific damage parameters and CDM [94]. Figure 22 provides an overview of this classification. Although there are other parameters, the most popular ones are presented here, which has been successfully applied for fretting fatigue problems.

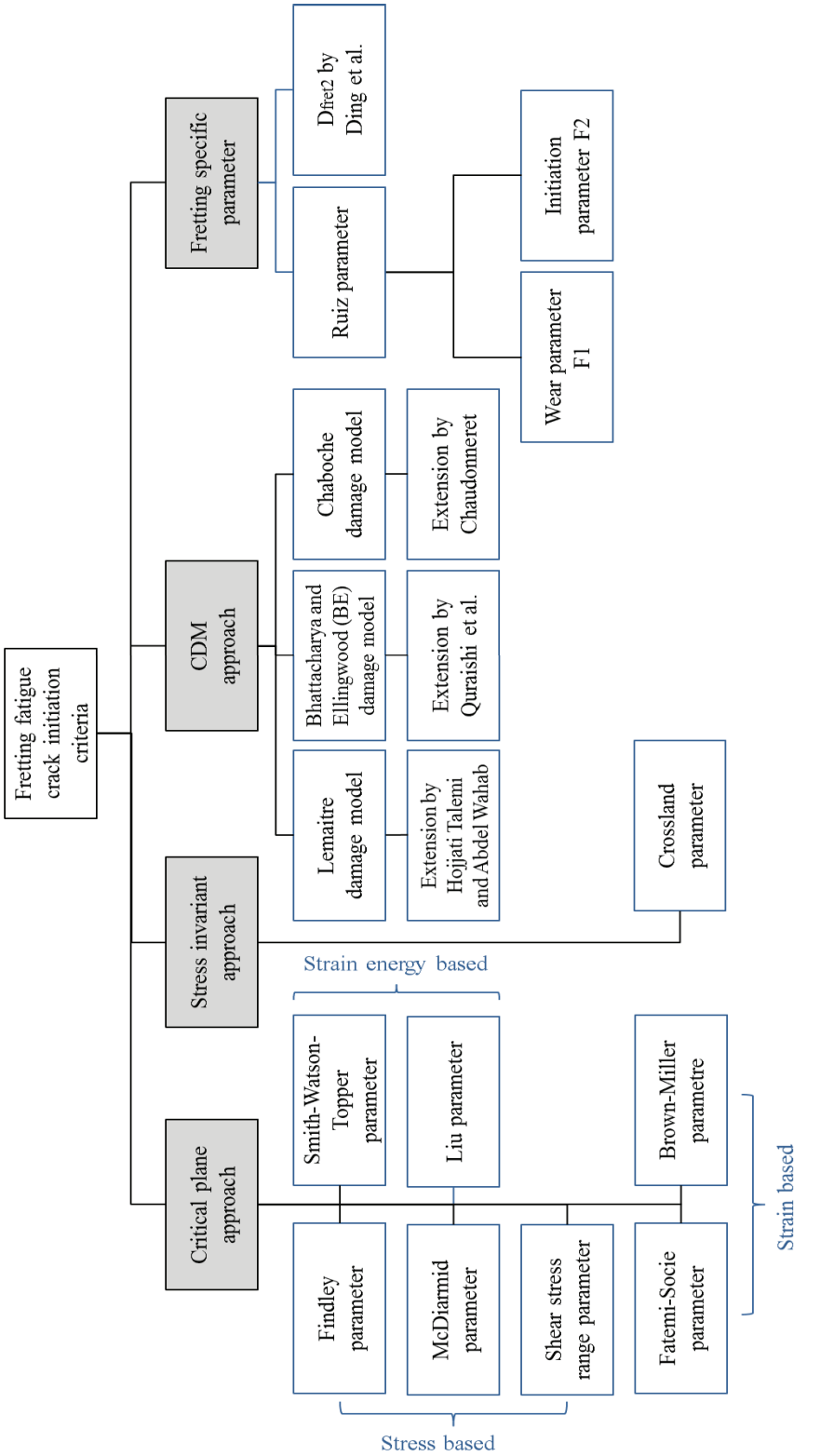

Figure 22. Generalized classification of crack initiation criteria, applied to fretting fatigue.

3.2 Critical plane approach (CP)

Critical plane approach refers to the calculation of damage parameters on specific planes, which are prone to cause failure. Depending on the failure mechanism, these planes are considered as maximum shear planes or planes perpendicular to maximum principal stress. The concept of critical plane was first introduced by Findley et al. [95] and Findley [96], by using stress components, under plain fatigue loading. Later, various damage models were developed for multiaxial plain fatigue application, where critical planes were identified by stress based, strain based and strain energy density based concept. Brown and Miller [97] analysed multiaxial fatigue by using state of strain on plane of maximum shear strain. Other promising work was contributed by Socie [98, 99], who proposed two parameters one for shear mode failure and the other for tensile mode failure. Socie equated the damage parameters to Smith-Watson-Topper equation [100] to compute total failure life. According to Socie, the characteristic failure behaviour of the material should be known in priori, to select the suitable damage parameter for life estimation. The other multiaxial fatigue parameters, which were originally developed for plain fatigue and later adopted for fretting fatigue includes, Fatemi-Socie [83], McDiarmid [101], Liu [102] parameter.

For fretting fatigue, the concept of critical plane was first adopted by Szolwinski and Farris [88] by using the concept proposed by Socie. They combined a damage parameter with stress components to predict crack nucleation site and fretting fatigue life. The concept of critical plane as proposed by Szolwinski and Farris is shown in Figure 23. Later, many other damage parameters, which were originally proposed for plain fatigue, were applied to fretting fatigue cases to predict crack nucleation location, initial crack orientation and crack initiation life. Based on the formulation, critical approach can further be classified as stress based, strain based and strain energy density based parameters. Although there are many damage parameters in literature [103, 104], this article presents the overview of only those parameters, which are frequently used for fretting fatigue scenario.

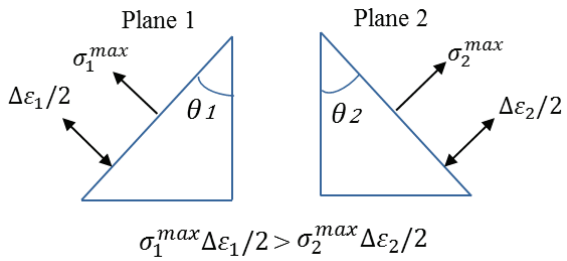

Figure 23. Concept of critical plane SWT for crack nucleation. The plane, where product of normal strain amplitude and maximum normal stress is highest, is the critical plane θ_1 [88].

3.2.1 Stress based parameters

3.2.1.1 Findley parameter (FP)

Findley et al. [95] analysed that alternating shear stress was the primary cause of fatigue failure, but the ability of the material to withstand alternating stress was influenced by the normal stress acting on the critical shear plane. They studied the effect of mean stress in combination with bending and torsion tests. It was realized that the alternating shear stress was not influenced by mean stress. However, the normal stress occurring on the critical plane was affected by mean stress. In other words, normal stress was the sum of all stresses resulting from both alternating and mean stress. They proposed a damage parameter for high cycle fatigue (HCF) regime [96]. It can be determined as a function of maximum shear stress amplitude and maximum normal stress. The critical plane is the one with highest value of damage parameter. The parameter can be expressed as:

$$FP = \frac{\Delta\tau_{max}}{2} + k_1\sigma_n^{max} \tag{92}$$

The number of cycles to crack initiation can be determined as [99, 105]:

$$\frac{\Delta\tau_{max}}{2} + k_1\sigma_n^{max} = \tau_f'(2N_i)^{b'} \tag{93}$$

where, $\Delta\tau_{max}$ is the maximum shear stress range, σ_n^{max} is the maximum normal stress in the direction perpendicular to maximum shear stress range, b' is the fatigue strength exponent in torsion and τ_f' is the fatigue strength coefficient in shear. k_1 is the material constant related to material sensitivity to normal stresses and can be determined experimentally by performing fatigue tests involving two or more stress states. For the stress ratio of $R_\sigma = -1$, k_1 can be expressed in terms of ratio of fatigue limit in tension, σ_{f-1}, to torsion, τ_{f-1} , using Eq. (94) [96, 106].

$$\frac{\sigma_{f-1}}{\tau_{f-1}} = \frac{2}{1 + \frac{k_1}{\sqrt{1 + k_1^2}}} \tag{94}$$

Findley showed that the orientation of critical shear plane, θ_c, varied with maximum stress and with combined stress state. For test with zero mean stress, θ_c varied from 45° to 21° for range of k_1 from 0 to 1.1. The critical plane was oriented few degrees from maximum shear plane for small value of k_1 (ductile materials) and few degrees from principal plane for large k_1. In addition, it was found that for compression cases, the calculated crack planes were oriented 45° to the specimen axis, which coincided with the experimental crack propagation direction and

not necessarily with initiation orientation. This implies that employing Findley parameter will be more suitable for the cases, when initiation and propagation directions are the same and failure is dominated by shear mode. Findley compared predicted value of FP with fatigue tests for various cases and found that the percentage deviation varies within ±10% [95]. The conventional Findley parameter does not provide any formulation to compute number of cycles to failure. However, later this relationship was proposed by [99] and [105] as expressed in Eq. (93), which is in practice for life estimation under fretting fatigue conditions.

3.2.1.2 McDiarmid parameter (MD)

This parameter can be applied to situations, where crack grow either parallel to surface or into the surface. The parameter was proposed by McDiarmid [101] and can be applied to multiaxial loading for HCF. The fatigue strength is defined in terms of maximum shear stress amplitude and maximum normal stress on critical plane. McDiarmid used two shear fatigue limits, one for the case where crack grows parallel to the surface (Case A) and one inwards the surface (Case B). The schematic of both cases is shown in Figure 24. This parameter can only be applied to range of loading conditions between $0.5\tau_{f-1} \leq \frac{\Delta\tau_{max}}{2} \leq \tau_{f-1}$ and $0 \leq \sigma_n^{max} \leq \sigma_u$ (ultimate tensile strength). McDiarmid parameter can be expressed as:

$$MD = \frac{\Delta\tau_{max}}{2} + \left(\frac{\tau_{f-1}}{2\sigma_u}\right)\sigma_n^{max} = \tau_{f-1} \tag{95}$$

MD parameter showed good correlation with the experimental results from literature. For combined bending and torsion cases, σ_{f-1}/τ_{f-1} =1.55~1.57, the correlation was found within ±5%. For σ_{f-1}/τ_{f-1} > 1.75, predicted values were greater than 5% on the conservative side, however, for σ_{f-1}/τ_{f-1} < 1.55, the predicted values were greater than 5% on the non-conservative side and therefore showed limitation for this parameter. For the case of out of phase loading, accuracy was found within ±10% except for one case of $\Delta\tau/\Delta\sigma$=0.5 and phase differene $\emptyset$ =90°. The critical shear planes were found to be 23° and 31° for $\emptyset$ =0° and 12° for $\emptyset$ =180° [101, 107, 108]. McDiarmid related the damage parameter with respective fatigue limits, however to estimate number of cycles to initiation, researchers [99, 105] suggested to used Basquin's equation in shear, similar to FP. Denoting σ_f' as the fatigue strength coefficient, the number of cycles to crack initiation can also be found as [109]:

$$\frac{\Delta\tau_{max}}{2} + \left(\frac{\tau_{f-1}}{2\sigma_u}\right)\sigma_n^{max} = \frac{1}{2}\left(1 + \frac{\tau_{f-1}}{2\sigma_u}\right)\sigma_f'(2N_i)^{b'} \tag{96}$$

3.2.1.3 Shear stress range parameter (SSR)

Lykins et al. [60] studied different pad geometries for Titanium alloy and introduced a parameter based on shear stress range for fretting fatigue crack initiation. They further studied different pad geometries to provide a variation in slip amplitude at the contact interface. The parameter was effective in determining initiation location and orientation, however with different pad geometries some variation in slip amplitude was observed. The experimental test results showed that cracks initiated along and across the grain boundaries. In addition, they found that initial crack orientation is independent of pad geometry. The initiation angles of the primary cracks were observed in both positive and negative quadrants. The experimental initiation angles varied from $40° \leq \theta \leq 50°$ in the positive quadrant and from $-70° \leq \theta \leq -39°$ in the negative quadrant. After about 50 to 100 μm, cracks changed the direction and propagated perpendicular to specimen axial direction. The experimental results showed the location of initiation at the trailing edge of the contact. SSR parameter predicted initiation life with ±3 N scatter band from plain fatigue data. By using the Walker's method, the effect of mean stress can also be incorporated using the following form:

$$SSR = \tau_{max}(1 - R_\tau)^m = C_1 N_i^{C_2} + C_3 N_i^{C_4} \tag{97}$$

where, R_τ is the shear stress ratio i.e. τ_{min}/τ_{max} , m is the fitting parameter and τ_{max} is the maximum shear stress. The maximum and minimum shear stresses were obtained using finite element analysis. The constants C_1, C_2, C_3 and C_4 were obtained by using best fit curve of plain fatigue data. The R.H.S of Eq. (97) has a similarity with strain life equation; however, these constants are not strain life constant. Therefore, using SSR parameter, these constants are required to be calibrated as they may change with change of geometry or loading conditions.

Namjoshi et al. [110] also performed experimental and numerical tests and showed that crack nucleation mechanism was governed by shear stresses on critical plane. The experiments showed that primary cracks initial orientations were $-45°$ or $45°$ with a variation of ±15° from the perpendicular to the flat surface of the specimen. Namjoshi et al. found that SWT and SSR parameter showed dependence on pad geometry, whereas Findley parameter did not. Therefore, they introduced normal stress term similar to Findley parameter, in SSR parameter and proposed MSSR parameter. The difference between Findley and MSSR parameter is that for Findley parameter critical plane was defined at maximum value of the damage parameter, however for MSSR, critical plane was defined at maximum shear stress range. The MSSR parameter can be expressed as:

$$MSSR = C_1 \Delta\tau_{crit}^{C_2} + C_3 \sigma_{n,max}^{C_4} \tag{98}$$

The MSSR parameter showed very little dependence on pad geometry and both plain fatigue and fretting fatigue data was found within a small scatter band having mean error of −0.48% and standard deviation of almost 1.98. The modified parameter also predicted initiation location and orientation accurately. For employing MSSR to predict crack initiation lives numerically, it is recommended to estimate the constants of Eq. (98) for each pad geometry, since numerical life models already use some additional constants from uniaxial plain fatigue tests e.g. τ_f' and b'.

3.2.2 Strain based parameters

3.2.2.1 Brown-Miller parameter (BM)

Brown and Miller [97] conducted combined tension and torsion tests with constant shear strain range and suggested that total fatigue failure is a combination of shear strain and normal strain. They proposed a parameter based on physical interpretation of mechanism involved in fatigue crack growth. They showed the importance of strain parameters in correlating fatigue data and suggested that total failure is a function of maximum shear strain amplitude and tensile strain normal to the plane of maximum shear. The contours of constant endurance can be graphically represented as:

$$\frac{\Delta\gamma_{max}}{2} = f(\varepsilon_n) \tag{99}$$

Brown and Miller found that fatigue crack initiated along plane of maximum shear strain, known as stage I. The crack then changed orientation and propagated either parallel (Case A) to the surface or inwards (Case B), known as stage II, when the stress strain condition at the crack tip reached a critical value. The physical representation of the phenomena is shown in Figure 24. The parameter was later presented as a linear combination of shear strain amplitude and maximum normal strain range by Kanazawa et al. [74] and Kandil et al. [111]. Wang and Brwon [112] tested the model for non-proportional and variable amplitudes effects. The number of cycles to failure can be obtained by using Eq. (100):

$$BM = \frac{\Delta\gamma_{max}}{2} + k_2\Delta\varepsilon_n = C_1\frac{\sigma_f'}{E}(2N_i)^b + C_2\varepsilon_f'(2N_i)^c \tag{100}$$

where, $\frac{\Delta\gamma_{max}}{2}$ is the maximum shear strain amplitude and $\Delta\varepsilon_n$ is normal strain range on the critical plane. k_2 is the material constant and characterizes the effect of normal strain on initial crack growth. It can be evaluated as the ratio of σ_y/σ_f' [113]. C_1 and C_2 are dependent on k_2 and Poisson's ratio.

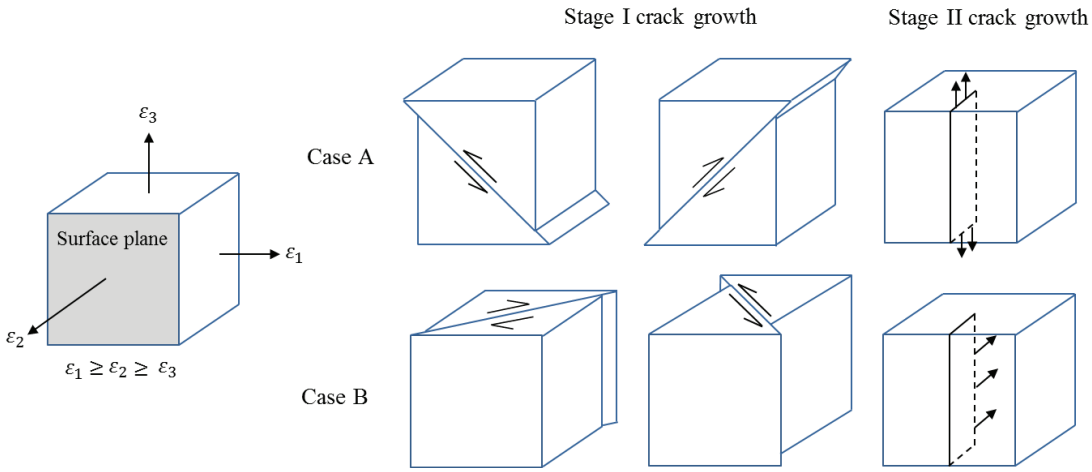

Figure 24. Schematic of crack growth phenomena including maximum shear strain plane (stage I) and propagation directions (stage II) [97].

3.2.2.2 Fatemi-Socie parameter (FS)

This parameter is based on Brown and Miller's parameter, which does not include non-proportional loading effects. Fatemi and Socie [83] performed multiaxial fatigue test for both in phase and out of phase loading on steel 1045 hot rolled specimen and proposed a parameter, which incorporated the effect of non- proportional loading and mean stress. They suggested to modify the normal strain term in Brown-Miller parameter with normal stress term and mentioned that as both controlling parameters were in terms of strain, the additional cyclic hardening due to rotation of principal axis during out of phase loading could not be accounted for. Fatemi and Socie also showed that out of phase loading of 90° was more damaging than in phase loading for LCF, while it was less damaging for HCF. Moreover, propagation phase can take significant proportion of life, where failure occurs in mode II. Therefore, this parameter is suitable for situations where material failure occurs in shear mode [83]. Furthermore, they showed that this parameter could predict the fatigue failure with in ±2 N error band both for in phase and out of loading cases. Fatemi-Socie parameter can be expressed as:

$$FS = \frac{\Delta\gamma_{max}}{2}\left(1 + k_2 \frac{\sigma_n^{max}}{\sigma_y}\right) \tag{101}$$

$$FS = (1+v_e)\frac{\sigma_f'}{E}(2N_i)^{b'} + \frac{n}{2}(1+v_e)\frac{\sigma_f'^2}{E\sigma_y}(2N_i)^{2b'} + \left(1+v_p\right)\varepsilon_f'(2N_i)^{c'} + \\ + \frac{n}{2}\left(1+v_p\right)\frac{\varepsilon_f'\sigma_f'}{\sigma_y}(2N_i)^{b'+c'} \tag{102}$$

Socie et al. [99] proposed an alternative form, as shown in Eq. (103). Most of the researchers employed this form to compute of cycles to initiation under fretting fatigue conditions [114-116]:

$$FS = \frac{\tau_f'}{G}(2N_i)^{b'} + \gamma_f'(2N_i)^{c'} \tag{103}$$

where, γ_f' is shear fatigue ductility coefficient, G is the shear modulus and c' fatigue ductility exponent in torsion.

3.2.3 Strain energy based parameters

3.2.3.1 Smith-Watson-Topper parameter (SWT)

This is one of the most popular criterion used to determine initiation location and life. This parameter can be applied to material and load conditions, where failure occur predominantly in mode I manner. The parameter is applicable to both LCF and HCF regime and also accounts for mean stress and non-proportional loading effects. The parameter, proposed by Smith et al. [100], can be defined as the product of maximum tensile stress and strain amplitude.

$$SWT = \sigma_{xx}\varepsilon_a \tag{104}$$

Several researchers have modified this parameter and applied to different situation using the same concept. Socie [98] applied this parameter to multiaxial loading as presented in Eq. (105) and correlated crack nucleation observations in strain controlled tension and torsion tests of SS 304 specimens. In torsion tests, cracks were observed to nucleate initially on shear plane, however the majority of life proportion was consumed by crack growth in mode I manner. They found that by correlating the non-proportional life data with SWT expression, crack initiation site could be predicted in case of tensile crack growth under multiaxial loading condition. Szolwinski and Farris [88] applied this criterion to fretting fatigue problem and computed the crack initiation location and orientation where the product of the normal strain range and maximum normal stress was highest. According to them, tensile stress, σ_{xx}, is the main contributor in fracture process and initiation location is mainly affected by it. The location of maximum damage was found at the trailing edge of the contact. The orientation of the critical plane was found perpendicular to free surface of the specimen showing the dominance of tensile mode failure. The predicted lives were found to lie within the scatter of experimental data for various contact half widths [59, 88]. To compute initiation life, they used the methodology of equating SWT parameter with strain life equation as shown in Eq. (106).

$$SWT = \sigma_n^{max}\frac{\Delta\varepsilon_1}{2} \tag{105}$$

$$\sigma_n^{max}\frac{\Delta\varepsilon_n}{2}=\frac{\sigma_f'^2}{E}(2N_i)^{2b}+\sigma_f'\varepsilon_f'(2N_i)^{b+c} \quad (106)$$

3.2.3.2 Liu parameter

Liu proposed two parameters based on biaxial fatigue data obtained from literature for SS 304 and steel 1045 tested for both in phase and 90° out of phase loading condition [102]. For multiaxial fatigue life prediction, damage parameter based on virtual strain energy was computed on critical planes. The virtual strain energy ΔW on a plane can be divided into elastic ΔW_e and plastic ΔW_p components. The distribution of the elastic and plastic work is depicted in Figure 25. ΔW_e is the sum of two triangular regions. According to strain life relationship the total work can be written as:

$$\Delta W = \Delta W_e + \Delta W_p \cong \Delta\sigma\Delta\varepsilon \quad (107)$$

Liu showed that multiaxial fatigue life correlated well with either ΔW_I or ΔW_{II} depending on the crack plane, along which the crack propagated in Mode I or Mode II. They observed that, crack nucleation and propagation phases were dependent on material, temperature, strain range, stress and strain histories and not on relative magnitude of virtual strain energy parameters. First parameter describes that the mode I failure is driven by principal stresses and strains. For mode I failure, the critical plane is determined by maximizing normal strain energy $\Delta\sigma_n\Delta\varepsilon_n$, whereas for life estimation both normal and shear strain energy $\Delta\tau\Delta\gamma$ are added as shown in Eq. (108).

$$\Delta W_I = (\Delta\sigma_n\Delta\varepsilon_n)_{\theta max}+(\Delta\tau\Delta\gamma)=\frac{4\sigma_f'^2}{E}(2N_i)^{2b}+4\sigma_f'\varepsilon_f'(2N_i)^{b+c} \quad (108)$$

where, $\Delta\sigma_n$ and $\Delta\varepsilon_n$ are normal stress and strain range, respectively and $\Delta\tau$ and $\Delta\gamma$ are shear stress and strain range, respectively. The second parameter Liu 2 suggests that mode II failure is driven by maximum shear stresses and strains. Liu also distinguished between case A type and case B type crack similar to Brown and Miller and McDiarmid. For mode II failure, the critical plane is determined by maximizing shear strain energy $\Delta\tau\Delta\gamma$, whereas for life estimation both normal $\Delta\sigma_n\Delta\varepsilon_n$ and shear strain energy are added as shown in Eq. (109).

$$\Delta W_{II} = (\Delta\tau\Delta\gamma)_{\theta max}+(\Delta\sigma_n\Delta\varepsilon_n)=\frac{4\tau_f'^2}{G}(2N_i)^{2b'}+4\tau_f'\gamma_f'(2N_i)^{b'+c'} \quad (109)$$

The prediction of Liu parameters showed good correlation with experimental data of SS 304 and SAE 1045 at elevated temperatures. The predicted results were found to lie within a scatter band of ±2 N. However, for out of phase loading they considered biaxial sinusoidal and trapezoidal strain histories in simplified form. The original non-proportional loading path was

replaced by two proportional loading paths at two axes of the ellipse and diagonals of the trapezoid.

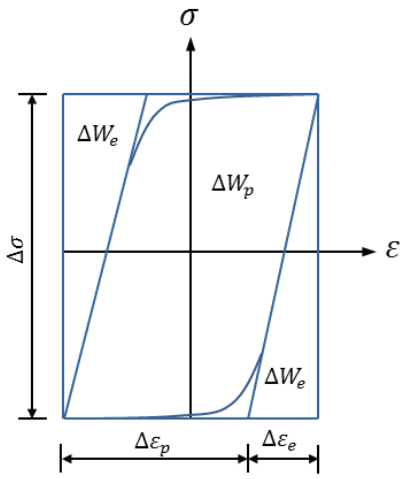

Figure 25. Conceptual diagram showing elastic ΔW_e and plastic strain energy ΔW_p [102].

3.2.4 Application of CP approach to fretting fatigue

This section summarizes the experimental and numerical work related to application of critical plane approach. Table 2 presents the summary of loads, materials and specimen and pad geometry details for studies, which adopted CP parameters. The primary objective of employing CP parameters for fretting fatigue cases is related to analyses of crack nucleation location, crack initiation orientation and number to cycles to crack initiation.

To study damage nucleation mechanism, Szolwinski and Farris [88] developed a quantitative tool by combining stress fields with multiaxial fatigue theory. For application of SWT parameter to multiaxial state, notion of critical plane was used. The concept of critical plane was later adopted by many researchers for fretting fatigue conditions. The critical plane was observed in the plane perpendicular to principal stress direction. The maximum value of damage parameter was found at the trailing edge of the contact, on or just under the surface. The results showed that initiation life took major proportion of the total estimated life. In their other work [59], the experimental observations showed that in every test crack initially grew inclined to the surface and then turned to grow perpendicular to the contact interface. The results matched well with the numerical solution of [117] and analytical solution of [88]. The results also matched well with the Hills and Nowell work [23]. The estimated lives also showed good correlation with experiment and analytical solution. However, the initiation life was computed for a relatively large initiation crack length of 1 mm for both studies due to availability of strain life data for this crack length.

To study crack initiation behaviour in Titanium alloy Ti-6Al-4V, Lykins et al. [115] studied various parameters under fretting fatigue conditions. Based on capability of equipment, the experimental crack initiation size was taken as 760×380 μm, they found that almost 90% of the specimen life was consumed in nucleation phase. The experimental and numerical crack initiation location was observed near the trailing edge ($x/a \simeq 1$) of the contact. Hence, a good agreement between experimental and numerical location was observed. The initiation angles (see Figure 26) estimated by SWT parameter varied from $-10° \leq \theta \leq -5°$ i.e. perpendicular to the specimen axis, whereas those with FS parameter varied from $35.9° \leq \theta \leq 40.1°$ i.e. near the maximum shear stress plane. However, no information related to experimental initiation angles were provided in that study. The study showed that strain life parameter was not capable of predicting cycles to initiation under different stress or strain ratio, whereas, CP parameters (SWT, FS) were equally effective in predicting initiation life. Later in another work, Lykins et al. [60, 118], studied the orientation and observed that cracks initiated along and also across the grain boundaries. After about 50 to 100 μm, they changed the direction and propagated perpendicular to specimen axial direction

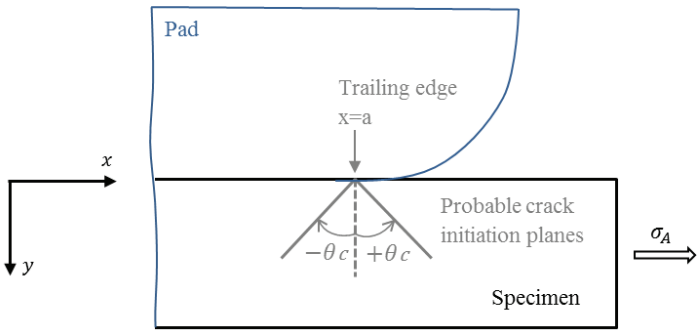

Figure 26. Crack initiation from the surface of specimen, at the trailing edge of the contact.

Namjoshi et al. [110], extended the work of Lykins et al. [60, 118] and investigated the effect of different pad geometries, by proposing a modified shear stress range parameter MSSR, which determines critical plane based on SSR parameter and minimizes pad geometry effect by incorporating normal term similar to FP. All parameters (SWT, SSR, FP) predicted the initiation site at the trailing edge of the contact, however some differences were observed in orientation of critical planes. The comparison of above three studies related to critical plane orientation and experimental crack initiation angles is shown in Table 1. From these studies, it can be seen that shear stress and strain based parameters showed better estimation.

Table 1. Comparison of case studies for prediction of critical plane orientation θ_c , measured from crack length of 50 to 100 μm from the surface [60].

Case study	Predicted θ_c (°)				Experimental θ_c (°)
	SWT	FS	FP	SSR	
Lykins et al. [115]	-10 ~ -5	35.9 ~ 40.1	-	-	-
Lykins et al. [60]	-	-	-	25 ~ 45, -65 ~ -45	40 ~ 50, -70 ~ -39
Lykins et al. [118]	-10 ~ -5	-	-	35.9~40.1, -54.1 ~ -49.9	40, -45, -39
Namjoshi et al. [110]	5 ~ 8	-	5 ~ 25	45 ~ 55, -55 ~ 45	(-45,45) ± 15

Notations: - Information not available ~ Range of values

Since in fretting fatigue micro plasticity exist in some grains of the material, therefore it should be considered to analyse crystallographic orientation dependence on cyclic plasticity. Some authors [54, 119, 120] used crystal plasticity finite element modelling to study influence of microstructure on fretting fatigue crack nucleation. Goh et al. [54] employed computational crystal plasticity constitutive law that considers discreteness of grains, surface texture and heterogeneity in plastic deformation of the grains. The numerical model consisted of discrete grains by grouping elements with same crystal orientation. As the material plastically deforms along crystallographic slip planes, the lattice undergoes elastic deformation and rigid body rotation. Kinematic hardening was assumed at a level of each slip system. At the level of grains, kinematic hardening was ensured by heterogeneous dislocation substructures within grain and interface boundaries. Another component of kinematic hardening was used for intergranular interactions. To define plastic deformation, planar triple slip model was employed with crystal plasticity model. The plastic shearing strain rate on the i^{th} slip system can be written as [54]:

$$\dot{\gamma^i} = \dot{\gamma_0} \left| \frac{\tau^i - \sigma^i}{I_s} \right|^m sgn(\tau^i - \sigma^i) \tag{110}$$

where, $\dot{\gamma_0}$ is the reference shear strain rate, I_s is the isotropic drag strength, m flow exponent, τ^i and σ^i are resolved shear stress and back stress for i^{th} slip system, respectively. The FS and SWT parameters were calculated using plastic shear strain and plastic normal strain, respectively. The numerical results showed crack location similar to experimental results i.e. at trailing edge. An initiation angle of 60° was predicted in comparison to experimental value of 40° to 60°. The cracks changed orientation nearly 50 μm from the surface of the specimen and propagated in perpendicular direction. Using similar crystal plasticity micro model for fretting fatigue crack initiation and wear, McCarthy et al. [121] showed that, multiple crack initiation site, initial crack

orientation and number of cycles to crack initiation can be accurately estimated. Moreover, the wear coefficient and two dimensional wear scar can be reasonably measured.

Araújo and Nowell [114, 122] conducted an experimental and analytical study on effect of rapidly varying stress field on initiation life for Al4%Cu and Ti-6Al-4V. They showed effect of high gradient at the contact interface and proposed averaging methods to predict initiation life, as shown in Figure 27. For Al4%Cu, cracks initiated near the contact edge and for Ti-6Al-4V within the slip zone. The estimated lives correlated well with the experimental data for large contacts; however, the results were under estimated by large factor for small contacts. The averaging methods showed that there was no single dimension that could precisely predict the effect of stress gradient for all cases. They suggested a range of critical dimensions between 20 ~ 80 μm for Al4%Cu and 5 ~ 20 μm for Ti-6Al-4V. These dimensions were of the order of grain size of the material and life estimations were mainly dependent on critical dimensions rather than averaging method.

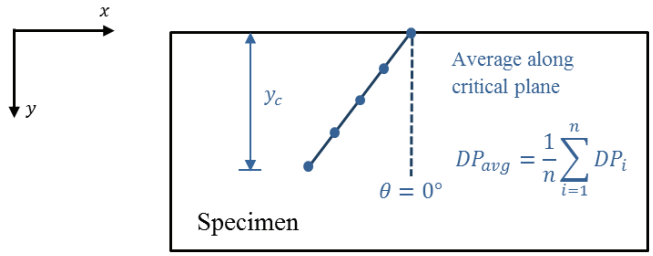

Figure 27. Line averaging method, considering nodes along critical plane. *DP* represents damage parameter and n is the number of nodes considered for averaging process.

Naboulsi and Mall [123] also analysed stress gradient effects on nucleation behaviour. For averaging process, they used two techniques inside process volume. It was found that SWT parameter was more dependent on size of process volume than SSR and FP. The change in orientation was not significant upon increasing process zone size. The localized approach provided conservative results for initiation life than with non-local approaches.

The spherical contact configuration of blade disc joint was analysed by Alfredsson and Cadario [86]. They performed 24 tests and the experimental results produced 40 macro scale cracks. In most of the tests, cracks grew at an angle nearly 45° to the radial direction. The comparison between different parameters (FP, MD, FS, SWT) was drawn based on, cracking risk, location of maximum value of parameter, relative decrease in parameter and number of cracks found within 5° of the respective criteria prediction. They observed that no criterion could meet all measures for the highest ranking and therefore ranking among different criteria depends on relative importance given to each measure.

Another study related to spherical contact was conducted by Navarro and Domínguez [124]. They adopted two methods, namely, variable initiation length and fixed initiation length. The schematic of variable initiation length method is shown in Figure 28. The variable initiation length showed deviation within ±1.5 N band of the experimental results. Using fixed initiation length, most of the data was found within ±1.5 N, for point, line and volume method. However, with surface stress, the results were found inaccurate and the estimated lives were much lower than the experimental ones. The proportion of the life spent in initiation phase with surface stresses was found in the range of, 0-20% for depth y_d=0.2, 0.5 mm and between 20-40% for y_d=1. With volume method, the proportion of life of initiation phase was estimated between 0-20% with variable initial length, 50-70% for y_d=0.2 mm and 80-100% for y_d=0.5 and 1 mm.

Later in another study, Navarro et al. [109] analysed fretting fatigue behaviour for cylindrical and spherical contacts. For prediction of initiation life MD, FS, SWT and Crossland parameters were adopted. Some parameters showed better prediction in some groups, while other parameters in others. The results showed that there was not any specific parameter that could be declared as best for all material and pads radii. They regarded influence of material properties more than the influence of damage parameters on results. However, better results were obtained with variable initiation length method. For comparison of pad configuration, they observed that for spherical contacts initiation lives were much shorter than cylindrical contacts, even though larger initiation lengths were observed for spherical contacts due to higher stress gradients produced for spherical contacts.

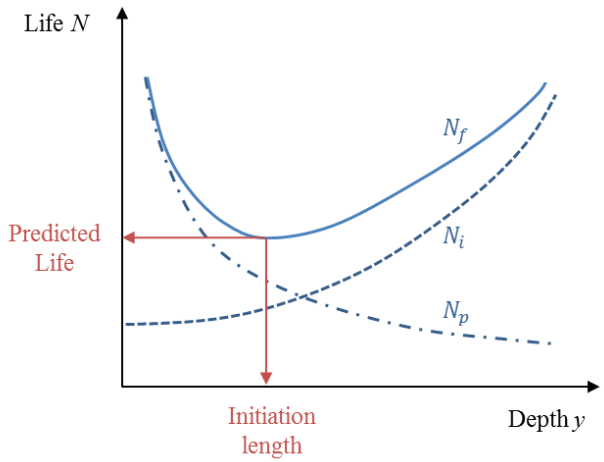

Figure 28. Schematic of variable initiation length method. Length of initial crack is determined from the point that gives minimum total life [124].

To study the crack nucleation threshold, Proudhon et al. [125] studied experimentally cylinder on a flat configuration and investigated the effect of surface roughness. The numerical value of critical tangential load, Q_c = 106 N/mm was found in comparison to experimental threshold as 240 N/mm. According to them, this difference was related to stress-gradient at the contact region and therefore they employed radial process volume approach to compute SWT parameter. They also showed that inside the singular process volume SWT parameter had the tendency to reduce the cracking risk, which was contrary to the experimental results.

Under fretting conditions, relative slip d_x can be generated, which is influenced by various factors such as cyclic stress and contact load, coefficient of friction, contact geometry and compliance of the components in the assembly. Therefore, evaluation and analysis of relative slip is imperative under fretting conditions. Jin and Mall [126] investigated the effect of slip on crack initiation through series of experiments and numerical approaches. It was found that, Q/P ratio increased initially with the increase of relative slip range Δd_x and then stayed constant after relative slip range reached nearly 60 µm. This change in slope was referred to the dividing line between partial slip and gross slip regimes. Correspondingly, the failure life N_f decreased with increase of Δd_x upto a certain point (partial slip limit) and then increased in gorss slip regime [127]. This shows that for analysis of gross sliding case, apart from crack initiation, wear effects should also be included [126].

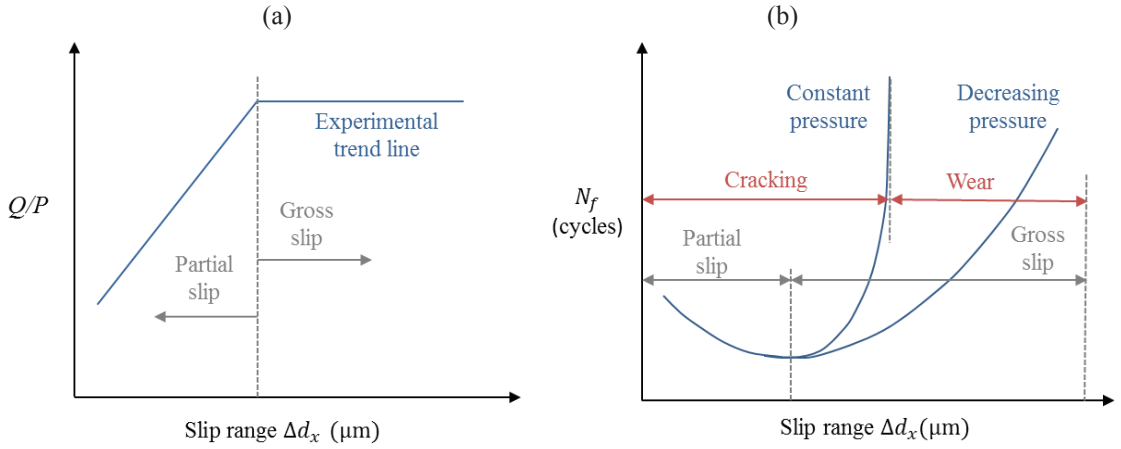

Figure 29. Schematic diagram showing concept of partial slip and gross slip regime by plotting (a) tangential to normal load ratio and slip range (b) number of cycles to failure and slip range.

Lee and Mall [128] also analysed experimentally the effects of relative slip on fretting fatigue behaviour of Ti-6Al-4V by applying the phase difference ∅ between axial cyclic stress σ_A and pad displacement. The maximum and minimum relative slips were observed for 0° and 180°

phase difference, respectively, where as an intermediate value for 90° phase difference. However, the values recorded experimentally showed that the applied axial stress σ_A and tangential load Q were not exactly in phase with each other for 0° phase difference and also not exactly out of phase for 90° and 180° phase difference. Due to this reason, the phase difference did not show any significant difference on fretting fatigue life. They showed that MSSR parameter can take into account the effect of stress ratio. However, no correlation wad made between MSSR and ∅, nor computed fretting fatigue life numerically for phase difference effect.

Apart from simple laboratory geometries, some researchers [129] applied crack initiation approaches on complex 3D structures. Sum et al. implemented SWT parameter to analyse spline coupling of aero engine for both plain and fretting fatigue initiation predictions. The orientation of a 3D critical plane was defined by two angles, θ_h and θ_v, about horizontal and vertical axis, respectively. The numerical computation of SWT parameter showed comparable results to experiments for all cases. The critical plane was predicted around 40° in comparison to experimental 45° CCW to the z-axis. The predicted life was found to fall in the error band of ±3 N of the experimental life. However, they showed that the predicted damage was insufficient to cause cracking within realistic number of operating cycles.

Most of the experimental and numerical work in fretting fatigue has been done for in phase loading. Only few case studies [130, 131] employed loading phase difference. Almajali [130] studied fretting fatigue behaviour experimentally and numerically by considering phase difference between normal contact load P and other loads σ_A, Q. Due to compliance of the various parts of the experimental setup, the perfect 90° phase difference was not achieved. The MSSR parameter was found to be effective in determining the initiation location and orientation. However, they did not predict fretting fatigue life numerically using MSSR parameter. By relating the experimental lives with numerically determined MSSR parameter, it showed good correlation for in phase loading only. For out phase cases, at the same axial stress the MSSR parameter was higher than in phase loading and at the same time lives were found higher also, whereas a lower value of damage parameter was expected. Hojjati-Talemi et al. [131] studied numerically the effect of phase difference between axial stress σ_A and tangential load Q on nucleation life, using FEA and CDM approach. It was found that phase difference affected the stress distribution, consequently shifting the damage initiation location. Furthermore, they showed that phase difference affects nucleation life. However, due to lack of experimental results for out of phase loading, no correlation was shown with experimental results.

Some researchers studied the combined effect of wear and nucleation under fretting fatigue conditions. Madge et al. [132-134] presented a finite element based methodology, for predicting effects of wear on nucleation and propagation phases. For nucleation phase, critical plane approach was combined with wear model. The numerical results showed that the study of

propagation in isolation could not give accurate prediction as nucleation can take a significant proportion (80 %) of life. They mentioned that under partial slip condition, a dormant crack could propagate from stick slip boundary and might cause failure. In contrast, neglecting the wear phenomenon showed that the crack tip loading remained below threshold stress intensity factor, predicting infinite life.

To analyse fretting damage in thin sheets Hirsch and Neu [135] analysed AISI 301 SS in contact with AISI 52100 steel and cast ANSI A356 aluminium. The FS parameter predicted the damage location correctly, however, SWT parameter could not provide accurate results. The maximum value of the FS parameter was found to be strongly dependent on coefficient of friction. Furthermore, they observed that maximum value of FS parameter correlated well with experimental fretting damage for 52100 steel. However, they found some disagreement at higher displacement amplitude because of reduction in thickness due to wear.

Most of the work in fretting fatigue involves cylindrical pad and flat specimen configuration, however some researchers have analysed flat pad configuration also. Sabsabi et el. [136] studied experimentally and numerically complete contact configuration using variable initiation length. An initial crack of 100 μm was used at the edge of the contact. The SWT parameter provided over estimated results for some of the cases. The percentage of initiation life was obtained as 11.1% and 19.6% with MD and SWT parameters, respectively. These shorter initiation lives were associated to steep stress gradients present at the edge of the contact which in turn led to rapid crack initiation.

Li at al. [116] purposed a fretting related damage parameter (FRD) based on fretting fatigue mechanism and experimental results from literature. The proposed parameter was formulated as:

$$FRD = \eta + \xi \sqrt{\frac{Q}{\mu P}} = \frac{DP^{PF}}{DP^{FF}} \tag{111}$$

where, DP^{PF} and DP^{FF} are damage parameters for plain and fretting fatigue, respectively. η and ξ are constants and can be found through fretting fatigue experimental data. The variables $\sqrt{Q/\mu P}$ and DP^{PF}/DP^{FF} calculated for different critical plane parameters showed linear relationship. The numerical and experimental lives showed that stress based and strain based parameters predicted lives within $\pm 3\,N$ band. In addition, the error between experimental and numerical damage parameters showed that the mean error value for strain-based parameters was the smallest.

Table 2. Summary of loads, geometry and materials of various studies using CP approach.

Authors	Load			Specimen material	Pad type	Pad radius (mm)	Damage parameters used
	P (N)	Q (N)	σ_A (MPa)				
Szolwinski et al.[88]	143~157 MPa	34.3~70.6 MPa	77.2~92.7	Al2024-T4	C	-	SWT
Szolwinski et al.[59]	4880~7562	1385~2705	81~115.8	Al2024-T3	C	127,178,229	SWT
Lykins et al.[60, 115]	1330~2220	-	400~700	Ti-6Al-4V	C,F	50.8,101.6	SSR
Lykins et al.[118]	1330	191~698	400~700	Ti-6Al-4V	C	50.8	SWT,FS
Namjoshi et al.[110]	1330~3990	-	200~800	Ti-6Al-4V	C,F	50.8,101.6	SWT,SSR,FP,MSSR
Goh et al. [54]	1350	-	100~150	Ti-6Al-4V	C	50	SWT,FS, $\gamma_{a,max}$
Araújo et al.[114]	p_o=120~650	Q/P=0.16~0.45	61.8~280	Ti-6Al-4V, Al4%Cu	C	12.5~25	SWT,FS
Naboulsi et al.[123]	210	-	-	Ti-6Al-4V	C	5.08,50.8	SWT,SSR,FP
Alfredsson et al.[86]	5440	1420~300	750	Ti-17	S	400	SWT,FS,FP,MD,DV
Navarro et al.[124]	8.3-30	8~15	70~85	Al7075-T6	S	25.4	MD
Navarro et al.[109]	-	-	-	Al(7075,2024, 4%Cu), Ti6	C, S	12.5~150,127~229,12.7.25.4,100	SWT,FS,MD, Crossland
Proudhon et al.[125]	220~700	-	-	Al2024-T351	C	49	SWT
Jin et al.[126]	1334	427~1401	203~315	Ti-6Al-4V	C	50.8	MSSR
Lee et al.[128]	1335~4005	-	267,550	Ti-6Al-4V	C	50.8	MSSR
Sum et al.[129]	47,94,141	21,42,63	92.7	CrMoV	C	25,50,75	SWT
Almajali et al.[130]	2224,4448	398~975.7	282~760	Ti-6Al-4V	C	50.8	MSSR
Madge et al.[132-134]	302	-	550	Ti-6Al-4V	C	50.8	SWT
Hirsch et al.[135]	100~375	-	u=10~200μm	SS 301	C	10	SWT,FS
Sabsabi et al.[136]	2000~8000	-	110~190	Al7075-T6	F	N.A	SWT,MD
Li et al. [116]	5400~7100	1432~2704	82.7~110	Al2024-T351	C	127,178,229	FP,MD,KBM,FS
O'Halloran et al.[137]	50 kN/mm	25 kN/mm	u=10 μm	Ti-6Al-4V	C	-	SWT

Notations:

C Cylindrical pad
S Spherical pad
F Flat pad
N.A Not applicable
- Information not available
Special units and values specified within cell
~ Range of values
u applied displacement

Similar to Sum et al. work, O'Halloran [137] implemented 3D critical plane SWT model, to study the effect of contact pressure, relative slip and sub-surface stresses in pressure armour layer of flexible risers. It was found that the effect of coefficient of friction μ on stresses under fretting condition was important since after sufficient number of cycles, surface degradation can cause an increase in μ. The value of μ was observed to rise from 0.3 to 0.7 or further above depending upon loading conditions [138]. At μ = 0.8, there was a significant decrease in tensile stress for elastic-plastic model than for lower μ and elastic case. For both elastic and elasto-plastic

cases, N_i decreased significantly with an increase in μ. For lower μ ($\leq$ 0.3) some difference in prediction was observed, however, better agreement was found for higher μ (0.5~0.8). Furthermore, they found that the applied displacement and pressure were inversely related to number of cycles to initiation.

3.3 Stress invariant approach (SI)

There are different criteria available, which are based on stress invariant approach, however only Crossland parameter is mostly used for fretting fatigue problems. This approach employs stress invariants to define failure parameter.

3.3.1 Crossland parameter (CL)

This parameter incorporates the effect of maximum amplitude of second invariant of deviatoric stress tensor, $\sqrt{J_2}$, and maximum hydrostatic pressure, H_{max} [139]. The parameter has a form similar to stress based parameters (MD and FP), where the first term describes distortion effect and the second term describes the volumetric effect. To incorporate mean stress effects, Crossland employed H_{max} instead of H_{mean} to differentiate between fully reversed torsional and tensile fatigue tests. In pure alternating torsional test H_{max}= 0 and for axial loading H_{max}=$\sigma_{max}/3$. However, H_{mean} would be equal to zero for both cases [140]. The material failure occurs if the value of parameter is greater than fatigue limit (in torsion) of the material. The parameter can be written as:

$$CL = \sqrt{J_2} + kH_{max} \leq \tau_{f-1} \tag{112}$$

where, k is the material constant and depends on fatigue limit in tension and torsion. This parameter can also be combined with Basquin's equation in shear to compute initiation life.

$$\sqrt{J_2} + kH_{max} = \tau_f^{'}(2N_i)^b \tag{113}$$

3.3.2 Application of SI approach to fretting fatigue

This section demonstrates the work of researchers employing SI approach to study fretting fatigue crack nucleation. The summary of loads, material and geometry of fretting fatigue studies using this approach is given in Table 3. To incorporate pad size effects, Bernardo et al. [141] proposed a FE based methodology which provides a direct evaluation of fatigue strength at nodal points. The numerical results were compared with experimental results of [122], using Crossland, Dang Van (DV) and Prismatic Hull (PRH) multiaxial parameters. To quantify the fatigue strength of a specimen, a fatigue strength index was defined as:

$$FSI = \frac{g_1(\tau) + k.\, g_2(\sigma_n) - \tau_{f-1}}{\tau_{f-1}} \times 100\% \tag{114}$$

The positive value of FSI implies the failure of the specimen. The Crossland and PRH parameters required the same element size to predict critical contact size while DV parameter showed a larger FSI (error). Neither of the parameters found a unique depth of refinement, capable to predict a_{cric} for every data set. The inconsistency might arise since (i) the fatigue limit was estimated for torsion and the size of the element was determined based on the whole parameter (ii) the models didn't take into account the effect of relative slip between contacting surfaces.

As in fretting fatigue, most of the work has been done in HCF regime and it is considered that plasticity only exists at a micro scale, it is usually neglected for life estimation. This micro plasticity is generally considered to encompass few grains at or near the contact region [1, 21, 58, 142]. Tsai and Mall [143] conducted finite element elasto-plastic analysis in pre-stressed strip (specimen). Bilinear elasto-plastic isotropic hardening was applied with von Mises criterion. The plastic zone was observed at trailing edge of the contact and propagation at 45° into strip. The study showed several aspects under fretting fatigue conditions by employing plastic model, however, nucleation lives were not estimated for these cases.

Nesládek et al. [89] designed new equipment for fretting fatigue testing and performed a comparative study of different multiaxial parameters on creep resistant chromium steel. The number of cycles to crack initiation were determined for 1 mm crack length. In general, the cracks were initiated at the surface inside the slip zone. The experimental results showed a significant decrease in fatigue life under fretting conditions. The Crossland parameter showed good results with fatigue index error of about 2.1% at lower loads, whereas up to 25% was observed at higher loads.

Using FEM based approach, Heredia et al. [144] proposed a principal stress weight function (PSWF) approach, to predict damage nucleation risk. The numerical results showed the results at surface nodes are strongly mesh dependent, however just below the surface nodes, results matched well with the analytical solution. The critical distance approach did not account for stress gradient effects below the contact and error ranges from -45% to -35% for smaller pads and from 15% to 70% for larger pads. Therefore, they proposed to consider maximum stress at critical distance, in which stress gradient parameter was corrected for mesh size effects by coupling a weight function and a mesh size coefficient. The damage nucleation risk was defined as:

$$\sigma_{1max}.(1 + k.\nabla\sigma_{1max}) < \sigma_{f-1} \tag{115}$$

where, k is the coefficient dependent on crack length, w_f is the weight function. The error between experimental and numerical damage thresholds at 5 µm mesh was found to be less than 5% (only except two cases) and less than 17% for 100 µm.

Gandiolle et al. [145] compared critical plane (SWT, MD) parameter with Crossland parameter by applying fatigue stress at different angles to fretting direction. By comparing predicted threshold tangential force with experimental results, they showed that Crossland parameter was unable to demonstrate threshold evolution. In addition, the prediction accuracy of MD parameter was found better than Crossland parameter.

Table 3. Summary of loads, geometry and materials of various FF studies using SI approach.

Authors	Load			Specimen material	Pad type	Pad radius (mm)	Damage parameters used
	P (N)	Q (N)	σ_A (MPa)				
Bernardo et al.[141]	p_o=120~157	Q/P=0.24~0.45	61.8~92.7	Al4%Cu	C	12.5~150	CL,DV,PRH
Tsai et al.[143]	60	-	-	Ti-6Al-4V	C	50.8	von Mises
Nesládek et al.[89]	5,15	-	15~30.1	Chrome steel	C	200	CL
Heredia et al.[144]	200~800	-	-	Ti-10V-2Fe-3Al	C	-	Principal stress weight function
Gandiolle et al. [145]	5000	-	400	35NiCrMo16, Cr steel 52100	S	200	CL,SWT,MD

Notations:
C Cylindrical pad
S Spherical pad
p_o Peak normal pressure
- Information not available
~ Range of values
Special units, values are specified within cell

3.4 Fretting specific parameter

In fretting fatigue, crack initiates from the surface of the contact due to high frictional forces at the interface. This implies that slip amplitude at the contact interface is an important parameter in fretting fatigue. The parameters incorporating the effect of slip amplitude that are included in this study are Ruiz parameters ($F1$, $F2$) and D_{fret2}. The summary of loads, material and geometry of fretting fatigue studies using this approach is given in Table 4.

3.4.1 Ruiz parameter

Ruiz et al. [146] studied dovetail joint between blade and disc of a gas turbine on a biaxial fatigue machine. The material tested were Titanium alloy, Nickel alloy and Steel alloy. It was observed that specimen life is strongly dependent on ratio between the amplitude of loads applied on both parts. This was ascribed as relative slip between the parts, which increased as dovetail opened up under increasing load rather than to a change in peak stress. They proposed that fretting damage and peak stress are responsible for reduction in fatigue life for the contact problems [146]. Based on their experimental observations, they proposed two parameters combining slip amplitude with stress components. The first parameter is known as damage parameter or wear parameter $F1$, which is defined as the product of shear stress τ and relative slip d_x between the

contacting bodies. This parameter can also be interpreted as frictional energy due to contact forces.

$$F1 = \tau . d_x \tag{116}$$

It was observed that maximum value of damage parameter $F1$ was close to the experimental maximum wear location. In fretting fatigue, number of surface crack may originate and, therefore, the maximum wear location and actual crack location may differ. They also observed that the surface damage converted to crack due to the presence of tensile stress. Hence, a second parameter was introduced known as initiation parameter $F2$.

$$F2 = \sigma_{xx} . \tau . d_x \tag{117}$$

3.4.1.1 Application of Ruiz parameter to fretting fatigue

By performing elastic-plastic analysis, Iyer and Mall [147] studied the effect of contact pressure on fretting fatigue life. Ruiz parameters $F1$ and $F2$ were applied to compare damage nucleation for different contact pressure and stress amplitudes. It was observed that fretting fatigue life decreased, with increasing contact pressure. This might be due to increase in local stress range escalation, without any contribution of shear traction and slip amplitude. Since boundaries of the primary slip zone and plastic deformation changed markedly after crack initiation, therefore its location cannot be determined precisely after any amount of growth[148]. According to them, Ruiz parameters $F1$ and $F2$ were unable to explain the effect of contact pressure on fretting fatigue life. These parameters assume equal influence of individual drivers and requires measurement of relative effect of each other on initiation life.

Lykins et al. [115] found that Ruiz parameter $F1$ was not effective in determining initiation site since maximum tangential stress and maximum frictional energy occurred at different locations. The $F2$ parameter showed initiation site close to experimental results. However, it did not show any specific trend with number of cycles to crack initiation. According to them, the $F2$ parameter can be applied only, when considering the effects of cyclic range or mean stress.

Missingham and Irving [149] studied the effect of variable amplitude load (VAL) on shear stresses by using FEM. They observed that with the application of overload to constant amplitude loading (CAL), the maximum shear stress at the stick-slip boundary was reduced and also the size of slip region. For VAL, the position of stick-slip boundary was continuously moving. Therefore, the damage initiation was observed over an area rather than on a single point

as in case of CAL. This effect would increase experimental lives in comparison to linear damage model.

To analyse the effect of different fretting fatigue primary variables on localized plasticity, Hojjati Talemi and Abdel Wahab [150] investigated the effect of contact radius, *R*, axial stress, σ_A, and friction coefficient, μ. It was found that the peak in the tensile stress σ_{xx} increased with decreasing pad radius. The plastic zone was initiated at the contact surface and propagated at an angle approximately 45° into the specimen. For lower μ (0.4 to 0.6), the locations of peak equivalent plastic strain and *F*2 were close to each other, however for lager μ (greater than 0.9) *F*2 parameter showed deviation from other two methods. These observations also reinforced the reservations of Hills and Nowell [1] about application of *F*2 parameter for neglecting surface conditions.

3.4.2 Fretting damage parameter (D_{fret2})

Ding et al. [151, 152] presented a fretting damage parameter D_{fret2} which combines multiaxial fatigue parameter and surface damage effect of fretting. This parameter incorporates the effect of relative slip on fretting fatigue life and contact size effect under fretting fatigue conditions. The key advantage of this parameter is that it can predict failure life accurately and replaces the conventional computationally expensive wear incremental techniques. More precisely this parameter is a modified form of critical plane SWT parameter and includes the effect of frictional work from Ruiz parameter $F1=\tau d_x$. In this way, wear effects are included in the fatigue parameter, which are usually neglected for life estimation. The parameter can be expressed as:

$$\sigma_n^{max}\frac{\Delta\varepsilon_n}{2}D_{fret2}=\frac{\sigma_f'^2}{E}(2N_i)^{2b}+\sigma_f'\varepsilon_f'(2N_i)^{b+c} \qquad \tau d_x \le (\tau d_x)_{th} \tag{118}$$

$$D_{fret2}=(1+C\tau d_x)\left\langle 1-\frac{\tau d_x}{(\tau d_x)_{th}}\right\rangle^n \tag{119}$$

where $(\tau d_x)_{th}$ is the threshold limit of τd_x beyond which wear becomes dominant over cracking. For the cases where $\tau d_x > (\tau d_x)_{th}$, conventional critical plane SWT parameter can be applied. For validation of proposed method, the experimental data of [114] and [126] was used. They observed that by using the volume averaging method at the location of maximum τd_x, the predicted lives correlated well with the experimental results at various slip ranges and semi contact widths. Especially, it could capture the increase in fatigue life with the increase in relative slip, from partial slip regime to gross sliding regime.

Table 4. Summary of loads, geometry and materials used in various studies using Fretting Specific parameters.

Authors	Load			Specimen material	Pad type	Pad radius (mm)	Damage parameters used
	P (N)	Q (N)	σ_A (MPa)				
Iyer et al.[147]	1338~1567	-	552	Ti-6Al-4V	C	50.8	F1,F2
Missingham et al.[149]	160	1200	60	Al2618	C	220	F1,F2
Hojjati Talemi et al.[150]	7000	2240	90~160	Al2024-T3	C	25~75	F1,F2
Ding et al.[151]	302	u=16~38μm	550	Ti-6Al-4V,Al4%Cu	C	25~75	D_{fret2}

Notations:
C Cylindrical pad u Displacement applied ~ Range of values
- Information not available Special units and values specified within cell

3.5 CDM approach

The CDM approach uses the concept of a damage variable D, which can be combined with an effective stress concept to estimate the damage evolution. The damage starts to nucleate at a certain level known as threshold damage and crack is initiated when the value of damage parameter reaches a critical value. This concept was introduced by Kachanov [153], which is based on thermodynamic laws and combines damage with stress and strain. The primary variable, which governs the damage phenomena, is the strain energy density release rate. Figure 30 shows a representative volume element (RVE) of a damaged body, where A is the total surface area of the plane containing damage and A_D is the total surface area of damage. The size of the RVE should be large enough to include defects and small enough to be considered as a material point of the mechanics of continua [154]. The effective stress and strain can be represented as:

$$\tilde{\sigma} = \frac{F}{A - A_D} = \frac{F}{A(1 - D)} \tag{120}$$

The CDM concept proposed by Kachanov, was later extended by many researchers and applied to various fields. Lemaitre proposed a damage model for LCF [155], ductile damage[156] and for creep fatigue [157]. Chaboche [158] introduced a model for HCF. Bhattacharya and Ellingwood [159] also presented a damage model to predict crack initiation. Although there are many other models available for elastic, elastic-plastic, visco-elastic (plastic) and composite behaviour, only those models are discussed here, which have been extended and applied to fretting fatigue problems.

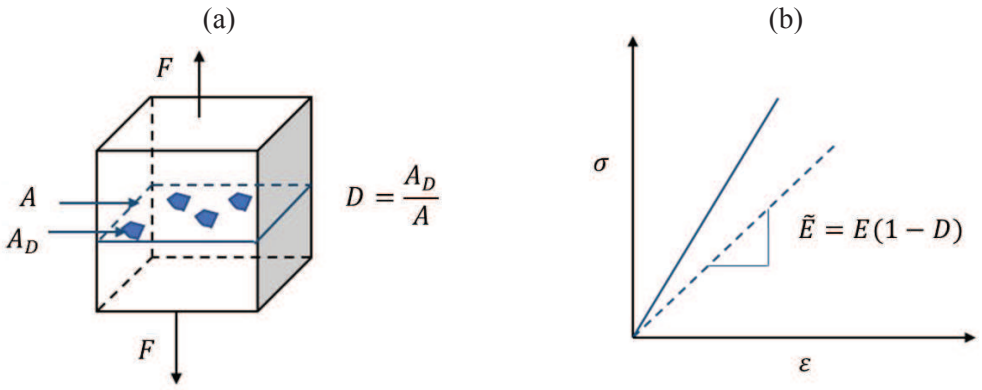

Figure 30. Concept of CDM approach showing (a) representative volume element (RVE) of a damaged body and (b) reduction in elasticity modulus E, due to damage.

3.5.1 Bhattacharya and Ellingwood model (BE)

Bhattiacharya and Ellingwood conducted experiments on different materials including steel 4130 and 4340 steel, A106 Gr-B steel and Al 2024 T4 and proposed a model which calculate initiation life using cumulative fatigue damage [159]. It incorporates mean stress effect, loading sequence effects, stress controlled and strain controlled loading cycle effects. The damage is assumed to accumulate with each loading cycle only if the cyclic stress range exceeds the fatigue limit. According to this model, the value of critical damage $D_c \leq 1$ for the failure to occur, opposed to other state variable type model (e.g. Miner's rule) where $D_c=1$, represents the failure.

$$D_N = 1 - (1 - D_0) \prod_{n=1}^{N} L \tag{121}$$

where, D_0 is the initial damage at fatigue cycle (for undamaged material $D_0 = 0$). L is a function, depending on material and loading conditions. The damage equations were applied incrementally in this model, which may produce changes in stress-strain behaviour due to cyclic softening and hardening. Cycle dependent material properties could also be used, however for simplicity stress stain curve from a stabilized cycle was used.

Qureshi et al. [160] extended this model and applied to fretting fatigue. The approach of decomposition was used, by resolving shear stresses into tensile and compressive components. The model assumed that only alternating shear stresses contribute to the damage nucleation and neglect static compressive stresses. They observed that the cyclic shear forces have the same effect as the cyclic tensile forces acting at 45° from the shear stress direction. Extending the theory to multiaxial loading (L_1 and L_2), the damage variable can be written as:

$$D = 1 - L_1^N L_2^N \tag{122}$$

$$D_c = 1 - L^{2N_i} \tag{123}$$

D_c is an experimental value and can be found by generating several SN curves for different D_c and by comparing with SN curve of plain fatigue. By conducting a parametric study, they showed that for higher critical damage, the number of cycles to initiation also increased. The predicted results of D_c were found in good agreement with experimental results. According to this model, failure refers to crack initiation and therefore propagation phase is neglected.

3.5.2 Chaboche damage model

Chaboche proposed a Non-Linear-Continuous-Damage (NLCD) fatigue damage model [158]. The NLCD model also caters short crack regime; micro-initiation and micro-propagation were included in the model. The damage variable D is regarded as 0 for initial undamaged state and to 1 for macro crack initiation where $N = N_f$. The state at a depth of 1mm is considered to be the rupture of fatigue specimen. The NLCD model can be applied precisely to predict; one level or two level stress controlled fatigue tests, influence of mean stress, block program loading conditions and LCF tests [161]. For a constant stress and uniaxial case, the number of cycles to failure can be obtained as [162].

$$N_f = \frac{1}{1+\beta} \cdot \frac{1}{c_1 M_0^{-\beta}} \frac{\langle \sigma_u - \sigma_{max} \rangle}{\langle \sigma_a - \sigma_{f-1}(1 - b_1 \sigma_m) \rangle} \cdot \left[\frac{\sigma_a}{1 - b_2 \sigma_m} \right]^2 \tag{124}$$

where, σ_a, σ_m, σ_{max} and σ_{f-1} are the stress amplitude, mean stress, maximum stress during one cycle and fatigue limit, respectively. β, M_0, c_1, b_1 and b_2 are material constants and can be determined from fatigue tests or SN curve. Chaboche and Lesne also mentioned some deficiencies in the model such as some correction to the total rupture life is required to get the macro initiation life i.e. by subtracting the final propagation life. In addition, there is no distinction between the rate equation for initiation regime and rate equation of micro propagation. This uniaxial model has been extended to 3D case by Chaudonneret [163].

3.5.3 Lemaitre damage model

Lemaitre proposed several damage models for ductile, creep and fatigue failure [40, 58, 154, 164]. They derived basic equations to model coupling between strain and damage behaviour using thermodynamics laws of irreversible process. The damage was represented as a scalar internal variable D, which characterized the strength loss of material in processes such as fatigue, creep or ductile strains. Applications were shown to be related to elasticity coupled with damage

for HCF (brittle failure), plasticity related to LCF (ductile failure) and visco-plasticity coupled with creep and fatigue damages. The number of cycles to initiation can be determined as a function of material parameters and induced stress.

$$N_i = \frac{(s_o + 1)\left(S_M^{s_o+2} - S_m^{s_o+2}\right)^{-1}}{2A(s_o + 2)(R_v)^{s_o}} \tag{125}$$

where, A is a material constant and R_v is the triaxiality function. S_M and S_m are the minimum and maximum equivalent Von Mises stress, respectively.

Hojjati Talemi and Abdel Wahab extended Lemaitre's work and derived an uncoupled model for elastic regime [165] and elasto-plastic condition [166]. They applied the model for fretting fatigue problems to determine initiation location and life. The initiation life for elastic and elasto-plastic cases can be determined as:

$$N_i = \frac{1}{A(s_o + 3)}\left(S_M^{s_o+2} - S_m^{s_o+2}\right)^{-1} R_v^{-\left(\frac{s_o}{2}\right)-1} \tag{126}$$

and

$$N_i = \frac{\left(S_M^{-m-2s_o} - S_m^{-m-2s_o}\right)R_v^{-s_o}}{A(m + 2s_o + 2)} \tag{127}$$

where, A and s_o are material dependent damage parameters. m is the power constant in Ramberg-Osgood equation. This model has shown that nucleation life can be estimated within ±2 N band as compared to experimental results. The details of damage model for elastic (HCF) regime and the proposed damage model of the present work for non-proportional loading are given in next chapter.

3.5.4 Application of CDM approach to fretting fatigue

This section demonstrates the work of researchers who employed CDM approach to study fretting fatigue damage nucleation. The summary of loads, material and geometry of fretting fatigue studies using this approach is given in Table 5. Zhang et al. [162] extended the work of Chaboche, Lesne [161] and Chaudonneret [163]. They developed an incremental non-linear continuous damage model (NLCD) and validated for plain fatigue and fretting fatigue. The predicted lives were also compared with critical plane SWT parameter. The crack nucleation was assumed to occur when the damage at any integration point reaches to 1.

$$E^{i+1} = E^i(1 - D^{i+1}) \tag{128}$$

The model showed a similar trend of life and relative slip as shown by SWT and experimental results. The nucleation locations were found inside the slip zone and results showed a good correlation between predicted and experimental results.

To estimate total life for fretting fatigue, Hojjati-Talemi et al. [166] developed an uncoupled damage evolution law for elasto-plastic condition. The comparison of estimated life and experimental life showed good correlation and all data was found with in ±2 N error band. These results were also compared with the previous work [136], where combination of critical plane (MD parameter) and XFEM was used along with variable initial crack length. Although total lives were quite similar, the CDM approach showed lower dispersion than with MD parameter. Furthermore, the proportion of initiation life with CDM approach was found to be 55% of the total life, however with critical plane approaches it was estimated as 11.1 % and 19.6 % using MD and SWT parameters, respectively [136]. The difference in initiation life for both cases can be associated with the estimation of different initial crack lengths applied to both cases.

Later, Hojjati-Talemi and Abdel Wahab [48, 131, 165], proposed an uncoupled damage law for HCF. The damage nucleation site was predicted using maximum principal stain range $\Delta\varepsilon_{p,max}$ and damage equivalent stress σ^* criteria. Both criteria showed damage initiation location at the trailing edge of the contact. A critical radius r_c approach, shown in Figure 31, was adopted to minimize the stress gradient and mesh dependency effects on initiation life. The critical radius can be determined as [48, 167]:

$$r_c = \frac{1}{\pi}\left[\frac{\Delta K_{th}}{\sigma_{f-1}}\right]^2 \tag{129}$$

where, ΔK_{th} and σ_{f-1} are the crack threshold stress intensity factor range and plain fatigue strength, respectively. They also showed that different process zone radii do not affect significantly on life. The two radii, 50 µm and 1 mm, showed maximum difference of 15 % in nucleation life.

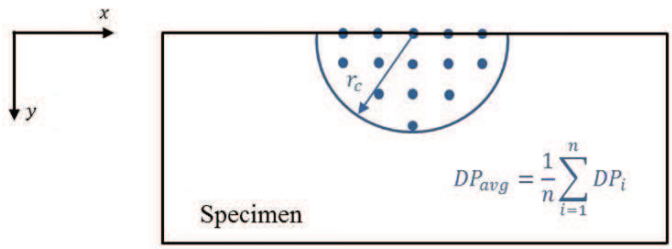

Figure 31. Volume averaging procedure using critical radius or length approach. *DP* represents damage parameter and n is the number of nodes considered for averaging process.

Shen et al. [168] combined continuum damage mechanics with wear analysis. For elastic damage evolution, Chaboche and Lesne [161] damage model was applied similar to Zhang et al.

[162], but with uniaxial application. The numerical results showed that all stresses increased at the stick-slip interface due to induced wear effect. The plastic damage occurred at stick slip interface. Wear accelerated the nucleation phase in the partial slip regime. For gross sliding case, the stresses were reduced, no plastic strain was found and wear delayed the nucleation phase significantly. Furthermore, they observed that there is no effect of plasticity on wear scar for partial slip case, however plasticity affected the total fretting fatigue life.

To analyse the crack initiation in real application (double lap bolted joint), Ferjaoui et al. [169] performed fretting fatigue experiments and numerical analysis using CDM approach. The cracks initiated at the side closer of applied axial load and almost 2mm from the edge of the hole. Using 3D numerical model, the crack initiation location was analysed using Ruiz *F*2 parameter and damage equivalent stress σ^* criteria. Both parameters gave good estimation of initiation location in comparison to experimental results. For computation of initiation life, critical radius approach was used for stress averaging with a radius of 0.2 mm at maximum damage location. The predicted initiation live was found within ±2 *N* band of total experimental life. The nucleation phase consisted of 80-90% of the total experimental life.

Table 5. Summary of loads, geometry and materials for various FF studies using CDM approach.

Authors	Load			Specimen material	Pad type	Pad radius (mm)	Damage models used
	P (N)	*Q* (N)	σ_A (MPa)				
Quraishi et al.[160]	-	-	$0.95fp_o$	Al2024, S45C	C	-	BE
Zhang et al.[162]	208 N/mm	-	550	Ti-6Al-4V	C	50.8	Chaboche-Lesne, Chaudonneret, SWT
Hojjati Talemi et al.[166]	2000~8000	-	110~190	Al7075-T6	F	N.A.	Lemaitre
Hojjati Talemi et al.[165]	5201~7562	1385~2705	81~115.8	Al2024-T3	C	127,178,229	Lemaitre
Hojjati Talemi et al.[48]	543	155.1~330.1	160~220	Al2024-T3	C	50	Lemaitre, F1
Shen et al.[168]	208 N/mm	u=32~44 μm	550	Ti-6Al-4V	C	50.8	Chaboche-Lesne
Ferjaoui et al.[169]	16kN~22kN	-	87.5~125	Al2024-T3	C	4	Lemaitre, F2

Notations:
C Cylindrical pad
F Flat pad
\- Information not available
~ Range of values
N.A. Not applicable
Special units and values specified within cell

3.6 Comparison between crack nucleation approaches

The previous sections presented different approaches and its applications under fretting fatigue conditions. Although there is very wide range of applications and various aspects have

been analysed by researchers, however the most common studied aspects include; applicable failure mode, critical plane angles, crack initiation location, prediction accuracy of approach or damage parameters and the crack-initiation length method. Therefore, a tentative comparison of these approaches and damage models is presented in Table 6, according to these measures. The values of initiation location, orientation and life are presented as a range, by combining different case studies. The critical plane approach has an advantage over other approaches to describe failure modes and determine initial crack orientation. On the other hand, it is also most computationally expensive since damage parameter are evaluated over large range of angles. The crack initiation orientation is usually determined up to a crack length of 50 to 100 μm form the surface. For most cases, these angles are found between 25° to 50° inside the contact and for some cases outside the contact. All approaches showed crack initiation location closer to experimental observations. The fretting specific parameters however, tends to predict initiation site with in slip zone (little away from contact edge), therefore can be more suitable for cases where wear effects are significant.

To estimate the life prediction accuracy of the various approaches and damage parameters, three popular ways are presented, i.e. error band, standard deviation and fatigue index error. The error band and standard deviation is usually measured comparing predicted nucleation life with experimental life whereas fatigue index error is determined by comparing damage parameter with fatigue limit in tension or torsion. Only Ruiz parameter $F2$ cannot be combined with any other formulation for life estimation. For most of the fretting fatigue cases, crack initiation life is observed to lie with in ±3N error band for most of the critical plane parameters using fixed crack initiation length, however, slightly better results are observed using variable initiation length, i.e. up to ±2N error band or 1.4 standard deviation. CDM approach has shown some improvement up to ±2N for some cases. Using stress invariant approach, the fatigue index error mostly ranges from 15% to 70% and standard from 1.4 to 2.1. For some cases SI invariant approach has shown results comparable to other approaches, while for cases slightly larger deviations are observed. Therefore, there is no significant difference between different approaches for numerical life prediction.

Table 6. Comparison of different approaches and damage models for fretting fatigue cases.

Appro-ach	Damage parameter	Applicable failure mode	Critical plane orientation θ_c (°)	Initiation location x/a	Accuracy			Crack initiation length method	Case study
					Error Band	Standard deviation	Fatigue index error (%)		
CP	FP	Shear	5~25, 35, 48.3~50	0.88~0.99	± 3N	1.98	-	Fixed	[86, 110, 116, 170]
	MD	Shear	36,48.3~50	0.88~0.99	± 3N		-	Fixed	[86, 116, 170]
					± 1.5, 2N	1.46~2.04	-	Variable	[109, 124, 136]
	SSR	Shear	25~50, -70~-39	0.85~1.0	± 3N	-	-	Fixed	[60, 110, 118, 123]
	MSSR	Shear	38~45	0.94~1.0	-	1.98	-	Fixed	[110, 128, 130]
	FS	Shear	35~48.3	0.86~0.99	± 3N		-	Fixed	[86, 114-116, 170]
						1.46~2.04, 1.74	-	Variable	[109, 136]
	BM,KBM	Shear	27,48.3~50	0.88~0.99	± 3N	-	-	Fixed	[116, 170]
	SWT	Tensile	-10~15	0.93~1.0, 0.79~-0.92	± 3N		-	Fixed	[59, 86, 88, 110, 114, 115, 123, 129, 137, 162, 170]
						1.46~2.08, 2.46	-	Variable	[109, 136]
	Liu	Tensile/ Shear	-5/38	0.87~1.0	± 3N	-	-	Fixed	[170]
SI	CL	N.A.	N.A.	≃1	-		15~45 -4~25.1	Fixed	[141] [89]
						1.46~2.12		Variable	[109]
	PSWF	N.A.	N.A.	-	-	-	-45~-35, 15~70	Fixed	[144]
Fret. Sp.	(F1,F2)	N.A.	N.A.	0.7~0.92	N.A.	N.A.	N.A.	N.A.	[115, 150, 171]
	D_{fret2}	Tensile/ Shear	-	0.82	-	-	-	Fixed	[151, 152]
CDM	Chaboche, Chaudonneret	N.A.	N.A.	0.957, -0.78~-0.91	± 3N	-	-	Fixed	[162]
	Chaboche, Lesne	N.A.	N.A.	x = -0.13 ~ - 0.71mm	-	-	-	Fixed	[168]
	Lemaitre, Hojjati-Talemi, Abdel Wahab	N.A.	N.A.	0.97~0.98	± 2N, ± 3N	-	-	Fixed	[48, 165, 166, 169, 172]

Notations:
N.A. Not applicable ~ Range of values - Information not available
Special units, values specified within cell

3.7 Summary of literature review

To study fretting fatigue damage initiation, different approaches and damage models can be adopted. These damage models can be divided into critical plane approach, stress invariant approach, continuum damage mechanics approach and fretting specific parameters. In general, it

can be said that initiation life can be predicted within ±2 N to ±3 N error band of the experimental values. The Ruiz initiation parameter $F2$, cannot be used to predict initiation life numerically. Most of the CP parameters and CDM models were originally developed/tested for plain fatigue cases and later applied under fretting fatigue conditions. Even the critical damage parameters and stress-strain life constants are taken from plain fatigue tests. Therefore, in general the error estimations under fretting fatigue are found much higher than plain fatigue cases for which the damage models were originally validated.

There is no standardized definition of crack initiation length, the proportion of life taken by each phase is dependent on the length of initial crack. The initiation length varied from 10 μm to 1mm depth, which ultimately affects the life estimation of each phase. For life estimation, two methods can be employed, namely, variable initiation length and fixed initiation length method. Depending upon the method employed and crack initiation length; nucleation phase may take from 10% to 90% of the total failure life. The CDM approach also utilizes two methods, to determine crack initiation life. Some damage models determine the critical damage value ranging from 0.2 to 0.8 experimentally while the other assume it as 1. The size of the RVE assumed also ranges from meso or macro scale.

Cracks nucleate in shear and grow either under shear or tensile forces. For fracture under tensile forces, after certain length, crack changes the direction and propagate perpendicular to contact surface. Considering the first few grains, the crack initiation orientation can be estimated. Most of the experimental and numerical results have estimated this angle between 25^{o} and 50^{o} depending upon material and loading conditions. The angles can be estimated numerically using critical plane approach, while the other approaches cannot be employed for this purpose. Since there is no clear definition of crack initiation length, researchers have used various depths for estimations of initial crack orientation. Mostly, this depth is taken up to 100 μm and sometimes even larger. However, using only surface stress for computation of relatively larger depths is not justified. After few grains size of the material the crack orientations should be modelled by propagation methods. Furthermore, for determination of initial crack orientations, shear (stress, strain and strain energy) based parameter should be used since the damage process is initiated due to shearing of slip band in the material.

In fretting fatigue, contact conditions are assumed to be in partial slip condition since contacting bodies undergo small oscillatory movements. However, under fretting conditions, depending upon relative slip and loading amplitude, gross sliding may also appear, where considering nucleation phase alone may result in inaccurate results. Therefore, wear models should be incorporated in crack initiation approaches for such cases.

The most potential point of crack initiation, is the trailing edge of the contact. The trailing edge is usually defined as the edge near to applied cyclic axial load. For some cases, slip zone cracking is observed for the cases where wear effects are dominant. Most the crack initiation approaches and criteria have shown similar results and in close agreement with the experimental failure location. The reason for prediction of this location is related to stress concentration, which is produced at the edges of contact.

Depending upon the loading magnitudes, contact type and pad radius, micro plasticity can be induced. In general, larger amplitudes, flat pad and small pad radius are prone to produce localized effects. Hence, numerical results can be singular at those points and local damage models may lead to inaccurate results. The mesh refinement strategy does help during this situation and non-local and regularization methods are required to reduce the mesh size and stress gradient effect. However, for the case of large cylindrical pad radii, critical length plays more significant role than the averaging methodology for life prediction.

There are other factors also, which affect crack initiation life such as loading sequence, stress ratio and coefficient of friction between the contacting bodies. There is no specific approach or damage model, which gives best results for all cases. Numerous factors are involved, which contribute in estimation of crack initiation life. Such factors include loading magnitudes, phase difference between the applied loads, material, load ratios, crack initiation length, pad radius, regularization approach, etc. Some parameters produced better results in one situation, while other parameters proved to be better for other cases.

Chapter 4

Methodology

This chapter describes the methodology adopted for the analysis of fretting fatigue crack nucleation. The methodology broadly covers three sections. In the first section, various aspects related to numerical model are discussed, which includes; geometrical model, loads and boundary conditions, mesh size effect, validation of numerical results and load displacement curves. The second section describes the mathematical modelling of damage models using CDM approach. The mathematical formulation of other approaches is already presented in Chapter 3, Literature review. Since these approaches are based on empirical results, therefore, there is no sequential derivation for CP, SI and Ruiz parameters. The third section provides details about the implementation of all approaches i.e. CP, SI, *F*2 and CDM.

4.1 Numerical modelling of fretting problems

With the growing capability in computational resources, implementation of numerical methods has become widely popular to solve fretting fatigue problems. The intrinsic details at the contact interface are particularly of great interest, which can lead to crack nucleation. Finite element methods can thus be used to analyze the effect of different fretting fatigue parameters on crack nucleation. Several computational tools can be used for preprocessing, solving and post processing purpose, e.g. ABAQUS, ANSYS, PYTHON and MATLAB, etc.

The numerical model plays an important role in fretting fatigue problems, not only in terms of accuracy of predicted results, but also for efficient solutions. Researchers have successfully used various numerical models; most popular ones are summarized in this section. The difference between these models is mainly due to the modelling approach of tangential load Q and the ways boundary conditions are applied. The most widely used numerical model is shown in Figure 32(a). This model has been used by several researchers to predict fretting fatigue initiation life [110, 115, 116, 130, 143, 147, 173]. It comprises fretting pad, half specimen (symmetric about x-axis) and a pad holder to support fretting pad. The normal load P is applied at the top surface of the specimen and tangential load Q is applied at the interface between the pad and pad holder. Pad holder and specimen is restrained in x-direction from the left side and axial cyclic stress σ_A is applied to the other side of the specimen. Using symmetry boundary conditions, the specimen is restrained in y-direction from the bottom. The pad holder is usually given a very low stiffness so that it does not alter the testing configuration. The purpose of pad holder is to provide stability to numerical model in initial few steps. However, the presence of extra elements also increases the computation time, which can be significant for large scale problems, such as in case of fretting wear analysis.

The second type of model is shown in Figure 32(b). Massingham and Irving used this model to study effect of variable amplitude loading on shear stress distribution [149]. In this model, Q was applied on one side of the pad and while the other side was restrained in x-direction.

This type of boundary conditions can produce higher tensile stresses than in actual case, since in test configuration the pad experiences micro oscillations. The Q load can also be applied by using spring of equivalent stiffness in place of pad holder as shown in Figure 32(c). Giner et al. [174] used this model in their study of crack-contact interaction. This method requires the calibration of spring stiffness through load displacement curve. The numerical modelling of springs, however, may add some complication for reversible or cyclic load in order to produce same spring stiffness in both directions. The tangential load can also be generated by applying displacement, U, to the fretting pad as shown in Figure 32(d). Researchers in references [133, 175-177] used this approach for fretting fatigue and wear applications. This type of boundary condition also requires experimental data of displacements to be applied to the fretting pad.

Hojjati-Talemi and Abdel Wahab have successfully used another approach for modelling contact parameters and fretting fatigue life [48, 150, 165] as shown in Figure 32(e). In this numerical model, the pad was restrained from both sides. Axial cyclic stress was applied on one side of the specimen and a reaction stress on the other side of the specimen. The resultant of both stresses will generate the required tangential load at the contact interface. The reaction stress can be calculated using Eq. (130). For flat pad configuration and cases where tangential load Q is absent, a quarter symmetry model can be used, as shown in Figure 32(f). Both pad and specimen are restrained from the left side and half of the normal load $P/2$ is applied at the top surface of the specimen. However, with flat pad configuration, singularities may be generated at the edge of the contact and therefore may require regularization technique for stress averaging. Sabsabi et al. [136] and Hojjati-Talemi [166] used this model in the numerical investigation of fretting fatigue life.

$$\sigma_R = \sigma_A - Q/A \tag{130}$$

For all models, usually loads are applied in four major steps. After establishing the boundary conditions in the initial step, first normal load P is applied until it achieves its maximum and then kept constant for subsequent load steps. The cyclic loads are applied to achieve maxima, minima and again maxima in second, third and four steps, respectively.

For the present work, a variant of the numerical model shown in Figure 32 (a) was used. The numerical model used in this study was constructed in ABAQUS, which consisted of only two parts, namely, pad and specimen. This implies that pad holder is not used in current configuration, as shown in Figure 33, and the fretting pad is not restrained in the x direction. The tangential load Q was applied directly on one side of the pad. The numerical model achieves stability due to the presence of normal load P, which can be supplemented by multipoint constraint (*MPC*) option. Specimen was restrained in the vertical direction from bottom and in horizontal direction from left side. The cyclic axial stress σ_A was applied on the right side of the

specimen. The model is applicable as long as $Q/\mu P < 1$. This model allows to: (i) reduce computation time due to less number of degree of freedom (as there is no pad holder); (ii) apply tangential load in a simpler and direct way as compared to the models shown in (c) and (e), without loss of accuracy. The comparison between the present model and two of the previous models is presented in the Chapter 5, Results.

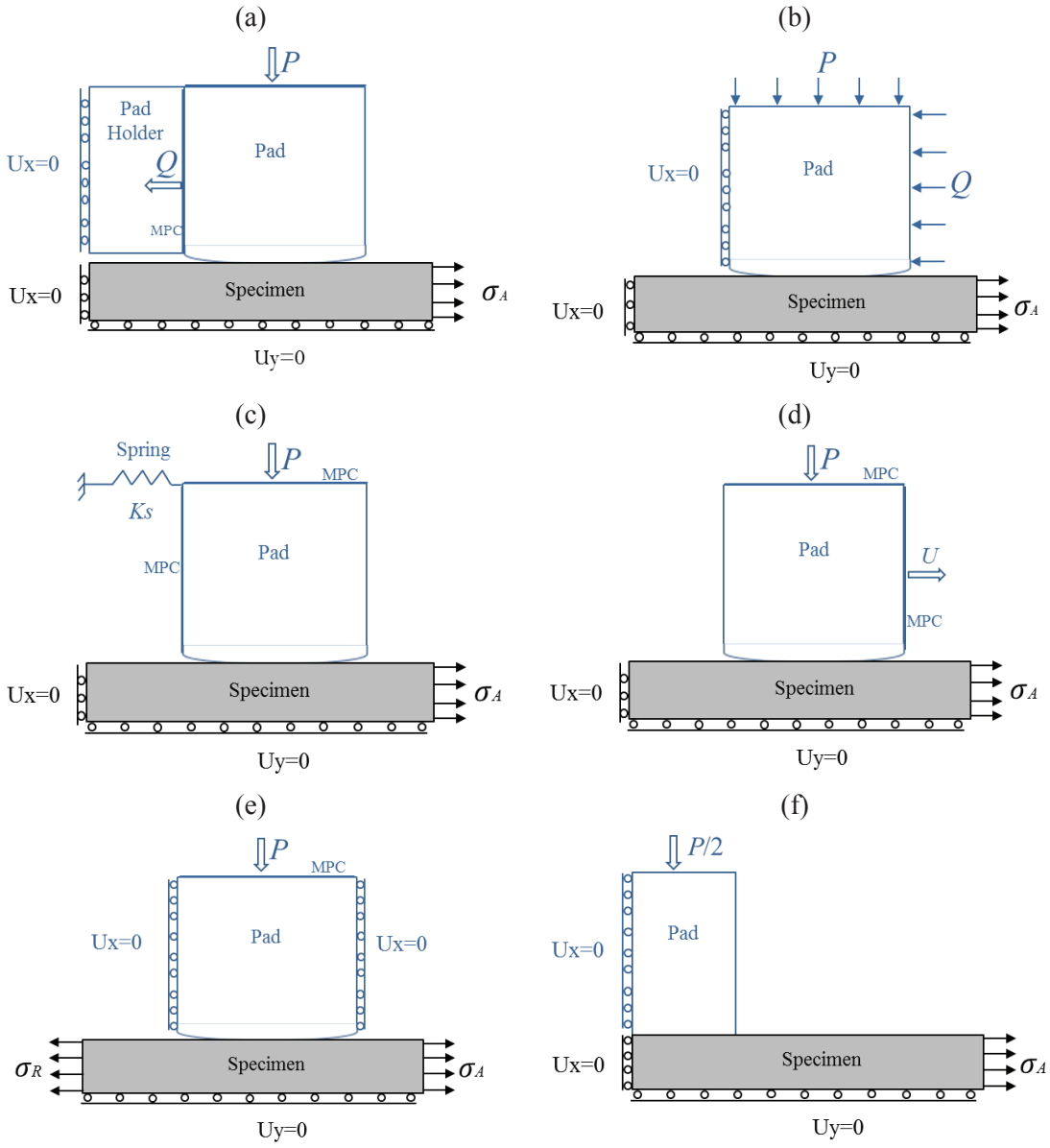

Figure 32. Different numerical models for fretting fatigue problems, with loads and boundary conditions.

For all numerical simulations, plane strain finite elements were used to describe sections for both components. 4-noded bilinear elements, CPE4R, were used to mesh both parts. The automatic master-slave algorithm was used to establish contact. Pad's cylindrical surface was defined as master and specimen's top surface was defined as slave. Surface to surface contact was established between the pad and specimen, as it improves the accuracy of contact stresses due to engagement of slave node with large number of master surface facets. For contact tracking, finite sliding formulation was used between master and slave surfaces. Lagrange multiplier method was used for contact enforcement, as it ensures strict enforcement of pressure-penetration relationship and enforces zero relative slip during stick, which is important for fretting problems. The coefficient of friction, μ, was kept constant throughout the analysis and defined as input to the problem.

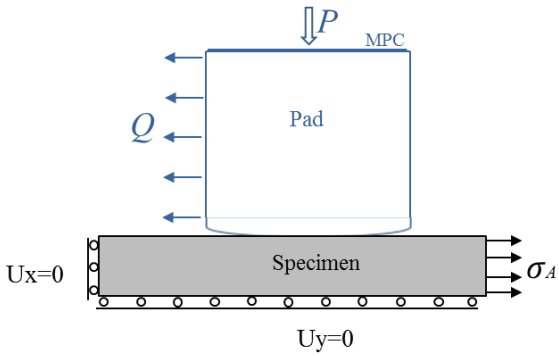

Figure 33. Numerical model used in present work.

4.1.1 Significance of mesh size

The other important aspect related to numerical modelling is the mesh size at the contact interface. Since in fretting fatigue, crack originates from the surface and high stress gradient is present at contact interface, therefore appropriate mesh size is important in order to determine crack initiation location precisely and to evaluate damage parameter. Most of the researchers used mesh size between 2×2 μm and 25×25 μm at the contact interface and showed good agreement with analytical solution [115, 129, 137, 143, 147, 149, 150, 165, 168, 174]. The details for mesh sizes used by other authors is given in Table 7. For the work presented in this thesis, mesh size of 5 × 5 μm was used.Table 7.

Table 7. Mesh sizes used by previous authors for fretting problems

Sr. Nr	Case study	Mesh size (μm)
1	Tsai and Mall [143]	5 × 2.5
2	Lykins e al. [115]	6.2 × 6.2
3	Iyer and Mall [147]	12.4 ×12.4
4	Naboulsi and Mall [123]	6 × 6
5	Sum et al. [129]	4 × 4
6	Massingham and Irving [149]	25 × 25
7	Hojjati-Talemi and Abdel-Wahab [150]	5 × 5
8	Shen et al. [168]	10 ×10
9	O'Halloran [137]	2 × 2
10	Yue and Abdel-Wahab [176]	5 × 10

The mesh size also has a relation with evaluation of stress concentration at the edge of the contact. It can lead to stress singularity, especially for flat pad or cylindrical pad with small radius. In general, there are two methods to determine stress singularity i.e. asymptotic method and numerical method. Sinclair presented an approach, which allows to determine stress singularity numerically [178]. The stress singularity can be determined if the peak stresses shows divergence after sequence of mesh refinements. The recommended sequence of mesh is, doubling the density of mesh for each case i.e. h, $2h$, $4h$, where h is the number of elements in a domain. The scaling factor can be represented as z and the number of elements as, h, zh and $z^2\ h$. Stress singularity can be of two types, power singularity and logarithmic singularity. By using ω as singularity exponent, for power singularity, the relationship between local stress σ and distance r from the singular point can be expressed as [179]:

$$\sigma = O(\sigma_A r^{-\omega}), \qquad \text{as } r \to 0 \tag{131}$$

The power singularity is present if:

$$\frac{2|\omega_c - \omega_m|}{\omega_c + \omega_m} \leq 0.1 \tag{132}$$

$$\omega_c = \frac{\left(ln\frac{\sigma_m}{\sigma_c}\right)}{lnz}, \qquad \omega_m = \frac{\left(ln\frac{\sigma_f}{\sigma_m}\right)}{lnz} \tag{133}$$

where, subscript c, m and f represents the coarse, middle and fine mesh, respectively. For logarithmic singularity, the expression relating local stress σ and distance r from the singular point can be written as:

$$\sigma = O(\sigma_A lnr), \qquad \text{as } r \to 0 \tag{134}$$

The logarithmic singularity is present if:

$$\frac{2|\Delta\sigma_c - \Delta\sigma_m|}{\Delta\sigma_c + \Delta\sigma_m} \leq 0.1 \tag{135}$$

where, $$\Delta\sigma_c = \sigma_m - \sigma_c \qquad and \qquad \Delta\sigma_m = \sigma_f - \sigma_m \tag{136}$$

If (after analysis it is found that) power singularity exists, the stresses are meaningless and mesh refinement is not required. However, if logarithmic singularity is present, mesh refinement may produce meaningful results. Logarithmic singularity is the weakest type of stress singularity [178, 179]. Sinclair also demonstrated that numerical singularity can be found by analyzing the percentage change in peak stresses with successive mesh refinements [180]. If the graph of percentage change converges with mesh refinements then no singularity is present. This relationship can be expressed as:

$$\text{Percentage change} = \left|\frac{\sigma_{max}^{i+1} - \sigma_{max}^{i}}{\sigma_{max}^{i+1}}\right| \tag{137}$$

4.1.2 Validation of numerical model

The main purpose of numerical modelling is to simulate the laboratory or experimental configuration using different design variables. Therefore, it is important that the numerical model must represent the experimental configuration as closely as possible. For simple geometries, analytical solutions for contact surfaces are already available in the literature. The analytical solutions are generally derived with some simple assumptions. The example of Hertzian contact solution is already given in Chapter 2, Theoretical background. Before implementation of damage models for analysis of crack nucleation, it is therefore important to verify the numerical model using analytical solution.

The analytical and numerical solution can be compared for a representative loading cycle shown in Figure 34. A sample case is presented here. The normal load, P, was applied as a constant pressure whereas tangential load, Q, and axial stress, σ_A, were applied in a cyclic manner. By taking P = 6994 N, Q = 2377.9 N, σ_A = 113.1 MPa and pad radius, R=178 mm, the analytical and numerical results were compared. Material of both parts was taken as Al 2024-T351, with a coefficient of friction μ of 0.65 at the interface. To analyse the accuracy of numerical model, the analytical and numerical semi contact widths, a, and shear traction profile were compared using half space models. For this case, the a_{anal} was found as 1.74 mm, in comparison to a_{FEM} as 1.76 mm. The a_{anal} was obtained using Eq. (10), whereas a_{FEM} was obtained from numerical results of shear traction at the contact interface.

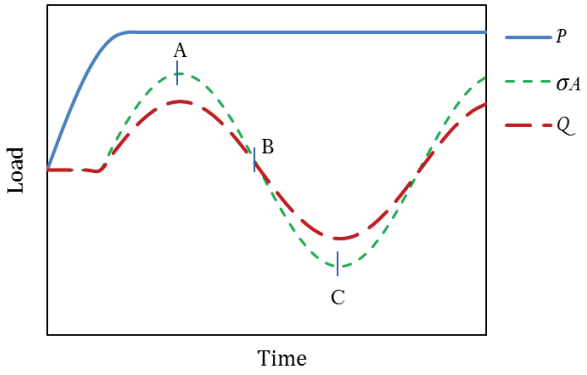

Figure 34. Representative loading sequence.

The shear traction profile was determined using Eq. (22) and numerical results were extracted for limits between $-a$ and $+a$ at the contact interface. The result of the shear traction was taken at instant A, since the applied loads are maximum at this instant. The numerical results of shear traction, $q(x)$, are compared with those obtained using analytical solution for different mesh sizes as shown in Figure 35 (a). The mesh sizes of 5, 10, 20 and 40 µm were used. It can be seen that, even with coarsest mesh, the profile at the contact interface is similar to that obtained using analytical solution. However, the peak values at the boundary of slip-stick zone is affected by mesh sizes. The finer the mesh size, the closer the result to the analytical solution and at 5 µm the error in peak shear traction is less than 2%. This convergence of peak shear traction is shown in Figure 35 (b). Due to this reason the mesh size of 5 × 5 µm is used in the present work. The results of semi contact width and shear traction shows good correlation between numerical and analytical results.

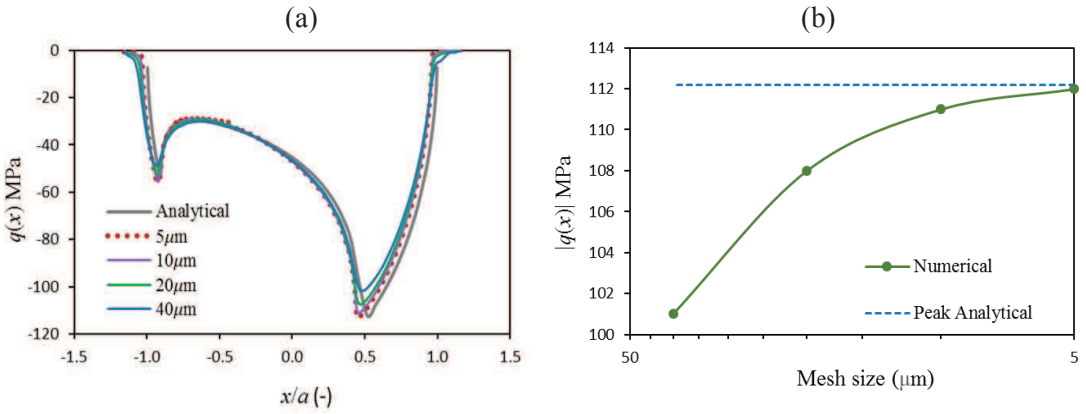

Figure 35. Effect of mesh refinement on (a) shear traction profile (b) peak shear traction.

The presence of contact introduces non-linearity in the problem and this can be seen in load-displacement curve. Figure 36 shows the effect of different mesh sizes on load displacement curve, which are plotted for step A and B of the loading cycle. The load (F) and displacement (Uy) was measured at the centre of the contact i.e. at specimen's top surface. From the graph, it can be seen that load-displacement profile is non-linear. Figure 36 (b) is the exaggerated view of Figure 36 (a) for the first few sub-steps. A change in slope of load displacement curve can be seen at initial steps in Figure 36 (b) i.e. at the time, when contact was established. A second change in slope can be seen in Figure 36 (a), when the axial loads were applied. Once again, different mesh sizes have shown variation in load displacement curve. The coarser the mesh, the higher the value of load, at particular point, is observed. This also shows the significance of appropriate mesh size for fretting fatigue problems.

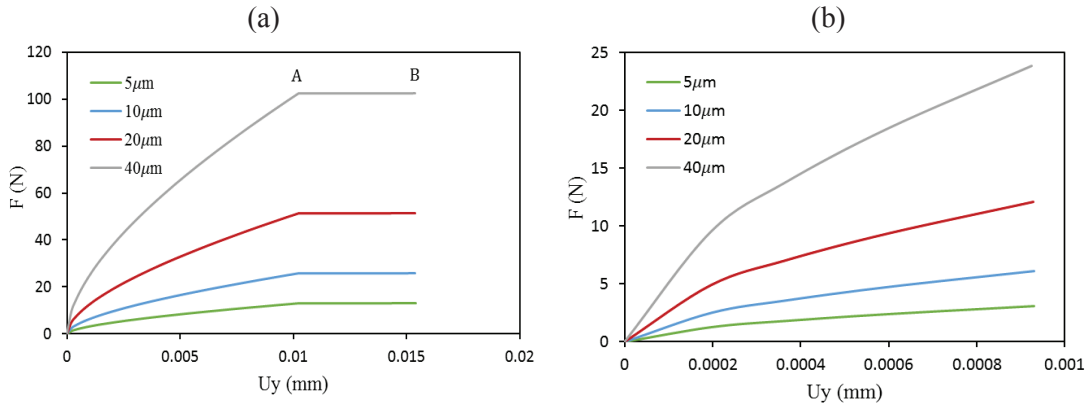

Figure 36. Effect of mesh refinement on (a) load displacement (F-Uy) curve for step A and B (b) exaggerated view of initial few sub-steps of step A.

4.2 Mathematical modelling

As mentioned in *chapter* 3, there are various approaches that can be applied to study crack nucleation behaviour. These include critical plane approach (CP), stress invariant approach (SI), fretting specific parameters and continuum damage mechanics approach (CDM). Out of these approaches the first three are formulated based on experimental observations and involves no derivation. Only the damage models based on CDM approach are derived on the basis of thermodynamic principles. The current section, therefore, only presents the derivation of damage models, based on CDM, that are used in this study. First, the derivation of damage equivalent stress criterion is presented, which is used to determine crack initiation location for CDM approach. It also provides the basis for derived damage models. Later on, damage model derived by Hojjati-Talemi and Abdel Wahab and its modified model for non-proportional loading of the present work, are presented.

4.2.1 Damage equivalent stress criterion

The primary variable, which governs the damage phenomena is the strain energy density release rate, $-Y$, which is a function of total elastic strain energy density, w_e, and damage, D [40, 156]. w_e is the sum of shear energy and volumetric energy.

$$-Y = \frac{w_e}{1-D} \tag{138}$$

$$w_e = \int \sigma_{ij}^d \, d\varepsilon_{ij}^{e,d} + \delta_{ij}\delta_{ij} \int H \, d\varepsilon_e^h \tag{139}$$

where, σ_{ij}^d and ε_{ij}^d are deviatoric stress and strain, respectively. H and ε_e^h are the hydrostatic stress and strain, respectively. δ_{ij} is the Kronecker delta. The linear elastic and isotropic law in conjunction with damage can be expresses as:

$$\varepsilon_{ij}^{e,d} = \frac{1+\nu}{E}\left(\frac{\sigma_{ij}^d}{1-D}\right) \tag{140}$$

$$\varepsilon_e^h = \frac{1-2\nu}{E}\left(\frac{H}{1-D}\right) \tag{141}$$

$$w_e = \frac{1}{2}\left[\frac{1+\nu}{E}\left(\frac{\sigma_{ij}^d \sigma_{ij}^d}{1-D}\right) + 3\frac{1-2\nu}{E}\left(\frac{HH}{1-D}\right)\right] \tag{142}$$

The von Mises equivalent stress, S, can be defined as:

$$S = \left(\frac{3\,\sigma_{ij}^d \sigma_{ij}^d}{2}\right)^{1/2} \tag{143}$$

Eq. (138) can becomes:

$$-Y = \frac{S^2}{2E(1-D)^2}\left[\frac{2}{3}(1+\nu) + 3(1-2\nu)\left(\frac{H}{S}\right)^2\right] \tag{144}$$

$$-Y = \frac{S^2}{2E(1-D)^2} R_\nu \tag{145}$$

where,
$$R_\nu = \frac{2}{3}(1+\nu) + 3(1-2\nu)\left(\frac{H}{S}\right)^2 \tag{146}$$

The damage equivalent stress σ^* is defined as the uniaxial stress, which gives the same amount of elastic strain energy as a multiaxial state of stress [156]. The damage equivalent stress is

analogous to plastic equivalent stress. This implies that for $S = \sigma^*$, H=S/3 and R_v=1, the damage equivalent stress can be written as:

$$w_e(\sigma^*) = w_e(S) = -Y(1-D) \tag{147}$$

$$\frac{\sigma^{*2}}{2E(1-D)^2} = \frac{S^2 R_v}{2E(1-D)^2} \tag{148}$$

$$\sigma^* = S(R_v)^{1/2} \tag{149}$$

This shows that damage equivalent stress, which incorporates the effect of damage, is different from von Mises stress by a factor, R_v, the triaxiality function. The von Mises stress can be used to determine plastic stress state, which occurs mainly due to slips at molecules level. The above expression allows to interpret that nucleation is mainly caused due to the shear in plastic slip bands and damage is driven due to the influence of triaxiality function. Damage is the debonding from atomic level to mesoscale level. The damage equivalent stress, σ^*, includes the triaxiality function R_v, in addition to von Mises stress S, which makes it suitable to apply for multiaxial cases. For non-proportional or out of phase loading, the triaxiality function varies with time.

The triaxiality function, R_v, includes the ratio of volumetric and distortion stresses, which is known as stress triaxiality ratio in terms of CDM. The change in stress ratio determines the amount of non-proportionality. It also has the similarity with CP approach, where normal and shear components are used in the multiaxial damage parameters. The contribution of each component influences the generation of slip bands and hence damage initiation. It affects the amount of plastic strain a material may undergo before failure or in other words it determines the brittleness or ductility of the material. Higher stress triaxiality implies that material will behave in a more brittle manner. R_v is also a function of Poisson's ratio and for most cases when Poisson's ratio decreases, R_v increases [40, 58].

4.2.2 CDM for Proportional Loading (CDM-PL)

In this section the CDM model introduced by Lemaitre [40] and extended by Hojjati-Talemi and Abdel Wahab [165] is presented. They applied the damage model (CDM-PL) successfully for fretting fatigue damage initiation cases. However, this model assumes that the triaxiality function does not vary with time. The dissipation potential function φ, which combines strain energy release rate and damage variable can be written as [40, 165]:

$$\varphi = \frac{C}{(s_o/2)+1}\left(\frac{-Y}{C}\right)^{(s_o/2)+1}(-\dot{Y}) \tag{150}$$

where, C is the damage strength of the material, s_o is the damage exponent and $-Y$ is the strain energy density release rate. By differentiating Eq.(150) and assuming linear accumulation of strain energy with respect to time ($\dot{Y}$=constant), the damage evolution can be written as:

$$\dot{D} = -\frac{\partial \varphi}{\partial Y} = \left(\frac{-Y}{C}\right)^{\frac{s_o}{2}} (-\dot{Y}) \tag{151}$$

Differentiating Eq. (145) with respect to time gives:

$$-\dot{Y} = \frac{2S\dot{S}R_v}{2E(1-D)^2} \tag{152}$$

Inserting Eqs. (145) and (152) in Eq. (151) and simplifying, the result becomes:

$$\dot{D} = \alpha \left(\frac{S^{s_o+1} {R_v}^{(s_o/2)+1}}{(1-D)^{s_o+2}}\right) \dot{S} \tag{153}$$

where,
$$\alpha = \frac{2}{C^{s_o/2}(2E)^{(s_o/2)+1}} \tag{154}$$

Assuming the variation of $(1-D)$ and triaxiality function within a cycle is negligible, integrating Eq. (153) leads to:

$$\frac{\partial D}{\partial N} = \int_{t_1}^{t_2} \dot{D} dt = \int_{t_1}^{t_2} \alpha \frac{S^{s_o+1} {R_v}^{(s_o/2)+1}}{(1-D)^{s_o+2}} \dot{S} dt \tag{155}$$

$$\frac{\partial D}{\partial N} = \frac{\alpha {R_v}^{(s_o/2)+1}}{(1-D)^{s_o+2}} \int_{S_m}^{S_M} S^{s_o+1} dS \tag{156}$$

$$\frac{\partial D}{\partial N} = A \frac{\left(S_M^{s_o+2} - S_m^{s_o+2}\right)}{(1-D)^{s_o+2}} {R_v}^{(s_o/2)+1} \tag{157}$$

where, $A = \alpha/(s_o+2)$, S_M and S_m are the maximum and minimum von Mises stresses. By integrating Eq. (157) and applying $N = 0 \rightarrow D = 0$, the damage variable can be expressed as:

$$D = 1 - \left[1 - A(s_o+3)\left(S_M^{s_o+2} - S_m^{s_o+2}\right) {R_v}^{(s_o/2)+1} N\right]^{1/(s_o+3)} \tag{158}$$

At $N=N_i \rightarrow D=1$, the number of cycles to crack initiation can be written as:

$$N_i = \frac{1}{A(s_o+3)\left(S_M^{s_o+2} - S_m^{s_o+2}\right) {R_v}^{(s_o/2)+1}} \tag{159}$$

The material parameters A, s_o and C are material and temperature dependent, usually estimated experimentally through SN curves and tensile tests. Generally speaking, elevated temperature accelerates the crack or void nucleation process and causes a decrease in material strength. Experimental results have shown that at the same stress level, higher temperature causes earlier failure than lower temperature [58, 154]. For the present work, material parameters were found by applying non-linear regression analysis, to find best least square fit between experimental and numerical values. The numerical results, therefore, may improve if material constants are found experimentally. It is also pertinent to mention here that the critical value of damage variable D was taken as 1, at which the crack initiation takes place since most of the data found in high cycle fatigue regime. For HCF, plasticity effects are generally neglected.

4.2.3 CDM for Non-Proportional Loading (CDM-NPL)

The fatigue damage model proposed by Lemaitre was based on triaxiality function and von Mises stress range, which was extended by Hojjati Talemi and Abdel Wahab as mentioned above. The previous work however was based on the assumption that triaxiality function does not vary with time. Since under non-proportional or out of phase loading conditions, it may vary with respect to time, in the present work the damage evolution law is extended for the case of non-proportional loading (CDM-NPL) [181], by considering the variation of triaxiality function. The dissipation potential function φ can be written as [40]:

$$\varphi = \frac{C}{s_o + 1}\left(\frac{-Y}{C}\right)^{s_o+1}(-\dot{Y}) \tag{160}$$

$$\dot{D} = -\frac{\partial \varphi}{\partial Y} = \left(\frac{-Y}{C}\right)^{s_o}(-\dot{Y}) \tag{161}$$

Considering the variation of both S and R_v with respect to time, differentiating Eq. (145) using product rule leads to:

$$-\dot{Y} = \frac{2S\dot{S}R_v + S^2\dot{R_v}}{2E(1-D)^2} \tag{162}$$

Inserting Eq. (145) and Eq. (162) in Eq. (161), the damage evolution can be rewritten as:

$$\dot{D} = \left(\frac{S^2 R_v}{C2E(1-D)^2}\right)^{s_o}\left(\frac{2S\dot{S}R_v + S^2\dot{R_v}}{2E(1-D)^2}\right) \tag{163}$$

$$\dot{D} = \frac{\alpha\left(2S^{2s_o+1}{R_v}^{s_o+1}\dot{S} + S^{2s_o+2}{R_v}^{s_o}\dot{R_v}\right)}{(1-D)^{2s_o+2}} \tag{164}$$

where,
$$\alpha = \frac{1}{C^{s_o}(2E)^{s_o+1}} \tag{165}$$

Integrating Eq.(164) and assuming the variation of $(1-D)$ within a cycle negligible.

$$\frac{\partial D}{\partial N} = \int_{t_1}^{t_2} \dot{D}dt = \frac{\alpha}{(1-D)^{2s_o+2}}\left(\int_{t_1}^{t_2} 2S^{2s_o+1} {R_v}^{s_o+1}\dot{S}dt + \int_{t_1}^{t_2} S^{2s_o+2} {R_v}^{s_o}\dot{R_v}dt\right) \tag{166}$$

Let, $\mathrm{v} = 2(1+v)/3$ and $\mathrm{w} = 3(1-2v)$, Eq. (166) can be written as:

$$\frac{\partial D}{\partial N} = \frac{\alpha}{(1-D)^{2s_o+2}}\left(\int_{S_m}^{S_M} 2S^{2s_o+1}\left(\mathrm{v}+\frac{\mathrm{w}H^2}{S^2}\right)^{s_o+1} dS + \int_{R_{vm}}^{R_{vM}} \left(\frac{\mathrm{w}^{1/2}H}{(R_v-\mathrm{v})^{1/2}}\right)^{2s_o+2} {R_v}^{s_o} dR_v\right) \tag{167}$$

where, R_{vM} and R_{vm} are the maximum and minimum triaxiality function, respectively. According to Lemaitre, for one dimensional damage models $s_o \simeq 1$ [156, 182]. Simplifying Eq. (167), the result leads to:

$$\frac{\partial D}{\partial N} = \frac{\alpha\left[0.5\mathrm{v}^2(S_M^4 - S_m^4) + 2\mathrm{w}^2H^4 ln\left(\frac{S_M}{S_m}\right) + 4\mathrm{vw}H^2(S_M^2 - S_m^2) + \mathrm{w}^2H^4(R_M - R_m)\right]}{(1-D)^4} \tag{168}$$

where, R_M and R_m are the maximum and minimum values of R which is a function of R_v and can be expressed as:

$$R = \ln(R_v - \mathrm{v}) - \frac{\mathrm{v}}{(R_v - \mathrm{v})} \tag{169}$$

By integrating Eq. (168) and applying initial conditions i.e. at N=0 → D=0, the damage variable D can be written interms of number of cycles.

$$D = 1 - \left[1 - 5\alpha\left\{0.5\mathrm{v}^2(S_M^4 - S_m^4) + 2\mathrm{w}^2H^4 ln\left(\frac{S_M}{S_m}\right) + 4\mathrm{vw}H^2(S_M^2 - S_m^2) + \mathrm{w}^2H^4(R_M - R_m)\right\}N\right]^{1/5} \tag{170}$$

By applying crack initiation condition i.e. at N=N_i→ D=1, the expression for number of cycles to crack initiation can be written as:

$$N_i = \frac{1}{5\alpha\left[0.5\mathrm{v}^2(S_M^4 - S_m^4) + 2\mathrm{w}^2H^4 ln\left(\frac{S_M}{S_m}\right) + 4\mathrm{vw}H^2(S_M^2 - S_m^2) + \mathrm{w}^2H^4(R_M - R_m)\right]} \tag{171}$$

Here, α is only unknown material parameter and can be found using regression analysis as explained in a later section.

The damage models presented above can be used to estimate number of cycles to crack initiation. However it is pertinent to mention its assumptions and limitations for appropriate application.

- The dissipation potential function is mainly dependent upon internal energy density release rate. For brittle or quasi brittle failure, damage is mainly governed by internal friction of the material. Although micro plasticity may exist, it is neglected here. Therefore, it is suitable for HCF regime only.
- The model is applicable where stress levels do not change with number of cycles to failure. This implies that cyclic plasticity and wear effects are not taken into account. Furthermore, the coefficient of friction is assumed to remain constant with time.
- The damage variable represents 1D damage. The case of isotropic damage is considered, where it is assumed that same damage will be caused in all directions. For anisotropic damage, this scalar variable becomes a tensor and damage may be different in different directions.
- Damage evolution is computed based on concept of effective stress and hypothesis of strain equivalence. According to this principal, strain behaviour of a damaged body can be estimated from a virgin material by simply replacing stress with effective stress. This implies that the effect of neighbouring damage is not considered in constitutive equations. In addition, the effective stress is computed for tension behaviour and no distinction is made between tension and compression cycle. In other words, crack closure effect is not considered.
- Coupling between elasticity and plasticity is not considered. To incorporate the effect of plasticity, state potential and dissipation potential function needs to be modified.
- The damage phenomenon is considered to be isothermal, i.e. effect of temperature change is not considered.

4.3 Implementation of damage models

This section illustrates the implementation of various damage modelling approaches that can be employed for analysis of crack nucleation. The implementation of each approach i.e. critical plane, stress invariant, fretting specific parameters and CDM approach is described by choosing one representative damage parameter. To model fretting fatigue condition with cylindrical pad and flat specimen, the numerical model was built and solved using ABAQUS, which employs Newton's method to solve non-linear system of equations iteratively. Once the contact problem was solved, damage models were then implemented in post processing. The post processing was completed using MATLAB code.

4.3.1 Implementation of CP approach

To explain the implementation of critical plane approach, a sample procedure is shown in Figure 37, for calculation of Findley parameter (FP). The first step was to solve the contact problem for any data set using numerical model. After completion of contact analysis, stress and

strain data was written in text files for each step during the loading cycle. To find the highest value of the damage parameter and orientation of critical plane, MATLAB code was written. Stored data was then read in MATLAB code for the nodes at the contact interface from $-a$ to a, where a represents semi-contact width. The MATLAB code first read the shear stresses for node 1 at maximum and minimum load during the cycle. The normal stress was taken at instant A during the loading cycle, as it gives maximum value during the loading cycle, even for out of phase loading condition. Then Mohr's circle transformation equations were applied to find stresses at the rotated planes from -90° to 90° with an increment of 1°.

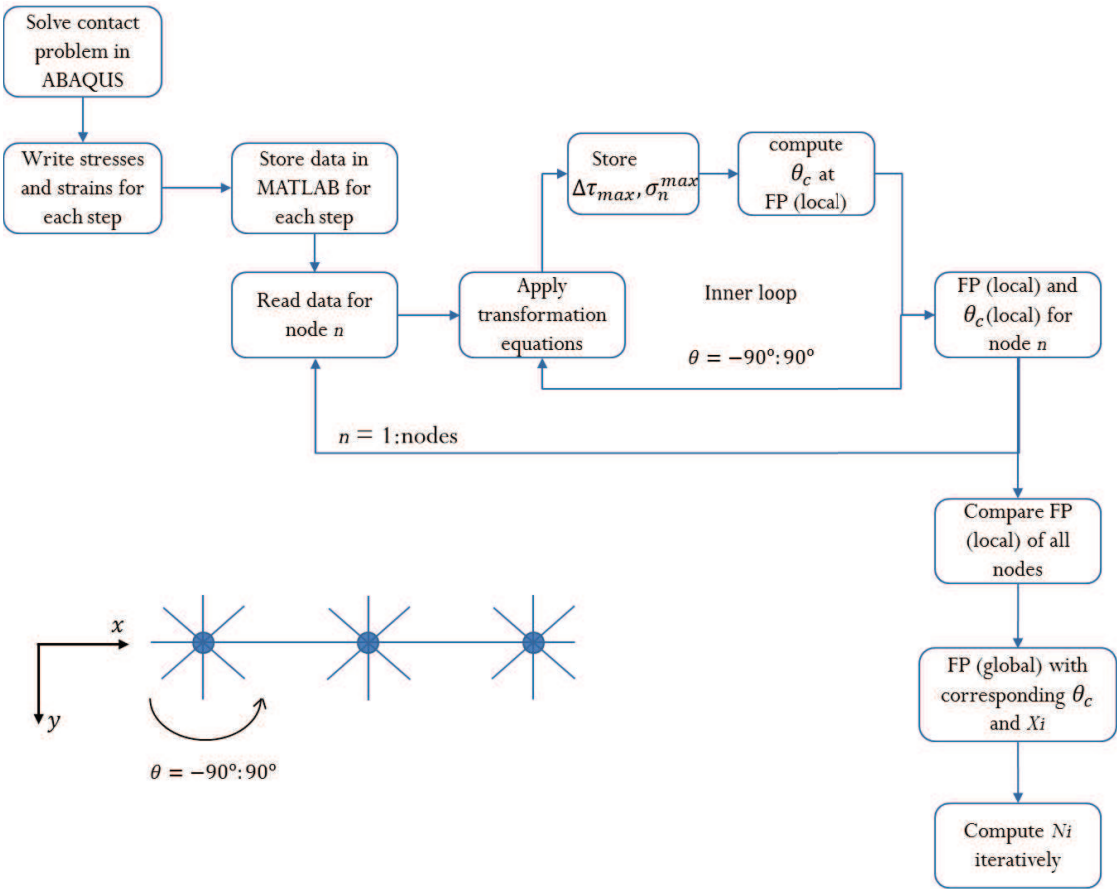

Figure 37. Schematic for implementation of critical plane approach (FP parameter).

The stresses and strains at rotated planes were found as follows:

$$\sigma_x' = \frac{\sigma_x + \sigma_y}{2} + \frac{\sigma_x - \sigma_y}{2} cos2\theta + \tau_{xy} sin2\theta \tag{172}$$

$$\tau_{x'y'} = -\frac{\sigma_x - \sigma_y}{2} sin2\theta + \tau_{xy} cos2\theta \quad (173)$$

$$\varepsilon'_x = \frac{\varepsilon_x + \varepsilon_y}{2} + \frac{\varepsilon_x - \varepsilon_y}{2} cos2\theta + \frac{\gamma_{xy}}{2} sin2\theta \quad (174)$$

$$\gamma_{x'y'} = -\frac{\varepsilon_x - \varepsilon_y}{2} sin2\theta + \frac{\gamma_{xy}}{2} cos2\theta \quad (175)$$

where, subscript x and y represent the Cartesian coordinates and x', y' represent the rotated coordinates.

For each of the rotated plane, shear stress range and normal stress was calculated to give a value of FP. For this node, values of all FP were compared and the angle with the highest value of FP was stored as local critical angle and parameter as local FP. Then, data for the next node was read and same procedure was applied to compute all local FP. Once all nodes were evaluated, then all local FP were compared to find global or maximum FP and the corresponding node and angle were stored as damage initiation location, X_i and critical plane, θ_c. Once the maximum value of the FP was known, Eq. (93) was iteratively solved to determine the crack initiation life.

All other damage criteria were evaluated in the same way, where the value of the whole damage parameter was maximized to determine the orientation of critical plane, except Liu parameter. For Liu 1, critical plane was determined as the plane where tensile work was maximum and then adding the shear work on the same plane. Similarly, for Liu 2 critical plane was determined by maximizing the shear work and then tensile work was added to it at same orientation.

4.3.1.1 Determination of stress strain ranges

The evaluation of all damage parameters requires calculation of different stress and strain ranges. This section explains these calculations for in-phase and out-of-phase loading conditions. Before going into the detail of stress strain ranges, the description of phase difference is explained. A sample schematic of the phase difference between applied loads is shown in Figure 38. Considering the axial stress σ_A as reference, phase difference is shown for the tangential load Q relatively. The load variation is shown at four different time instants, i.e. A, B, C and D. Both stress ratio R_σ and tangential load ratio R_Q are shown as -1, i.e. the maxima and minima are symmetric about x-axis.

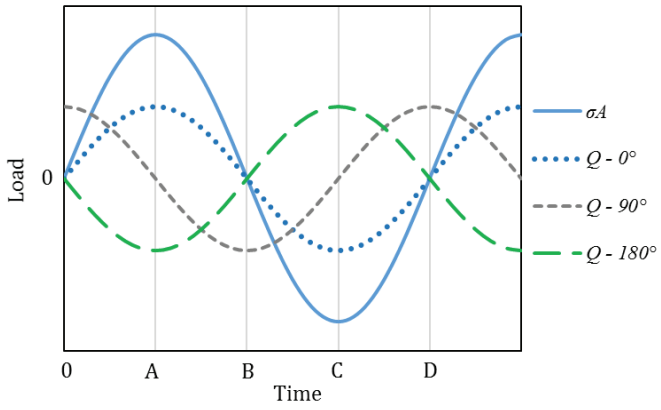

Figure 38. Schematic diagram of 0°, 90°, 180° phase difference between axial stress σ_A and tangential load Q.

For in-phase loading, both axial stress and tangential load attain maximum at point A and minimum at point C during the cycle. Point B is also of interest since the value of both loads change sign at this point. An example is shown here using P = 6176 N, Q = 1667.5N, σ_A = 84.7 MPa and pad radius R=178 mm. The stress ranges were computed at points AB, AC and BC. Figure 39 (a) and (b) present, normal and shear stress ranges at these points during the cycle. The highest stress ranges are observed between point A and C since both loads are at their peaks. Therefore, for computation of damage parameters, values at point A and C were used.

For loading phase difference of 180°, the situation is the same as for in-phase loading since both loads attain the maximum and minimum at the same instants. However, for 90° phase difference, the selection of points for calculation of stress or strain ranges is not very obvious. The axial stress attains its maximum at point A and minimum at C, while tangential load reaches its minimum at point B and maximum at point D. As we are looking for the maximum stress or strain ranges during the complete loading cycle, these ranges at various points during the cycles are required to be compared. As an example, Figure 40 (a) and (b) show the normal and shear stress ranges at some of the points during the cycle. At all other points during the load cycle stress magnitudes were found lower than these points and hence not shown here. It is observed that normal stress or strain ranges are highest between points A and C, whereas shear stress or strain ranges are highest between points B and D. This mismatching of maxima for both stresses calls for the computation of damage parameter using both stress ranges i.e. AC and BD. The points, which gave the highest value of damage parameter, were selected for the computation of critical plane orientation and initiation life.

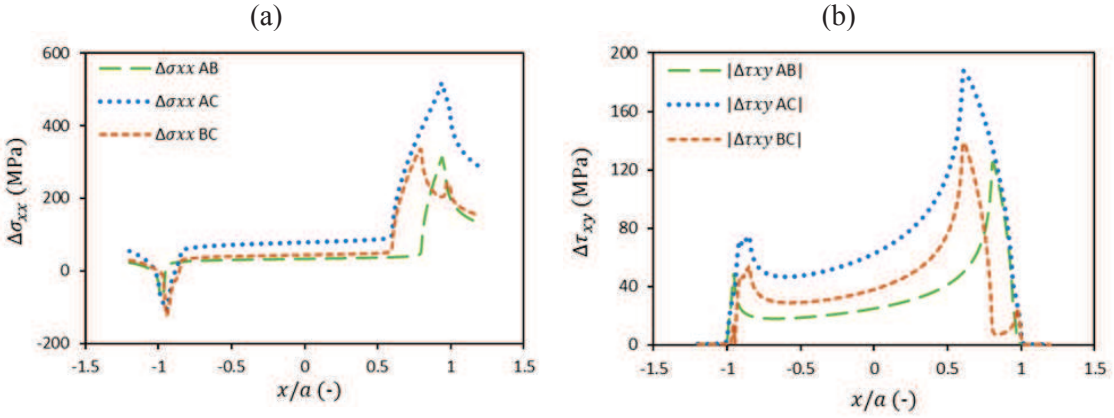

Figure 39. (a) Normal and (b) shear stress ranges, between different points during the load cycle for ∅ = 0°.

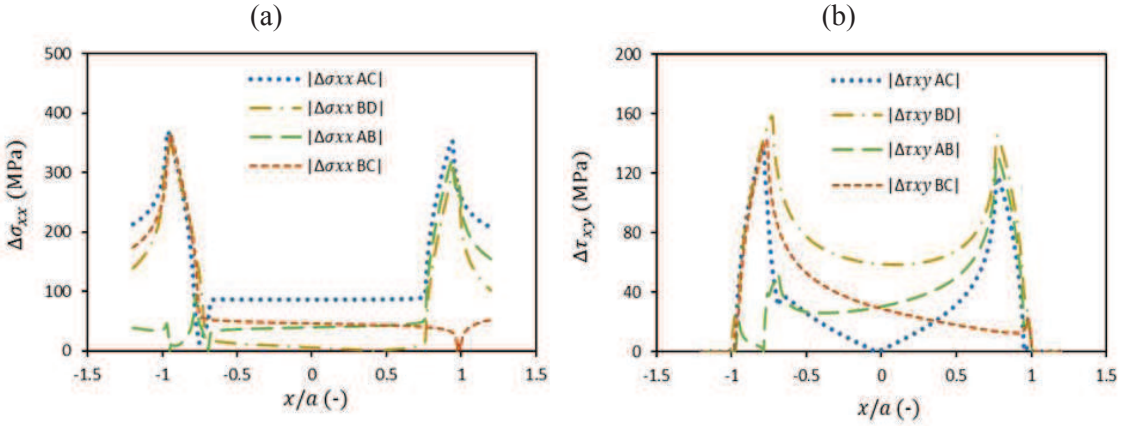

Figure 40. (a) Normal and (b) shear stress ranges, between different points during the load cycle for ∅ = 90°.

4.3.2 Implementation of SI approach

To describe implementation of stress invariant approach, schematic of Crossland (CL) parameter is shown in Figure 41. After contact analysis, the results were stored for the nodes at the contact interface. The second invariant of stress $\sqrt{J_2}$ was stores for both maximum and minimum load during the loading cycle. The hydrostatic stress H_{max} was extracted at the maximum loading condition. The CL parameter was computed at each node at the contact interface. As mentioned earlier, for stress invariant approach there are no preferred (critical) planes and the damage is measured globally in the bulk material. Therefore, damage parameter was computed at the contact interface, without applying Mohr's circle transformation. The point with the maximum value of the damage parameter was taken as crack initiation location and by applying Eq. (113), crack initiation lives were computed.

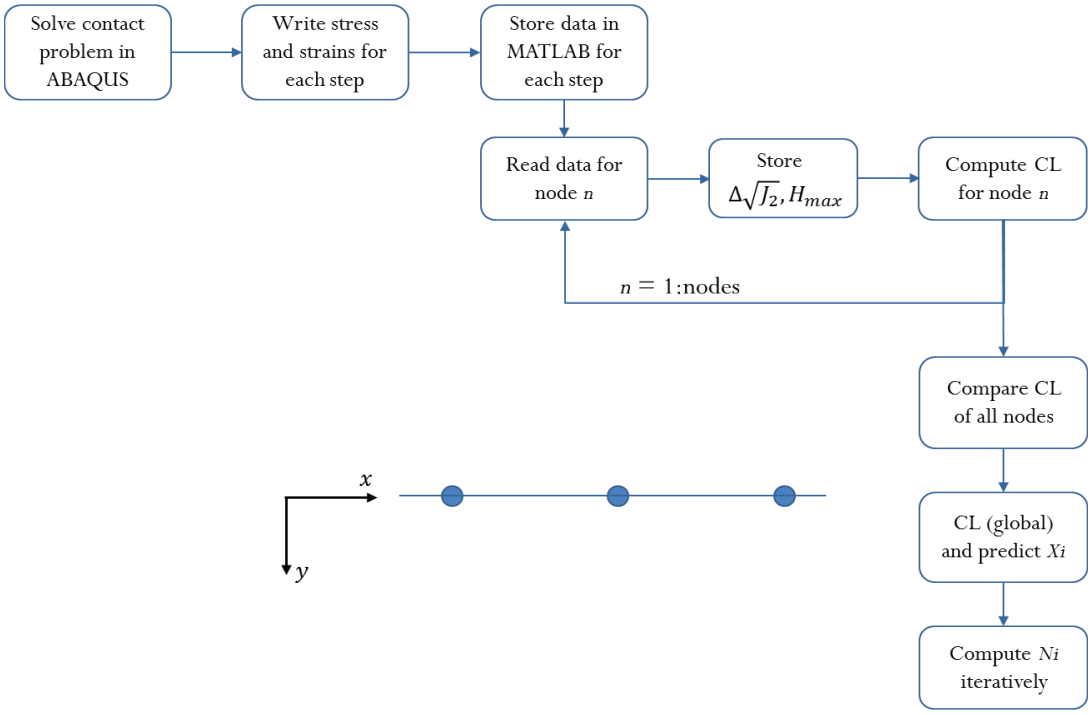

Figure 41. Schematic for implementation of stress invariant approach (CL parameter).

4.3.3 Implementation of Ruiz F2 parameter

The implementation of Ruiz parameters can be demonstrated by schematic diagram of Figure 42. The flow chart is presented for initiation parameter *F*2. The procedure to solve the contact problem and storing the data is same as in the previous two approaches. However, the data extracted is different from the previous approaches, in two ways. Firstly, there are no ranges involve in formulation of initiation parameter. Therefore, all values i.e. shear stress and tensile stress were extracted for maximum loading condition. Secondly, in order to compute the relative displacement between the surfaces, u_1 was extracted as displacement from the specimen's top surface and u_2 from the pad's cylindrical surface that was in contact with the specimen. The difference of the two displacements lead to relative displacement. If the value of the parameter is required for different time instants or with phase difference, same procedure can be adopted to calculate *F*2 parameter. Since *F*2 parameter cannot be related to any stress or strain life equation, therefore, it cannot be used to compute crack initiation life. The point with the highest value of parameter was taken as damage initiation location.

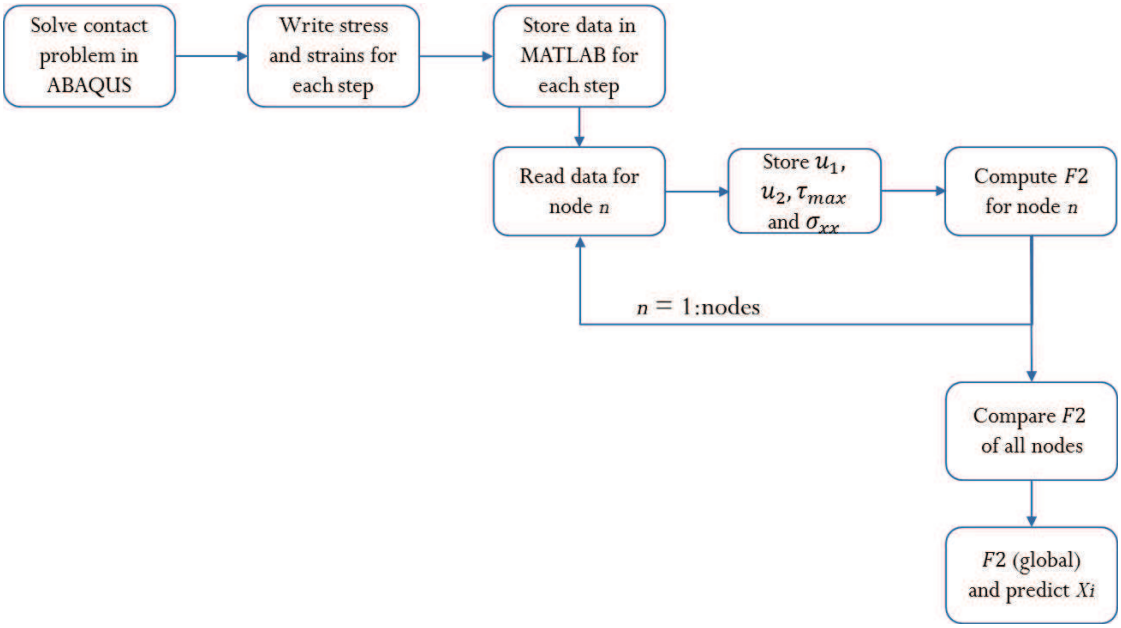

Figure 42. Schematic for implementation of Ruiz *F*2 parameter.

4.3.4 Implementation of CDM approach

The methodology adopted to determine numerical lives using CDM-NPL formulation is described in this section. After solving the contact problem, the required data was stored for the complete loading cycle. First, von Mises and hydrostatic stresses were extracted for the maximum loading condition. Then, maximum equivalent damage stress σ^*_{max} was computed for all nodes at the contact interface. The location with the maximum value of the σ^*_{max} was stored as damage initiation location. At the location of σ^*_{max}, the critical radius for the process zone can be determined using Eq. (129). Araújo and Nowell [114] have shown that critical radius dimension of the order of grain size of material provided good estimation of fatigue life. They proposed critical radius range of 5 µm to 20 µm for Ti-6Al-4V and 20 µm to 80 µm for aluminium. In the present study, the critical radius of 20 µm was used for titanium and 50 µm for aluminium. These critical radii corresponds to the grains size of the material. All required parameters, S_M, S_m, R_{vM} , R_{vm} and average H inside critical radius, were calculated.

The material parameter, α, was estimated by inserting the required values in Eq. (171) and performing non-linear regression analysis. For the case of aluminium, 3 out of 27 data values were used for the estimation of material parameters. However, for the case of titanium only six experimental tests were available, therefore they were used for the estimation of α. By using least

square fit, experimental trend was generated. Choosing the arbitrary value for the unknown constant, numerical results were predicted for the same data set. A similar trend was drawn from numerical results. Using optimization scheme, the error between the two trends was minimized. The constant α was obtained, for which root mean square error (RMSE) was minimum as shown in Figure 43. During the error minimization, both the curves maintain their respective dispersion and trend comes closer to each other by affecting the mean. However, it is interesting to note that the slope of mean trend itself depends upon scatter of the data. The RMSE was obtained using the following equation.

$$RMSE = \sqrt{\frac{1}{n}\sum_{i=1}^{n}\left(N_{exp} - N_{num}\right)^2} \tag{176}$$

Where n is the number of data points used. Once material parameter was found, all the numerical results were predicted. For the case of titanium, the correlation between predicted trend and experimental results is shown in Figure 43.

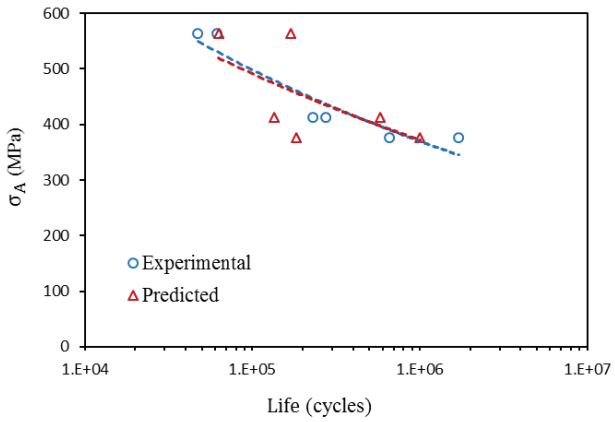

Figure 43. Regression analysis by minimizing error between numerical and experimental data.

The initiation lives were then computed by inserting numerical results and estimated constant into Eq. (171). The methodology for implementation of CDM-PL formulation is also similar. The difference in methodology between the two formulations is that for CDM-NPL the unknown constant is α, whereas for CDM-PL, A and s_0 are estimated using non-linear regression.

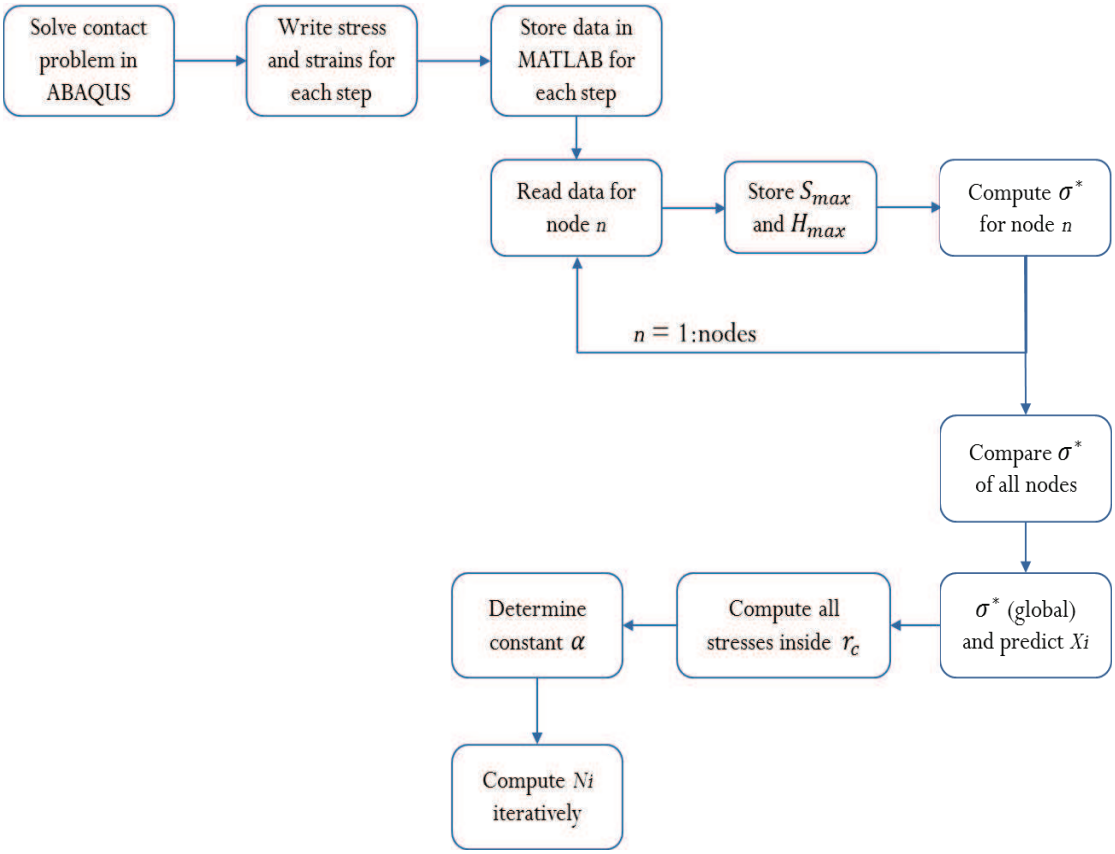

Figure 44. Schematic for implementation of CDM-NPL approach.

4.4 Summary

Fretting fatigue analysis can be performed by using different kinds of boundary conditions. The main difference in these approaches exist in modelling of tangential load at the contact interface. The mesh sensitivity also plays important role, especially at the contact interface due to high stress gradient. Various researchers have used mesh size ranging from 2×2 μm to 25×25 μm. It is also important to analyse the presence of stress singularity at the contact edges. For model verification, a good strategy is to compare numerical results at contact stresses with analytical solution before implementation of damage models.

Most approaches that are being used for modelling of crack nucleation are based on empirical results. These approaches include CP, SI and Ruiz parameters. Whereas, CDM approach is derived on the basis of thermodynamics principles. Similar methodology can be adopted for modelling different approaches. First step is to perform contact analysis and store the required stresses and strains. After contact analysis, post processing can be performed using

MATLAB or Python scripting. The post processing differs according to the damage model, since each damage model requires specific stress or strain components. The implementation of CP approach takes more effort than other approaches, since it requires computation of damage parameters on all possible planes.

Chapter 5

Results and discussion

In this chapter results of various approaches and damage models are presented, that are used in the present work. For analysis of fretting fatigue crack nucleation, several aspects are discussed, however the focus of discussion will remain on estimation of crack nucleation location, initial crack orientation and life. Most of the previous work in fretting fatigue crack nucleation is done for in phase loading. The present work therefore focusses on investigation of above mentioned areas under out of phase loading condition. For this purpose, different approaches are used and the results are compared to determine their effectiveness.

The results are divided into six main sections. The first provides basic understanding on variation of contact stress under application of different coefficients of friction and load ratios for in phase loading. The simplest of the parameters i.e. Ruiz parameters is analysed at the contact interface. The second section includes the effect of phase difference on numerical modelling, convergence rate and damage initiation location using Ruiz parameter and SWT critical plane parameters. The third section presents the results for different critical plane models to determine the efficacy to prediction of initiation location, orientation and life. Section four compares critical plane approach with CDM-PL for in phase and out of phase loading. In section five, proposed damage model CDM-NPL is presented and results are compared with experimental results from literature. The last section shows the comparison of critical plane approach and stress invariant approach.

5.1 Variation of contact stresses and Ruiz parameters

Fretting fatigue phenomena occurs due to interaction between contacting bodies under application of cyclic and normal loads. In addition to environmental conditions and material properties, the response at the contact interface highly depends on the combination of applied loads. High stress concentration is present at the contact interface, which can start the damage nucleation process. At the culmination of nucleation process several micro cracks are initiated, ultimately leading to the structural failure. Therefore, the analysis of contact stresses provides basic understanding of the contribution of each stress. In this section, the effect of two important factors, namely coefficient of friction and load ratio, on contact stresses, slip amplitude and damage initiation is studied using finite element analysis. The results are evaluated for Ruiz parameter as it involves the slip amplitude, which is an important factor in fretting fatigue problems.

The experimental data set used in this section is taken from the work presented in [59]. Four selected experiments, shown in Table 8, were used based on different $Q/\mu P$ ratio (μ is coefficient of friction). The pad radius selected was 178 mm. The Aluminium 2024-T351 was used for both specimen and fretting pads. Poisson's ratio, ν, was 0.33 and modulus of elasticity, E, was 74.1 GPa. The value of coefficient of friction was specified as 0.65. The heights of 25 mm

and 6.35 mm were used to model pad and specimen, respectively. Thickness of both fretting pad and the specimen was 12.7 mm. The lengths of fretting pad and specimen were 25 mm and 40 mm, respectively. The geometrical model including loads and boundary conditions is presented in Figure 33. All loads were applied in four steps for one complete loading cycle as shown in Figure 45. The cyclic axial load σ_A and tangential load Q were applied in first step simultaneously, however, the normal load was kept constant for all steps. Both stress ratio R_σ and tangential load ratio R_Q were equal to -1. Crack initiation life was determined by subtracting propagation life from total number of cycles to failures.

Table 8. Selected data from experimental tests.

Exp. Nr.	P (N)	R (mm)	$Q/\mu P$ (-)	σ_A (MPa)	$N_{i,exp}$ (cycles)	$N_{f,exp}$ (cycles)
1	7085	178	0.32	85.2	600638	665073
2	6176	178	0.42	84.7	555830	621442
3	6460	178	0.52	106.4	195200	225535
4	5319	178	0.55	97.4	418911	459882

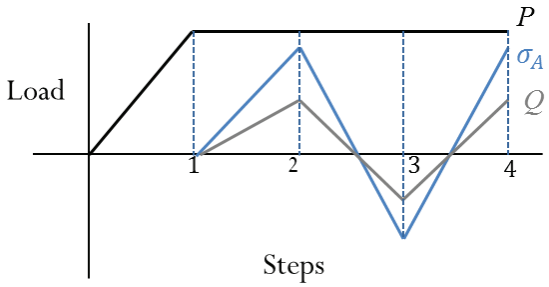

Figure 45. Schematic of loading sequence of one complete cycle.

5.1.1 Effect of COF

The coefficient of friction affects the surface characteristics and hence the nucleation process. Therefore, it is important to analyse its effect on internal stresses and damage parameter. The effect of changing coefficient of friction, μ, on shear traction, q(x), normal stress, p(x), tensile stress, σ_{xx}, and ultimately on the Ruiz parameters $F1$ and $F2$ are shown in Figure 46. Data of the experiment 3 was used and considering the variation of μ, from 0.65 to 0.85, 1.0 and 1.25, the results were computed at the contact interface. The horizontal axis is normalized with semi contact width, a. It was observed that with the increase of μ, the magnitude of maximum shear traction and maximum tensile stress increased, whereas normal stress remained constant. This implies that normal stress is independent of μ. Two peaks of shear traction were observed at the interface of

stick slip zone, however the maximum shear traction and tensile stress was observed at the trailing edge as shown in Figure 46 (a) and (c). It is also interesting to note, in Figure 46 (d), that for any value of coefficient of friction, tensile stress shows the highest value, followed by normal stress and least for shear traction. For the purpose of comparison, the absolute values of the peak stresses were taken. The trend also showed that for further increase in μ the shear traction might surpass the normal stress. The stick zone width also increased with increase of μ as shown in Figure 46 (e), causing a corresponding decrease of slip zones at both ends.

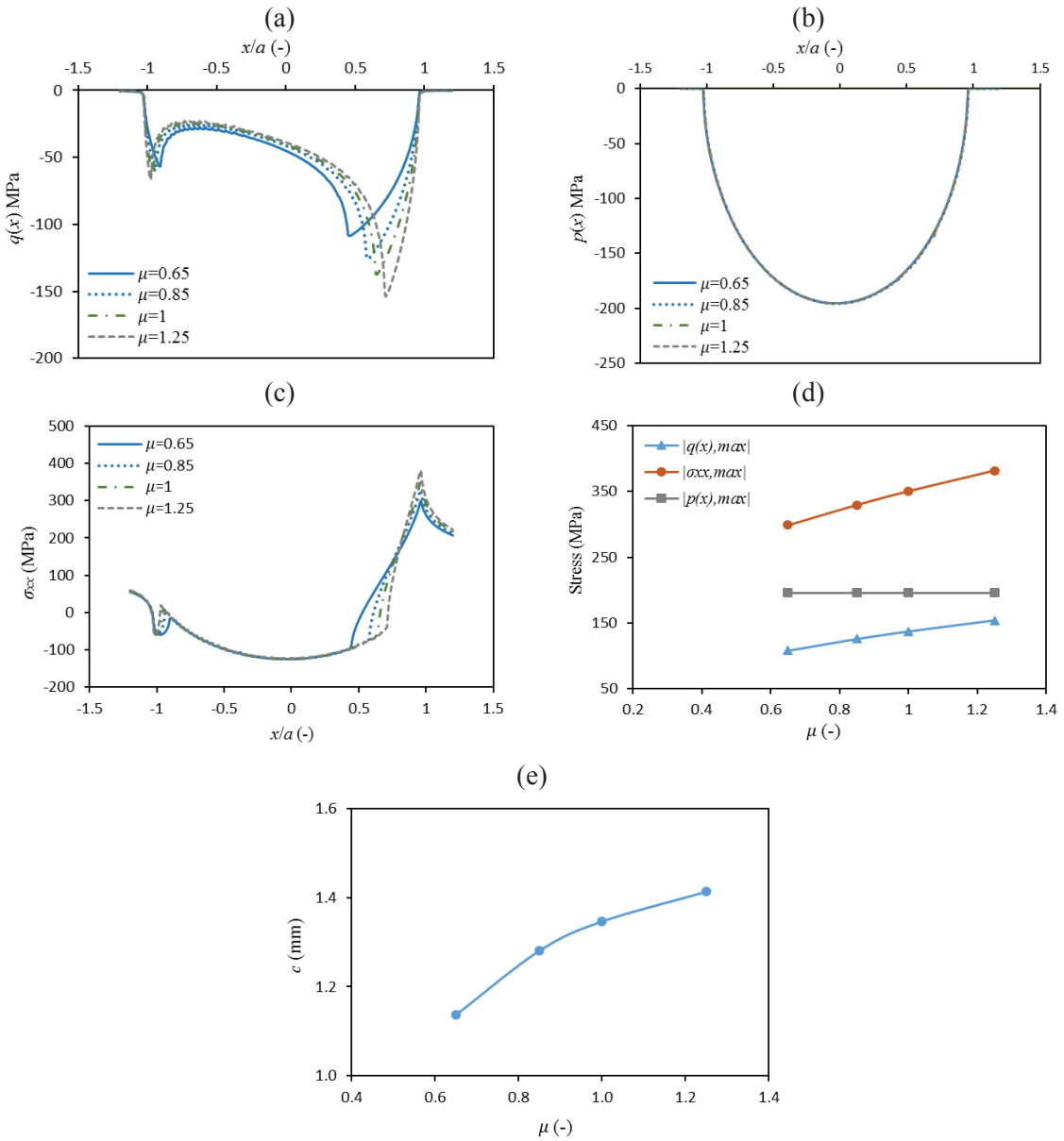

Figure 46. Effect of μ on (a) shear traction $q(x)$, (b) normal stress $p(x)$, (c) tensile stress σ_{xx}, (d) peak stresses (e) semi stick zone width c.

The maximum value of damage and initiation parameters was also observed towards the trailing edge of the contact. The location of wear and initiation parameters $F1$ and $F2$ shifted more towards the trailing edge of the contact with the increase of μ. Although, at all values of μ, the location of damage initiation was in the slip zone of the trailing edge of the contact, there exists subtle variation of $F2$ with variation of μ as depicted in Figure 47 (b). With an increase of μ, the location of maximum damage was shifted from slip zone towards the contact edge x/a = 1, as shown in Figure 47 (c). Furthermore, the peak value increased continuously with as increase in μ, which shows an increase in failure probability.

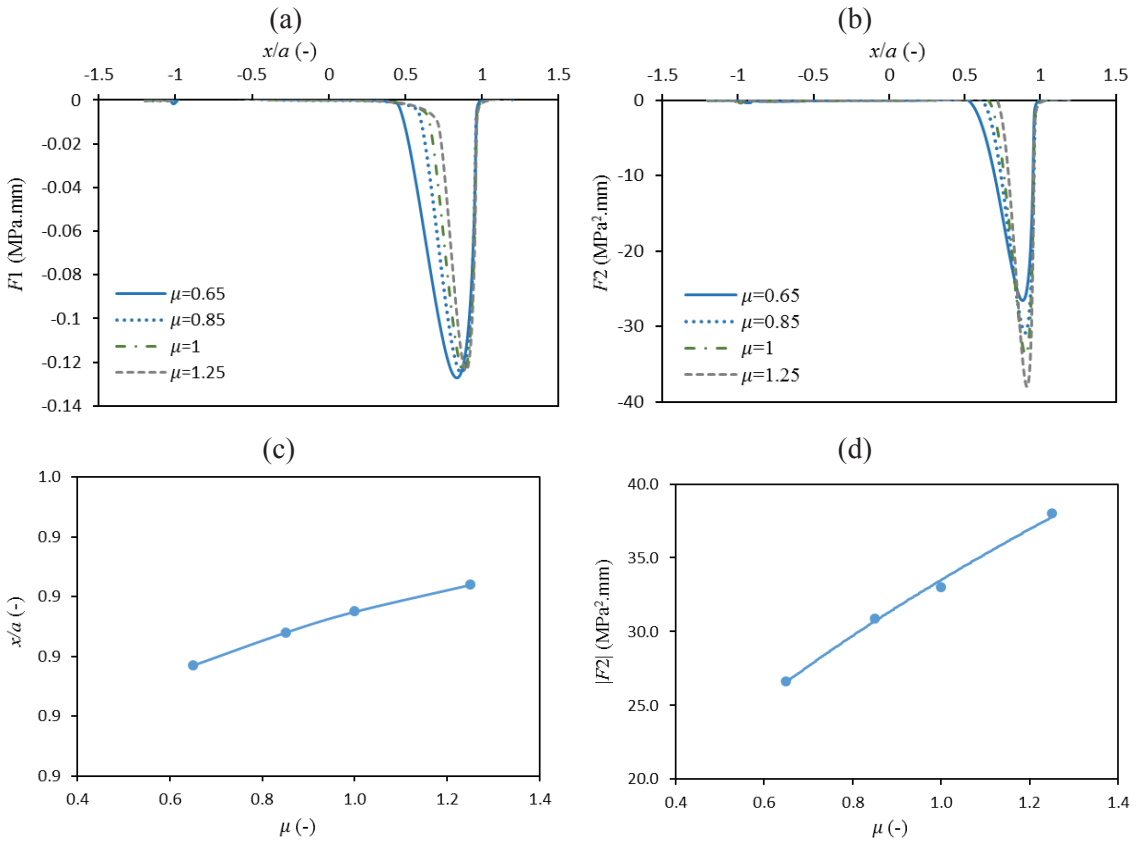

Figure 47. Effect of μ on variation of (a) Ruiz parameter $F1$, (b) $F2$, (c) damage initiation location, (d) peak $F2$.

5.1.2 Effect of Q/fP ratio

To analyse the effect of tangential to normal load ratio, data set of four experiments was used, as stated in Table 8. The coefficient of friction was kept constant at 0.65. Figure 48 shows the effect of variable $Q/\mu P$ on stresses and damage parameters.

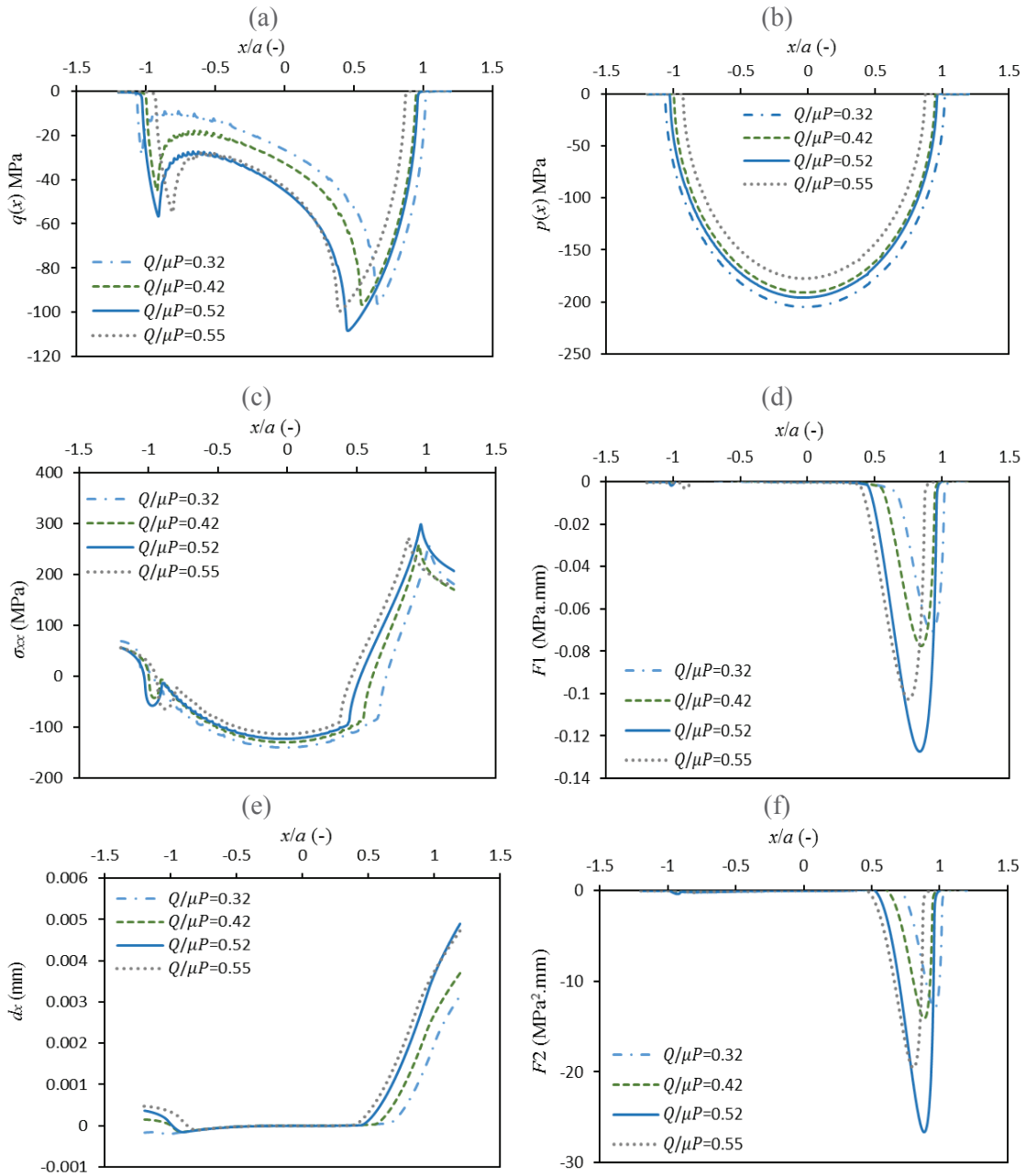

Figure 48. Effect of $Q/\mu P$ on (a) shear traction $q(x)$, (b) normal stress $p(x)$, (c) tensile stress σ_{xx}, (d) Ruiz parameter $F1$, (e) Relative displacement d_x (f) Ruiz parameter $F2$.

From Figure 48 (a) it can be seen that the stick and slip zone widths changes with changing load ratios. The magnitude of maximum shear traction and locations for maximum shear tractions were also different for all cases. For lower values of $Q/\mu P$, larger stick zone width was observed and vice versa. This implies that stick zone width is inversely proportional to $Q/\mu P$.

However, peak of the shear traction was directly linked with the axial stress. The experiment with the highest value of applied axial stress showed the highest peak for shear traction. Same is true for the tensile stress as depicted in Figure 48(c). The normal stress directly depends on magnitude of normal load as shown in Figure 48(b). The higher the magnitude of normal load, higher the normal stress was found, whereas no uniform pattern was observed with $Q/\mu P$.

The relative displacement was computed for each case and it is observed, in Figure 48(e), that outside the stick zones the relative displacement amplitude increased with increase of $Q/\mu P$. It is also intuitive because higher tangential load will produce larger slip between the contacting bodies. The values of Ruiz parameters calculated are shown in Figure 48 4(d) and 4(f) and for all cases peaks were observed at the trailing side of the contact. Since the damage parameter is dependent on shear traction and relative slip, higher values of $F1$ and $F2$ were found for the experiment with larger shear tractions.

Moreover, it was observed that for lower values of $Q/\mu P$, the initiation parameter was predicted more towards the trailing edge. Figure 49 shows the trend for variation of locations for maximum values of $F2$ parameter, normal stress, tensile stress and shear traction against $Q/\mu P$. It can also be interpreted that the magnitude of damage and initiation parameters depend on individual loads, whereas the location depends more on the ratio $Q/\mu P$.

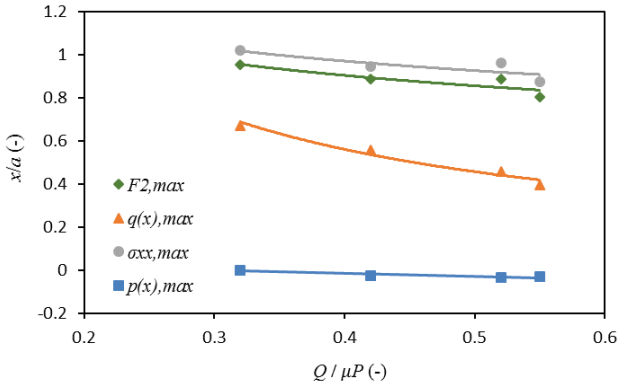

Figure 49. Variation of peak stresses and $F2$ parameter with $Q/\mu P$.

5.1.3 Variation of experimental initiation life with F2

In this section, the results of the current numerical work are combined with the experimental results, since $F2$ parameter cannot be used to determine lives numerically. The stresses shown above were computed at the contact interface only, as in fretting fatigue damage initiates at the surface. It was observed that when the initiation parameter $F2$ was higher, the number of cycles to initiation was lower. It is also logical and intuitive to expect the decrease in

damage initiation life on increase of damage parameter. The variation of $F2$ parameter versus cycle to initiation is presented in Figure 50(a). However, this trend may be dependent on material properties. Lykins et al. [115] used this parameter for titanium alloy Ti-6Al-4V and found no specific correlation between $F2$ parameter and number of cycles to initiation. Figure 50(b) shows the relationship between peak stresses and number of cycles to initiation. For cases with higher number of cycles to initiation, lower value of shear tractions and tensile stresses were observed while no specific trend was observed for normal stresses. For comparison purposes absolute values are plotted for each case. It was observed that for all experiments normal stresses were higher than shear tractions and tensile stresses were higher than normal stress.

Considering the above discussion and the experimental results presented in [59] (showed that the failure occurred in the direction perpendicular to the specimen axis), it can be said that the peak in the tensile stress at the trailing edge of the contact is the primary reason that energies damage initiation to failure for the cases, where failure occurs in mode I.

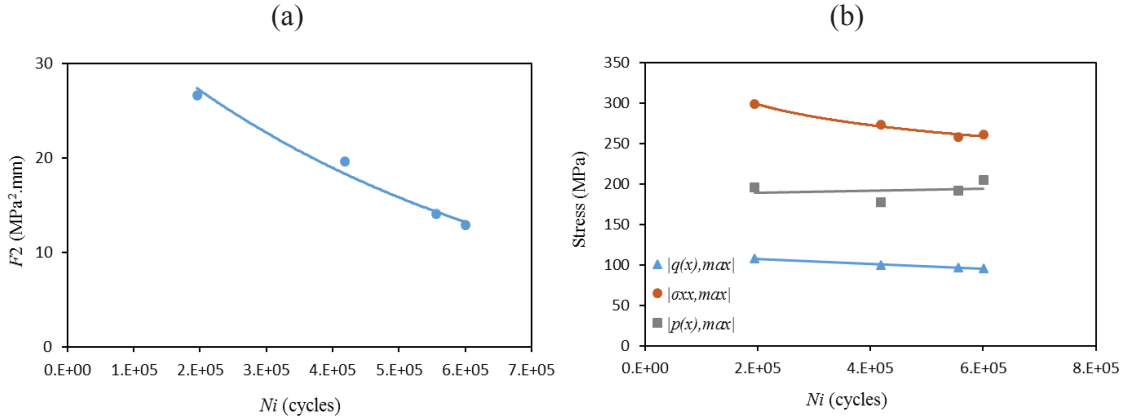

Figure 50. Variation of number of cycles to failure with (a) $F2$ parameter (b) absolute values of maximum tensile stress σ_{xx}, normal stress $p(x)$ and shear traction $q(x)$.

5.2 Loading phase difference

The phenomenon of fretting fatigue is influenced by many factors, such as slip amplitude, coefficient of friction, loading magnitudes and ratio, etc. Apart from loading magnitude, sequence of the loads may also play important role on crack nucleation location, orientation and life. In the proceeding sections, the effect of phase difference, ∅, on various crack nucleation aspects are discussed, which is also the main objective of the present work.

This section is mainly divided into two sections. In the first half, three numerical models are used to model effect on contact stresses and damage initiation locations for both in phase and

out of phase loading. Three phase difference angles are considered i.e. 0°, 90° and 180° for this purpose. The numerical models are also compared based on number of iterations required for convergence. In the second half, SWT parameter (which belongs to critical plane approach) and Ruiz parameter are adopted as two crack initiation criteria to investigate their performance in case of out of phase loading. In short, this section answers the following three research questions. In case of phase loading difference: 1) What are the best way to apply boundary conditions in fretting fatigue finite element simulations? 2) What is the effect of phase loading on contact stresses? And 3) what is the most suitable parameter that can be used to predict fretting fatigue crack initiation?

The experimental data and material properties used in this study was taken from Szolwinski and Farris [59]. The contact was studied under partial slip condition for the cylindrical pad and flat specimen. The schematic diagram in Figure 51 illustrates the experimental setup. Both specimen and fretting pads were of same material i.e. Aluminium 2024-T351 with Poisson's ratio ν = 0.33 and modulus of elasticity E=74.1 GPa. The experimental data used is shown in Table 9, the pad radius was 178 mm and coefficient of friction μ was 0.65.

Table 9. Experimental data from fretting fatigue test [59].

Exp. Nr.	P (N)	Q (N)	σ_A (MPa)	N_i^{exp} (cycles)
1	7085	1487.8	85.2	684658
2	6176	1667.5	84.7	555830
3	6460	2196.4	106.4	195200
4	5319	1914.8	97.4	418911
5	6994	2377.9	113.1	431062
6	5310	2017.8	85.8	519963
7	6268	1692.4	100	312062

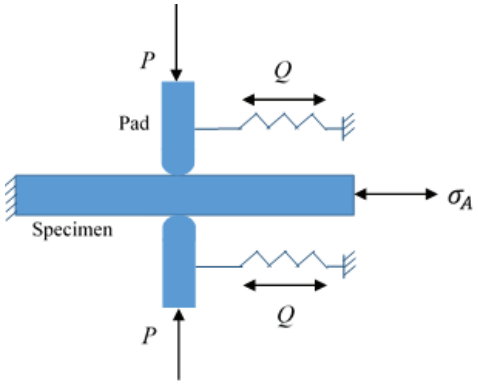

Figure 51. Fretting fatigue test configuration.

5.2.1 Influence of boundary conditions

Out of various numerical models, three numerical models were used to analyse damage initiation under out of phase loading. The models were selected considering their applicability for out of phase loading conditions. Accuracy of peak contact stresses, damage initiation locations and convergence was also studied for each model. Since the description of these models is already presented in *methodology* chapter, therefore only finite element models are shown in Figure 52 to designate a name. The thickness of both fretting pad and the specimen was 12.7 mm. Lengths of fretting pad and specimen were modelled 25 mm and 40 mm, respectively. The heights of 25 mm and 8.35 mm were used to model pad and specimen respectively. To capture the stress concentration and high gradient effect at contact surface, mesh size of 5 µm × 5 µm was used at and near the contact region. However, relatively coarser mesh was used for regions away from the centre using biasing approach.

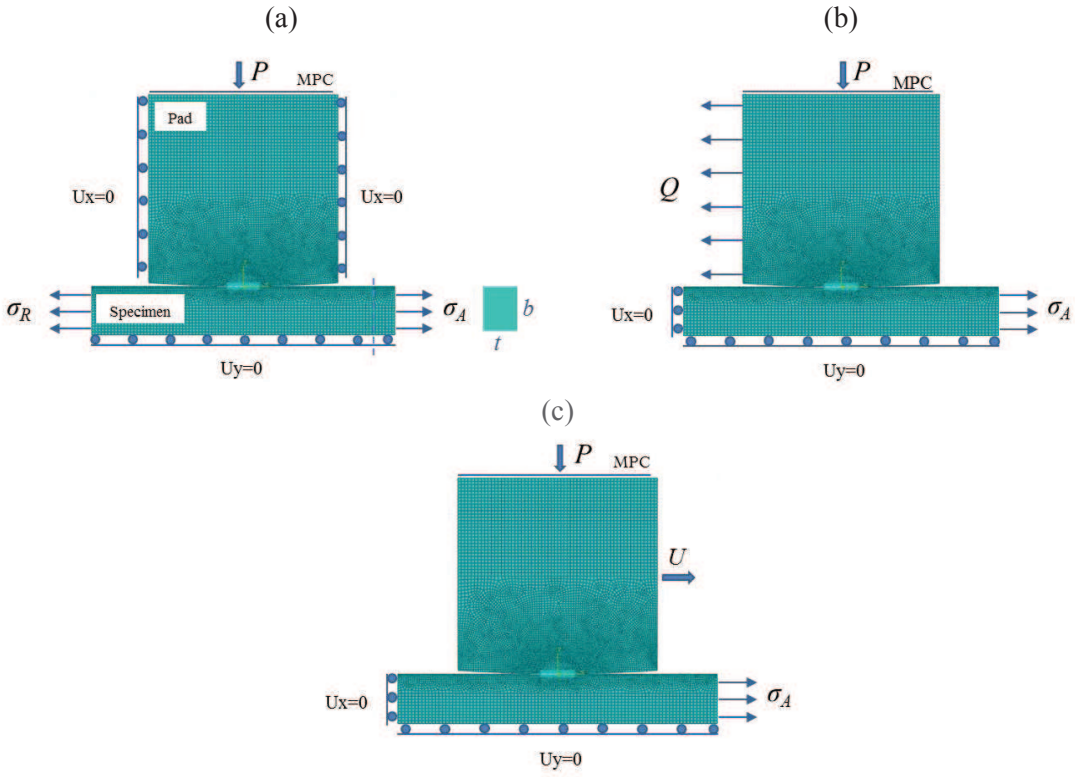

Figure 52. Loads and boundary conditions for (a) Model 1 (b) Model 2 and (c) Model 3.

For all numerical models, three phase difference angles (ø = 0°, 90°, 180°) were considered between cyclic axial stress σ_A and tangential load Q. All loads were applied in four steps for the case of 0° and 180°, whereas seven steps for the case of 90° phase difference as

shown in Figure 53. Additional steps were required for 90° in order to model intermediate steps during the load cycle. Step 0 was used to generate phase difference between cyclic axial stress and tangential load. The normal load was applied in the initial step and kept constant for subsequent steps. The cyclic axial stress and tangential load were applied in step 1 simultaneously for 0° phase difference, as shown in Figure 53 (a). Both stress ratio R_σ and tangential load ratio R_Q were equal to -1. Figure 53 (b) and (c) show the loading sequence for one complete cycle with a phase difference of 90° and 180°, respectively. For 90° phase difference, the tangential load reaches the maximum value in step 1 and axial stress reaches the maximum value in step 2. For the case of 180° phase difference, the axial stress reaches the maximum value in step 2, whereas the tangential load reaches the minimum value at the same time.

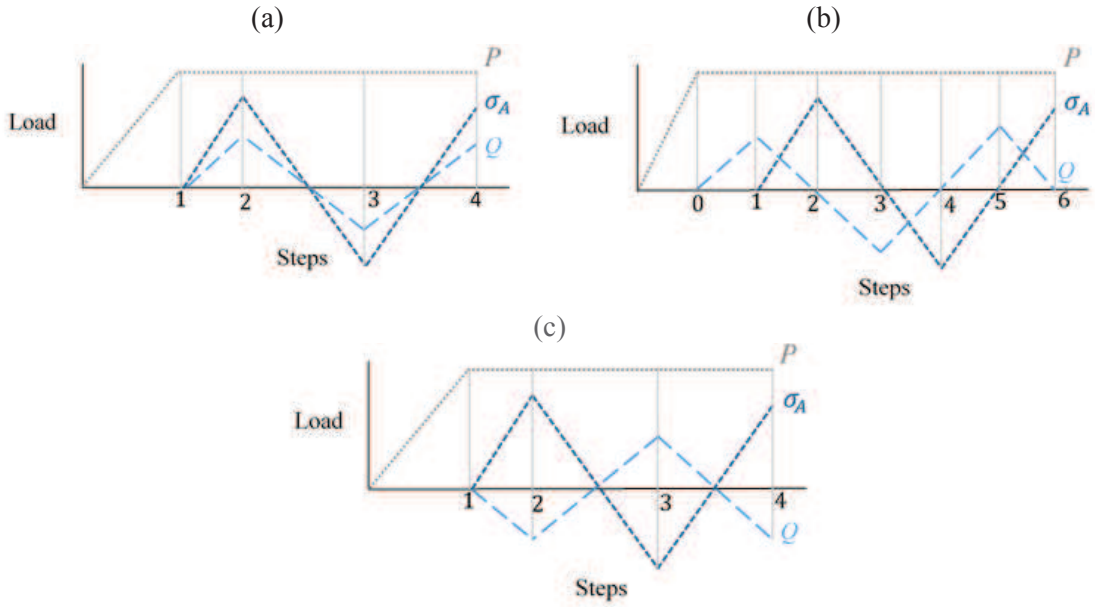

Figure 53. Loading sequence of one complete cycle for (a) $\emptyset = 0°$ (b) $\emptyset = 90°$ and (c) $\emptyset = 180°$.

5.2.1.1 Effect on contact parameters

To compare different numerical models, contact stresses, relative displacement (or slip) and Ruiz *F*2 parameters are compared for different $\emptyset$. First, the numerical results are compared with analytical solution for shear traction, to analyse the proximity of results. Figure 54 shows this comparison and it is observed that all models accurately captured the shear traction profile variation at the contact interface. The results were extracted at load step 2, using data set of experiment 3. The percentage error between analytical peak shear traction and finite element solution was found less than 5%.

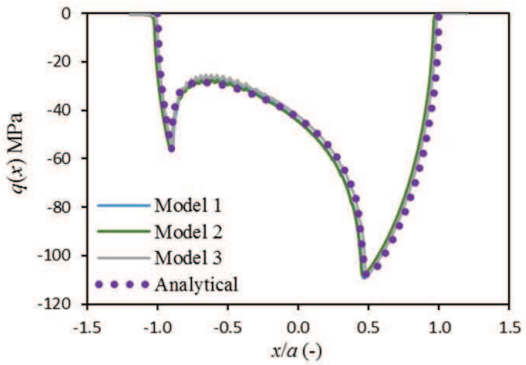

Figure 54. Comparison between analytical and numerical solution of shear traction $q(x)$ for all models at the contact interface.

Figure 55 shows comparison of results for in phase loading ($\emptyset = 0°$). From Figure 55 (a) it can be seen that the peak of the normal stress is almost at the same location with all models. Figure 55 (b) depicts that the maximum tensile stress is present at the trailing edge of the contact for all models. Also, the peak of the tensile stress appeared to be same for all models. For in phase loading, there was not much difference in results between all three FE models. The relative slip and $F2$ also showed similar distribution along contact interface, the peak values also matched closely with each other. All models seem suitable to model fretting fatigue initiation problems.

For the case of 90° phase difference between axial stress and tangential load, there were subtle observations for model 1 and 2. Figure 56 shows the results for 90° phase difference. Figure 56 (a) represents a typical case for generation of reverse slip. This reverse slip is usually produced when normal load becomes insufficient at higher applied axial stress. It can be seen that model 1 and model 2 produced perturbations in the contact stress profiles at the interface of stick slip zone near leading edge and at trailing edge of the contact. Whereas, model 3 was able to generate smoother profile at the interface of stick-slip zone of the leading edge. At trailing edge this perturbation was also observed for model 3, however lower than that observed for models 1 and 2. These numerical perturbations were generated due to convergence difficulties during unloading steps as a result of applied boundary conditions and loading history. The same perturbations were also observed for the case of tensile stress. It should also be noted here that, the load ratio for cyclic axial and tangential load ratio was taken as -1. This implies that during the loading cycle Q changes from positive to negative.

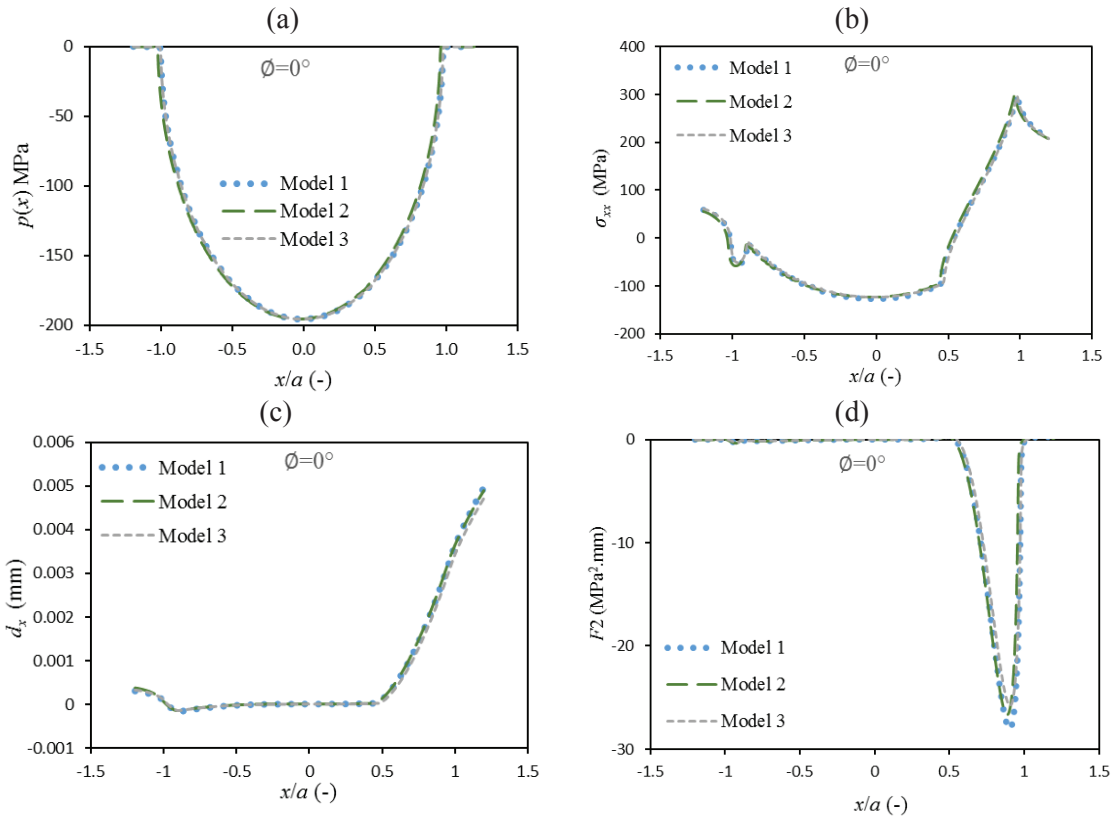

Figure 55. Comparison between FE models for Ø = 0° for (a) normal stress (b) tensile stress (c) relative displacement and (d) Ruiz parameter *F*2.

The results for the contact stresses, relative slip and Ruiz parameter *F*1 and *F*2 for phase difference of 180° were similar to those for phase difference of 0° as far as profiles are concerned. However, the maximum of all parameters shifted to leading edge. To avoid monotony, these results are not presented herein. However, for comparison purpose the results for 180° phase difference are covered in the next section using model 2 only.

Considering the results of all phase angles, it was observed that the peaks of the shear traction and tensile stress were directly influenced by phase difference, whereas normal stress appeared to be independent of phase difference. Regarding effect of numerical models, no significant difference was observed in peak and contact stress profiles. However slight variations were observed with 90° phase difference at the boundary of stick slip zone and at trailing edge.

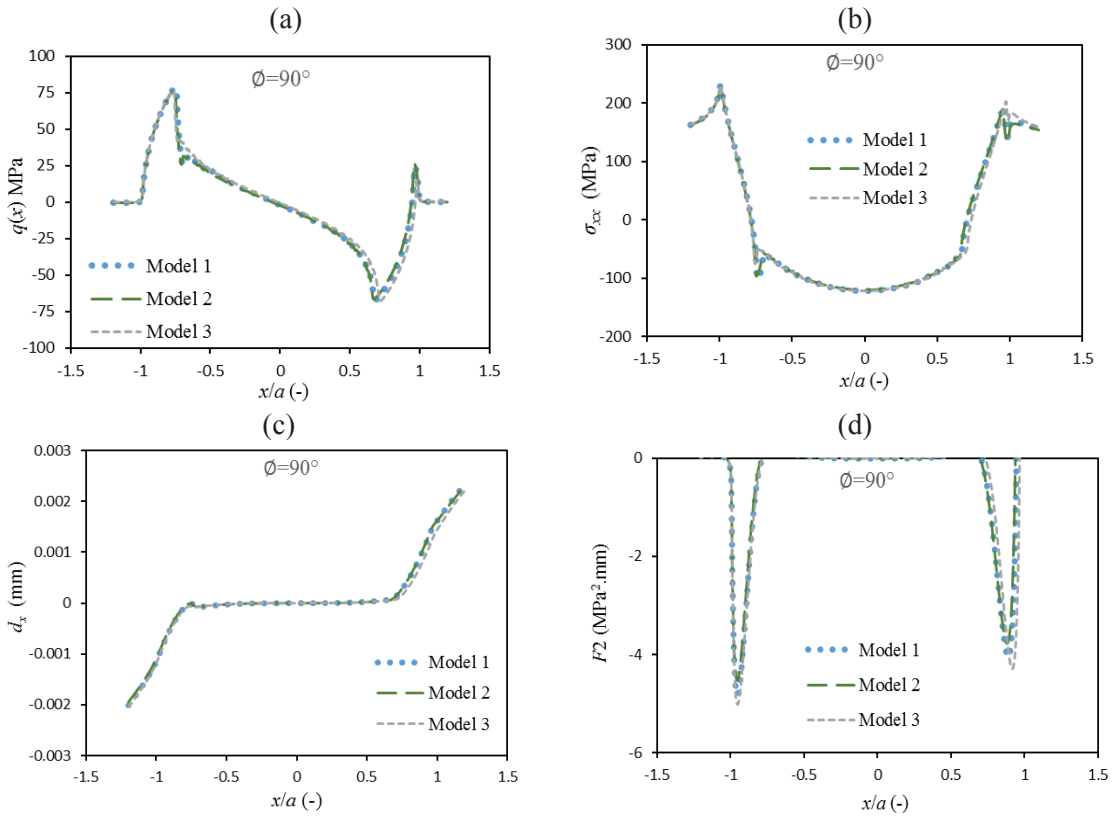

Figure 56. Comparison between FE models for Ø = 90° for (a) normal stress (b) tensile stress (c) relative displacement and (d) Ruiz parameter *F*2.

5.2.1.2 Effect on convergence rate

As different models have different method of application of loads and boundary conditions, therefore the number of iterations is also expected to be different for each model. The comparison of this convergence efficiency required to solve one simulation is given in Table 10. It was found that among all models there was not significant difference in total number of iterations for any particular phase difference, however for phase difference of 0° and 180°, model 2 showed slightly faster convergence during unloading step than for other cases. Also, no significant effect of phase difference on convergence rate was observed, nor any regular pattern was observed for all models.

From convergence point of view, unloading step appeared to be more critical than loading step as it consumed most of the computation time. It was observed that the number of iterations required for unloading steps were greater than those required for loading steps. This is the main reason to use number of iterations as convergence parameter instead of CPU time, so as to analyze

the efficiency of each numerical model during the complete loading cycle. The reason for slow convergence during unloading step is explained below.

Table 10. Comparison between number of iterations required for convergence for all three FE models and different phase angles.

Model	Normal Load	Ø = 0 °			Ø = 90 °			Ø = 180 °		
		Loading 1	Un-loading	Loading 2	Loading 1	Un-loading	Loading 2	Loading 1	Un-loading	Loading 2
1	125	89	164	113	61	137	125	93	232	94
2	126	105	140	97	69	169	136	94	152	94
3	126	90	178	89	61	134	128	90	208	99

In fretting fatigue, the contact stresses and displacement depends on the history of loading. Due to oscillating axial fatigue load, the tangential load generated also vary between maximum and minimum. To analyze the effect oscillating tangential load on convergence, the results for in phase loading were extracted during the cycle at different times as shown in Figure 57. Point O is the initial step, when normal load is applied. The applied loads reach the maximum at point A. Point B, C and D are the intermediate points of the unloading step, where B is the point just after A, and D is point with zero tangential load and axial stress. Point E is the minimum of unloading step.

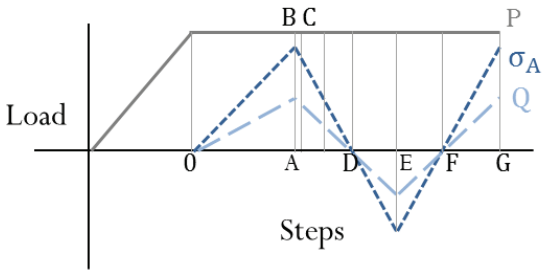

Figure 57. Loading sequence for one complete cycle, with intermediate steps during unloading.

The change of displacement and stresses during the complete cycle changes the stick zone width at each sub-step as described by Hills and Nowell [1]. The stick zone at point A can be calculated using Eq. (177):

$$c = a\sqrt{1 - \frac{Q_{max}}{\mu P}} \tag{177}$$

Figure 58 shows the variation of shear traction at different points during one complete load cycle. At point B, where the load has just started to decrease, the shear traction and displacement also decreases. Correspondingly, the rate of relative displacement changes sign from positive to negative and instantaneous stick zone condition will be generated. At this instantaneous point the stick zone width, 2*c*, becomes equal to complete contact width, 2*a*. At point C on further reduction of loads, reverse slip is generated which indicates the existence of insufficient normal load. This change in stick zone c' also alters the shear traction profile at the contact interface. The new stick zone width and shear tractions can be expressed as [1]:

$$q(x) = -\mu p_0 \sqrt{1 - \left(\frac{x}{a}\right)^2} \qquad c' < |x| \leq a \qquad (178)$$

$$q(x) = -\mu p_0 \sqrt{1 - \left(\frac{x}{a}\right)^2} + 2\mu p_0 \left(\frac{c'}{a}\right) \sqrt{1 - \left(\frac{x}{c'}\right)^2} \qquad c \leq |x| \leq c' \qquad (179)$$

$$q(x) = -\mu p_0 \sqrt{1 - \left(\frac{x}{a}\right)^2} + 2\mu p_0 \left(\frac{c'}{a}\right) \sqrt{1 - \left(\frac{x}{c'}\right)^2} - \mu p_0 \left(\frac{c'}{a}\right) \sqrt{1 - \left(\frac{x}{c}\right)^2} \qquad |x| \leq c \qquad (180)$$

$$\left(\frac{c'}{a}\right)^2 = 1 - \frac{1}{2\mu P}(Q_{max} - Q) \qquad (181)$$

The value of new stick zone c' is greater than *c*. At point D, the new stick zone is dependent on maximum value of tangential load Q_{max} and not on the instantaneous *Q*. Also, shear traction is not zero even though there is no instantaneous tangential load.

This shows that during the unloading steps, the size of the stick zone at points B, C and D is greater than that at points A and E. Due to this increase of stick zone the convergence rate during the unloading steps is found to be slower than during the loading step. It is also observed that once the tangential load becomes negative, the perturbation in the shear traction profile is generated near the interface of stick slip zone and remain even in the subsequent steps. Considering the above results and discussion, it can be summarized that modelling techniques and phase difference used in this study showed no significant effect on convergence rate, however, slower convergence was observed during the unloading step.

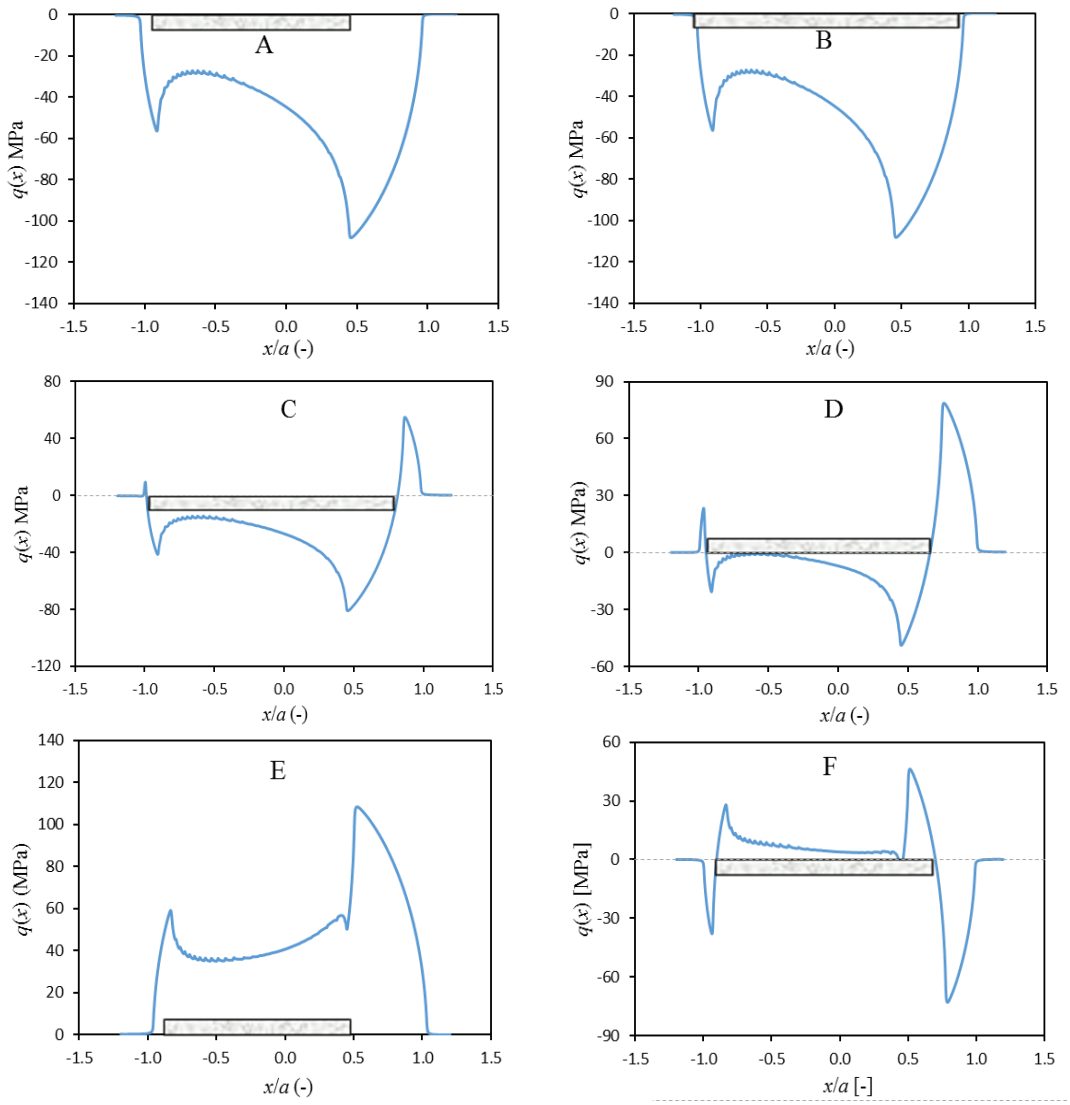

Figure 58. Variation of shear traction at different points (A, B, C, D, E and F) during one complete load cycle - the solid bar represents the stick zone.

5.2.2 Influence on initiation location

In this section effect of phase difference on damage initiation is analysed using model 2. Several researchers have shown in the past that the location of maximum damage initiation is observed at the trailing edge of the contact [88, 165] for the case of in phase loading. The normal stress and shear traction approach to zero at this point [183] and tensile stresses are maximum. This also demonstrates that damage initiation is supplemented under the influence of tensile stress. For out of phase loading, relatively less work has been done under fretting fatigue conditions.

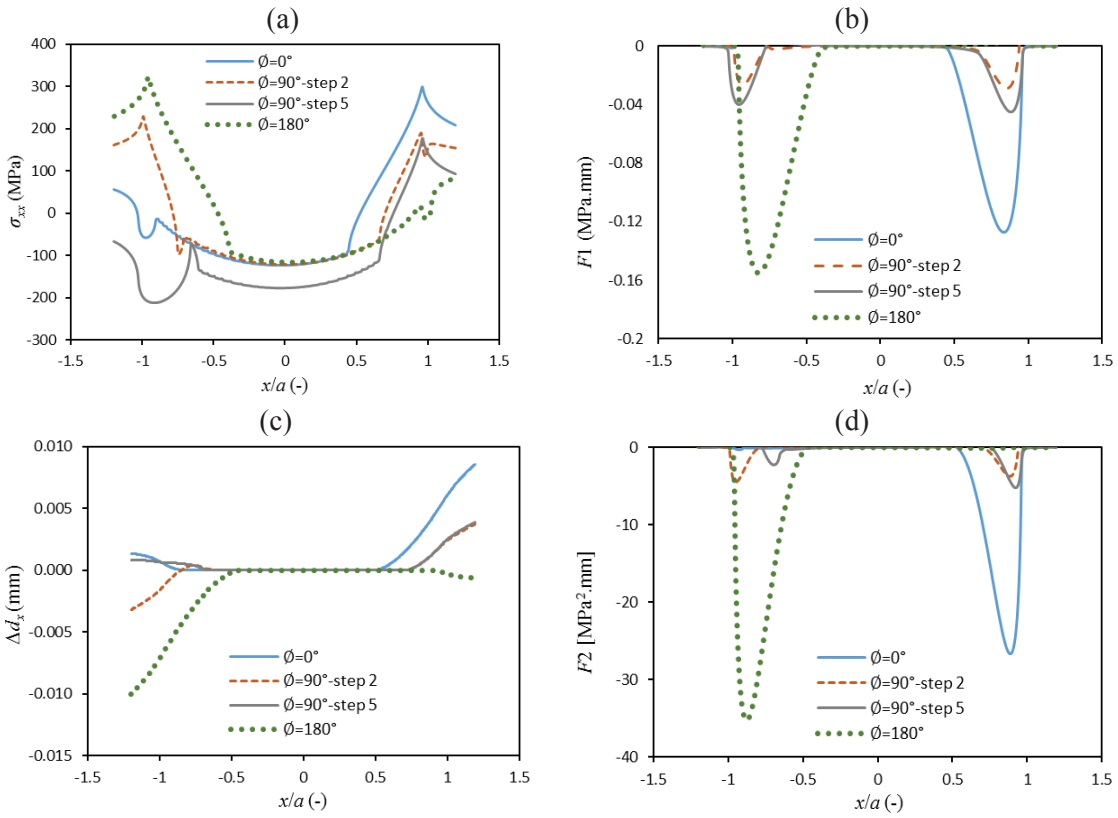

Figure 59. Effect of Ø with 0°, 90° and 180° on (a) maximum tensile stress (b) maximum $F1$ parameter (c) relative slip range (d) maximum $F2$ parameter.

To analyse the effect of phase difference on damage initiation location, three phase difference angles were considered as before, i.e. 0°, 90° and 180°. The stress ratio R_σ and tangential load ratio R_Q both were equal to -1. Coefficient of friction was 0.65 and normal load was kept constant for all phase angles. From Figure 59, it can be seen that for 0° phase difference between the axial and tangential load, peak of the tensile stress, damage parameter $F1$ and initiation parameter $F2$ were observed at the trailing edge, however with the phase difference of 180°, the peak of all parameters shifted to leading edge of the contact.

For 90° phase difference, two peaks were observed, one at each edge, but with lower magnitude. The lower peaks were present because of the fact that when maximum of axial stress was achieved, then tangential load was zero and vice versa. To model this phenomenon during the complete cycle, the results were extracted for step 2 and step 5. Step 2 is point of interest because the applied axial stress reaches the maximum value at this point and tangential load is zero. At step 5, tangential load reaches the maximum value, whereas the axial stress is zero. The

peaks of tensile stress and shear traction were lower for the case of 90° than for the case of 0° and 180°, ultimately producing lower value of both damage and initiation parameters. From Figure 59 (a), it can be seen that for the point, where axial stress reaches the maximum value during the cycle, maximum tensile stress is observed at the leading edge. Whereas, when the tangential load reaches the maximum value, peak tensile stress is observed at the trailing edge and also higher compressive stresses are observed among all phase angles.

From Figure 59 (c), it is observed that the relative slip range is maximum for 0° phase difference and minimum for 180° and intermediate slip range is observed for 90° phase difference. The slip range was computed as the difference between relative slips at the maximum and minimum loading points during the cycle. Since the contact was studied under partial slip condition, the relative slip was zero in the stick zone and varied in the slip zone. These numerical results correlate well with the experimental observation by Lee and Mall [128]. They studied the effect of phase difference on relative slip for Ti-6Al-4V titanium alloy under partial slip condition. According to them maximum and minimum slip ranges were observed in the case of 0° and 180° phase differences, respectively. With 90° phase difference an intermediate relative slip range was observed.

5.2.2.1 Comparison of *F*2 and SWT

During fretting fatigue loading multi-axial stress fields are produced in the vicinity of the contact [184], therefore multiaxial theory is required to define failure [185]. In the present study, in addition to Ruiz parameter *F*2, critical plane SWT parameter was also used to predict fretting fatigue damage initiation.

In this section, the numerical results of model 2 are compared with experimental results presented in [59]. According to experimental results, the failure occurred at the trailing edge of the contact for all experiments. This implies that the critical site of failure is located at $x/a \approx 1$ for all experiments. The range of normalized damage initiation location (ΔX_i) and mean ($\overline{X_i}$) predicted by both parameters are listed in Table 11. It was observed that for all data sets the initiation site predicted by both parameters was at the trailing edge of the contact, which correlated well with the experimental observations. Lykins et al. [115] studied (experimentally and numerically) the effect of various parameters on fretting fatigue crack initiation in titanium alloy, Ti-6Al-4V. They also found that experimental failure occurred at the trailing edge of the contact. For comparison purpose, the predicted initiation sites for their study using SWT and Ruiz parameters are also given in Table 11. This shows that both SWT and *F*2 parameters can be used to model fretting fatigue initiation problems.

Table 11. Comparison of initiation location ranges (ΔX_i) and mean ($\overline{X_i}$) for Ruiz $F2$ and SWT parameter between the present study (experimental results from [59]) and Lykins et al. [115].

Case study	SWT_{max}		$F2_{max}$		Exp. Location
	ΔX_i	$\overline{X_i}$	ΔX_i	$\overline{X_i}$	x/a
Present	$0.87 \leq x/a \leq 1.0$	0.947	$0.81 \leq x/a \leq 0.96$	0.881	≈ 1
Lykins	$0.929 \leq x/a \leq 0.957$	0.938	$0.7 \leq x/a \leq 0.814$	0.749	≈ 1

After validating the results for in phase loading the results can be extended for out of phase loading. To demonstrate the effect of phase difference on initiation site predicted numerically, results for all phase angles are presented in Table 12. The results are consistent for all experiments and it was observed that for the case of 0° phase difference the initiation site was predicted at the trailing edge and for 180° phase difference at leading edge. For 90° phase difference, it was observed that tensile stresses were higher at step 2 than at step 5, however, shear tractions were higher at step 5 than at step 2. Therefore, the initiation site was predicted at leading edge, when tensile stresses were higher during the loading cycle and at trailing edge, when shear tractions were higher. This implies that initiation may occur either at leading or trailing edge.

Table 12. Comparison of initiation location between Ruiz parameter F2 and SWT parameter for ∅ = 0°, 90°, 180°.

Exp. Nr.	SWT_{max} location (x/a)				$F2_{max}$ location (x/a)			
	∅ = 0°	∅ = 90° (step 2)	∅ = 90° (step 5)	∅ = 180°	∅ = 0°	∅ = 90° (step 2)	∅ = 90° (step 5)	∅ = 180°
1	1.0	-1.0	1.0	-1.0	0.96	-1.0	0.99	-0.94
2	0.95	-0.97	0.95	-0.94	0.89	-0.93	0.92	-0.88
3	0.96	-0.99	0.96	-0.96	0.89	-0.95	0.93	-0.88
4	0.87	-0.9	0.88	-0.87	0.81	-0.86	0.84	-0.79
5	1.0	-1.0	1.0	-0.99	0.92	-0.98	0.96	-0.91
6	0.87	-0.9	0.87	-0.87	0.81	-0.87	0.83	-0.79
7	0.96	-0.97	0.96	-0.95	0.89	-0.94	0.93	-0.88

Figure 60, shows the variation of both parameters along the contact interface for Exp. 3. Notice that the exaggerated views are presented for ∅ = 90° cases, the magnitudes are much lower as compared to other phase angles.

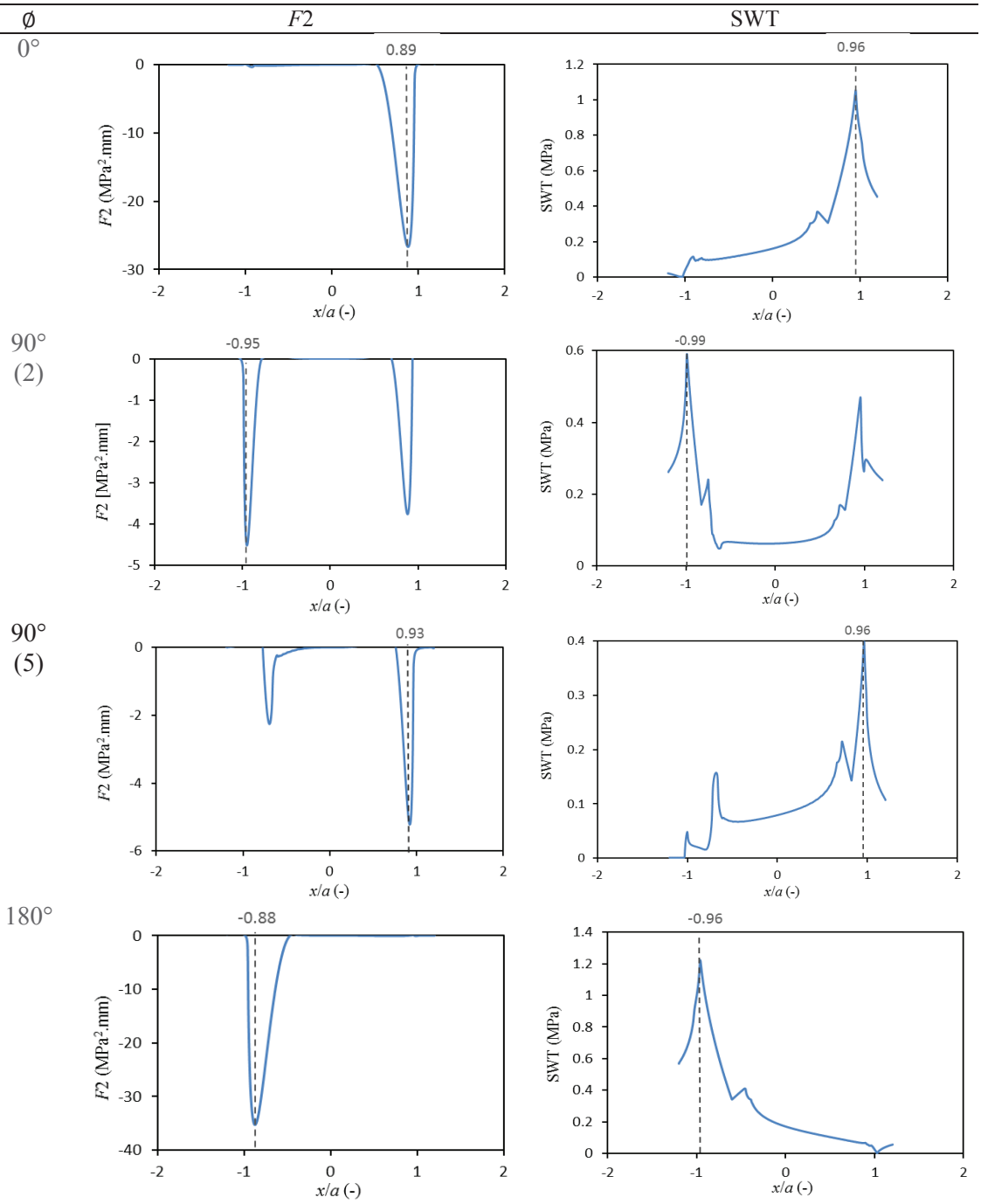

Figure 60. Comparison of damage initiation variation along the contact interface between *F2* parameter and SWT parameter with phase difference 0°, 90°, 180°.

Figure 61 (a) and (b) show the computed values of SWT and *F*2 parameters for all phase angles and it is observed that for ∅ = 180° both parameters achieved maximum value, therefore the damage initiation life would be lowest for this case. In other words the damage initiation life would be lower than that for in phase loading. Whereas, lowest values were observed for 90° phase difference, which implies that initiation life will be higher than that for in phase loading.

Considering the results and discussion, it can be summarized that for the case of 0° phase difference, failure was predicted at the trailing edge of the contact and for 180° phase difference at the leading edge of the contact. However, for the case of 90° failure might occur at any of the leading or trailing edge depending upon whether the shear tractions are dominant or tensile stresses. Hence, more experimental work is required to ensure the damage initiation location for this case with Al 2024-T351.

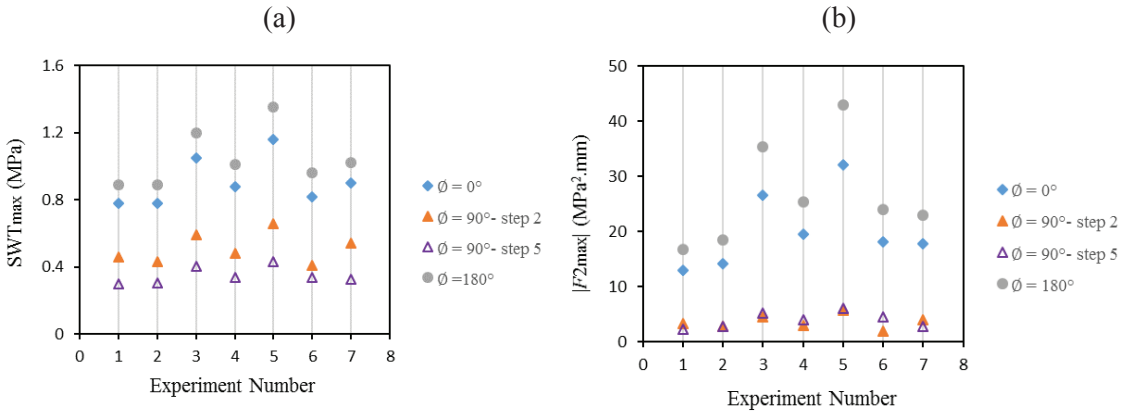

Figure 61. Maximum values of SWT parameter (b) maximum absolute values of *F*2 at ∅ = 0°, 90°, 180° for all experiments.

5.3 Crack initiation orientation and life

The previous section focused on effect of phase difference on crack initiation location under out of phase loading. This section investigates the effect of phase difference on initial crack orientation and life. For this purpose the efficacy of different multi axial critical plane parameters is examined. The damage parameters included for this study are stress-based (Findley and McDiarmid parameter), strain-based (Brown-Miller and Fatemi-Socie parameter) and virtual strain energy-based (Smith-Watson-Topper, Liu 1 and Liu 2 parameter). The numerical results are also discussed in the light of experimental results from literature.

The loads and experimental crack initiation life used in this section is similar to section 5.2, as shown in Table 9. The numerical model, coefficient friction and basic material properties (of Al. 2024-T351) are also same. The material properties and stress and strain life constants were

taken from [59], as specified in Table 13. Stress and strain constants under shear were estimated from uniaxial strain life constants as $\tau_f' \approx \sigma_f'/\sqrt{3}$, $\gamma_f' \approx \varepsilon_f'\sqrt{3}$ and $b' \approx b, c' \approx c$.

Table 13. Material properties, stress and strain life constants for Aluminium 2024-T351 [59].

Property	Value (MPa)	Property	Value (-)
σ_u	425	b	-0.078
σ_y	310	c	-0.538
τ_y	179	ε_f'	0.166
σ_{f-1}	140	γ_f'	0.287
τ_{f-1}	80.8	b'	-0.078
σ_f'	714	c'	-0.538
τ_f'	412.2		

5.3.1 Analysis of stress state

Under fretting fatigue condition, non-proportional stress state may be produced, and can have a significant effect on fatigue life as compared to plane fatigue. The criterion or parameter employed for nucleating phase, therefore, should be able to accommodate this effect. The non-proportional loading can produce non-proportional stress state and is characterized by change of principal axis directions. This rotation of principal axis of stress and strain may have influence on fatigue damage nucleation [186].

To visualize the stress state for the current problem, the damage nucleation site at the contact interface was analyzed. The stress state was extracted for the element with highest damage parameter value (using MD criterion) at different instants during the loading cycle. In Figure 62, two stress states are plotted at the instant *A* and *C* (see Figure 38), using Mohr's circle. The stresses were extracted from the deformed state of the element. Since the analysis of non-proportionality is linked with the change of principal plane during cyclic loading, orientation of principal plane was determined using the stress states at two different time instants. The blue circle represents the Mohr's circle and red line passing through the centre indicates the principal plane. The letters *X* and *Y* denotes the stress state at *X* and *Y* face of the element. The orientation of the principal plane is denoted by $2\theta_p$. It can be seen in Figure 62(a) that, at instant *A* the principal plane is almost at 0° while at instant *C*, Figure 62(b), the principal plane is rotated anti-clockwise by almost 80°. This shows that the existence of non-proportional stress state at the contact interface at the damage nucleation point. The critical plane, θ_c, generally lies near the maximum shear plane which is theoretically ±45° from the principal plane.

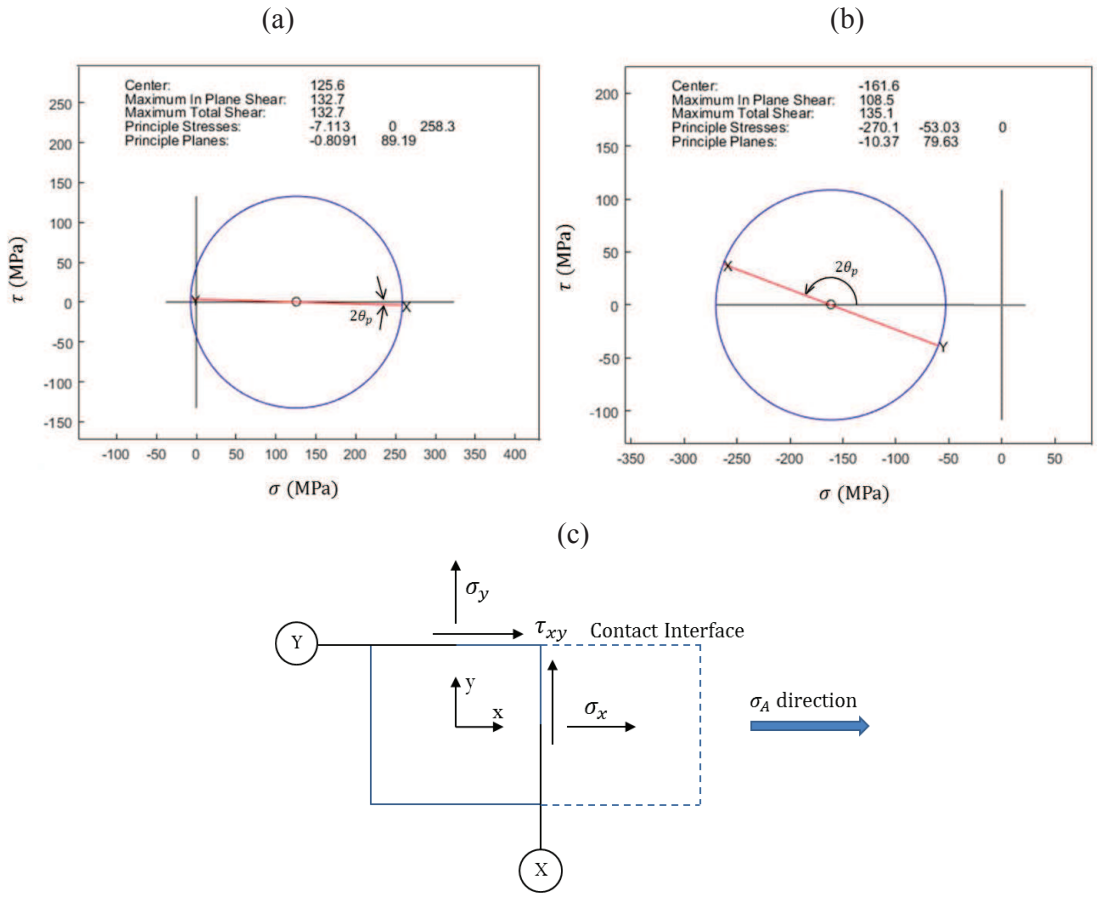

Figure 62. Mohr's circle representation of stress state at (a) point A, (b) point C during the load cycle (see Figure 38) and (c) element at damage nucleation site.

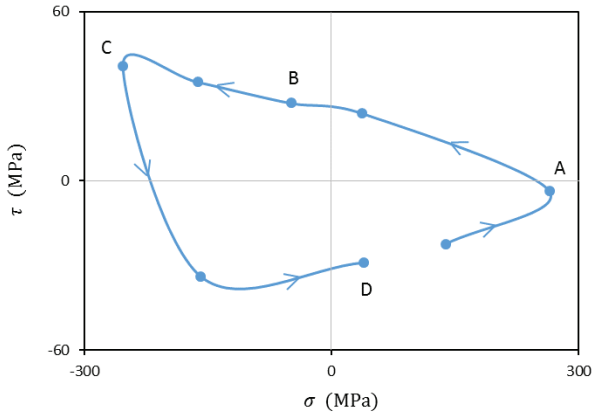

Figure 63. Non-proportional variation of normal and shear stress during the load cycle (according to Figure 38).

A clearer picture of the variation of stress state during the loading cycle is presented in Figure 63. The figure is plotted using points *A* to *D* and with some additional intermediate steps. It is observed that variation of normal σ and shear stresses τ during the loading cycle is not proportional, as slope of the line continuously changes. Therefore, under fretting fatigue, non-proportional stress state may exists even with in-phase loading condition.

5.3.2 Comparison of critical plane parameters

Different damage initiation parameters are compared in this section considering their effectiveness to predict the orientation of critical plane and initiation life. First the results are explained for in-phase loading i.e. $\emptyset = 0°$, then extended for out-of-phase loading i.e. $\emptyset = 90°$ and 180°. To determine the orientation of critical plane it is necessary to first define the sign convention used in this study. Figure 26 shows the sign convention for the orientation of critical plane. The angles are taken with respect to y-axis i.e. perpendicular to free surface of the specimen. An angle with the minus sign represents the left (negative) quadrant and plus sign represents the right (positive) quadrant. This sign convention is adopted herein since most of the researchers have used the same sign convention in their work.

To estimate the critical plane, Mode (value appearing most number of times) was taken. If Mode did not exist, then Median (central value of the data) was noted. For estimating accuracy of the predicted initiation life, a statistical approach presented in [109] was adopted. Normalized mean $\bar{x}$ and normalized standard deviation SD_x was measured to evaluate the proximity of predicted results with experimental results. The values closer of 1 implies perfect prediction. The calculation procedure is shown in Eqs. (182) - (186).

$$\alpha_j = log \frac{N_j^{pred}}{N_j^{exp}} \tag{182}$$

$$\bar{\alpha} = \frac{1}{n}\sum_{j=1}^{n} \alpha_j \tag{183}$$

$$SD_\alpha = \sqrt{\frac{1}{n-1}\sum_{j=1}^{n}\left(\alpha_j - \bar{\alpha}\right)^2} \tag{184}$$

$$\bar{x} = 10^{\bar{\alpha}} \tag{185}$$

$$SD_x = 10^{SD_\alpha} \tag{186}$$

Comparison between all damage parameters is shown in Table 14. All criteria showed the initiation location almost at the same point i.e. at $x/a \approx 1$. The stress-based, strain-based and Liu 2 showed the orientation of the critical plane near the maximum shear stress or strain plane. Whereas Liu 1 and SWT predicted the initiation angles nearly perpendicular to specimen surface. Furthermore, it was found that most of the parameters predicted critical plane only in one preferred direction, however with BM parameter, in 3 out of 7 and with Liu2, in 2 out of 7 tests, the critical plane was predicted in negative quadrant as well. Since in fretting fatigue it is believed that the damage initiation starts at the surface of the contact, therefore only nodes at the contact interface were considered for determination of critical plane and initiation life. Although all parameters showed good prediction for mean $\bar{x}$ and standard deviation SD_x, the best prediction was observed for strain based parameters. The standard deviation of ≈2 was observed with all parameters which implies that most of the predicted initiation lives lie in the band of $\pm 2N_i$.

Table 14. Comparison between damage parameters for initiation location, orientation, normalized mean and standard deviation for $\emptyset = 0°$

Damage Criteria	$\bar{X}_i$	θ_c (°)	$\bar{x}$	SD_x
FP	0.943	35	0.75	2.18
MD	0.941	36	0.81	2.17
FS	0.943	35	0.92	1.97
BM	0.937	27/-40	0.99	1.78
Liu 2	0.941	38/-51	1.95	1.98
Liu 1	0.946	-5	1.25	1.98
SWT	0.940	-4	1.45	1.97

The numerical results showed good correlation with experimental results from literature as summarized in Table 15. All criteria predicted initiation location at the trailing edge of the contact. For orientation of the critical plane researchers have shown experimentally that initiation process is mainly controlled by maximum shear stress or strain. Lykins et al. [118] found that initiation angles for Titanium alloy were 40°,-45° and -39° in their various tests. Namjoshi et al. [110] also mentioned that experimental initiation angles were observed either at -45° or +45° with a variation of ±15°. Hojjati-Talemi et al. [48] measured the initiation angles between -35° to -45° for the Aluminium alloy. It is also pertinent to mention here that the value of critical plane angles, shown in Table 15, have been transformed to the unified sign convention as described above, since some researchers have measured the angles with a different sign convention in their work. From the experimental results summarized in Table 15, it can be seen that initiation at the surface can occur either inwards or outwards with reference to the fretting pad.

Table 15. Experimental results from literature for initiation location and critical plane orientation for $\emptyset = 0°$

Material	*Xi*	θ_c (°)	Reference
Ti–6Al–4V	0.91-0.92	40, -45, -39	Lykins et al. [118]
Ti–6Al–4V	≈1	(45/-45) ± 15	Namjoshi et al. [110]
Al 2024-T351	≈1	≈ - 55	Proudhon et al. [187]
Ti–6Al–4V	≈1	41	Almajali [130]
Al 2024-T351	≈1	≈ -50	Szolwinski MP, Farris TN [59]
Al 2024-T351	≈1	-35 to -45	Hojjati-Talemi et al. [48]

Figure 64 provides an insight to the cause of initiation orientation on any of the two maximum shear planes. At the damage initiation location, two damage parameters (Liu2 and FS) were computed and their variation is shown with respect to plane angle, θ. As mentioned earlier that in order to find the initiation angles maximum of the damage parameter was computed on all possible planes. From Figure 64 (a) it can be seen that Liu 2 parameter attains the maximum value at two angles i.e. at θ =-51° and 39°. Also, for FS parameter as shown Figure 64 (b) two maxima, are observed at θ =-45° and 36°, which are very close to each other. These planes exist on both sides of the principal plane and are close to maximum shear stress planes. Therefore, both planes have potential to initiate damage in any of the directions. Depending upon the microstructure of the material, during experiments the crack may take any preferred direction.

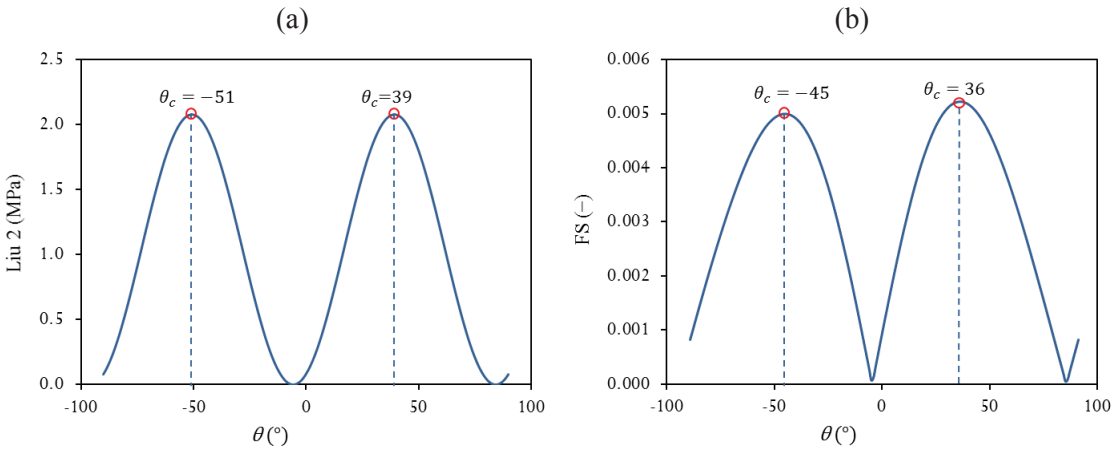

Figure 64. Variation of damage parameter with respect to angle at damage initiation location with (a) Liu 2 criteria (b) FS criteria. Graphs plotted for Exp. 2.

The angles mentioned in Table 14 are the one with the highest value of damage parameter even if the difference was very small. It is also important to mention here that initiation angle was predicted considering only the surface elements and no subsurface stresses were analyzed. Therefore the predicted angles are related to surface elements only. Nowell and Hills [1] mentioned that stage I growth is usually controlled by shearing or dislocations along persistent slip bands therefore initiation occurs along plane of maximum shear (or near maximum if preferred planes are not oriented ideally), which lie at ±45° to the free surface.

From these experimental and numerical results presented above, it can be said that the parameters based on shear stress or strain were able predict the damage initiation angles. The criteria based on normal stress or strain i.e. SWT and Liu 1 were unable to predict initiation direction. However, critical plane orientation predicted by these criteria coincided well with the fracture direction.

The prediction of initiation life in comparison to experimental results by all damage parameters is shown in Figure 65. It can be seen that for both stress and strain-based criteria all data lie within ±2*Ni* scatter band except for experiment 5. The results also appeared to be relatively symmetric about the central line. For energy-based criteria almost all of the data lie within ±3*Ni* scatter band, however most of the data appeared to be on the non-conservative side, i.e. the predicted value was higher than the experimental one. The data for all parameters is presented together in Figure 65 (d) and it is observed that around 85% of the data lie within ±2*Ni* scatter band and more than 90% lie within ±3*Ni* scatter band. Hence, a good correlation was observed between experimental and predicted results.

Although the stress based criteria showed good prediction capabilities, but for data set 5, they showed the highest deviation from experimental results. The in-depth analysis revealed that for this data set the tensile stress σ_{xx} was higher than the yield strength of the material at the initiation location. Figure 66 shows that maximum tensile stress occurred at the trailing edge of the contact ($x=a$). It is generally believed that fatigue crack initiation involves localized plastic deformation in slip bands even in HCF region [83]. Since the stress-based parameters do not account for plastic effect in their formulation therefore highest deviation is observed with Findley and McDiramid parameters.

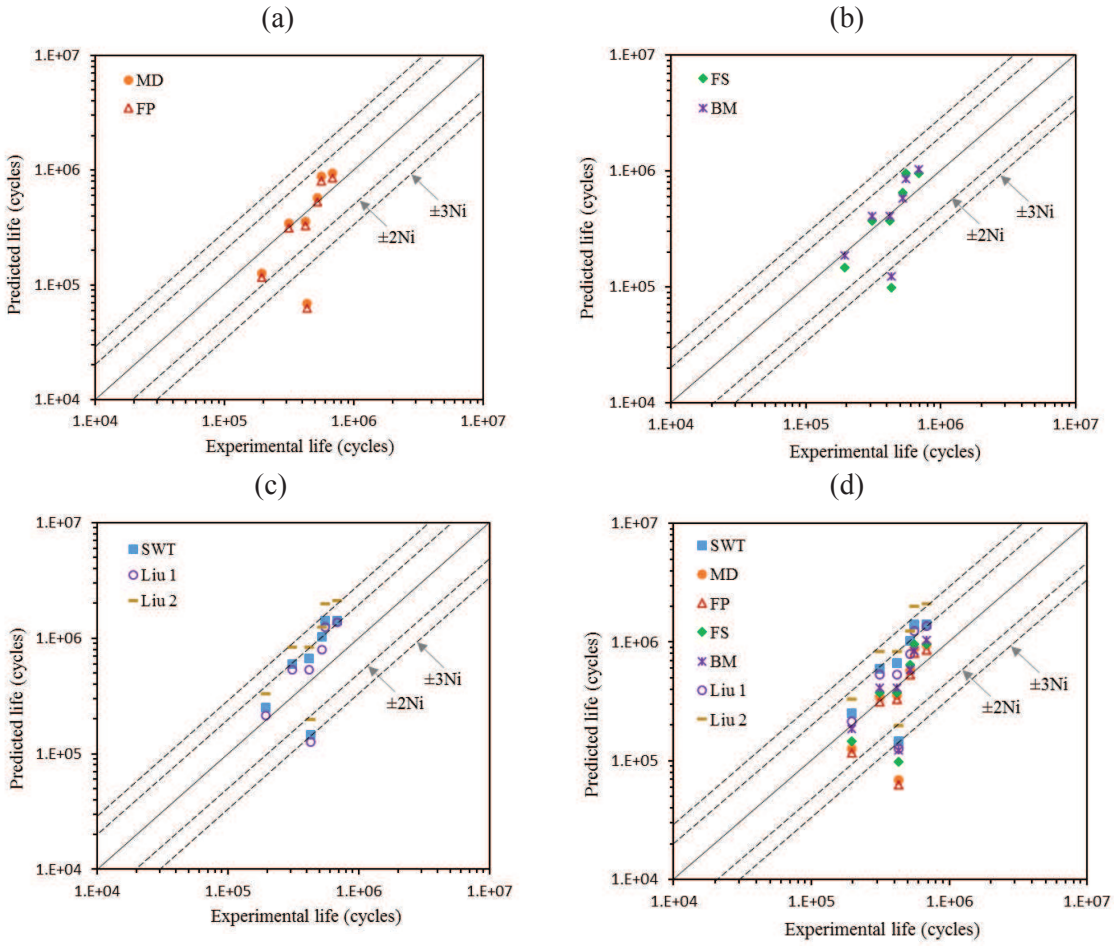

Figure 65. Comparison between predicted and experimental life for (a) stress based (b) strain based (c) strain energy based parameters, (d) all parameters plotted together, for $\emptyset = 0°$.

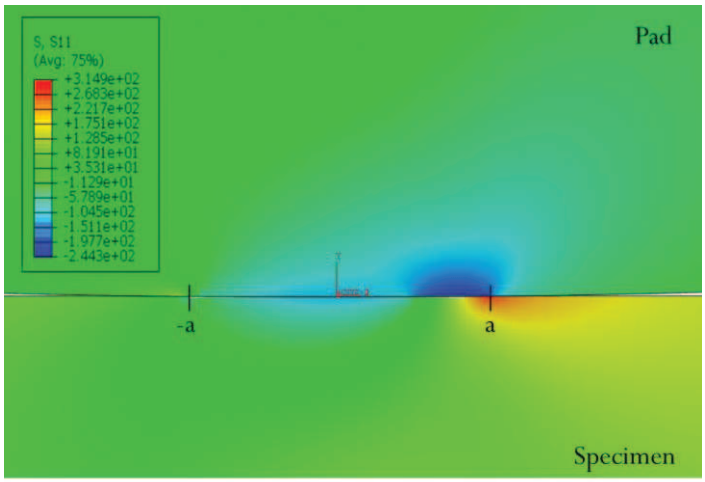

Figure 66. Tensile stress σ_{xx} at the contact interface of pad and specimen.

5.3.3 Effect of ∅ on initial crack orientation

After verifying the results of in-phase loading, the results can be extended for out-of-phase loading using the same numerical model. The orientation of critical plane at the surface of the specimen allows to determine the possible direction for damage initiation. Since for tensile mode failure cases, initiation phase takes most of the fatigue life, therefore study of initiation angle is important. It was found that phase difference affected the critical plane in general due to change in direction of maximum shear stress and strain. For the case of 180° phase difference, the direction of the critical plane was observed in the opposite direction to that for in-phase loading, however the magnitude of angles remained almost the same for all damage parameters. For the case of 90° phase difference, all parameters predicted initiation angle in both quadrants except SWT parameter. Table 16 shows the effect of phase difference on critical plane orientations for all parameters.

Table 16. Effect of phase difference on critical plane orientation.

Damage Parameter	Critical plane θ_c (°)		
	∅ = 0°	∅ = 90°	∅ = 180°
FP	35	-37/38	-35
MD	36	-38/40	-37
FS	36	-38/40	-35
BM	27/-40	-28/39	-27/39
Liu 2	39/-51	-40/49	-39/51
Liu 1	-5	-3/4	5
SWT	-4	2	3

In addition, it was noticed that the change of critical plane also has a connection with site for maximum damage. Just as the maximum damage location shifted from trailing edge to the leading edge, the initiation angles also reversed for ∅ = 180° as compared to ∅ = 0°. For the case of ∅ = 90° two peaks of damage parameters were observed at end of each slip zone and so as the initiation angles were predicted in both directions. Figure 67 shows the variation of damage parameter in the stick-slip zone for all phase angles. This implies that with inclusion of 90°phase difference between the loads, more shearing planes are approaching the critical value.

This observation also coincides with the experimental work of Kanazawa et al. [188] under out-of-phase loading between axial and torsion load for 1%CrMoV. They considered phase difference of 0°, 30°, 45° and 90° and found that, maximum number of cracks were initiated in the direction of maximum shear stress. Further, they observed that with the phase shift of 90°,

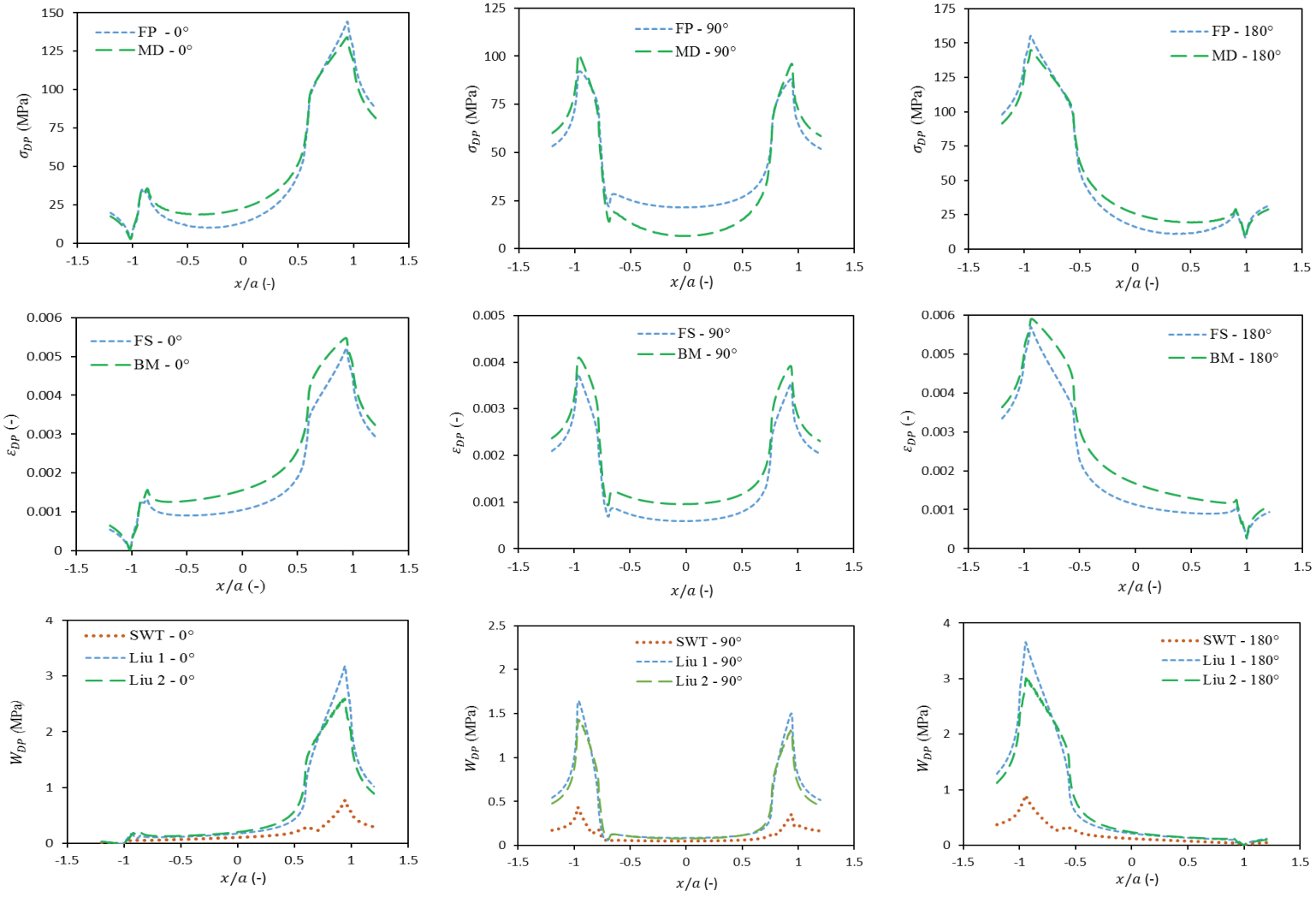

Figure 67. Variation of damage parameters in stick-slip zones with all phase difference angles.

more variation of initiation angle was observed, as with loading phase difference more directions approach a critical value for damage initiation [189]. From the numerical results of this study, it can be said that with phase difference of 180° the orientation angle was opposite to that observed for in-phase loading, however the magnitude remained same. The initiation angle coincided with the maximum shear plane orientation depending upon material and applied loads. With phase difference of 90° more number of planes were activated to undergo initiation. The criteria based on normal stress and strain were again far from accurate prediction for initiation angles.

5.3.4 Effect of ∅ on crack initiation life

The phase difference between axial stress and tangential load has a significant effect on fretting fatigue life as it affects the magnitude of surface stresses and slip amplitude [171, 190]. In this section, initiation life is computed with various damage parameters and three phase difference angles i.e. ∅ = 0°, 90° and 180°. Figure 68(a), (b) and (c) shows the trend of peak damage value for stress based, strain based and energy based parameters, respectively. It was observed that, for the cases with higher damage parameter value, lower fretting fatigue lives were observed and vice versa. Intuitively, the higher damage value should cause an early failure.

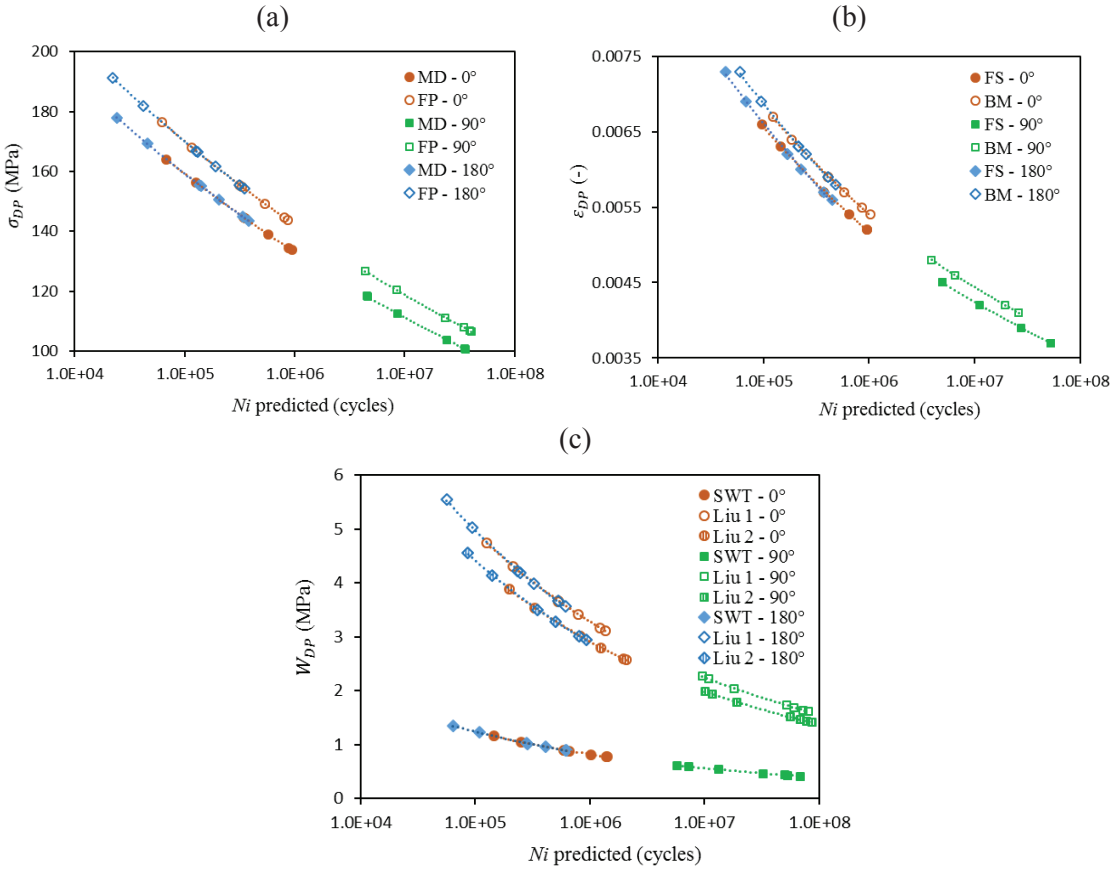

Figure 68. Variation of damage parameter with predicted life for (a) stress based (b) strain based and (c) strain energy based parameters.

With all damage parameters similar trend was observed for all phase angles. The data of ∅ = 0° and ∅ = 180° are closer to each other and away for ∅ = 90° since values of damage criteria were lowest for this case. This implies that fretting fatigue life will be maximum if the loads are applied with 90° phase difference. By taking mean of the initiation lives, a comparison of initiation lives with respect to phase difference for all damage criteria is shown in Figure 69. It was found that the initiation life with phase difference of 180° was less than that for in-phase loading whereas for ∅ = 90° the initiation life was much higher than that for in-phase loading.

The experimental work of Fatemi and Socie [83] also showed that with 90° out-of-phase loading the fatigue life increased in HCF region, whereas in LCF, the fatigue life decreased due to additional cyclic hardening in the material. Since the initiation life for 90° phase difference was much higher than for 0° and 180°, therefore in order to validate percentage increase in life for this case, further experimental work is recommended.

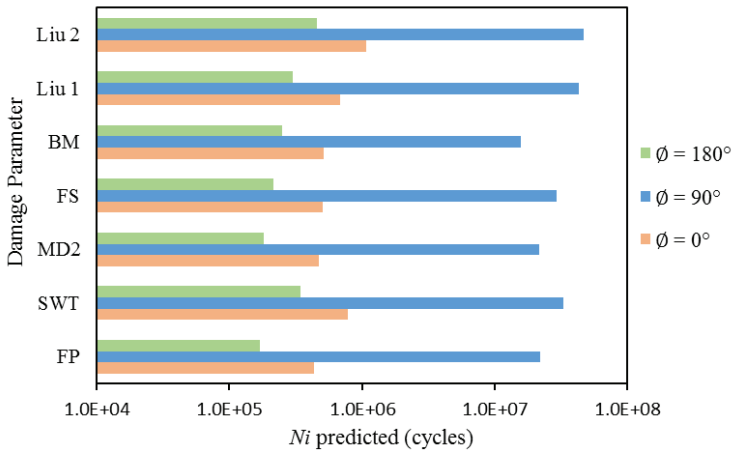

Figure 69. Mean initiation life for all damage parameters with ∅ = 0°, 90° and 180°.

To compare the dispersion of the predicted initiation lives with phase difference angles, the set of Eqs. (187) - (189) can be used to measure standard deviation (SD_N) and its range (R_{SD}). Figure 70 shows the dispersion range with all damage parameters and for each phase angle. It was observed that dispersion range with all parameters were comparable and does not change significantly due to phase difference. In general, the dispersion with 90° phase difference was found to be lowest and highest for 180° phase difference. For all phase angles the dispersion range lies nearly in the band of ±1 and ±1.5.

$$\overline{N^{pred}} = \frac{1}{n}\sum_{j=1}^{n} N_j^{pred} \tag{187}$$

$$SD_N = \sqrt{\frac{1}{n-1}\sum_{j=1}^{n}\left(N_j^{pred} - \overline{N^{pred}}\right)^2} \tag{188}$$

$$R_{SD} = \pm\left[\frac{N_j^{pred} - \overline{N^{pred}}}{SD_N}\right] \tag{189}$$

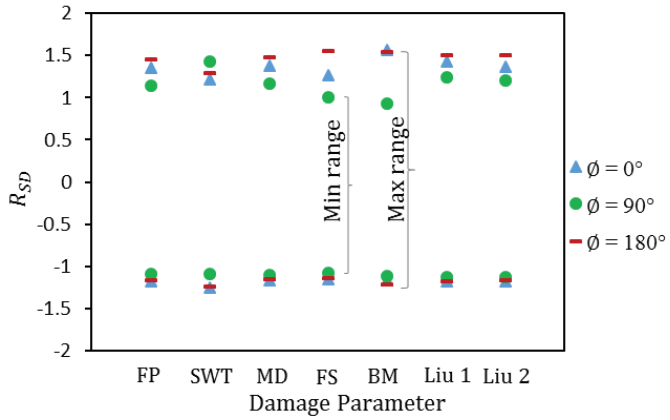

Figure 70. Comparison of dispersion range between phase angels for all damage parameters.

5.4 Comparison between CP and CDM approach

This section aims to investigate the effectiveness of continuum damage mechanics (CDM) approach in comparison to critical plane (CP) approach, under in phase and out of phase loading. Two cases with different material and loading conditions were considered for this analysis. The first case included constant normal load and phase difference was generated between axial cyclic stress and tangential load. Whereas in the second case, cyclic normal load was applied and phase difference was generated between normal load and other two loads, i.e. between cyclic axial stress and tangential load. For both cases, cylindrical pad and flat specimen configuration was used.

The results of case 1 computed with CP approach, are taken from the previous section 5.3, for comparison with CDM-PL approach. For simplification, CDM-PL is denoted as only CDM in this section. Two CP parameters, namely, FS and SWT parameters were chosen for this purpose. Only two phase angles were considered, i.e. 0° and 90°, which herein called as in phase

(IP) and out of phase (OP), respectively, in the sequel of the section. The results of case 2 were computed again using both approaches for a new material, experimental data and loading conditions, which are described later in the section. Since for case 2, the experimental fretting fatigue lives were computed for the complete failure of the specimen, therefore, for computation of total numerical lives, propagation lives were also computed in addition to nucleation life.

5.4.1 Case 1: Constant P and phase difference between σ_A and Q

For this case, the experimental data and material properties were taken from [59]. The experimental data is given in Table 9 and material properties are presented in Table 13. The load history is presented in Figure 53 (a) and (b). Since the main objective of this study was to apply CDM-PL approach to fretting fatigue under out of phase loading condition and compare it with CP approach, the damage initiation location and fretting fatigue lives were evaluated for both approaches.

5.4.1.1 Comparison of initiation location

To determine the damage initiation location using CDM approach, damage equivalent stress σ^* was used. For CP approach, both parameters (SWT and FS) were evaluated at the contact interface. For IP loading, both approaches predicted the highest value of damage parameter at the trailing edge ($x = a$) of the contact as shown in Figure 71. This result matches well with experimental observation of many researchers [48, 88, 115, 191].

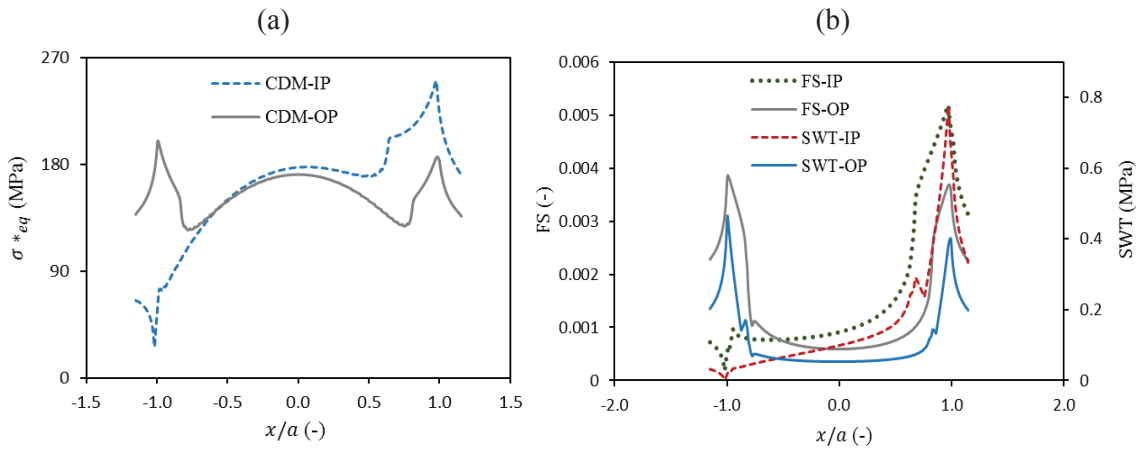

Figure 71. Variation of damage parameters at the contact interface for Exp. 1 with (a) CDM and (b) CP approach. IP denotes in phase and OP denotes out of phase.

For OP loading, both approaches showed two peaks of relatively lower magnitude at both edges of the contact. The lower peaks were observed since both loads (σ_A and Q) reached their maxima at different time instants. This implies that failure can occur at either sides of the edges. Similar results were obtained by other CP parameter, as shown in the previous section. These results show that damage initiation location is dependent on the loading sequence, and phase difference changes the damage parameters profile at the contact interface. In addition, both approaches showed similar results for in-phase and out of phase loading conditions.

5.4.1.2 Comparison of life prediction

The crack initiation life predicted by both approaches for in phase loading is shown in Figure 72, the numerical results are compared with experimental results of Szolwinski and Farris [88]. Both approaches showed good correlation with experimental results. Most of the numerical data was found within ±2 Ni band, which indicates that both approaches are equally suitable for in-phase loading.

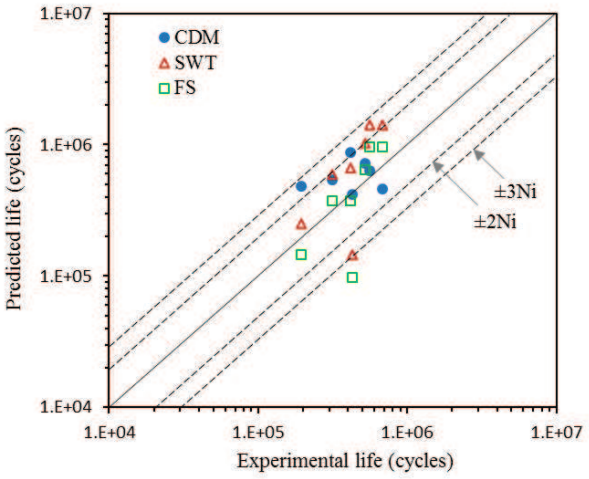

Figure 72. Comparison of predicted life with experimental life using CDM and CP approaches for IP loading.

After validating the results for IP loading, the results were extended for out of phase condition. For OP loading, marked difference was observed between the two approaches. Figure 73 (a) and (b) shows the variation of predicted life with change in damage parameters of CDM and CP approach, respectively. It was found that, for CDM approach with OP loading, the predicted lives were of the same order as for IP loading, although slightly higher than for IP loading. Whereas the numerical lives predicted using CP parameters were much higher than for IP loading. This shows that initiation lives are very sensitive to strain life constants and slight

change in damage parameters significantly influences the initiation life prediction. It also highlights the need to determine the strain life constants for OP loading, if loads are applied with phase difference under fretting fatigue conditions.

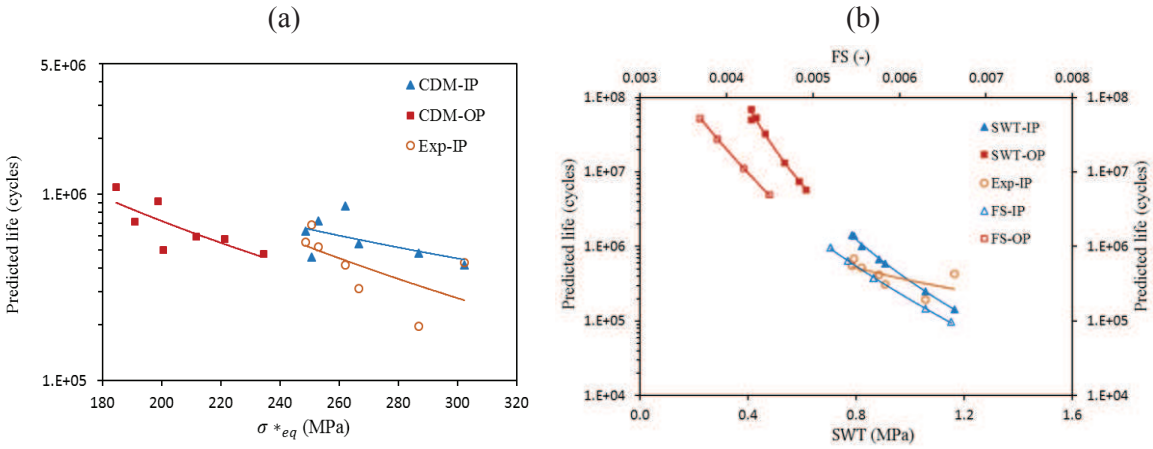

Figure 73. Variation of initiation life with all damage parameters with phase difference using (a) CDM and (b) CP approach.

Table 17 quantifies the increase in life, for out of phase loading, predicted by both approaches. It can be seen that with CDM approach the ratio of out of phase to in-phase loading ranges from 1.06 to 1.52, whereas, with CP approach this ratio escalates up to 140.43, which implies that initiation life for out of phase loading is 140 times more than for in phase loading. To this end, it was observed that both approaches showed significant difference in life prediction under out of phase loading. Since for case 1, experimental results were not available for out of phase loading therefore it could not be ascertained which approach is more accurate. To compare the prediction accuracy with both approaches, case 2 was considered in the study where numerical results were also compared with experimental results for both in phase and out of phase loading conditions.

Table 17. Ratio of out of phase to in phase nucleation life ($N_{i\text{-}OP}/N_{i\text{-}IP}$)

Exp. Nr.	SWT	FS	CMD
1	23.29	28.45	1.10
2	37.78	54.52	1.12
3	29.35	33.47	1.19
4	75.63	140.43	1.06
5	39.82	49.98	1.15
6	67.46	81.19	1.52
7	22.33	29.73	1.09

5.4.2 Case 2: Cyclic P and phase difference between P and σ_A, Q

In this section both approaches are compared using another experimental data for which experimental results were also available for out of phase loading condition. Before presenting the comparison for crack initiation location and life, the case study is explicated first along with numerical propagation life, variation of contact stresses and effect of variable contact load on stick zone. The experimental data and material properties were taken from [130].

Almajali [130] studied the effect of phase difference between normal load and the axial /tangential load for titanium alloy. The test setup included two servo hydraulic actuators capable to vary magnitude, frequency and generate phase difference between normal *P* and axial load σ_A. They conducted several experiments, in which axial stress was varied with the ratio of 0.1. The normal load varied from maximum of 4448 N to minimum value of 2224 N. The values of the tangential loads i.e. Q_{max} and Q_{min} were measured experimentally for in phase and out of phase loading tests. The radius of the pad *R* used in all experiments was 50.8 mm. The coefficient of friction μ used for the study was 0.5 for all experiments. The found that by applying phase difference, fretting fatigue life increased from 30% to 150% (depending on stress range) as compared to in phase loading. Here, the experimental data is selected for test cases where the phase difference was generated with the same loading magnitudes as applied for in phase loading. Table 18 shows the experimental data used in this study.

Table 18. Experimental data from fretting fatigue tests for case 2 [130].

Exp. Nr.	P_{max} (N)	P_{min} (N)	σ_{Amax} (MPa)	σ_{Amin} (MPa)	Q_{max} (N)	Q_{min} (N)	∅	$N_{f,exp}$ (cycles)
1	4448	2224	564	56	475.7	−824.3		47298
2	4448	2224	413	41	403	−555	IP	229477
3	4448	2224	376	37	219.5	−648.5		657432
4	4448	2224	564	56	218.4	−912.8		61428
5	4448	2224	413	41	110	−715	OP	275172
6	4448	2224	376	37	58.3	−682.3		1706847

Both parts, pad and specimen, were of same material i.e. Ti-6Al-4V. The geometrical dimensions of both parts are given in Table 19. The yield strength, σ_y, of the material was 930 Mpa, Poisson's ratio, ν, was 0.33 and modulus of elasticity, *E*, was 126 GPa. The critical plane approach uses strain life constant to determine initiation life. For this case, strain life constants were taken from work of Madge et al. [132]. σ_f' and ε_f' were 714 MPa and 0.166 respectively, while *b* and *c* were − 0.078 and − 0.538, respectively.

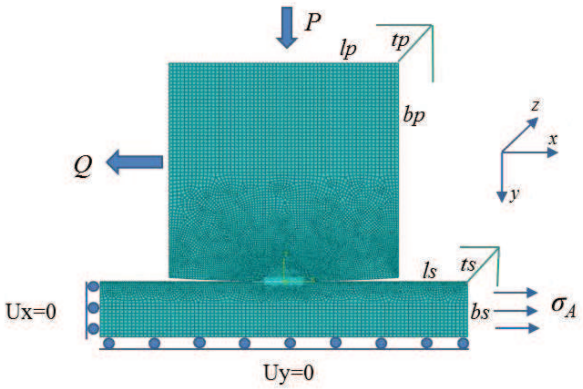

Figure 74. Numerical model with geometrical description.

The loads were applied in five steps (0 to 4) as shown in Figure 75. The axial stress σ_A and tangential load Q were applied using phase difference with normal load P. However, axial stress and tangential load were in phase with each other. The axial stress and tangential load achieved maximum and minimum values at step 1 and 3, respectively. The out of phase loading was applied as measured in the experimental work of Almajali [130]. From the experimental data mentioned in Table 18, it can be seen that the load ratios R_P = 0.5, R_σ= 0.1 and R_Q varies as measured in the experiment [130].

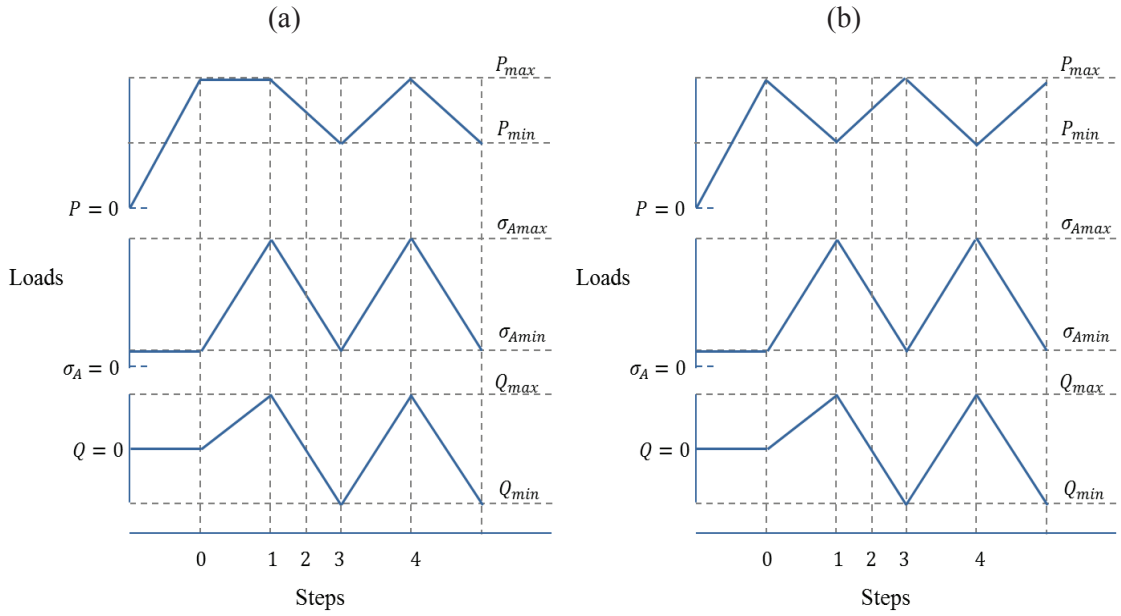

Figure 75. Loading sequence for (a) in-phase and (b) out of phase loading. P is normal load, σ_A is axial stress and Q is tangential load.

Table 19. Geometrical dimensions of pad and specimen.

Material	*R* (mm)	*ls* (mm)	*bs* (mm)	*ts* (mm)	*lp* (mm)	*bp* (mm)	*tp* (mm)
Ti-6Al-4V	50.8	19.05	1.905	6.35	9.525	9.525	6.35

5.4.2.1 Estimation of propagation life

The experimental results for this case were reported for total failure life. Therefore, in order to compare numerical results with the experimental ones, propagation life was numerically determined and added to the predicted initiation life to get the total numerical life. The conventional finite element method with re-meshing technique was used to model the propagation phase, taking into consideration possible contact interaction between the crack faces. Giner et al. [192, 193] showed that, proper modelling of crack faces interaction is essential for a good numerical prediction of propagation phase.

The same model details (dimensions, material properties, boundary conditions, mesh details and loading conditions) were used as shown in Figure 74, with the addition of a crack to the specimen. The initial crack lengths of 1 mm and 20 μm were inserted at the trailing edge of the contact for CDM and CP approaches, respectively. For critical plane approach, propagation life was computed from 1mm crack length since strain life parameters (used in initiation phase) were evaluated for 1mm depth and for CDM approach, it was computed from 20 μm as this length was used as the critical radius for initiation phase. The crack initiation orientation of 35° was used for in phase and 23°, 17° and 15° for out of phase tests respectively as measured numerically by critical plane approach.

For detailed procedure on numerical estimation of propagation life, the readers are referred to [194]. The following stepwise procedure was performed: the stress intensity factors K_I and K_{II} were obtained for each time increment of the fretting loading cycle. These stress intensity factors were then used to determine the propagation direction, based on the orientation criterion proposed by Hourlier et al. [195], which is an extension of the maximum tangential stress criterion for a non-proportional loading case. The crack was then advanced in this direction by a fixed length increment of 30 μm during the first 30 increments of crack propagation and by a length increment of 60 μm for the remaining steps of propagation, until final rupture of the specimen. The model was re-meshed and re-analysed after each increment of crack length.

The stress intensity factors were also used to estimate the propagation life by integrating Paris' Law. The propagation life was considered as the number of cycles N_p necessary to cause a crack growth from an initial length l_i until a critical failure length l_f and can be estimated as:

$$N_p = \int_{l_i}^{l_f} \frac{dl}{C\Delta K^m} \tag{190}$$

where C and m are material constants, $C = 1.25\text{x}10^{-11}\ (\text{mm/cycle})/\left(\text{MPa}\sqrt{\text{mm}}\right)^m$ and $m = 2.59$ [132], dl is the infinitesimally small increment in crack length and ΔK is the stress intensity factor range. For mixed-mode conditions, ΔK can be evaluated as [196]:

$$\Delta K = \Delta K_{eff} = \sqrt{\Delta K_I^2 + \Delta K_{II}^2} \tag{191}$$

where, ΔK_I and ΔK_{II} are the stress intensity range at crack tip for mode I and II, respectively.

5.4.2.2 Variation of contact stresses

Figure 76 shows the tensile stress, σ_{xx}, shear traction $q(x)$ and normal stress $p(x)$ at the contact interface at step 1 and 3 during the loading cycle. Figure 76 (a) shows that at maximum loading condition, maximum tensile stress is produced at the trailing edge of the contact. The shear traction profile at the contact interface shows, in Figure 76 (b), the presence of reverse slip at step 1. This implies that the normal pressure is insufficient to prevent the occurrence of reverse slip. The reverse slip is generated, if axial stress is significant compared to tangential load and thereby violating Eq. (23). For larger values of applied stress one edge of the stick zone $\pm c$ reaches the edge of the contact $\pm a$ and generates reverse slip at one edge of the contact. The normal stress $p(x)$ intuitively is maximum at the center of the contact and follows parabolic curve reducing to zero at the both edges as shown in Figure 76 (c). Since the normal load at step 3 is lower than that at step 1, the normal stress at step 3 is lower than that at step 1. All the stresses are higher at step 1 as compared to step 3. It is also interesting to note that just outside the contact zone shear stress and normal are zero at any stage of the load history. Whereas the tensile stress still persist along x-axis, although tends to reduce just outside the contact.

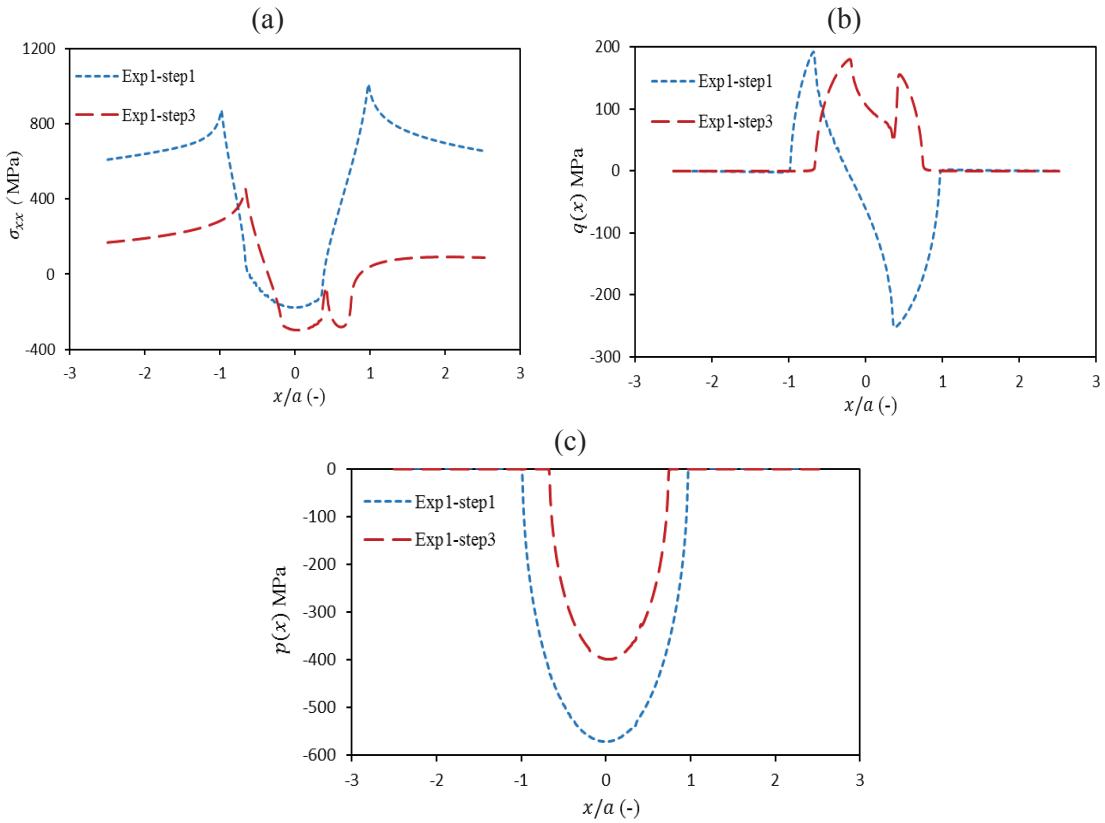

Figure 76. Variation of (a) tensile stress and (b) shear traction (c) normal stress at contact interface at step 1 and 3 during loading cycle, for Exp. 1.

5.4.2.3 Effect of variable contact load on stick zone

The size of contact width, $2a$, changes with the change in normal load and therefore stick zone width also changes accordingly. In this section, the effect of normal load on stick zone size is analyzed under variable and out of phase loading conditions. From Eq. (192), it can be seen that stick zone size depends on normal load and tangential load. Figure 77 shows the variation of relative displacement, d_x, along the contact interface for in phase and out of phase condition. At the stick zone, the relative displacement between the pad and specimen is zero. Figure 77 (a) shows that the stick zone at step 1 is larger than stick zone at 3 due to higher normal load at 1 for both representative experiments 1 and 3. In addition, for any particular instant (let's say step 1) the stick zone size for experiment 1 was smaller than for experiment 3. Due to lower tangential load for experiment 3, the contribution of normal load thus increased.

$$c = \frac{2P}{\pi p_0 t}\sqrt{1 - \frac{Q}{\mu P}} \tag{192}$$

For out of phase loading, Figure 77 (b), the stick zone size remains same at step 1 and 3 for both representative experiments 4 and 6. As both loads achieved maxima at different time instant and therefore they compensated the effect of each other. For this case also, at lower tangential load (experiment 6) the stick zone size appeared to be larger than at higher tangential load (experiment 4). Therefore, stick zone width and contact width changed during the loading cycle.

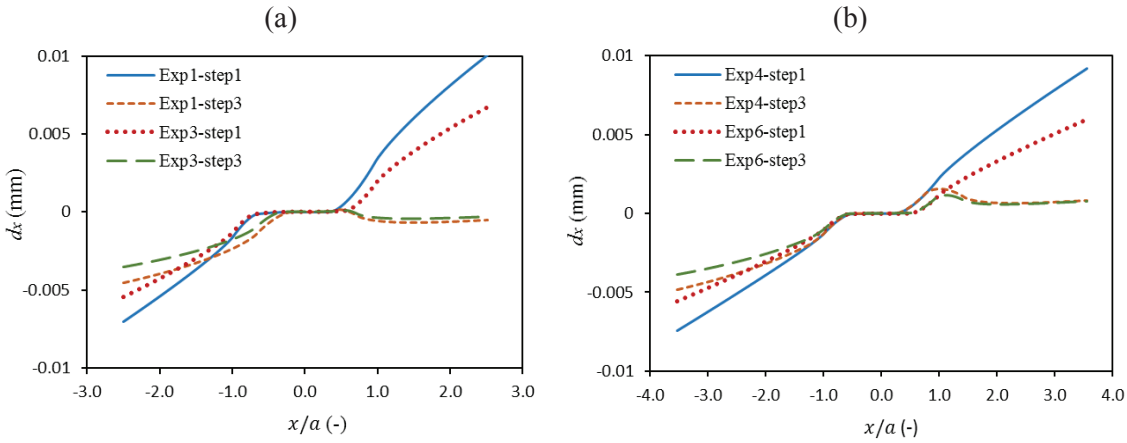

Figure 77. Variation of relative displacement in the stick-slip zone, at step 1 and 3 of the loading cycle (a) Exp. 1 and Exp. 3 (IP). (b) Exp. 4 and Exp. 6 (OP)

5.4.2.4 Comparison of initiation location

The damage initiation location predicted by both approaches is compared with experimental results. The experimental results showed that damage initiated at the trailing edge (x/a =1) of the contact for all in phase and out of phase test cases [130]. Figure 78 shows the variation of all damage parameters at the contact interface. The results are plotted for experiments 1 and 4 to represent in phase and out of phase condition, respectively. It was observed that both approaches predicted damage initiation location at the trailing edge of the contact. The initiation location predicted by CDM approach varied from $0.962 \leq x/a \leq 0.989$ for all tests. For SWT and FS parameters, the predicted initiation location varied from $0.962 \leq x/a \leq 0.998$ and $0.956 \leq x/a \leq 0.981$, respectively. Hence, with both approaches good correlation was observed between experimental and numerical results. It is also interesting to note that for case 2 with out of phase loading, the initiation location was same as in phase loading i.e. at trailing edge. However, for

case 1, it was observed that for out of phase loading two peaks of damage parameters were observed, which implies that initiation could occur at any side of the edges. These results also show that the type of loading sequence affects the initiation location.

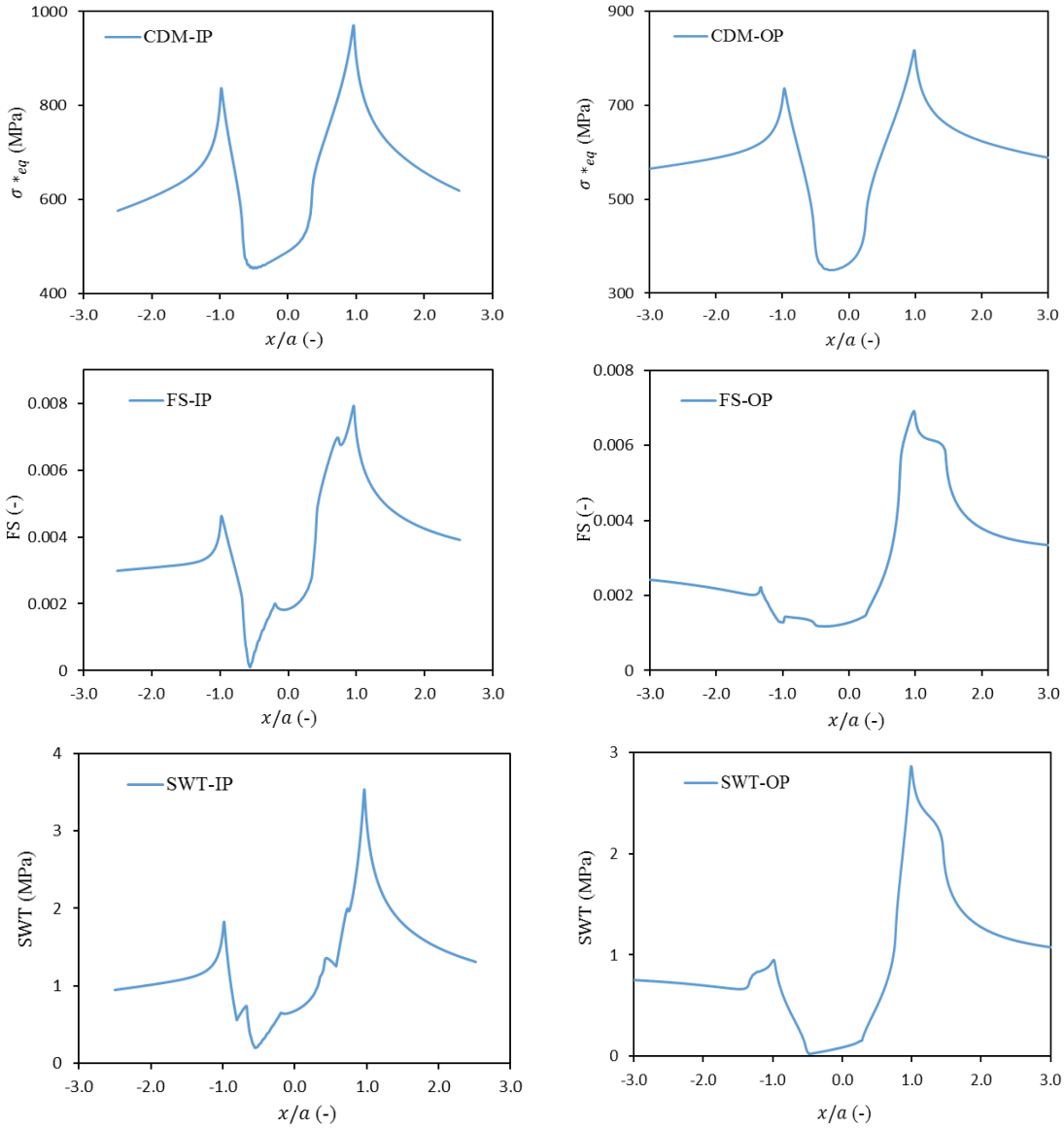

Figure 78. Variation of damage parameters at the contact interface for Exp. 1 (IP) and Exp. 4 (OP).

5.4.2.5 Comparison of fretting fatigue life

The ratio of predicted life for out of phase to in phase loading is presented in Table 20 and compared with experimental ratio. The maximum deviation was observed for data set of experiment 3 where tangential load and applied axial stress was minimum. Figure 79 (a) and (b) provides the comparison of experimental and numerical results for both approaches. The fretting fatigue life for out of phase loading was found to be higher than in phase for this case also. In addition, it was observed that at higher amplitude of loads, the order of magnitude for out of phase loading was closer to in phase loading and deviated at the lower loads. For CDM approach, all data was found within ±3 N_f band for both in phase and out of phase tests. However, with CP approach for in phase test all data was within ±3 N_f band, whereas larger deviation was observed for some out of phase tests. The cause of this deviation may be due to the fact that FS parameter is mainly formulated for cases where failure occurs predominantly in mode II manner. The experimental results showed that failure occurred under tensile mode, therefore the accuracy of criterion may be affected under out of phase loading condition.

Table 20. Ratio of out-of-phase to in-phase fretting fatigue life ($N_{f\text{-}OP}/N_{f\text{-}IP}$).

Exp. Nr.	SWT	FS	CDM	Exp.
1	2.38	1.99	1.80	1.298
2	4.83	6.56	3.31	1.199
3	6.55	10.27	4.05	2.596

The implemented CDM approach uses the combination of experimental and numerical technique to determine the damage constant. These constants are material and temperature dependent and therefore may require to be estimated when experimental data is not available in literature. On the other hand, for CP approach the fatigue properties and strain life constants are determined experimentally. However, the prediction of fretting fatigue life is very sensitive to strain life constants. Under out of phase loading conditions, a slight change in damage parameter caused a significant change in fatigue life. Better prediction of life (for both approaches) can be achieved if the related constant are determined experimentally for each load ratio and phase difference.

Experiments related to both cases considered in this study showed that the failure predominantly occurred in mode I. The CDM approach used in this study, is still required to be verified for the cases where failure occurs predominantly in mode II as they may have a significantly higher propagation life. However, researchers have successfully used the shear based critical plane approaches to predict fretting fatigue life for mode II dominant failure.

The current study did not provide a comparison of initiation angle between different approaches, since CDM approach is based on energy (which is a scalar quantity), it has a disadvantage of not providing the information of initiation angle. However, CP approach based on shear stress or strain, can predict initiation angles. To study damage initiation mechanism for fretting fatigue conditions under out of phase loading, the selection of preferred approach or criteria depends on various factors like loading magnitudes, phase difference, load ratio and material under study.

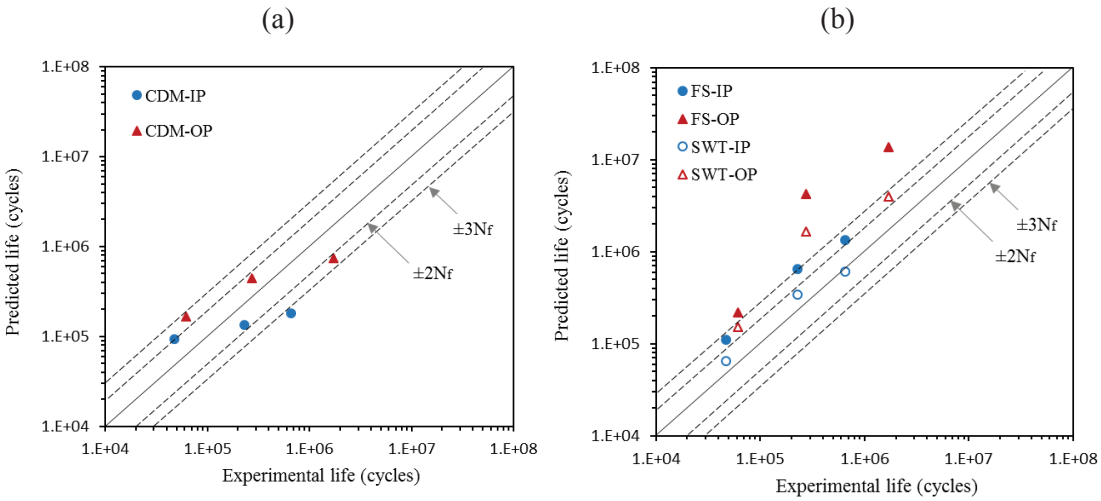

Figure 79. Comparison of predicted life with experimental life using (a) CDM and (b) CP approach.

5.5 Effect of triaxiality function on initiation life

Continuum Damage Mechanics (CDM) approach provides a tool to study damage nucleation under plane and fretting fatigue conditions. As fretting fatigue involves multiple loads in different directions, therefore multiaxial and non-proportional stresses may be produced. In addition, if the phase difference exists between the applied loads, the degree of non-proportionality between the stresses may be increased. This section presents the effect of non-proportional loading on damage nucleation. For this purpose, the derived damage model for non-proportional loading (CDM-NPL) is applied to cylindrical pad and flat specimen configuration. The numerical results are also compared with CDM-PL model to analyse the effect of triaxiality function variation. Thus, a comparison of crack initiation life using the two above mentioned damage models, with experimental results is presented. In addition, sensitivity analysis is preformed showing the effect of related parameters on crack initiation life using modified damage model. The experimental data and numerical model for this study is same as shown in Figure 74, Figure 75, Table 18 and Table 19.

Before analysing the efficacy of the damage model, the variation of parameters related to damage nucleation under non-proportional loading is analysed. In fretting fatigue the damage initiates at the surface, therefore areas of interest include the contact interface and high stress concentration area near the contact edge. Also, triaxiality function varies with respect to time for non-proportional loading, thus it is imperative to analyze its variation over the contact interface and also with respect to time. Figure 80 (a) shows the distribution of triaxiality function at the contact interface for the in-phase tests. It was observed that at the centre and at the edges of the contact R_v was greater than 1, whereas inside the slip zone it was less than 1. For the case of uniaxial loading R_v= 1 (for $\nu = 0.3$) and the damage equivalent stress reduces to σ^*=σ_u. For multiaxial stress states, R_v >1 and an increase in the triaxiality function reduces the fatigue limit. By defining $T_r = H/S$, the regions where R_v is greater than 1, can be determined as:

$$\frac{2}{3}(1+\nu) + 3(1-2\nu)(T_r)^2 > 1 \tag{193}$$

$$(T_r)^2 > 0.111 \tag{194}$$

This implies that $R_v > 1$ for the regions where triaxiality ratio $T_r > 0.33$ or $T_r < -0.33$. In addition, it was observed that due to higher axial stress σ_A and tangential load Q for experiment 1 (than 2 and 3), the contribution of deviatoric part was higher and thus reduced the value of R_v. For out of phase loading, shown in Figure 80(b), distribution of R_v is similar to in phase loading, however, magnitude of R_v is lower for all cases due to asynchronous loads. For both figures, the results were extracted at step 1 of the loading cycle. It shows that phase difference only causes the scaling of magnitude without causing any change in distribution of triaxiality function. Furthermore, it was observed that R_v varied inside the contact zone and converged to a single value at the edges of the contact for any loading sequence.

Figure 81 shows the variation of different stresses at the contact interface for experiment 4. It is interesting to note that both von Mises (S) and hydrostatic static stress (H) showed the peak value at the trailing edge of the contact. The tensile stress σ_{xx} also showed the maximum value at the same edge, which matches the damage initiation location observed in the experiments [130]. The same initiation location is observed by many researchers in their studies [23, 48, 88, 115]. More precisely, the damage equivalent stress (σ^*), can be used to determine initiation location using CDM approach [58, 165].

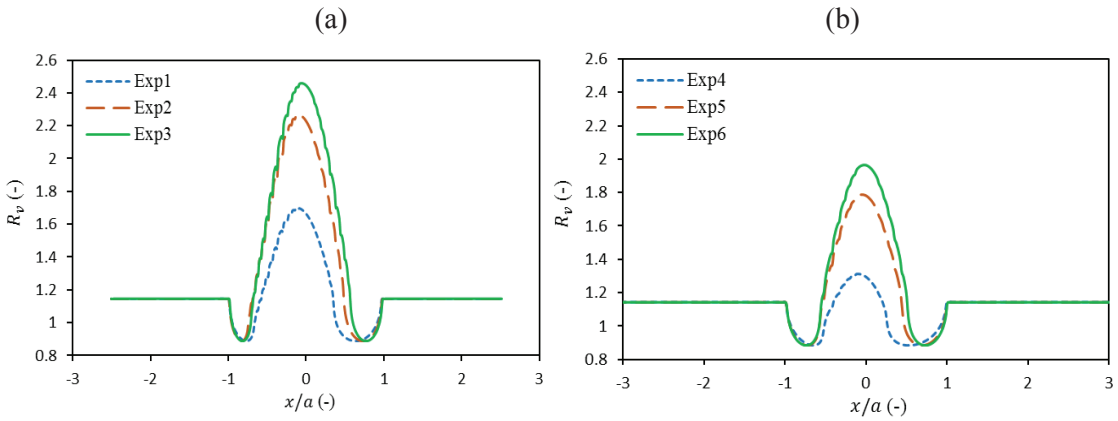

Figure 80. Triaxiality function at maximum axial stress for (a) in-phase loading and (b) out of phase loading.

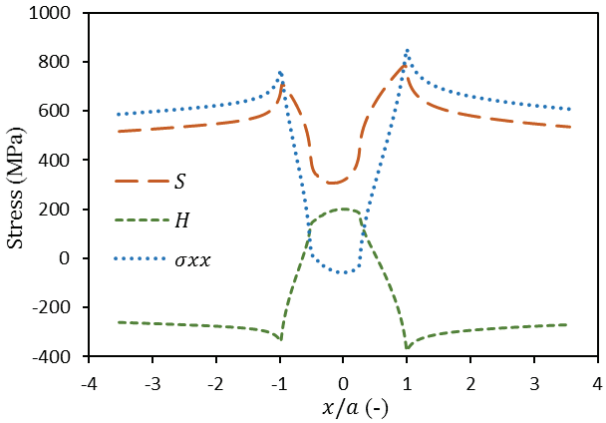

Figure 81. Variation of von Mises (S), hydrostatic (H) and tensile stress (σ_{xx}) at contact interface for Exp. 4.

The multiaxial damage equivalent stress, σ^*, is a combination of von Mises stress and triaxiality function, therefore it is also interesting to analyze the variation of both parameters with respect to time. The variation of these parameters eventually leads to variation of initiation life, which is shown in a later section as a sensitivity analysis. Figure 82 (a) and (b) presents the variation of von Mises stress for in phase and out of phase loading, respectively. It was observed that due to cyclic loads, stress vary with respect to time. Once again, the impact of out of phase loading only reduced the magnitude of stress, however, no change in pattern was observed. The highest stresses were observed at an instant when applied cyclic stress σ_A reached the maximum value, similarly lowest stresses were observed at minimum σ_A, for all experiments.

Figure 83 (a) shows the variation for of triaxiality function at different instants for in phase tests. The value of R_v was computed at the location of damage nucleation inside the critical radius as explained in the section 4.3.4. It was found that for in phase loading there was almost no variation of R_v during the complete loading cycle. However, for out of phase loading as shown in Figure 83 (b), R_v varies at different instants during the cycle. Since the stress ratio varies with time, therefore triaxiality function is also cyclic in nature, however, the magnitude of variation depends on the magnitude of loads and phase difference. This shows the existence of non-proportional stresses under out of phase condition. For the cases considered, R_v varied from 0.8 to 1.4 (approximately) over the complete loading cycle. Therefore, inclusion of triaxiality function variation in damage evolution law may provide more realistic prediction of fretting fatigue crack initiation life.

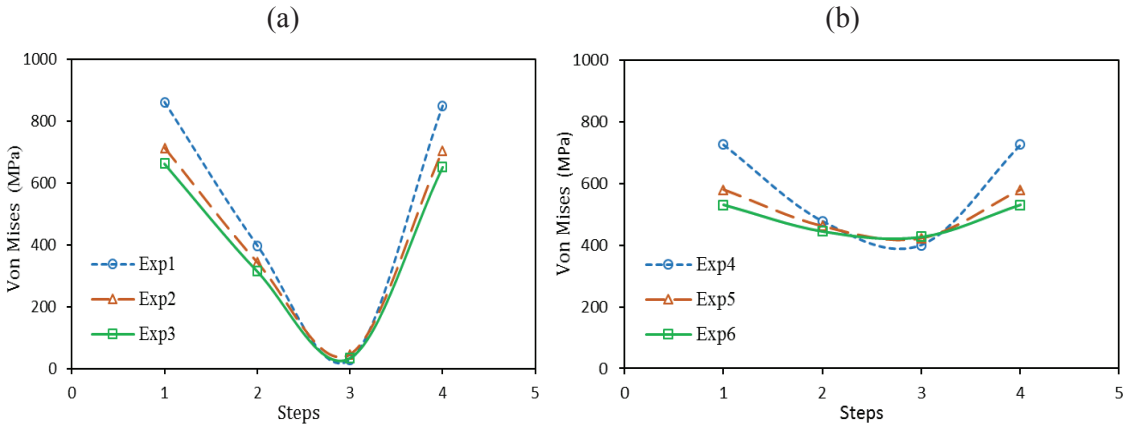

Figure 82. Variation of von Mises stress for (a) in phase and (b) out of phase tests at different time steps.

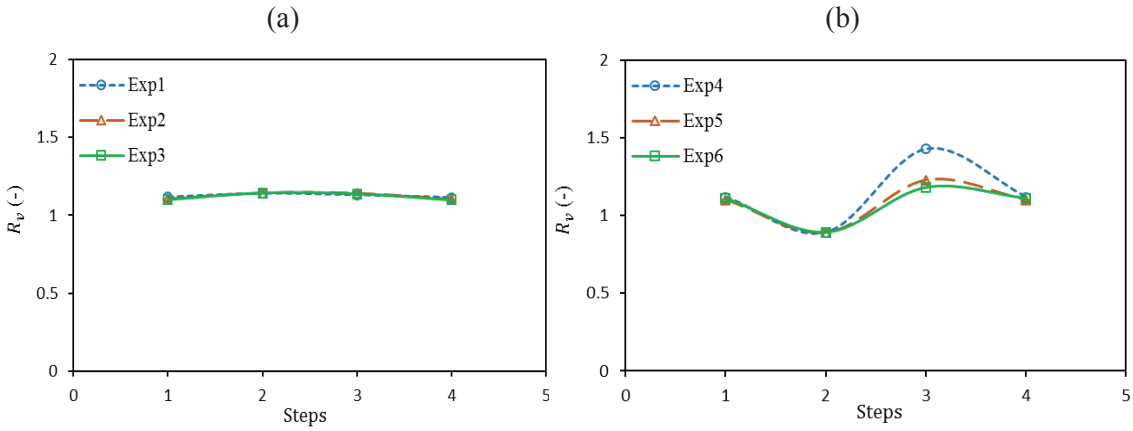

Figure 83. Variation of triaxiality function over one complete cycle for (a) in-phase and (b) out of phase tests.

5.5.1 Comparison of crack initiation lives

Considering the initial (D=0 at N=0) and final conditions (D=1 at N= Ni), the damage variable D varies between 0 and 1. The non-linearity of the phenomenon depends on the damage exponent. By using Eq. (170) the damage evolution with respect to number of cycle to initiation can be analyzed. Figure 84 shows the variation of damage for all experiments. The damage variable was computed at damage initiation location inside critical radius, where initiation location was determined by locating maximum σ^* at the contact interface. It was observed that for higher loading magnitude the damage variable converged faster than for lower magnitudes. This implies shorter lives at higher loads and vice versa. Furthermore, it was observed that for similar magnitude of loads, D reached to 1 much earlier for in phase cases, which implies shorter lives for in phase loading than for out of phase loading. The CDM-NPL model showed that the damage accumulation is highly non-linear.

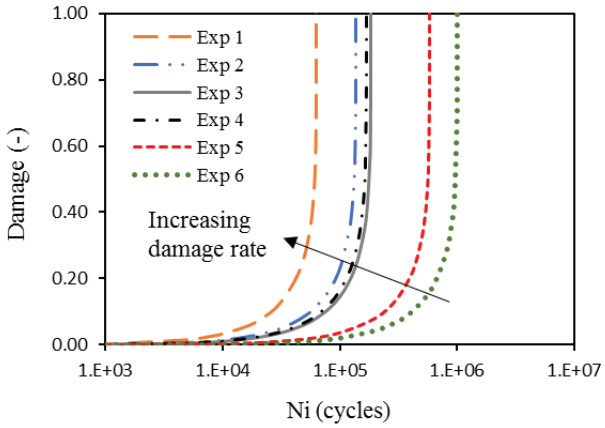

Figure 84. Evolution of damage with number of cycles to initiation using CDM-NPL.

By using the damage model CDM-NPL, the initiation lives can be predicted using Eq. (171). The value of α for this case was found to be 9.5×10^{-18}. Figure 85 shows the comparison of predicted initiation lives and experimental failure lives. A good correlation was observed between experimental and numerical lives as most of the data was found within ±3N scatter band. For comparison purpose the predicted lives are also plotted using the previous damage model CDM-PL. The crack initiation lives using CDM-PL are taken from previous section 5.4.2, where it was observed that the numerical propagation lives only accounted for 10~15% of the total life. Therefore, to avoid the inclusion of errors by numerical propagation lives, they are neglected for statistical analysis. The accuracy and dispersion of both models can be determined by using set of Eqs. (182) to (186). Table 21 shows the comparison of statistical analysis for both damage

models. By including the variation of triaxiality function in damage model both mean $\bar{x}$ and dispersion SD_x are improved to some extent as both values are relatively closer to 1. Although the improvement in life prediction is not much significant for the analysed case study, however, the approach can be useful where magnitudes of loads or degree on non-proportionality are much higher.

Table 21. Comparison of normalized mean and standard deviation.

Damage model	$\bar{x}$	SD_x
CDM-PL	0.77	2.67
CDM-NPL	0.94	2.40

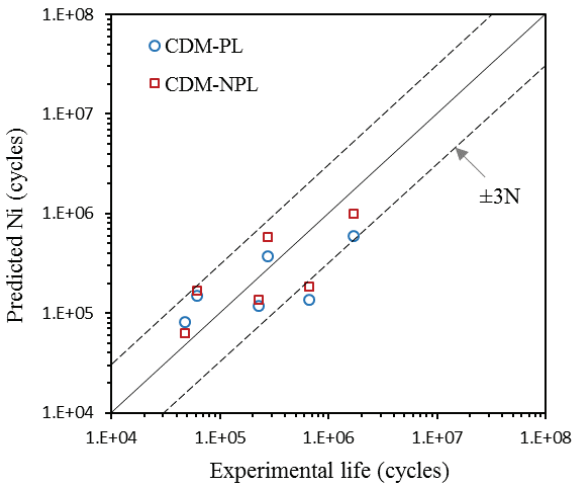

Figure 85. Comparison of predicted life using CDM-PL and CDM-NPL with experimental results.

5.5.2 Sensitivity analysis

The effect of stress range and triaxiality function range on initiation life is studied using CDM-NPL. For sensitivity analysis, the numerical results of experiments 1 and 4 are used to represent in phase and out of phase cases, respectively. The stress range was calculated by varying the stress from average value to the minimum value and triaxiality function range was calculated by varying value from minimum to maximum observed during one cycle. By changing one parameter at a time, its effect on initiation life was studied. For in phase loading, as shown in Figure 86 (a), it is observed that initiation life remains almost constant with change of R_v since its variation was very small within one loading cycle (see Figure 83a). Whereas, the effect of stress range is found to be more pronounced and initiation life changes exponentially, as shown in Figure 86 (b).

For out of phase loading, shown in Figure 87 (a), logarithmic variation in initiation life is observed for change in R_v. The graph shows very small variation in initiation life at lower ranges of triaxiality function, however at higher ranges the variation is significant. The sensitivity analysis shows that, at ΔR_v nearly equal to 0.5, change in initiation life becomes prominent. However, in order to generalize the threshold value where variation in triaxiality function makes an impact on crack nucleation life, further studies are required with different material, loads and phase difference. Once again, an exponential trend is observed with variation in stress range as presented in Figure 87(b). The results showed that for in phase loading, initiation life was only influenced by stress range whereas for out of phase or non-proportional loading both stress and triaxiality function ranges affected initiation life.

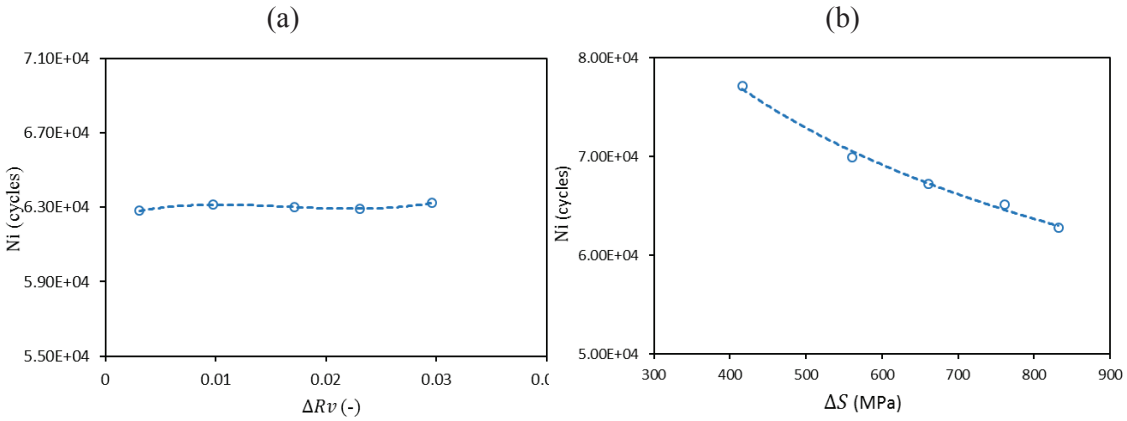

Figure 86. Effect of (a) triaxiality function and (b) von Mises equivalent stress range on number of cycle to initiation, for test 1.

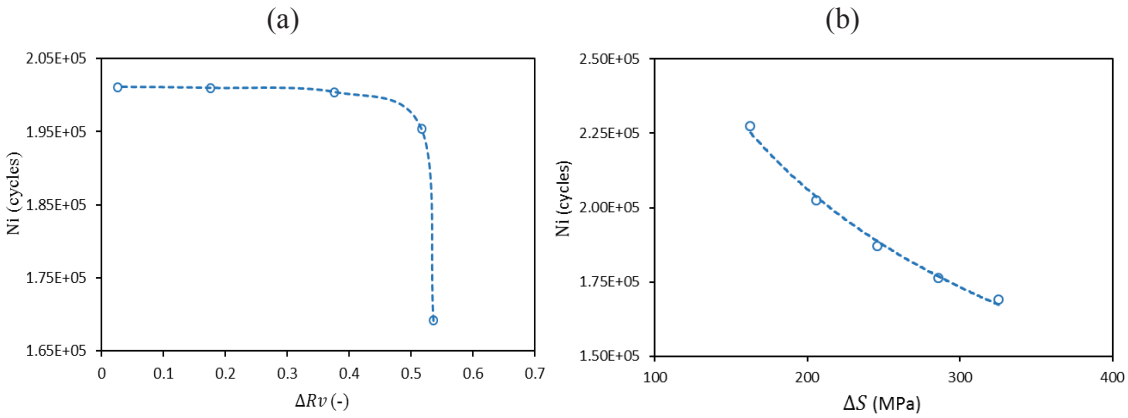

Figure 87. Effect of (a) triaxiality function and (b) von Mises equivalent stress range on number of cycle to initiation, for test 4.

5.6 Comparison between CP and SI approach

Previously, for life estimation, critical plane (CP) and continuum damage mechanics approaches are discussed and compared. This section, aims to compare Stress Invariant (SI) and CP approach. Smith Watson Topper (SWT), McDiarmid (MD) parameters, which represent critical plane approach, and Crossland parameter (CL) which represents SI approach, are adopted for this purpose. These parameters are applied to cylinder on a flat configuration and predicted numerical results are also compared with experimental results from literature.

The experimental data for the present numerical work is taken from the work of Hojjati-Talemi et al. [48]. They performed fretting fatigue experiments on Al 2024-T351 (for both pad and specimen) to study crack nucleation behavior. All tests were performed with axial stress ratio of R_σ = 0.1 and tangential load ratio of R_Q = −1 with a frequency of 10 Hz. The normal load was kept constant at 534 N for all tests. The cross section of the specimen was 10 × 4 mm and the radius of fretting pad was 50 mm. The yield stress and ultimate tensile strength of the material were found as 383 and 506 MPa, respectively. The modulus of elasticity, E = 72.1 GPa and Poisson's ratio, ν = 0.33, for both parts. The total life time for all cases were recorded after complete failure of the specimen. The summary of loading conditions and recorded life cycles, used in the present work are tabulated in Table 22. For further details on experimental setup and material composition, readers are referred to [48].

Table 22. Experimental data for fretting fatigue tests [48].

Test number	σ_A (MPa)	P (N)	Q (N)	N_f (cycles)
1	160	543	193.7	245690
2	190	543	330.15	141890
3	205	543	322.1	114645
4	220	543	267.15	99607
5	220	543	317.845	86647

The experimental results for the present work represents the total fatigue life that includes crack initiation life, as well as, propagation life. Therefore, in order to compute total numerical lives, the propagation lives were also computed by considering crack faces interaction [194]. FEM was used along with re-meshing technique to model propagation phase with an initial crack length of 50 μm and with initial crack orientation of 35°. The procedure adopted, to obtain propagation life, was similar as explained in section 5.4.2.1.

5.6.1 *Crack initiation location*

As mentioned in the previous section, damage parameters were computed at the contact interface. The location of highest value of the damage parameter can be regarded as the damage initiation location. Figure 88 shows a comparison of damage parameters for test 5. The results for other tests are not plotted since the results showed a similar trend. The x-coordinate is normalized with semi contact width, a. All graphs showed the highest peak near the trailing edge of the contact i.e. at $x/a \approx 1$. These results also matched well with the experimental results observed in [48]. This shows that all parameters where equally effective to determine the crack initiation location. The mean initiation location using these parameters are given in Table 23. Similar experimental results were also shown by several authors [59, 118], which demonstrate that the most probable damage initiation site is at the trailing edge of the contact, especially under partial slip regime. The difference of magnitude between the parameters exist due to the fact that SWT parameter is based on normal stress and strain whereas MD and CL parameters are based on shear stress and stress invariants, respectively.

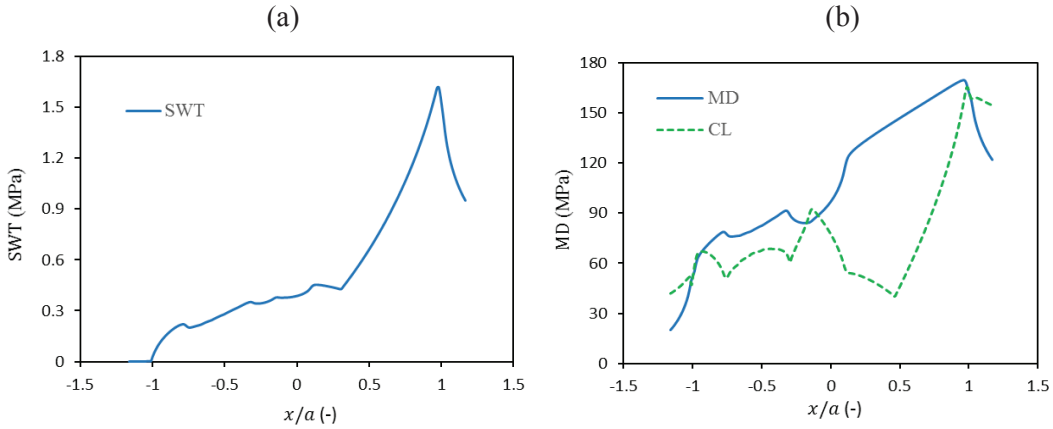

Figure 88. Variation of damage parameter at contact interface with (a) SWT (b) MD and CL parameter - graphs plotted for Test 5.

5.6.2 *Fretting fatigue life*

To compare total predicted lives with experimental results, both nucleation and propagation lives were added. The results are shown in Figure 89 (a) and it is found that most of the predicted data lie with in ±2 N error band. For critical plane approach, all numerical values were observed with in ±3 N band, however, for SI approach, larger deviation was observed at higher number of cycles to failure. Figure 89 (a) shows that CP approach is better for life estimation for both HCF and LCF regimes, whereas SI approach may lead to larger deviations at

HCF. This fact is plotted in Figure 89 (b), where it can be seen that for CP approach the error almost remains constant with increasing number of cycles. On the other hand, the error escalates for SI approach with increase in number of cycles to failure.

The life prediction capability for both approaches can be measured by computing normalized mean, $\bar{x}$, and standard deviation, SD_x, and the results are summarized in Table 23. The value of $\bar{x}$ equals 1 represents that the mean of all predicted value lie at the diagonal line, which characterizes perfect prediction. The value of SD_x describes the scatter or dispersion of the predicted data. Hence, both values closer to 1 indicate good prediction. It was observed that dispersion for both approaches is nearly same, whereas significant difference was observed for mean life.

Since the results of SI approach showed significant difference for in phase loading, therefore, no phase difference was considered for further analysis.

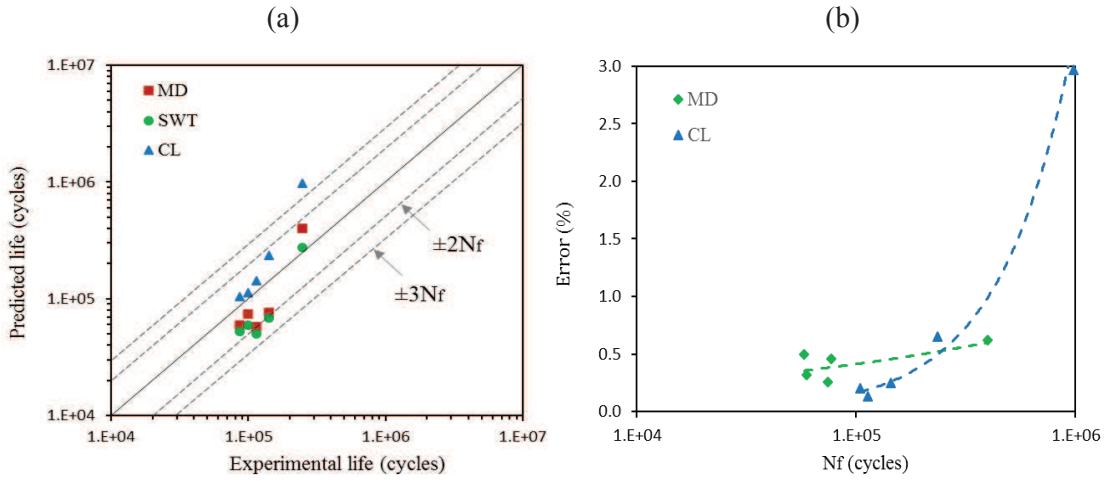

Figure 89. Comparison of (a) fretting fatigue life and (b) % error between MD and CL parameters.

Table 23. Summary of comparison between SWT, MD and CL parameters.

Parameter	x/a	$\bar{x}$	SD_x
SWT	0.991	0.97	1.62
MD	0.972	1.17	1.78
CL	0.995	2.57	1.82

5.7 Effect of stress averaging and gradient

This section presents the effect of stress averaging and gradient on initial crack orientation and life. The previous work related to critical plane approach employed only surface results. However, under fretting fatigue, there can be situation where stress gradient is very high due to geometry and loading magnitudes. For such cases, critical locations may produce singular results and therefore need some regularization method. Considering only surface stresses for such cases, may lead to larger deviations in predicted crack initiation life. Since initiation phase is considered up to few grains of the material, therefore for estimation of crack initiation life, it is more logical to include subsurface results.

The present work is intended to answer three main research questions related to crack initiation under fretting fatigue conditions. First, which averaging method is more suitable to predict crack initiation angle? Second, is it necessary to employ stress averaging techniques, if yes, then for which cases. Third, what is the critical length or radius that should be considered for better life prediction? To answer these questions, a modified stress averaging technique, here in called quadrant method, is presented and compared with existing point method and volume averaging methods. Two cases are considered for this purpose. The first case study consists of cylindrical pad and flat specimen and the second considers flat pad and flat specimen.

5.7.1 Stress averaging methods

To compute multiaxial damage parameters (DP), various methods in vogue are described here. In addition, the proposed method is described in the latter half of the section. Most of the researchers used point method for computation of DP, as shown in Figure 90 (a). In this method, critical plane parameter is computed along the contact interface and for all possible angles, which crack can follow. The point with the highest value of damage parameter is considered as crack initiation location and the angle producing the highest value is recorded as crack initiation angle. This method is adopted by many researchers [59, 60, 88, 110, 114-116, 118, 124, 170, 171, 197]. In this method since no sub-surface stresses are considered, therefore it assumes that the measured crack initiation angle will remain the same beneath the surface. The second method is known as line method, as shown in Figure 90 (b). In this method damage parameter is computed along predefined radial lines. The damage parameter is averaged along these lines and the angle with highest value of the parameter is taken as crack initiation angle. This method was adopted by [114, 124, 198] and has shown some success. However, for the cases where critical zone is small, e.g. 10 μm, this method will only include one or two points near the surface. For stress averaging most of the researchers have used volume stress averaging method, as shown in Figure 90 (c). In this method, after locating maximum damage location, a semi-circular radius is considered where the average value of the damage parameter is computed. This method has been adopted by many

researchers [48, 114, 123-125, 165, 166, 172, 181]. Most often, this method is used with critical plane and continuum damage models, where crack angles are not determined. This method has shown good results to compute crack initiation life. However for estimation of crack initiation angle, it may lead to errors due to the fact the stress state changes rapidly just outside the contact zone.

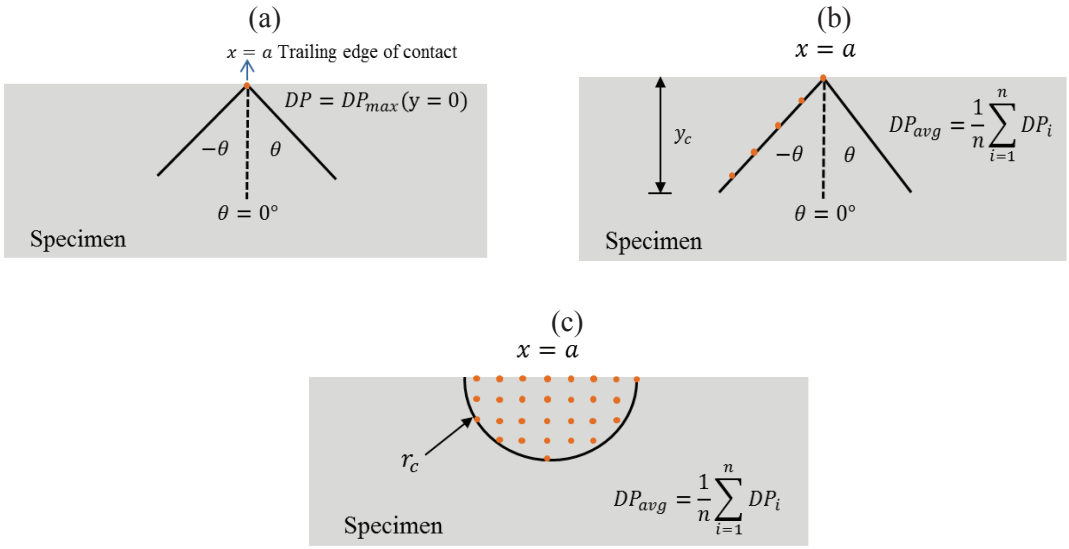

Figure 90. Description of (a) point method, (b) line method and (c) volume averaging method. Sign convention for critical plane orientation is shown using angle θ.

Since we are trying to address the question, if the crack travels inside the contact zone ($-\theta$) or outside the contact zone (θ) after initiation, therefore the process zone can be divided into two regions. In the sequel of the section, the left zone is known as left quadrant, right zone is known as right quadrant and the methods is termed as quadrant method. The idea is to compare the value of the damage parameter in both quadrants and the quadrant with the highest value of the DP is the most probable orientation of crack initiation. In this way, the process zone accounts for the orientation feature of line method and averaging feature of volume method. The concept of quadrant method is shown in Figure 91. The adopted stepwise procedure is described below.

- Contact analysis is performed and stresses are extracted at the contact interface.
- The damage parameter is computed at each node and angle from -90° to 90°.
- The point with the highest value of damage parameter is taken as crack initiation location.
- The process zone of various critical sizes (20, 35 and 50 μm) is used to define the process zone.

- Averaging of the stresses is performed for both left and right quadrants for any particular process zone size.
- The damage parameters are computed for both left and right quadrants. For left quadrant, the highest value of the damage parameter is found by varying θ from -90° to 0°. For right quadrant, the highest value of the damage parameter is taken by varying θ from 0° to 90°.
- The two maxima of both quadrants are compared, and the highest value and corresponding angle is taken to define crack initiation angle.
- Numerical initiation life is measured by taking the highest value of the damage parameter.

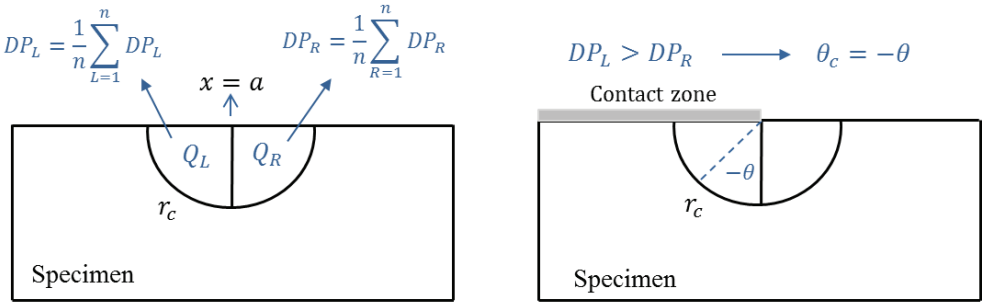

Figure 91. Illustration of quadrant averaging method. Q_L and Q_R represent left and right quadrants, respectively. If $DP_L > DP_R$, crack will grow inside the contact zone i.e. in Q_L

5.7.2 Case 1: Cylindrical pad

Case I consists of cylindrical pad and flat specimen. For this case, two aspects are analysed. First the comparison of different stress averaging methods and point method, to compute crack initiation angle, is presented. Then, effect of stress averaging on fretting fatigue life is shown. Experimental data and material properties for this case are taken from experimental work of Hojjati-Talemi et al. [48]. They conducted fretting fatigue test on Aluminium 2024-T351 to analyse crack orientation and fretting fatigue life. Both fretting pads and specimen had same material properties. The yield strength of the material was 383 MPa and ultimate tensile strength of the material was 506 MPa. The elasticity modulus was 72.1 GPa with Poisson's ratio of 0.33. The width and thickness of the specimen were 10 mm and 4 mm, respectively. The radius of fretting pad was 50 mm for all the tests. Normal contact load P was kept constant to maintain constant fretting load. Tangential load Q was generated with the application of spring stiffness at load ratio of R_Q = -1. The axial cyclic load σ_A was applied with stress ratio of R_s = 0.1. The loads were applied with the frequency of 10 Hz. The loads and experimental failure lives are given in Table 24. The experimental lives are taken for the complete failure of the specimen. The constants for critical plane parameters are taken from [199].

Table 24. Experimental data for cylindrical pad tests [48].

Exp. Nr.	P (N)	σ_A (MPa)	Q (N)	$N_{f,exp}$ (cycles)
1	543	100	155.165	1407257
2	543	115	186.25	1105245
3	543	135	223.7	358082
4	543	135	195.55	419919
5	543	160	193.7	245690
6	543	190	330.15	141890
7	543	205	322.1	114645
8	543	220	267.15	99607
9	543	220	317.845	86647

5.7.2.1 Effect of averaging method on initiation angle

This section demonstrates the application of critical plane methods to estimate initial crack orientation. Researchers have used shear stress or strain based parameters for this purpose. Here, two critical plane parameters MD and FS are considered. Regarding application of these parameters different methods prevail, which may lead to different results. Using numerical results most of the researchers found that the dominant crack angle was oriented out of the contact, $(+\theta)$, whereas most of the experimental results showed the crack initiation orientation inside the contact region $(-\theta)$, according to Figure 90 (a). Szolwinski and Farris [59], Goh et al. [54], Proudhon et al. [125], Hojjati-Talemi et al. [48], Walvekar et al. [200], Vázquez et al. [198] found negative crack initiation angles experimentally. Some researchers also found crack initiation in both directions. The experimental results of Lykins et al. [60, 118] and Namjoshi et al. [110] showed the crack initiation in both directions i.e. $-\theta$ and θ. The numerical results of Lykins [115, 118], Naboulsi and Mall [123] and Li et al. [116] have shown dominant crack angle in positive directions. Although the difference between damage parameters which led to two possible angles predicted by Mohr's circle formulation may be small, however the dominant angles were predicted in positive directions.

In the previous sections, the variation of CP parameters with respect of crack orientation was shown using point method. This section compares the result of point method with volume and quadrant averaging methods. The aim is therefore to develop a strategy, which provides more realistic estimate of crack initiation angle. Figure 92 shows the variation of MD parameter using point method, volume method and quadrant method. For averaging of damage parameter critical radii of 20, 35 and 50 μm are considered. Figure 92 (a) shows the results of point method using data of experiment 1. The damage parameter shows two peaks, 107.48 MPa at θ = 35° and the

other 105.18 MPa at $\theta = -49°$. The value of damage parameter at $\theta = 35°$ is larger, as shown by dotted line. The dominant value of the parameter suggests that the most probable orientation of the crack is out of the contact. The results of volume method are similar to that of point method, as shown in Figure 92 (b). The values of damage parameters are lower than those of point method due to averaging over volume. However, with all critical radii dominant values of damage parameters are found with positive angles. The results of 50 µm are similar to those of 20 and 35 µm, therefore they not shown in the figure. With the increase of critical radius, value of damage parameter decreases accordingly.

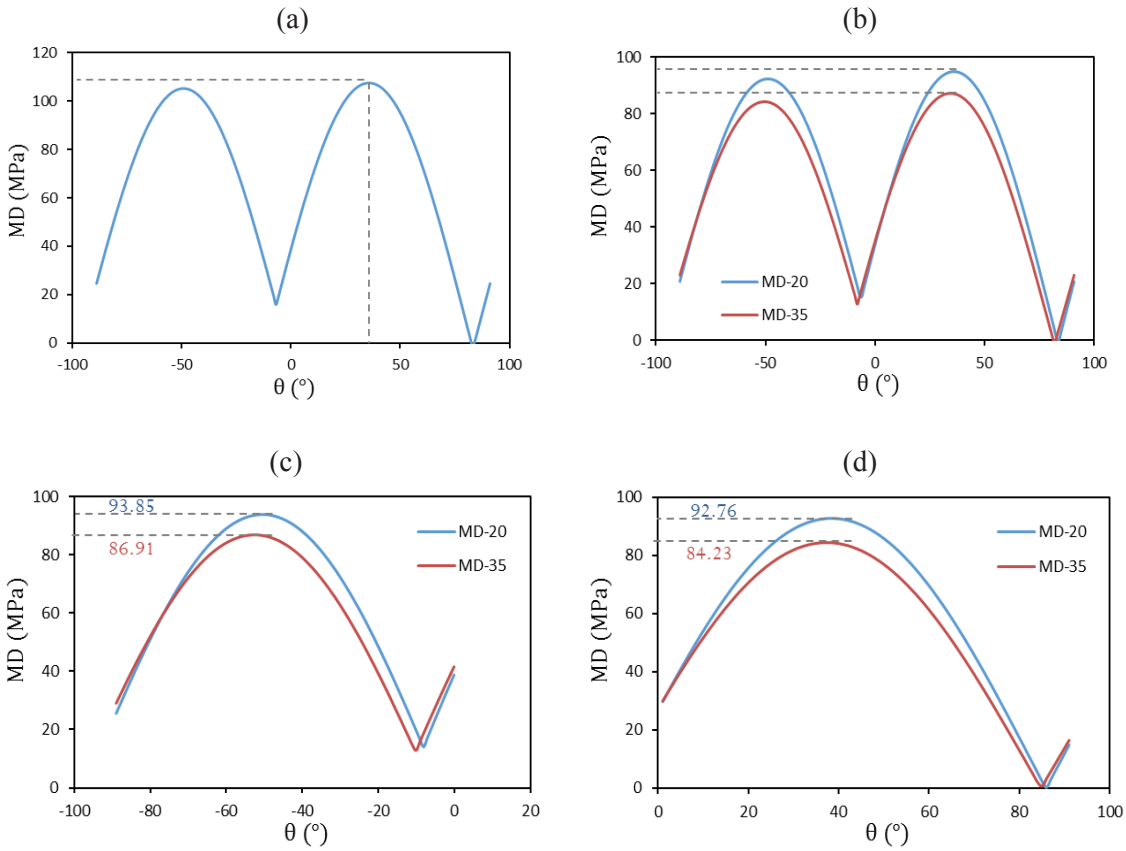

Figure 92. Variation of MD parameter with angle for (a) point method (b) volume method (c) quadrant method-left (d) quadrant method-right; using critical radii of 20 and 35 µm.

The results of the quadrant method are found to be different from other two methods. Figure 92 (c) and (d) shows the results of left and right quadrant, respectively. It is observed that the value of damage parameter in the left quadrant is higher than that of right quadrant. This shows that according to quadrant methods, the probability of crack initiation towards the negative

quadrant (or below the contact zone) is higher than that of positive quadrant. The reason of this difference is due to the fact that stress state changes rapidly below the contact surface. Furthermore, just outside the contact zone (along x-direction) the stress state also changes rapidly. The shear traction and normal stress reach to zero at the edge of the contact i.e. at $x = a$ [171, 172]. Due to unsymmetrical distribution of stresses in x-direction, at the surface and below the surface, the averaging technique plays a role.

With FS parameter, the result of point method and volume method produced the same results as for MD parameter. The dominant angles were observed for positive angles, showing the initial crack orientation going out of the contact for all radii. The variation of FS parameter with orientation angle for point and volume method is shown in Figure 93 (a) and (b), respectively. The results are plotted for data of experiment 1. Using quadrant method, as shown in Figure 93 (c) and (d), the results of FS parameter were found slightly different from those of MD parameter. At critical radius of 20 μm, the value of FS was exactly the same for both left and right quadrants. On increasing critical radius to 35 and 50 μm, the negative quadrant gave the higher FS value. Although the difference seems to be not very large, however it suggests that till depth of 20 μm, crack may take left or right direction. After 20 μm, the probability of the crack to grow inwards is higher than going outside the contact. Crack may therefore change the orientation after 20 μm.

This observation of change of crack path with FS parameter was also observed with the results of experiment 5. For the first 20 μm, the orientation of crack is predicted in the positive quadrant. After 20 μm, the dominant value is found in negative quadrant. The results for all methods, critical radii and experiment 1 and 5 are summarised in Table 25. It can be said that, point method and volume methods produce similar results and predict initial crack growing outwards. The quadrant method predicts crack orientation inwards using MD parameter for all radii. With FS parameter inward orientation is predicted after depth of 20 μm.

The results presented in Table 25 can be compared with experimental crack initiation angles of Hojjati-Talemi et al. [48], since the loading data and martial properties are taken from that study. The experimental results show that for all the specimens crack initiates inwards the contact zone. The initiation angles for all the specimens vary between -35° to -45°. The numerical results show that quadrant method provides more realistic results than the other two. The numerical values for two considered experiments vary between -49° to -54°. The predicted angles are slightly on the higher side, however the proposed approach is able to predict the right direction. In addition, it shows that taking a single value may not be appropriate for estimation of initiation angle, and a suitable averaging technique is thus recommended. Most of the researchers have shown experimentally that crack initiated inwards the contact region. Some researchers also found initiation angles in both directions. The summary of experimentally determined angles from different studies are also given in Table 25 for comparison purpose.

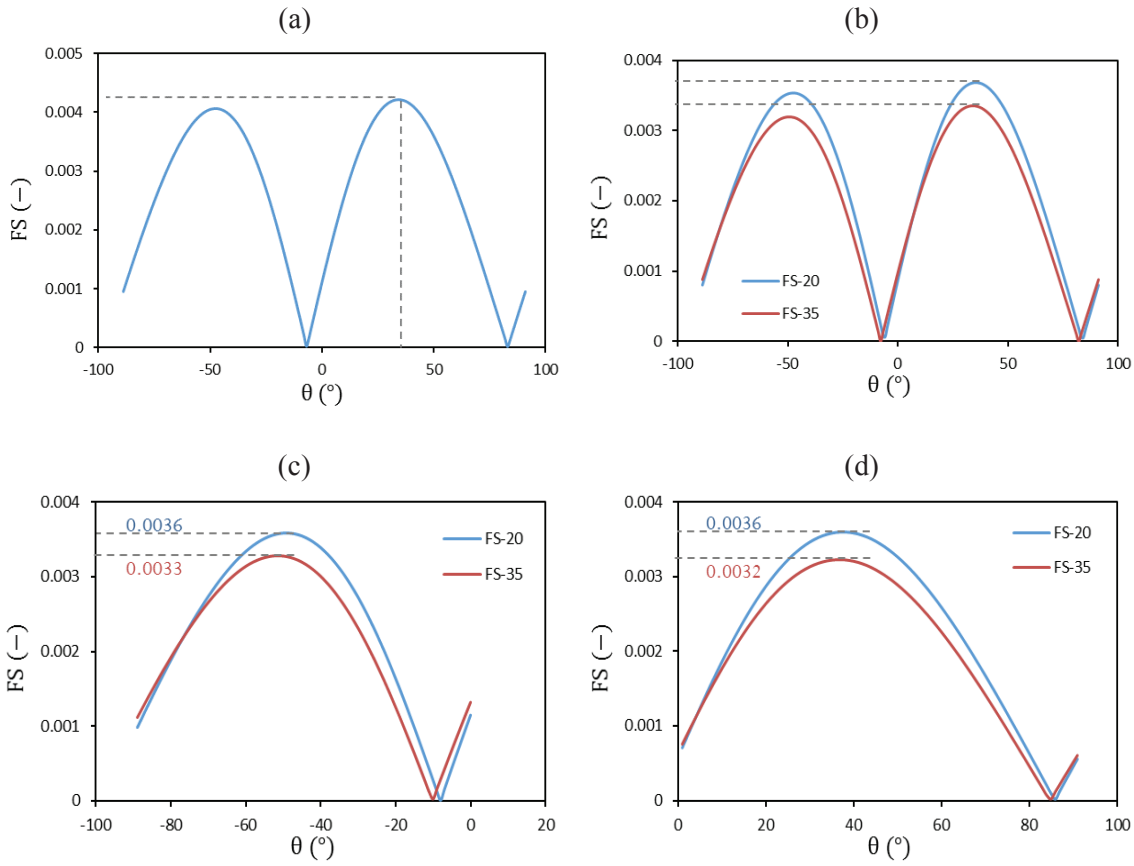

Figure 93. Variation of FS parameter with angle for (a) point method (b) volume method (c) quadrant method-left (d) quadrant method-right; using critical radii of 20 and 35 µm.

Table 25. Comparison of critical plane orientation using point, volume and quadrant methods.

Exp. Nr.	Depth (µm)	Point Method θ_c (°)		Vol. Method θ_c (°)		Quad. Method θ_c (°)		Experimental angle θ (°)
		MD	FS	MD	FS	MD	FS	from literature
1	$y = 0$	35	33	.	.	.	.	-35 to -45 [48]
	$r = 20$	.	.	35	34	-50	-49/37	≈ -55 [125]
	$r = 35$	.	.	34	33	-53	-51	-45 [200]
	$r = 50$	.	.	32	32	-54	-53	-20 to -28 [198]
5	$y = 0$	36	34	.	.	.	.	-39 to -70 [60, 118]
	$r = 20$	.	.	36	35	-49	37	20 to 50 [60, 118]
	$r = 35$	.	.	35	34	-50	-49	-45±15 [110]
	$r = 50$	.	.	36	33	-52	-50	45±15 [110]

5.7.2.2 Effect of stress averaging on life

On one hand considering the sub-surface stresses may provide useful information about the initiation angle, and on the other hand it may affect the prediction of fretting fatigue life. Therefore, detailed analysis of sub-surface stresses is required. This can be achieved by analysing the variation of damage parameters below the contact interface. Figure 94 shows the effect of different averaging methods on damage parameters by using the results of experiment 5. The highest value of the damage parameter is found with point method as shown by dotted line. With increase in process zone radius, the damage parameters were found to decrease. This decrease is found nearly linear for volume and quadrant methods. It is also interesting to note that the value of damage parameters was found nearly the same for volume and quadrant methods. Moreover, the similar patterns are observed for both MD and FS parameters.

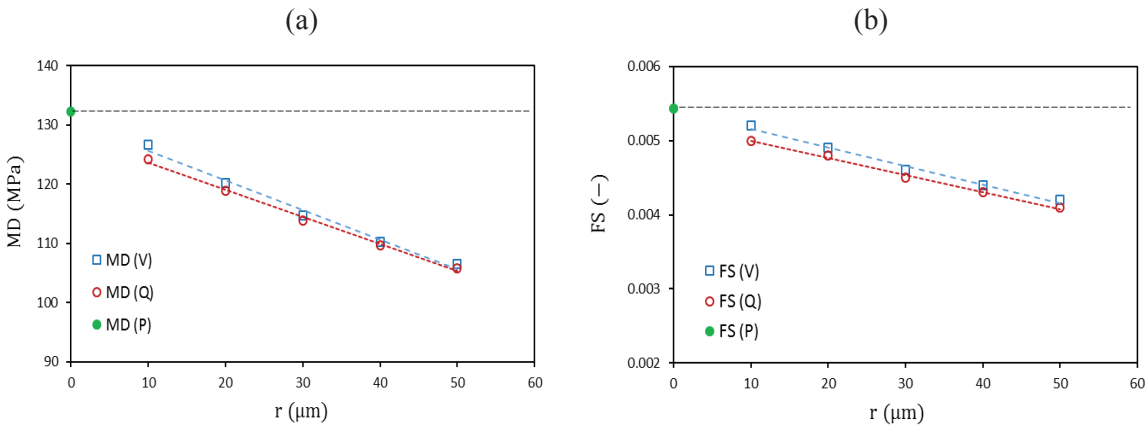

Figure 94. Change in damage parameter with critical radii for (a) MD and (b) FS parameter, using results of Exp.5.

A clearer picture of the damage parameter along the depth in *y*-direction can be seen in Figure 95. The damage parameter was computed at the predicted damage initiation location ($x/a \approx 1$) and along y-axis. Two curves are plotted, one for experiment 1 and the other for experiment 5. For the two test cases considered, similar gradient is observed for both parameters, in spite of different loading conditions. Up to the first 5 µm depth, MD and FS parameters decrease by 5.5 % and 6.2 % for experiment 1 and by 4.7 % and 5.3 % for experiment 5, respectively. Up to the depth of 10 µm, percentage decrease of 14.4 % and 15.9 % for experiment 1 and 12.1 % and 13.7 % for experiment 5, are observed. Therefore, for case I loading and geometrical conditions, the stress or damage parameter gradient is not significant. Going further till the depth of 50 µm, the variation of damage parameter is nearly linear.

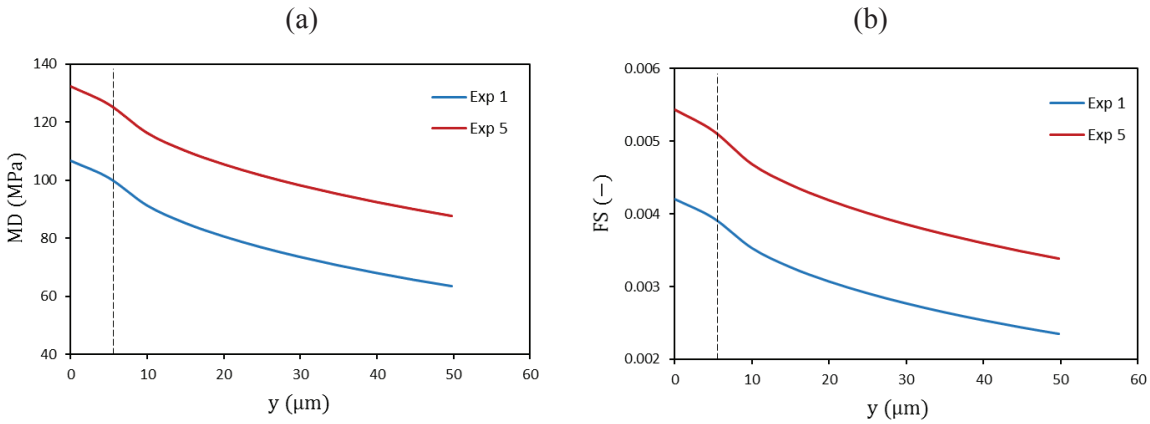

Figure 95. Variation of damage parameter along depth at initiation location for (a) MD and (b) FS parameter, using results of Exp. 1 and 5.

The sensitivity of crack initiation life with critical averaging radius is shown in Figure 96 (a). The results are plotted using quadrant method for experiment 5, up to a radius of 50 µm, In addition to MD and FS parameters, strain energy based Smith Watson Topper (SWT) parameter is also included in the analysis. It can be seen that all the parameters show similar trend, the slope of the initiation life is gradually increasing with averaging radius. MD and FS parameters are close to each other, whereas SWT parameter predicts slightly lower lives and appears to be less sensitive to different radii.

The effect of different stress averaging radii on fretting fatigue life is shown in Figure 96 (b). Since the experimental results were available for total failure, therefore total numerical lives were obtained by adding predicted crack initiation lives to propagation lives. The propagation lives for the same problem were taken from [194], where re-meshing technique was used along with Paris' law. As mentioned above the value of damage parameters are almost same for volume and quadrant method, therefore the comparison of numerical and experimental life is shown only for point method and quadrant method. It is observed that point method produced better estimation of fretting fatigue life in comparison with averaged results. Since for averaging up to 20 µm deviation greater the 3N is observed, further increase in process zone would give further deviations due to decrease in damage parameter. This shows that for the cases, where stress or damage parameter gradient is not significant, point method gives better life estimation and averaging techniques are not required.

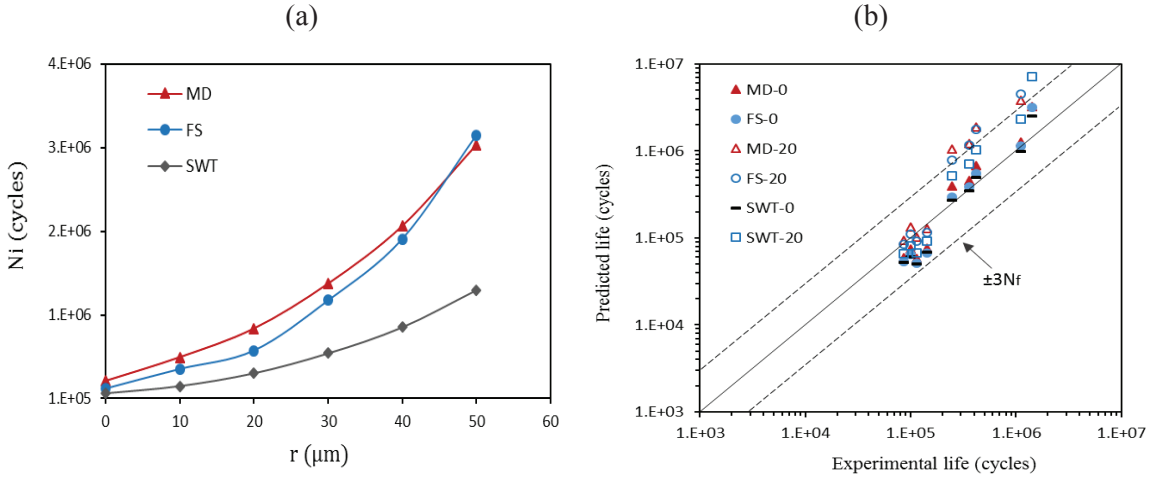

Figure 96. (a) Variation of initiation lives with averaging radius (b) Comparison between numerical and experimental lives using point method and quadrant method with 20 µm radius.

5.7.3 Case 2: Flat pad

The second case with flat pad was considered to analyse the effect of geometry on crack initiation life. The flat pad was used, as it may produce higher stress gradient at the edge of the contact. Therefore, a comparison of crack initiation life can be made for cases with different stress gradient beneath the surface. Furthermore, it will also help to determine critical crack length for stress averaging. The experimental configuration and data of Sabsabi et al. [136] is used, as shown in Figure 97. For experiments, the normal load varied from 2 kN to 8 kN, whereas bulk load varied from 110 MPa to 190 MPa. There was no tangential load for this study. For each case, the normal load was kept constant and bulk cyclic load was applied with stress ratio of -1 and a frequency of 15 Hz. The material of specimen and pad was Al 7075-T6. The squared edge pad had a radius of the order of 10 µm. The specimen had a cross section of 10×5 mm. The yield strength of the material was 503 MPa with an elasticity modulus of 72 GPa. The constants for critical plane parameters were taken from [136, 166, 199]. The complete experimental study consisted of fifteen experiments, however for the present work only five experiments are considered. The experimental initiation lives are calculated by subtracting propagation lives [166] from total experimental lives. The loads and experimental data for this case are shown in Table 26.

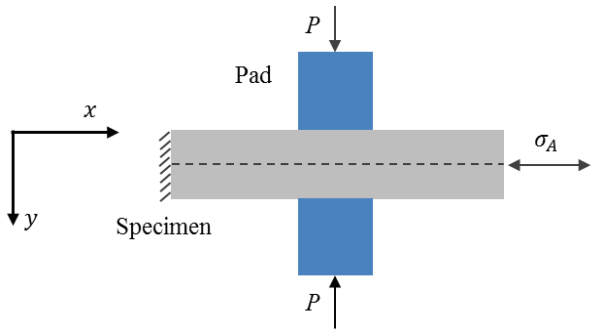

Figure 97. Schematic of experimental setup for flat pad.

Table 26. Experimental data for flat pad tests [136, 166].

Exp. Nr.	P (kN)	σ_A (MPa)	$N_{f,exp}$ (cycles)	$N_{i,exp}$ (cycles)
1	2	110	105958	74890
2	8	110	82549	30952
3	2	190	12509	4244
4	4	190	9590	2071
5	8	190	8760	131

5.7.3.1 Effect of stress gradient on initiation life

To confirm the inference of case 1, another case with flat specimen is considered. Due to the presence of sharp corner, a high stress gradient is expected near the edge of the contact. This would also allow to analyse the effect of pad geometry on sub-surface results. Similar to case I, the variation of damage parameter is extracted at predicted damage initiation location and along *y*-axis. For this case, exponential variation of damage parameters are observed, as shown in Figure 98. Up to depth of 5 µm, MD and FS parameters decrease by 45.8 % and 46.8 % for experiment 1 and by 44.4 % and 47.8 % for experiment 5. Whereas at the depth of 10 µm, MD and FS parameters decrease by 60.2 % and 61.9 % for experiment 1, respectively and by 58.2 % and 63.1 % for experiment 5, respectively. It can be seen that for case II, stress gradient is much higher than that for case I.

For this case also, the sensitivity of crack initiation life is observed with respect to averaging radius. Crack initiation lives are computed for experiment 1 for different radii. Due to high stress gradient, an exponential increase in lives is observed as shown in Figure 99 (a). A significant increase in the slope of initiation lives is observed after 20 µm radius for FS and MD parameters. Once again SWT parameter is found to be the least sensitive to averaging radii. A possible reason for this less sensitivity is due to lower gradient of normal stresses than shear

stresses. The influence of high stress gradient on crack initiation life is shown in Figure 99 (b). The predicted crack initiation lives are compared with experimental initiation lives of [166]. For this case, the point method provides significantly conservative results. For higher magnitude of loads, the lowest lives do not appear in the figure. The crack initiation lives were then estimated with critical radius of 10 µm and 20 µm using quadrant method. With 20 µm, overestimated lives are observed, whereas best estimation is provided at 10 µm for both MD and FS parameter. The estimation of critical radius matched well with predicted initiation length of Sabsabi et al. [136] using variable initiation length method. They predicted critical length of 10.8 µm and 9.3 µm with MD and Smith Watson Topper (SWT) parameter, respectively. This shows that for life estimation, stress averaging is required for the cases where stress gradients are high.

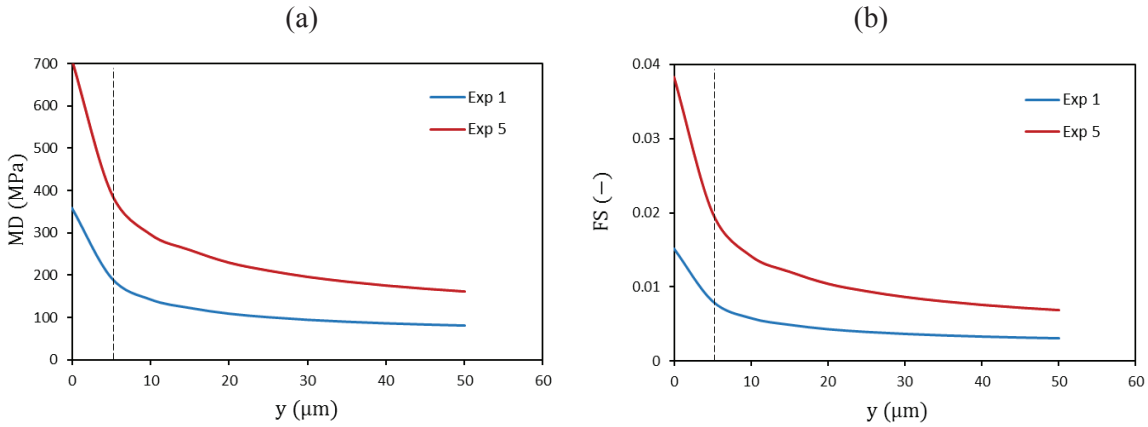

Figure 98. Change in damage parameter along depth at initiation location for (a) MD and (b) FS parameter, using results of Exp. 1 and 5.

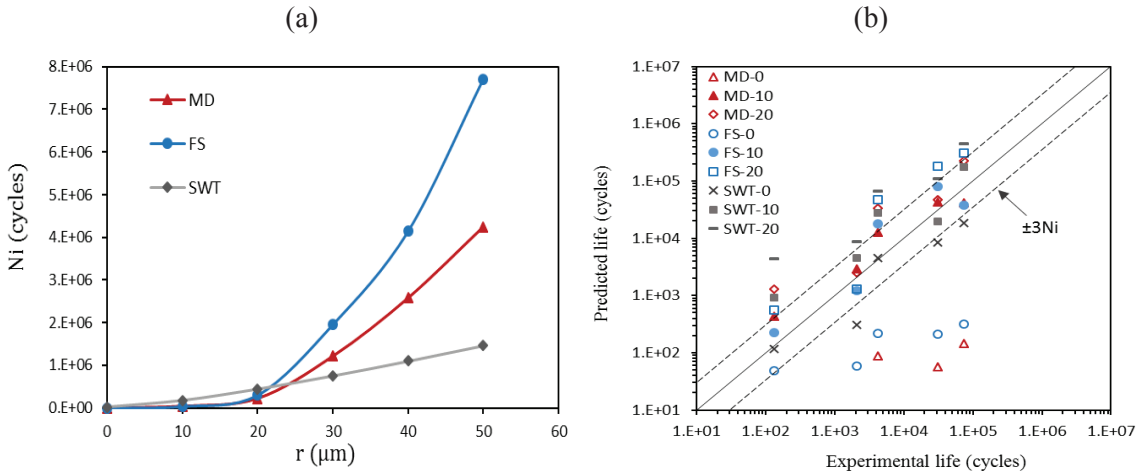

Figure 99. (a) Variation of initiation lives with averaging radius (b) Comparison between numerical and experimental lives using point method and quadrant method with 10 and 20 µm radius.

These results also correlate with the finding of Araújo and Nowell [114], where cylindrical pad with different radii and contact sizes were analysed to estimate crack initiation lives using SWT and FS parameters. It was found that with small pad radii using point method significantly conservative lives were predicted, whereas volume averaging provided better life estimation for such cases. They suggested the critical length of 5 to 20 μm for Ti-6Al-4V and 20 to 80 μm for Al4%Cu. Some researchers [48, 165, 166] used El Haddad [167] equation, which is based on threshold stress intensity factor range ΔK_{th} and fatigue limit σ_{f-1}, as shown in Eq. (195);

$$r_c = \frac{1}{\pi}\left[\frac{\Delta K_{th}}{\sigma_{f-1}}\right]^2 \tag{195}$$

The critical length of nearly 50 μm was estimated for Al 2024-T3/ Al 7075-T6 and numerical results were found in good agreement with experimental results using continuum damage mechanics approach. This shows that for estimation of crack initiation life, critical length or radius depends on various factors such as, material, loading magnitudes, geometry, contact size and damage model. Therefore it can vary for each case; in general it varies from 5 to 80 μm.

5.8 Summary

The above results and discussions are summarized in this section. The increase of coefficient of friction showed that shear stress, tensile stress and stick zone width also increased. This in turn lead to increase in wear and initiation parameters, which showed that increase in coefficient of friction can produce detrimental effect at the contact interface. In addition, with increase of μ, the damage initiation location moved from slip zone towards the contact edge. In fretting fatigue configuration, damage initiation is also dependent on $Q/\mu P$ ratio. When $Q/\mu P$ ratio decreased, the stick zone size increased and the initiation location shifted more towards the trailing edge of the contact. The peak of the shear traction and tensile stress was directly linked with applied axial stress. The higher the values of applied axial stress, the higher the values of shear traction and tensile stress. The magnitude for tensile stresses was much higher than shear and normal stresses for any particular case. The initiation process is believed to be caused by shear stresses and tensile stress to assist in crack propagation. This can also be the reason of much longer initiation lives than propagation lives (for the cases where failure occur in tensile dominant mode), since the shear stresses were much lower than tensile stresses. Although there is no way to compute numerically number of cycles to initiation using Ruiz parameter, however, it can be related to experimental data if available. Results suggest that, higher the value of damage initiation parameter F2, the lower number of cycles will be required for damage initiation and vice versa.

With the change of phase difference between applied axial and tangential load, the shear traction and tensile stress profiles and their peaks changed significantly. However, there was no significant effect of numerical models and phase difference on convergence efficiency. Due to applied loads and boundary conditions, perturbation in the contact stresses and damage parameter profiles can be generated at negative values of tangential load. These perturbations were attributed to the convergence problem, which can arise at the interface of stick-slip zone. During the load history, stick zone width changed at each step. Due to larger stick zone widths during the unloading steps, the convergence can be much slower during the unloading steps than for loading steps.The fretting fatigue crack initiation location is highly dependent on loading sequence. With different phase angles between axial and tangential load, crack initiation location changed significantly. For phase difference of 180°, Ruiz parameter *F*2 and SWT parameter showed the highest value and therefore the fretting fatigue initiation life would be lowest for this case. Whereas, for 90° phase difference the initiation life would be higher than that for in phase loading since lowest values of both parameters were observed. To determine the crack initiation location, both SWT and Ruiz parameter *F*2 can be used. Both parameters showed good correlation with experimental results. However, for the case of 90° phase difference, crack initiation location can be either at leading or trailing edge depending upon the material and stress state. Therefore, more experimental results are required to ascertain the crack initiation location for material under consideration.

The critical plane approach was able to predict damage initiation site, initiation angle and fretting fatigue life. Energy based models, which employ normal stress/strain were unable to predict initiation angles, whereas criteria which uses maximum shear stress or strains are suitable to predict initiation angles. However, criteria with normal stress or strain components showed good estimation of fracture direction, for cases where failure occurs in tensile mode. Crack initiation can occur on either of the preferred shearing planes depending on material and loading condition. The orientation of critical plane for 180° phase difference was opposite to that observed for in-phase loading, however, the magnitude remained same. In addition, with phase difference of 90°, more number of planes showed potential to start damage nucleation than for in-phase loading. Fretting fatigue life for 180° phase difference was observed to be lower than for in-phase loading, whereas it was higher for 90° phase difference than for in-phase loading. For validation of percent increase in life for 90° phase difference, more experimental work is suggested. All models were able to predict initiation life with normalized standard deviation (SD_x) nearly equal to 2. The normalized mean ($\bar{x}$) calculated for shear stress and strain based criteria were closer to 1, which suggests that numerical results were closer to experimental results than for strain energy based criteria. For most of the results for strain energy based criteria initiation life was over predicted. For some cases, larger deviation was also observed for stress-based criteria, where internal stresses were higher than yield strength of the material.

Two cases of phase difference between applied loads were considered to study fretting fatigue damage initiation location and life. Both CDM and CP approaches provided good estimation of initiation location for in phase and out of phase loading. When phase difference was applied between axial and tangential load (case 1), two possible location of damage initiation, i.e. at either edge of the contact, were observed. However, when the phase difference was applied between normal load and other loads (case 2) then initiation location was observed only at the trailing edge. For in phase loading, both approaches showed reasonable accuracy for each case, the predicted results were found within ±3 N scatter band. For out of phase loading, the CDM approach showed better prediction for the case of variable normal load especially at lower loading amplitudes. The accuracy and dispersion depends on strain life and initiation life constants. For better prediction, the constants are required to be evaluated at specific applied load ratio and phase difference. Higher dispersion was observed for case 2 than for case 1, even for in phase loading. The selection of the preferred approach and criteria depends on various factors such as loading magnitudes, phase difference between the applied loads, material failure mechanism and load ratios.

This study focusses on the influence on fretting fatigue crack initiation life by using a CDM based damage model for non-proportional loading (CDM-NPL). The results depicted that for out of phase loading, the triaxiality function R_v varies with respect to time due to change in ratio of stresses. This shows the existence of non-proportional stresses under phase difference condition. The modified damage model provided good estimate of fretting fatigue lives in comparison with experimental results, which implies that including the effect of triaxiality function variation in damage model may produce more realistic results for non-proportional loading cases. Although the improvement in life prediction was not much significant, still the investigation highlights the influence of involved factors on crack nucleation life. The damage evolution is a highly non-linear phenomenon. The modified damage model showed that for same magnitude, in phase loading produced higher damage than for out of phase loading. For non-proportional loading cases, two important parameters which govern the damage initiation are stress range and triaxiality function range. For in phase loading only stress range affected the initiation life whereas for out of loading both stress and triaxiality function range affected initiation life especially at higher ranges.

Both CP and SI approaches are suitable to determine crack initiation location. All parameter SWT, MD and CL predicted initiation location at the trailing edge of the contact. However, SI approach showed higher deviation of mean $\bar{x}$ life than CP approach. Fretting fatigue life can be predicted using both approaches for medium and low cycle regimes, however, CL parameter showed larger deviation for high cycle fatigue which is generally the regime for fretting fatigue cases.

For estimation of crack initiation angle, different methods (point, volume and quadrant) have shown different results. The quadrant averaging approach provided more realistic results for initial crack orientation in comparison to point method and volume averaging method. Although peak values of MD and FS parameters were close to each other for both quadrants, dominant orientation was observed inside the contact zone. MD parameter showed initiation direction inside the contact for all radii, whereas FS parameter showed same orientation for radius equal to or greater than 20 μm. The stress concentration near the contact zone depends upon loading magnitude and contact geometry. For cylindrical pad, the stress gradient or damage parameter variation with depth was nearly linear, whereas for flat pad exponential variation was observed. Therefore, stress averaging is required for cases where gradients are very high, e.g. for flat pad or cylindrical pad with small radii. For better prediction of fretting fatigue life, the dependence of critical radius on rate of decay of damage parameters should be considered. This decay of damage parameters depends on multiple factors like material, loading condition, geometry, contact width and damage model and therefore may vary from case to case.

Chapter 6

Conclusions and future recommendations

6.1 Conclusions

This thesis presents analysis on various aspects related to crack nucleation under fretting fatigue conditions. Different approaches and damage models have been discussed, which are applied under multiaxial and non-proportional fretting fatigue scenario. The role and strength of finite element methods have also been witnessed, as it can be efficiently applied to analyze the influence of numerous factors on fretting fatigue behaviour. From above results and discussions, following conclusions can be drawn.

- The analysis of fretting fatigue damage initiation can be carried out using different approaches and damage models. These approaches can be classified into critical plane approach, stress invariant approach, continuum damage mechanics approach and fretting specific parameters. With application of these approaches various aspects can be analysed, however, the most widely studied features includes, critical plane angles and their failure modes, crack initiation location and depth, and prediction of crack initiation life.
- The critical plane approach has an advantage over other approaches, as it can characterize failure modes. However, it is also computationally most expensive than other approaches. The fretting specific parameters mostly predicted crack initiation site inside the slip zone, therefore, they more suited to the situation where, wear effects are dominant. Generally, crack initiation life was predicted within error band of ±2 to ±3 times the experimental lives. However, Ruiz initiation parameter $F2$, cannot be correlated to any stress life, strain life or other life estimating models to predict initiation life numerically. Since the crack initiates due to shearing of slip band in the material, therefore, in order to determine crack initiation angles, shear stress, shear strain or shear strain energy based parameters should be used.
- The important factors analyzed, which influenced damage nucleation, were coefficient of friction, load ratio and magnitude of bulk axial stress. The increase in coefficient of friction led to an increase in shear and tensile stress. The stick zone size also increased and caused an increase in damage parameters. The coefficient of friction also influenced the crack initiation site by shifting towards the contact edge. The tangential to normal load ration on the other hand was inversely proportional to stick zone size. However, a decrease in load ratio also shifted the nucleation site towards the contact edge. The magnitude of applied axial stress directly affected shear and tensile stress. For the analyzed case studies, the tensile stress appeared to be higher than shear traction and normal stresses. Since the shear stresses are generally believed to initiate the crack and tensile stresses to assist in crack propagation, therefore, longer initiation lives can be expected for the cases where shear stresses are smaller.

- Apart from coefficient of friction, load ratio and magnitude, the loading sequence also played important role in crack nucleation. Two cases of phase difference were used. The first case included the phase difference between axial stress and tangential load. When this phase difference was generated between the loads, the peak stresses and profile at the contact interface changed significantly. This also implies that value of phase difference affects the crack initiation location. For in phase loading, the crack initiation location was predicted at the trailing edge of the contact. The predicted location also matched well with experimental results from literature. For phase difference of 180°, the crack initiation location shifted towards the leading edge of the contact. However, with phase difference of 90° between the said loads, two peaks of the damage parameters were observed, which showed that both contact edges have the potential to initiate a crack.
- The phase difference between the applied loads, also influenced the crack initiation angle. This angle can be determined using critical plane approach. The critical plane approach includes models, which are based on, normal stress/ strain or shear stress/ strain. The models, which are based on maximum shear stress or strain, were found most suitable for estimation of initial crack orientation, whereas models with normal stress or strain can be used to estimate fracture direction for tensile mode failure cases. Since there are two maximum shear planes, one of each side of the principal plane, therefore initiation can occur on any of the maximum shear plane depending upon grain orientation and loading conditions. The orientation of critical plane for 180° phase difference (between axial stress and tangential load) was found opposite to that for in phase loading. For 90° phase difference more number of planes were initiated than for in phase loading.
- As mentioned above, the phase difference changed the stress peak and profile. Therefore, it consequently affected the fretting fatigue life also. With the phase difference between axial stress and tangential load, the fretting fatigue life with 90° phase difference was observed to be higher than for in phase loading, whereas minimum life was observed with 180° phase difference. However, to generalize percentage increase or decrease in fretting fatigue life, further experimental results are needed with different phase angles and materials. For the cases analyzed using critical plane approach, the damage models, which are based on shear stress and strain showed better life estimation than strain energy based models. However, it is important here to mention that while selecting any critical plane parameter for estimation of initiation angle and life, dominant failure mode of the material should be considered.
- The second case of phase difference consisted of phase angle between normal load and other two loads. With this loading phase difference, it was observed that the initiation location was only at the trailing edge, as opposed to the previous case where for out of phase loading two potential failure sites were observed, one on each contact edge. Both CDM-PL and CP approaches showed similar results. The comparison for fretting fatigue

life using both approaches showed comparable results for in phase loading. However, for out of phase loading CDM-PL approach showed better prediction than CP approach especially at lower loading magnitudes. The estimation of fretting life depends on strain life or material constants, therefore evaluation of these constants for specific load ration and phase difference may improve the numerical results.

- For the cases where stress gradient is low, local damage models may provide good life estimation. However, for the cases where stress gradient is high, they may lead to larger errors. Regularization or stress averaging techniques are imperative for these cases. To determine the critical radius for stress averaging, some quantification of decay of damage parameter is required. This variation of damage parameter depends on various factors such as material properties, loading amplitude, geometry, contact width and damage model used for analysis. Therefore, this critical length may vary from case to case.
- To estimate crack initiation angle, different methods are available in the literature. Most often researchers have used surface results or volume method for numerical estimation. These methods generally predict dominant angle going out of the contact whereas most of the researchers have experimentally shown the inward crack initiation orientation. Some of the researchers have also shown crack initiation in both directions. Quadrant approach seems more suitable than existing method, as it predicted dominant crack angle inwards the contact region. Since the crack initiation considers few grains length, therefore it is more meaningful to employ averaging method rather than considering only surface results.
- Due to existence of non-proportional stresses for out of phase loading, the triaxiality function varied with respect to time. The proposed damage model CDM-NPL showed slight advantage over CDM-PL for life estimation. By considering the phase difference between normal load and other loads, higher fretting fatigue lives were observed for out of phase loading than for in phase loading. This implies that crack nucleation is dependent upon stress range for the case of in phase loading, however for out of phase loading both stress range and triaxiality function range are important. Therefore, incorporating the effect of traixiality function variation in damage model may produce better life estimation. Both CDM approaches used in the present work were compared with experimental results where failure occurred in dominant tensile mode. Further validation of these formulations for dominant shear mode failure may lead to comprehensive comparison between these models.

There are several factors which affects crack initiation life, e.g. loading magnitudes and load ratios, sequence or phase difference between the applied loads, material properties of contacting bodies, surface and environmental conditions, crack initiation length, pad and specimen geometry, etc. The present work included some case studies with loading magnitude

and phase difference effects. For the cases considered in the present work, CDM approach showed comparatively better results than CP approach under out of phase loading condition. For in phase loading both approaches were found equally effective. Whereas SI approach showed larger deviations than CP approach especially at large number of cycles to failure. The CP approach on the other hand has advantage to provide information about crack angles. Considering other variables for the analysis of crack nucleation may lead to different results. Therefore, selection of the preferred approach and criteria depends on various factors and hence may vary from case to case.

The application of different approaches has shown their prediction capability to model nucleation phenomenon. However exact matching with experimental results cannot be ensured. The predicted results show that there can be differences between numerical and experimental results under fretting fatigue conditions. The probable reasons for these deviations are as follows.

- The multiaxial fatigue parameters were originally developed for homogeneous loading, whereas they are generally applied over a small RVE, since the stress concentration exists at a localized area under fretting fatigue conditions.
- Although most of the damage models using CDM approach are derived from principles of thermodynamics, however they assume proportional stress state or sometimes linear accumulation of damage. Since in fretting fatigue non-proportional stress state may exist, therefore the assumption of proportionality and linear damage may induce errors.
- Most of the damage models do not incorporate the effect of microstructure. In fretting fatigue, micro plasticity may also exist, which is generally neglected. Depending upon the loading magnitudes, contact type and pad radius, micro plasticity can be induced. Assuming elastic regime for such cases may lead to errors.
- Generally speaking, information related to the cause of damage initiation e.g. voids, crack, porosity, inclusion or surface damage is missing in experimental results. In addition, the type of failure i.e. ductile, brittle or quasi brittle is assumed from number of cycles to failure. The lack of analysis or information of experimental failure does not allow to choose appropriate damage model.
- Most of the approaches applied in fretting fatigue are empirical and based on physical observations (e.g. CP and Ruiz parameter). Therefore, the suitable damage parameter under one condition might not produce results with same accuracy under other conditions. The fretting fatigue is also complemented by wear and environmental effects, which are usually neglected.
- Most of the parameters, which were originally verified under plain fatigue conditions, were later adopted for fretting fatigue. The empirical constant e.g. stress or strain life constants or SN curves used in formulations are also taken from plain fatigue. Hence, the constants do not represent the true phenomena. Due to this fact the errors found under

fretting fatigue are observed to be higher than plain fatigue cases for which the damage models were originally validated. The application of these constants for out of phase loading conditions can also lead to large deviations.

- The estimation of crack initiation angle generally neglects grain size, grains orientation and grain boundary effect. Therefore, an estimated crack angle is assumed to follow the same orientation up to a specific length. Experimentally, cracks may change orientation continuously or follow zigzag behaviour.
- The crack initiation life is usually determined by subtracting numerical or analytical propagation life from the total fretting fatigue life. An initial crack length is generally assumed in propagation analysis. Thus, the errors of estimated propagation life also affect the initiation life. The initiation life should be measured independent of the propagation life along with a length scale that describes initiation phase.

6.2 Future recommendations

Although advanced computational resources and application of numerical methods have provided great ease in modelling of complex phenomena like fretting fatigue, there are areas, which still require careful attention for better prediction and analysis. The way forward to the current research can be derived from the above mentioned points, which can induce error in predicted results. The following recommendations are suggested for future work.

- The effect of grain size, orientation and micro plasticity can be added in damage models to provide more realistic material behaviour under fretting fatigue conditions. A combination of micro or macro approach, thus can be used to model local and bulk behaviour of the material.
- As fretting fatigue leads to wear and crack initiation, further work can be done in areas by combining wear models with crack initiation models. Furthermore, the effect of surface roughness can be added. The inclusion of coefficient of friction and slip amplitude needs to be incorporated in the damage models. These factors may also produce more realistic results.
- Since the fretting fatigue life is dependent on initial crack length, the damage model should be formulated so that it incorporates crack length effect. This will exclude the reliance of initiation life from estimated propagation life. As it is widely accepted that the total failure comprises nucleation and propagation phase, modelling of both phases should be independent of each other.
- The analysis of crack nucleation phase may be extended to heterogeneous and anisotropic materials. So far most of the work has been done for homogeneous and isotropic material. In practical, most of the materials induce heterogeneity due to manufacturing and heat

treatment process. At present not much work is performed by considering heterogeneity under fretting fatigue conditions.

- The damage model can be extended to include thermal effects. This requires introduction of some more state variables, additional terms in state potential and dissipation potential function. Since the material properties are also dependent on temperature, inclusion of thermal effect may improve life estimation.
- In the present work, numerical results are compared with experimental results from literature for the cases where failure occurred predominantly in tensile mode. It would be interesting to compare various approaches for the cases where failure occurred dominantly under shear mode.

The accurate modelling of fretting fatigue is still a challenging task, as the damage initiates at micro scale and practical observation of crack is also difficult to monitor since crack nucleates under the contact region. The actual phenomenon is much more complicated than what is usually modelled. Hence, the prediction accuracy of damage models can be improved by incorporating micro models describing plasticity effects, wear effects, inclusion of slip amplitude and by determining empirical constants under fretting conditions. Moreover, realistic and consistent definition of experimental and numerical crack initiation length may also improve the prediction accuracy. Apart from laboratory configurations, further studies, with real scale components and assemblies, under real life multidimensional loading data are required to build strong confidence on these damage models and to improve their prediction capability.

APPENDIX A. PUBLICATIONS

Journal

1. N. A. Bhatti and M. Abdel Wahab, "Finite element analysis of fretting fatigue under out of phase loading conditions," *Tribology International,* vol. 109, pp. 552-562, May 2017.
2. N. A. Bhatti and M. Abdel Wahab, "A numerical investigation on critical plane orientation and initiation lifetimes in fretting fatigue under out of phase loading conditions," *Tribology International,* vol. 115, pp. 307-318, Nov 2017.
3. N. A. Bhatti and M. Abdel Wahab, "Fretting fatigue damage nucleation under out of phase loading using a continuum damage model for non-proportional loading," *Tribology International,* vol. 121, pp. 204-213, May 2018.
4. N. A. Bhatti and M. Abdel Wahab, "Fretting fatigue crack nucleation: A review," *Tribology International,* vol. 121, pp. 121-138, May 2018.
5. N. A. Bhatti, K. Pereira, and M. Abdel Wahab, "A continuum damage mechanics approach for fretting fatigue under out of phase loading," *Tribology International,* vol. 117, pp. 39-51, Jan 2018.
6. K. Pereira, N. A. Bhatti and M. Abdel Wahab, " Prediction of fretting fatigue crack initiation location and direction using cohesive zone model," *Tribology International*, vol. 127. pp. 245-254, 2018.
7. N. A. Bhatti, K. Pereira, and M. Abdel Wahab, "Effect of stress gradient and quadrant averaging on fretting fatigue crack initiation angle and life," *Tribology International.* vol. 131. pp. 212-221, 2019.

Conference proceedings

1. N. A. Bhatti and M. Abdel Wahab, "A review on fretting fatigue crack initiation criteria," in *5th International Conference on Fracture Fatigue and Wear*, 2016, pp. 78-85.
2. N. A. Bhatti and M. A. Wahab, "Numerical investigation of contact stresses for fretting fatigue damage initiation," in *Journal of Physics*: *Conference Series*, 2017, pp. 012054.
3. N. A. Bhatti, K. Pereira, and M. Abdel Wahab, "A comparison between critical-plane and stress-invariant approaches for the prediction of fretting fatigue crack nucleation," *Proceedings of the 7th International Conference on Fracture Fatigue and Wear*. In *Lecture Notes in Mechanical Engineering*: *Springer*, 2018, pp. 530-538.

REFERENCES

[1] D. A. Hills and D. Nowell, *Mechanics of fretting fatigue*: Dordrecht : Kluwer Academic Publishers, 1994.

[2] O. Vingsbo and S. Söderberg, "On fretting maps," *Wear,* vol. 126, pp. 131-147, 1988/09/01/ 1988.

[3] E. M. Eden, W. N. Rose, and P. L. Cunningham, "The Endurance of Metals: Experiments on Rotating Beams at University College, London," *Proceedings of the Institution of Mechanical Engineers,* vol. 81, pp. 839-974, 1911/06/01 1911.

[4] G. Tomlinson, "The rusting of steel surfaces in contact," *Proceedings of the Royal Society of London. Series A, Containing Papers of a Mathematical and Physical Character,* vol. 115, pp. 472-483, 1927.

[5] E. Warlow-Davies, "Fretting corrosion and fatigue strength: brief results of preliminary experiments," *Proceedings of the Institution of Mechanical Engineers,* vol. 146, pp. 32-38, 1941.

[6] J. McDowell, "Fretting corrosion tendencies of several combinations of materials," in *Symposium on fretting corrosion*, 1953.

[7] H. Liu, H. T. Corten, and G. Sinclair, *Fretting fatigue strength of titanium alloy RC 130B*: Department of Theoretical and Applied Mechanics, University of Illinois, 1957.

[8] A. Fenner and J. E. Field, "La fatigue dans les conditions de frottement," *Revue de metallurgie,* vol. 55, pp. 475-485, 1958.

[9] R. Waterhouse, "Influence of local temperature increases on the fretting corrosion of mild steel," *J. Iron Steel Inst,* vol. 197, p. 301, 1961.

[10] K. Nishioka, S. Nishimura, and K. Hirakawa, "Fundamental investigations of fretting fatigue: Part 1, on the relative slip amplitude of press-fitted axle assemblies," *Bulletin of JSME,* vol. 11, pp. 437-445, 1968.

[11] K. Nishioka and K. Hirakawa, "Fundamental Investigations of Fretting Fatigue:(Part 5, The Effect of Relative Slip Amplitude)," *Bulletin of JSME,* vol. 12, pp. 692-697, 1969.

[12] K. Nishioka and K. Hirakawa, "Fundamental investigations of fretting fatigue: part 3, some phenomena and mechanisms of surface cracks," *Bulletin of JSME,* vol. 12, pp. 397-407, 1969.

[13] K. Nishioka and K. Hirakawa, "Fundamental investigations of fretting fatigue:(part 2, fretting fatigue testing machine and some test results)," *Bulletin of JSME,* vol. 12, pp. 180-187, 1969.

[14] K. Nishioka and K. Hirakawa, "Fundamental investigations of fretting fatigue: part 4, the effect of mean stress," *Bulletin of JSME,* vol. 12, pp. 408-414, 1969.

[15] K. Nishioka and H. Kenji, "Fundamental investigations of fretting fatigue: Part 6, effects of contact pressure and hardness of materials," *Bulletin of JSME,* vol. 15, pp. 135-144, 1972.

[16] R. B. Waterhouse and D. E. Taylor, "The initiation of fatigue cracks in A 0.7% carbon steel by fretting," *Wear,* vol. 17, pp. 139-147, 1971/02/01/ 1971.

[17] R. B. Waterhouse, *Fretting corrosion*: Pergamon Press, 1972.

[18] R. B. Waterhouse, "Fretting wear," *Wear,* vol. 100, pp. 107-118, 1984/12/01/ 1984.

[19] R. B. Waterhouse, *Fretting fatigue*: Applied Science Publishers, 1981.

[20] M. H. Attia and R. B. Waterhouse, *Standardization of Fretting Fatigue Test Methods and Equipment*: ASTM, 1992.

[21] K. Endo and H. Goto, "Initiation and propagation of fretting fatigue cracks," *Wear,* vol. 38, pp. 311-324, 1976/07/01/ 1976.

[22] D. Hills, D. Nowell, and J. O'Connor, "On the mechanics of fretting fatigue," *Wear,* vol. 125, pp. 129-146, 1988.

[23] D. Nowell and D. Hills, "Crack initiation criteria in fretting fatigue," *Wear,* vol. 136, pp. 329-343, 1990.

[24] J. Dobromirski, "Variables of fretting process: are there 50 of them?," *ASTM Special Technical Publication,* vol. 1159, pp. 60-60, 1992.

[25] H. Hertz, "On the contact of elastic solids," *J. Reine Angew Math.,* vol. 92, pp. 156-171, 1882.

[26] R. Mindlin, "Compliance of elastic bodies in contact," *J. appl. Mech.,* vol. 16, pp. 259-268, 1949.

[27] K. Johnson, "Surface interaction between elastically loaded bodies under tangential forces," in *Proceedings of the Royal Society of London A: Mathematical, Physical and Engineering Sciences*, 1955, pp. 531-548.

[28] G. P. Wright and J. J. O. Connor, "The Influence of Fretting and Geometric Stress Concentrations on the Fatigue Strength of Clamped Joints," *Proceedings of the Institution of Mechanical Engineers,* vol. 186, pp. 827-835, 1972/06/01 1972.

[29] R. Bramhall, *Studies in Fretting Fatigue*: University of Oxford, 1973.

[30] G. Hamilton and L. Goodman, "The stress field created by a sliding circular contact," *ASME J. Appl. Mech,* vol. 33, pp. 371-376, 1966.

[31] G. M. Hamilton, "Explicit equations for the stresses beneath a sliding spherical contact," *Proceedings of the Institution of Mechanical Engineers, Part C: Journal of Mechanical Engineering Science,* vol. 197, pp. 53-59, 1983.

[32] D. Hills, D. Nowell, and A. Sackfield, *Mechanics of elastic contacts*: Elsevier, 2013.

[33] Y. Lindblom and G. Burman, "Fatigue failure under fretting conditions," in *High Temperature Alloys for Gas Turbines 1982*, ed: Springer, 1982, pp. 673-684.

[34] C. Ruiz and K. Chen, "Life assessment of dovetail joints between blades and discs in aero-engines," *Mechanical Engineering Publications,* pp. 187-194, 1986.

[35] T. Lindley, P. Mclntyre, D. Snow, J. Wilson, and A. Lichnowski, "Fatigue and environmental cracking in turbo-generators," in *Sixth Thermal Generation Specialists Meeting, Madrid*, 1981.

[36] R. Hobbs and K. Ghavani, "The fatigue of structural wire strands," *International Journal of Fatigue,* vol. 4, pp. 69-72, 1982.

[37] A. Okazaki, C. Urashima, K. Sugino, H. MASUMOTO, and M. Hattori, "Upper fillet crack in bolted joint of rail and its causes improvement in enduracen of the bolted rail-joint. 1," in *Transactions of the Iron and Steel Institute of Japan*, 1983, pp. B22-B22.

[38] E. Smethurst and R. Waterhouse, "Causes of failure in total hip prostheses," *Journal of Materials Science,* vol. 12, pp. 1781-1792, 1977.

[39] N. T. S. B. AAB-13-02. (2018, 26 Jan). *Rapid compression due to fuselage rupture, Southwest Airline flight 812*. Available: [online] at https://www.ntsb.gov/investigations/AccidentReports/Pages/AAB1302.aspx

[40] J. Lemaitre, *A course on damage mechanics*: Springer-Verlag Berlin Heidelberg., 1996.

[41] V. L. Popov, *Contact Mechanics and Friction: Physical Principles and Applications*: Springer Berlin Heidelberg, 2017.

[42] D. Nowell and D. A. Hills, "Mechanics of fretting fatigue tests," *International Journal of Mechanical Sciences,* vol. 29, pp. 355-365, 1987/01/01/ 1987.

[43] W. Rust, *Non-linear finite element analysis in structural mechanics*: Springer, 2016.

[44] E. Zahavi and D. Barlam, *Nonlinear Problems in Machine Design*: CRC Press, Inc., 2000.

[45] A. Manual. Abaqus Documentation Version 6.13 [Online].

[46] P. Forsyth, "A two stage process of fatigue crack growth," in *Proceedings of the Crack Propagation Symposium*, 1961, pp. 76-94.

[47] B. N. Leis, J. Ahmad, and M. F. Kanninen, "Effect of local stress state on the growth of short cracks," in *Multiaxial Fatigue*, ed: ASTM International, 1985.

[48] R. Hojjati-Talemi, M. Abdel Wahab, J. De Pauw, and P. De Baets, "Prediction of fretting fatigue crack initiation and propagation lifetime for cylindrical contact configuration," *Tribology International,* vol. 76, pp. 73-91, Aug 2014.

[49] S. Chhith, W. De Waele, and P. De Baets, "Rapid Determination of Fretting Fatigue Limit by Infrared Thermography," *Experimental Mechanics,* pp. 1-9, 2017.

[50] S. Chhith, W. De Waele, P. De Baets, and T. Van Hecke, "On-line detection of fretting fatigue crack initiation by lock-in thermography," *Tribology International,* vol. 108, pp. 150-155, 2017.

[51] Q. Shan and R. Dewhurst, "Surface-breaking fatigue crack detection using laser ultrasound," *Applied Physics Letters,* vol. 62, pp. 2649-2651, 1993.

[52] A. Klepka, W. Staszewski, R. Jenal, M. Szwedo, J. Iwaniec, and T. Uhl, "Nonlinear acoustics for fatigue crack detection–experimental investigations of vibro-acoustic wave modulations," *Structural Health Monitoring,* vol. 11, pp. 197-211, 2012.

[53] B. Zhang, D. Poirier, and W. Chen, "Microstructural effects on high-cycle fatigue-crack initiation in A356. 2 casting alloy," *Metallurgical and Materials Transactions A,* vol. 30, pp. 2659-2666, 1999.

[54] C. H. Goh, J. M. Wallace, R. W. Neu, and D. L. McDowell, "Polycrystal plasticity simulations of fretting fatigue," *International Journal of Fatigue,* vol. 23, pp. 423-435, 2001/01/01/ 2001.

[55] P. P. Milella, *Fatigue and corrosion in metals*: Springer Science & Business Media, 2012.

[56] N. Thompson, N. Wadsworth, and N. Louat, "Xi. The origin of fatigue fracture in copper," *Philosophical Magazine,* vol. 1, pp. 113-126, 1956.

[57] H. Nisitani, "Behaviour of small cracks in fatigue and relating phenomena," *Elsevier Applied Science, Current Research on Fatigue Cracks,* pp. 1-16, 1987.

[58] J. Lemaitre and R. Desmorat, *Engineering damage mechanics: ductile, creep, fatigue and brittle failures*: Springer Science & Business Media, 2005.

[59] M. P. Szolwinski and T. N. Farris, "Observation, analysis and prediction of fretting fatigue in 2024-T351 aluminum alloy," *Wear,* vol. 221, pp. 24-36, Oct 1998.

[60] C. Lykins, S. Mall, and V. Jain, "A shear stress-based parameter for fretting fatigue crack initiation," *Fatigue & Fracture of Engineering Materials & Structures,* vol. 24, pp. 461-473, 2001.

[61] P. Forsyth, "Some observations on the nature of fatigue damage," *Philosophical Magazine,* vol. 2, pp. 437-440, 1957.

[62] A. H. Cotrell and D. Hull, "Extrusion and intrusion by cyclic slip in copper," in *Proc. R. Soc. Lond. A*, 1957, pp. 211-213.

[63] N. Mott, "A theory of the origin of fatigue cracks," *Acta Metallurgica,* vol. 6, pp. 195-197, 1958.

[64] R. Boettner, A. McEvily Jr, and Y. Liu, "On the formation of fatigue cracks at twin boundaries," *Philosophical magazine,* vol. 10, pp. 95-106, 1964.

[65] K. Jagannadham, "Debonding of circular second phase particles," *Engineering Fracture Mechanics,* vol. 9, pp. 689-696, 1977.

[66] W. Duckworth and E. Ineson, "The effects of externally introduced alumina particles on the fatigue life of En24 steel," *Clean steel,* vol. 77, pp. 87-103, 1963.

[67] T. L. Anderson, *Fracture Mechanics: Fundamentals and Applications, Third Edition*: Taylor & Francis, 2005.

[68] B. Derby, D. A. Hills, and C. Ruiz, *Materials for engineering: a fundamental design approach*: Halsted Press, 1992.

[69] K. Walker, "The effect of stress ratio during crack propagation and fatigue for 2024-T3 and 7075-T6 aluminum," in *Effects of environment and complex load history on fatigue life*, ed: ASTM International, 1970.

[70] P. C. Paris, M. P. Gomez, and W. P. Anderson, "A rational analytic theory of fatigue," *Trends Engin,* vol. 13, pp. 9-14, 1961.

[71] C. M. Sonsino, H. Zenner, A. Carpinteri, and L. P. Pook, "Selected papers from the 7th International Conference on Biaxial/Multiaxial Fatigue and Fracture (ICBMFF), held in Berlin (Germany), on 28 June to 1 July 2004," *International Journal of Fatigue,* vol. 28, pp. 449-450, 2006/05/01/ 2006.

[72] D. Skibicki, *Phenomena and computational models of non-proportional fatigue of materials*: Springer, 2014.

[73] A. Carpinteri, R. Brighenti, E. Macha, and A. Spagnoli, "Expected principal stress directions under multiaxial random loading. Part II: numerical simulation and experimental assessment through the weight function method," *International Journal of Fatigue,* vol. 21, pp. 89-96, 1999/01/01/ 1999.

[74] K. Kanazawa, K. Miller, and M. Brown, "Low-cycle fatigue under out-of-phase loading conditions," *Journal of Engineering Materials and Technology,* vol. 99, pp. 222-228, 1977.

[75] D. McDowell, O. Stahl, S. Stock, and S. Antolovich, "Biaxial path dependence of deformation substructure of type 304 stainless steel," *Metallurgical Transactions A,* vol. 19, pp. 1277-1293, 1988.

[76] I. Ohkawa, H. Takahashi, M. Moriwaki, and M. Misumi, "A study on fatigue crack growth under out-of-phase combined loadings.," *Fatigue & Fracture of Engineering Materials & Structures,* vol. 20, pp. 929-940, 1997.

[77] J. Zhang and Y. Jiang, "An experimental investigation on cyclic plastic deformation and substructures of polycrystalline copper," *International Journal of plasticity,* vol. 21, pp. 2191-2211, 2005.

[78] A. Ahmadi and H. Zenner, "Simulation of microcrack growth for different load sequences and comparison with experimental results," *International journal of fatigue,* vol. 27, pp. 853-861, 2005.

[79] Y. Verreman and H. Guo, "High-cycle fatigue mechanisms in 1045 steel under non-proportional axial-torsional loading," *Fatigue & Fracture of Engineering Materials & Structures,* vol. 30, pp. 932-946, 2007.

[80] T. Nishihara and M. Kawamoto, "The strength of metals under combined alternating bending and torsion with phase difference," *Memoirs of the College of Engineering, Kyoto Imperial University,* vol. 11, pp. 85-112, 1945.

[81] D. McDiarmid, "Fatigue under out-of-phase bending and torsion," *Fatigue & Fracture of Engineering Materials & Structures,* vol. 9, pp. 457-475, 1987.

[82] D. Skibicki, J. Sempruch, and Ł. Pejkowski, "Steel X2CrNiMo17-12-2 testing for uniaxial, proportional and non-proportional loads as delivered and in the annealed condition," in *Materials Science Forum*, 2012, pp. 171-180.

[83] A. Fatemi and D. F. Socie, "A critical plane approach to multiaxial fatigue damage including out-of-phase loading," *Fatigue & Fracture of Engineering Materials & Structures,* vol. 11, pp. 149-165, 1988.

[84] J. A. Bannantine, J. J. Comer, and J. L. Handrock, *Fundamentals of Metal Fatigue Analysis*: Prentice Hall, 1990.

[85] eFatigue.com. (Access date: 02 Mar 2017). *Multiaxial Strain-Life Technical Background*. Available: [online] at https://www.efatigue.com/multiaxial/background/strainlife.html

[86] B. Alfredsson and A. Cadario, "A study on fretting friction evolution and fretting fatigue crack initiation for a spherical contact," *International Journal of Fatigue,* vol. 26, pp. 1037-1052, 2004/10/01/ 2004.

[87] D. Nowell, D. Dini, and D. A. Hills, "Recent developments in the understanding of fretting fatigue," *Engineering Fracture Mechanics,* vol. 73, pp. 207-222, 2006/01/01/ 2006.

[88] M. P. Szolwinski and T. N. Farris, "Mechanics of fretting fatigue crack formation," *Wear,* vol. 198, pp. 93-107, Oct 1996.

[89] M. Nesládek, M. Španiel, J. Jurenka, J. Růžička, and J. Kuželka, "Fretting fatigue – Experimental and numerical approaches," *International Journal of Fatigue,* vol. 44, pp. 61-73, 2012/11/01/ 2012.

[90] T. Rabczuk and T. Belytschko, "Cracking particles: a simplified meshfree method for arbitrary evolving cracks," *International Journal for Numerical Methods in Engineering,* vol. 61, pp. 2316-2343, 2004.

[91] T. Rabczuk, G. Zi, S. Bordas, and H. Nguyen-Xuan, "A simple and robust three-dimensional cracking-particle method without enrichment," *Computer Methods in Applied Mechanics and Engineering,* vol. 199, pp. 2437-2455, 2010/08/01/ 2010.

[92] H. Ren, X. Zhuang, Y. Cai, and T. Rabczuk, "Dual-horizon peridynamics," *International Journal for Numerical Methods in Engineering,* vol. 108, pp. 1451-1476, 2016.

[93] H. Ren, X. Zhuang, and T. Rabczuk, "Dual-horizon peridynamics: A stable solution to varying horizons," *Computer Methods in Applied Mechanics and Engineering,* vol. 318, pp. 762-782, 2017/05/01/ 2017.

[94] N. A. Bhatti and M. Abdel Wahab, "Fretting fatigue crack nucleation: A review," *Tribology International,* vol. 121, pp. 121-138, 5// 2018.

[95] W. Findley, J. Coleman, and B. Hanley, "Theory for combined bending and torsion fatigue with data for SAE 4340 steel. Technical Report No. 1 on basic reseearch on fatigue failures under combined stress," Brown Univ., Providence. Engineering Materials Research Lab.1956.

[96] W. N. Findley, "A theory for the effect of mean stress on fatigue of metals under combined torsion and axial load or bending," *Journal of Engineering for Industry,* pp. 301-306, Nov. 1959.

[97] M. W. Brown and K. J. Miller, "A Theory for Fatigue Under Multiaxial Stress-Strain Conditions," in *A Theory for Fatigue Under Multiaxial Stress-Strain Conditions," Proceedings of the Institute of Mechanical Engineers*, 1973, pp. 745-756.

[98] D. Socie, "Multiaxial Fatigue Damage Models," *Journal of Engineering Materials and Technology,* vol. 109, pp. 293-298, 1987.

[99] D. Socie, "Critical plane approaches for multiaxial fatigue damage assessment," in *Advances in multiaxial fatigue*, ed: ASTM International, 1993.

[100] K. Smith, T. Topper, and P. Watson, "A stress-strain function for the fatigue of metals," *Journal of materials,* vol. 5, pp. 767-778, 1970.

[101] D. L. McDiarmid, "A general criterion for high cycle multiaxial fatigue failure," *Fatigue & Fracture of Engineering Materials & Structures,* vol. 14, pp. 429-453, 1991.

[102] K. C. Liu, "A Method Based on Virtual Strain-Energy Parameters for Multiaxial Fatigue Life Prediction," in *Advances in Multiaxial Fatigue*, D. L. McDowell and R. Ellis, Eds., ed American Society for Testing and Materials, Philadelphia: ASTM STP 1191, 1993, pp. 67-84.

[103] B.-R. You and S.-B. Lee, "A critical review on multiaxial fatigue assessments of metals," *International Journal of Fatigue,* vol. 18, pp. 235-244, 1996/05/01 1996.

[104] A. Karolczuk and E. Macha, "A review of critical plane orientations in multiaxial fatigue failure criteria of metallic materials," *International Journal of Fracture,* vol. 134, pp. 267-304, 2005.

[105] J. Park and D. Nelson, "Evaluation of an energy-based approach and a critical plane approach for predicting constant amplitude multiaxial fatigue life," *International Journal of Fatigue,* vol. 22, pp. 23-39, 1// 2000.

[106] eFatigue.com. (Access date: 02 Mar 2017.[online] Available at: https://www.efatigue.com/multiaxial/background/stresslife.html, 02 Mar). *Multiaxial Stress-Life Technical Background*. Available: [online] Available at: https://www.efatigue.com/multiaxial/background/stresslife.html

[107] D. McDiarmid, "Crack systems in multiaxial fatigue," in *ICF7, Houston (USA) 1989*, 1989.

[108] D. McDiarmid, "Mean Stress Effects in Biaxial Fatigue where the Stresses are Out-of-Phase and Different Frequencies," in *ICBMFF3*, 1991.

[109] C. Navarro, S. Muñoz, and J. Domínguez, "On the use of multiaxial fatigue criteria for fretting fatigue life assessment," *International Journal of Fatigue,* vol. 30, pp. 32-44, 1// 2008.

[110] S. A. Namjoshi, S. Mall, V. K. Jain, and O. Jin, "Fretting fatigue crack initiation mechanism in Ti–6Al–4V," *Fatigue & Fracture of Engineering Materials & Structures,* vol. 25, pp. 955-964, 2002.

[111] F. A. Kandil, M. W. Brown, and K. Miller, "Biaxial low-cycle fatigue failure of 316 stainless steel at elevated temperatures," in *Mechanical behaviour and nuclear applications of stainless steel at elevated temperatures*, ed, 1982.

[112] C. Wang and M. Brown, "A PATH-INDEPENDENT PARAMETER FOR FATIGUE UNDER PROPORTIONAL AND NON-PROPORTIONAL LOADING," *Fatigue & fracture of engineering materials & structures,* vol. 16, pp. 1285-1297, 1993.

[113] R. W. Neu, J. A. Pape, and D. R. Swalla, "Methodologies for linking nucleation and propagation approaches for predicting life under fretting fatigue," in *Fretting Fatigue: Current Technology and Practices*. vol. 1367, D. W. Hoeppner, V. Chandrasekaran, and C. B. Elliott, Eds., ed, 2000, pp. 369-388.

[114] J. A. Araújo and D. Nowell, "The effect of rapidly varying contact stress fields on fretting fatigue," *International Journal of Fatigue,* vol. 24, pp. 763-775, 7 2002.

[115] C. D. Lykins, S. Mall, and V. Jain, "An evaluation of parameters for predicting fretting fatigue crack initiation," *International Journal of Fatigue,* vol. 22, pp. 703-716, Sep 2000.

[116] X. Li, Z. Zuo, and W. Qin, "A fretting related damage parameter for fretting fatigue life prediction," *International Journal of Fatigue,* vol. 73, pp. 110-118, 2015.

[117] P. A. McVeigh and T. N. Farris, "Finite Element Analysis of Fretting Stresses," *Journal of Tribology,* vol. 119, pp. 797-801, 1997.

[118] C. D. Lykins, S. Mall, and V. K. Jain, "Combined experimental–numerical investigation of fretting fatigue crack initiation," *International Journal of Fatigue,* vol. 23, pp. 703-711, 9// 2001.

[119] C.-H. Goh, R. W. Neu, and D. L. McDowell, "Crystallographic plasticity in fretting of Ti–6AL–4V," *International Journal of Plasticity,* vol. 19, pp. 1627-1650, 2003/10/01/ 2003.

[120] F. P. E. Dunne, A. J. Wilkinson, and R. Allen, "Experimental and computational studies of low cycle fatigue crack nucleation in a polycrystal," *International Journal of Plasticity,* vol. 23, pp. 273-295, 2007/02/01/ 2007.

[121] O. McCarthy, J. McGarry, and S. Leen, "The effect of grain orientation on fretting fatigue plasticity and life prediction," *Tribology International,* vol. 76, pp. 100-115, 2014.

[122] D. Nowell, "An analysis of fretting fatigue," University of Oxford, 1988.

[123] S. Naboulsi and S. Mall, "Fretting fatigue crack initiation behavior using process volume approach and finite element analysis," *Tribology International,* vol. 36, pp. 121-131, 2003/02/01/ 2003.

[124] C. Navarro and J. Domínguez, "Initiation criteria in fretting fatigue with spherical contact," *International Journal of Fatigue,* vol. 26, pp. 1253-1262, 2004/12/01/ 2004.

[125] H. Proudhon, S. Fouvry, and J.-Y. Buffière, "A fretting crack initiation prediction taking into account the surface roughness and the crack nucleation process volume," *International Journal of fatigue,* vol. 27, pp. 569-579, 2005.

[126] O. Jin and S. Mall, "Effects of slip on fretting behavior: experiments and analyses," *Wear,* vol. 256, pp. 671-684, 2004/04/01/ 2004.

[127] O. Jin and S. Mall, "Effects of independent pad displacement on fretting fatigue behavior of Ti–6Al–4V," *Wear,* vol. 253, pp. 585-596, 2002/09/01/ 2002.

[128] H. Lee and S. Mall, "Investigation into Tangential Force and Axial Stress Effects on Fretting Fatigue Behavior," *Journal of Engineering Materials and Technology,* vol. 128, pp. 202-209, 2005.

[129] W. S. Sum, E. J. Williams, and S. B. Leen, "Finite element, critical-plane, fatigue life prediction of simple and complex contact configurations," *International Journal of Fatigue,* vol. 27, pp. 403-416, 4// 2005.

[130] M. Almajali, "Effects of Phase Difference Between Axial and Contact loads on Fretting Fatigue Behavior of Titanium Alloy," DTIC Document2006.

[131] R. Hojjati-Talemi, M. A. Wahab, and P. De Baets, "Finite element simulation of phase difference effects on fretting fatigue crack nucleation behaviour," *Proceedings of the Institution of Mechanical Engineers Part J-Journal of Engineering Tribology,* vol. 228, pp. 470-479, Apr 2014.

[132] J. J. Madge, S. B. Leen, and P. H. Shipway, "A combined wear and crack nucleation–propagation methodology for fretting fatigue prediction," *International Journal of Fatigue,* vol. 30, pp. 1509-1528, 2008/09/01/ 2008.

[133] J. J. Madge, S. B. Leen, I. R. McColl, and P. H. Shipway, "Contact-evolution based prediction of fretting fatigue life: Effect of slip amplitude," *Wear,* vol. 262, pp. 1159-1170, Apr 2007.

[134] J. J. Madge, S. B. Leen, and P. H. Shipway, "The critical role of fretting wear in the analysis of fretting fatigue," *Wear,* vol. 263, pp. 542-551, 2007/09/10/ 2007.

[135] M. R. Hirsch and R. W. Neu, "Fretting damage in thin sheets: Analysis of an experimental configuration," *Tribology International,* vol. 44, pp. 1503-1510, 2011/10/01/ 2011.

[136] M. Sabsabi, E. Giner, and F. Fuenmayor, "Experimental fatigue testing of a fretting complete contact and numerical life correlation using X-FEM," *International Journal of Fatigue,* vol. 33, pp. 811-822, 2011.

[137] S. M. O'Halloran, A. D. Connaire, A. M. Harte, and S. B. Leen, "Modelling of fretting in the pressure armour layer of flexible marine risers," *Tribology International,* vol. 100, pp. 306-316, Aug 2016.

[138] I. R. McColl, J. Ding, and S. B. Leen, "Finite element simulation and experimental validation of fretting wear," *Wear,* vol. 256, pp. 1114-1127, 2004/06/01/ 2004.

[139] B. Crossland, "Effect of large hydrostatic pressures on the torsional fatigue strength of an alloy steel," *Proc. Int. Conf. Fatigue of Metals,* pp. 138-149, 1956.

[140] F. Ellyin and D. Kujawski, "A multiaxial fatigue criterion including mean-stress effect," in *Advances in Multiaxial Fatigue*, ed: ASTM International, 1993.

[141] A. T. Bernardo, J. A. Araújo, and E. N. Mamiya, "Proposition of a finite element-based approach to compute the size effect in fretting fatigue," *Tribology International,* vol. 39, pp. 1123-1130, 2006/10/01/ 2006.

[142] J. A. Alic, A. L. Hawley, and J. M. Urey, "Formation of fretting fatigue cracks in 7075-T7351 aluminum alloy," *Wear,* vol. 56, pp. 351-361, 1979/10/01/ 1979.

[143] C. T. Tsai and S. Mall, "Elasto-plastic finite element analysis of fretting stresses in pre-stressed strip in contact with cylindrical pad," *Finite Elements in Analysis and Design,* vol. 36, pp. 171-187, 2000/09/01/ 2000.

[144] S. Heredia, S. Fouvry, B. Berthel, and E. Greco, "Introduction of a "principal stress–weight function" approach to predict the crack nucleation risk under fretting fatigue using

FEM modelling," *International Journal of Fatigue,* vol. 61, pp. 191-201, 2014/04/01/ 2014.

[145] C. Gandiolle, S. Garcin, and S. Fouvry, "A non-collinear fretting-fatigue experiment to compare multiaxial fatigue criteria: critical shear plane strategy is better than invariant formulations," *Tribology International,* vol. 108, pp. 57-68, 2017/04/01/ 2017.

[146] C. Ruiz, P. H. B. Boddington, and K. C. Chen, "An investigation of fatigue and fretting in a dovetail joint," *Experimental Mechanics,* vol. 24, pp. 208-217, 1984.

[147] K. Iyer and S. Mall, "Analyses of contact pressure and stress amplitude effects on fretting fatigue life," *Journal of Engineering Materials and Technology-Transactions of the Asme,* vol. 123, pp. 85-93, Jan 2001.

[148] K. Iyer and Mall, *Effects of cyclic frequency and contact pressure on fretting fatigue under two-level block loading* vol. 23, 2001.

[149] M. Massingham and P. E. Irving, "The effect of variable amplitude loading on stress distribution within a cylindrical contact subjected to fretting fatigue," *Tribology International,* vol. 39, pp. 1084-1091, Oct 2006.

[150] R. H. Talemi and M. A. Wahab, "Finite Element Analysis of Localized Plasticity in Al 2024-T3 Subjected to Fretting Fatigue," *Tribology Transactions,* vol. 55, pp. 805-814, Nov 2012.

[151] J. Ding, D. Houghton, E. Williams, and S. Leen, "Simple parameters to predict effect of surface damage on fretting fatigue," *International Journal of Fatigue,* vol. 33, pp. 332-342, 2011.

[152] J. Ding, W. Sum, R. Sabesan, S. Leen, I. McColl, and E. Williams, "Fretting fatigue predictions in a complex coupling," *International Journal of Fatigue,* vol. 29, pp. 1229-1244, 2007.

[153] L. Kachanov, "Time of the rupture process under creep conditions, Izu," *Akad. Nauk SSR Otd. Tech,* pp. 26-31, 1958.

[154] J. Lemaitre, "How to use damage mechanics," *Nuclear Engineering and Design,* vol. 80, pp. 233-245, 1984/07/02/ 1984.

[155] J. Lemaitre, "Evaluation of dissipation and damage in metals submitted to dynamic loading," *Mechanical behavior of materials,* pp. 540-549, 1972.

[156] J. Lemaitre, "A continuous damage mechanics model for ductile fracture," *Transactions of the ASME. Journal of Engineering Materials and Technology,* vol. 107, pp. 83-89, 1985.

[157] J. Lemaitre and J. Chaboche, "A non-linear model of creep-fatigue damage cumulation and interaction(for hot metallic structures)," *Mechanics of visco-elastic media and bodies,* p. 1975, 1975.

[158] J.-L. Chaboche, *Une loi différentielle d'endommagement de fatigue avec cumulation non linéaire*: Office Nationale d'Etudes et de Recherches Aérospatiales, 1974.

[159] B. Bhattacharya and B. Ellingwood, "Continuum damage mechanics analysis of fatigue crack initiation," *International journal of fatigue,* vol. 20, pp. 631-639, 1998.

[160] S. Quraishi, M. Khonsari, and D. Baek, "A thermodynamic approach for predicting fretting fatigue life," *Tribology Letters,* vol. 19, pp. 169-175, 2005.

[161] J. L. Chaboche and P. M. Lesne, "A NON-LINEAR CONTINUOUS FATIGUE DAMAGE MODEL," *Fatigue & Fracture of Engineering Materials & Structures,* vol. 11, pp. 1-17, 1988.

[162] T. Zhang, P. E. McHugh, and S. B. Leen, "Finite element implementation of multiaxial continuum damage mechanics for plain and fretting fatigue," *International Journal of Fatigue,* vol. 44, pp. 260-272, 11/01/ 2012.

[163] M. Chaudonneret, "A Simple and Efficient Multiaxial Fatigue Damage Model for Engineering Applications of Macro-Crack Initiation," *Journal of Engineering Materials and Technology,* vol. 115, pp. 373-379, 1993.

[164] J. Lemaitre, "Formulation and Identification of Damage Kinetic Constitutive Equations," in *Continuum Damage Mechanics Theory and Application*, D. Krajcinovic and J. Lemaitre, Eds., ed Vienna: Springer Vienna, 1987, pp. 37-89.

[165] R. Hojjati-Talemi and M. A. Wahab, "Fretting fatigue crack initiation lifetime predictor tool: Using damage mechanics approach," *Tribology International,* vol. 60, pp. 176-186, Apr 2013.

[166] R. Hojjati-Talemi, M. A. Wahab, E. Giner, and M. Sabsabi, "Numerical estimation of fretting fatigue lifetime using damage and fracture mechanics," *Tribology Letters,* vol. 52, pp. 11-25, 2013.

[167] M. H. El Haddad, N. E. Dowling, T. H. Topper, and K. N. Smith, "J integral applications for short fatigue cracks at notches," *International Journal of Fracture,* vol. 16, pp. 15-30, February 01 1980.

[168] F. Shen, W. Hu, and Q. Meng, "A damage mechanics approach to fretting fatigue life prediction with consideration of elastic–plastic damage model and wear," *Tribology International,* vol. 82, pp. 176-190, 2015/02/01/ 2015.

[169] A. Ferjaoui, T. Yue, M. Abdel Wahab, and R. Hojjati-Talemi, "Prediction of fretting fatigue crack initiation in double lap bolted joint using Continuum Damage Mechanics," *International Journal of Fatigue,* vol. 73, pp. 66-76, Apr 2015.

[170] N. A. Bhatti and M. Abdel Wahab, "A numerical investigation on critical plane orientation and initiation lifetimes in fretting fatigue under out of phase loading conditions," *Tribology International,* vol. 115, pp. 307-318, 11// 2017.

[171] N. A. Bhatti and M. Abdel Wahab, "Finite element analysis of fretting fatigue under out of phase loading conditions," *Tribology International,* vol. 109, pp. 552-562, May 2017.

[172] N. A. Bhatti, K. Pereira, and M. Abdel Wahab, "A continuum damage mechanics approach for fretting fatigue under out of phase loading," *Tribology International,* vol. 117, pp. 39-51, 2018/01/01/ 2018.

[173] H. S. Kim, S. Mall, and A. Ghoshal, "Two-Dimensional and Three-Dimensional Finite Element Analysis of Finite Contact Width on Fretting Fatigue," *MATERIALS TRANSACTIONS,* vol. 52, pp. 147-154, 2011.

[174] E. Giner, M. Tur, A. Vercher, and F. J. Fuenmayor, "Numerical modelling of crack–contact interaction in 2D incomplete fretting contacts using X-FEM," *Tribology International,* vol. 42, pp. 1269-1275, Sep 2009.

[175] T. Yue and M. Abdel Wahab, "A numerical study on the effect of debris layer on fretting wear," *Materials,* vol. 9, p. 597, 2016.

[176] T. Yue and M. Abdel Wahab, "Finite element analysis of fretting wear under variable coefficient of friction and different contact regimes," *Tribology International,* vol. 107, pp. 274-282, 3// 2017.

[177] J. Ding, S. B. Leen, and I. R. McColl, "The effect of slip regime on fretting wear-induced stress evolution," *International Journal of Fatigue,* vol. 26, pp. 521-531, 2004/05/01/ 2004.

[178] G. B. Sinclair, "Stress singularities in classical elasticity—II: Asymptotic identification," *Applied Mechanics Reviews,* vol. 57, pp. 385-439, 2004.

[179] G. B. Sinclair and S. Sezer, *Practical Convergence-Divergence Checks for Stresses from FEA*, 2006.

[180] G. B. Sinclair, "Stress singularities in classical elasticity–I: Removal, interpretation, and analysis," *Applied Mechanics Reviews,* vol. 57, pp. 251-298, 2004.

[181] N. A. Bhatti and M. Abdel Wahab, "Fretting fatigue damage nucleation under out of phase loading using a continuum damage model for non-proportional loading," *Tribology International,* vol. 121, pp. 204-213, 5// 2018.

[182] J. Lemaitre, "Coupled elasto-plasticity and damage constitutive equations," *Computer Methods in Applied Mechanics and Engineering,* vol. 51, pp. 31-49, 1985/09/01/ 1985.

[183] S. Fouvry, P. Kapsa, L. Vincent, and K. Dang Van, "Theoretical analysis of fatigue cracking under dry friction for fretting loading conditions," *Wear,* vol. 195, pp. 21-34, Jul 1996.

[184] D. Nowell, D. Dini, and D. Hills, "Recent developments in the understanding of fretting fatigue," *Engineering Fracture Mechanics,* vol. 73, pp. 207-222, 2006.

[185] I. V. Papadopoulos, "A high-cycle fatigue criterion applied in biaxial and triaxial out-of-phase stress conditions," *Fatigue & Fracture of Engineering Materials & Structures,* vol. 18, pp. 79-91, Jan 1995.

[186] D. Skibicki, "Introduction," in *Phenomena and Computational Models of Non-Proportional Fatigue of Materials*, ed Cham: Springer International Publishing, 2014, pp. 1-7.

[187] H. Proudhon, S. Fouvry, and J. Y. Buffière, "A fretting crack initiation prediction taking into account the surface roughness and the crack nucleation process volume," *International Journal of Fatigue,* vol. 27, pp. 569-579, 5// 2005.

[188] K. Kanazawa, K. J. Miller, and M. W. Brown, "Low-Cycle Fatigue Under Out-of-Phase Loading Conditions," *Journal of Engineering Materials and Technology,* vol. 99, pp. 222-228, 1977.

[189] D. Skibicki, "The Phenomena of Non-Proportionality in Loading Fatigue," in *Phenomena and Computational Models of Non-Proportional Fatigue of Materials*, ed Cham: Springer International Publishing, 2014, pp. 9-47.

[190] H. Lee and S. Mall, "Investigation into tangential force and axial stress effects on fretting fatigue behavior," *Journal of Engineering Materials and Technology-Transactions of the Asme,* vol. 128, pp. 202-209, Apr 2006.

[191] D. Nowell and D. A. Hills, "Crack initiation criteria in fretting fatigue," *Wear,* vol. 136, pp. 329-343, Mar 1990.

[192] E. Giner, J. Díaz-Álvarez, M. Marco, and M. H. Miguélez, "Orientation of propagating crack paths emanating from fretting-fatigue contact problems," *Frattura ed Integritá Strutturale,* vol. 35, p. 285, 2016.

[193] E. Giner, M. Sabsabi, J. J. Rodenas, and F. J. Fuenmayor, "Direction of crack propagation in a complete contact fretting-fatigue problem," *International Journal of Fatigue,* vol. 58, pp. 172-180, Jan 2014.

[194] K. Pereira and M. Abdel Wahab, "Fretting fatigue crack propagation lifetime prediction in cylindrical contact using an extended MTS criterion for non-proportional loading," *Tribology International,* vol. 115, pp. 525-534, 11// 2017.

[195] F. Hourlier, H. d'Hondt, M. Truchon, and A. Pineau, "Fatigue crack path behavior under polymodal fatigue," in *Multiaxial Fatigue*, ed: ASTM International, 1985.

[196] L. Liu, "Modeling of mixed-mode fatigue crack propagation," Vanderbilt University, 2008.

[197] K. Pereira, N. Bhatti, and M. A. Wahab, "Prediction of fretting fatigue crack initiation location and direction using cohesive zone model," *Tribology International,* 2018.

[198] J. Vázquez, S. Astorga, C. Navarro, and J. Domínguez, "Analysis of initial crack path in fretting fatigue," *Frattura ed Integrità Strutturale,* vol. 10, pp. 38-45, 2016.

[199] A. Fatemi, A. Plaseied, A. K. Khosrovaneh, and D. Tanner, "Application of bi-linear log–log S–N model to strain-controlled fatigue data of aluminum alloys and its effect on life predictions," *International Journal of Fatigue,* vol. 27, pp. 1040-1050, 9// 2005.

[200] A. A. Walvekar, B. D. Leonard, F. Sadeghi, B. Jalalahmadi, and N. Bolander, "An experimental study and fatigue damage model for fretting fatigue," *Tribology International,* vol. 79, pp. 183-196, 2014.